Frode Grytten

Low-Velocity Penetration of Aluminium Plates

Thesis for the degree of philosophiae doctor

Trondheim, April 2008

Norwegian University of
Science and Technology
Faculty of Engineering Science and Technology
Department of Structural Engineering

NTNU
Norwegian University of
Science and Technology

NTNU
Norwegian University of Science and Technology

Thesis for the degree of philosophiae doctor

Faculty of Engineering Science and Technology
Department of Structural Engineering

ISBN 978-82-471-6826-4 (printed ver.)
ISBN 978-82-471-6843-1 (electronic ver.)
ISSN 1503-8181

Theses at NTNU, 2008:46

Printed by Tapir Uttrykk

Preface

This thesis is submitted in partial fulfilment of the requirements for the degree "philosophiae doctor" at the Norwegian University of Science and Technology (NTNU), Trondheim, Norway.

The work has been carried out at the Faculty of Engineering Science and Technology, Department of Structural Engineering under supervision of adjunct Professor Tore Børvik, Professor Magnus Langseth and Professor Odd Sture Hopperstad.

The work described in part I of this thesis was done in collaboration with Mr Bernt Førre and Mr Egil Fagerholt at the Department of Physics. Fagerholt established the described measurement methodology as part of his M.Sc. thesis under supervision of adjunct professor Tore Børvik, Mr. Bernt Førre and PhD-student Frode Grytten.

Part III of this thesis was done in collaboration with Dr Bjørn Holmedal at Department of Materials Science and Technology, who carried out the crystal plasticity calculations.

Abstract

The present thesis describes research on quasi-static and low velocity perforation of rolled aluminium plates, where the main objective has been to gain a better knowledge of the physical processes taking place during this type of structural problem. The objective has been met by a combination of laboratory tests, material modelling and non-linear finite element simulations.

The thesis is organized in a synopsis, giving a brief introduction to the problem and summarising the main findings and conclusions, in addition to four independent papers.

Paper I presents an experimental technique for measuring the deformations the plate undergoes during impact and perforation. This information can be used to validate numerical models and to increase the understanding of how energy is absorbed by the plate.

Paper II presents an experimental and numerical investigation on the quasi-static perforation of AA5083-H116 aluminium plates. In the tests, square plates were mounted in a circular frame and penetrated by a cylindrical punch. A full factorial design was used to investigate the effects of varying plate thickness, boundary conditions, punch diameter and nose shape. Based on the obtained results, both the main and interaction effects on the maximum force, displacement at fracture and energy absorption until

perforation were determined. The perforation process was then computer analysed using the nonlinear finite element code LS-DYNA. Simulations with axisymmetric elements, brick elements and shell elements were conducted. Slightly modified versions of the Johnson-Cook constitutive relation and fracture criterion were used to model the material behaviour. It was shown that the FEM models were able to predict the trends observed in experiments.

Paper III evaluates methods for determination of the anisotropic properties of polycrystalline metallic materials. Four calibration methods were evaluated for the linear transformation-based anisotropic yield function YLD2004-18p (Barlat et al., 2005) and the aluminium alloy AA5083-H116. The different parameter identifications are based on least squares fits to combinations of uniaxial tensile tests in seven directions with respect to the rolling direction, compression (upsetting) tests in the normal direction and stress states found using the full-constraint (FC) Taylor model for 690 evenly distributed strain paths. An elastic-plastic constitutive model based on YLD2004-18p has been implemented in a non-linear finite element code and used in finite element simulations of plane-strain tension tests, shear tests and upsetting tests. The experimental results as well as the Taylor model predictions can be satisfactorily reproduced by the considered yield function. However, the lacking ability of the Taylor model to quantitatively reproduce the experiments calls for more advanced texture models.

Paper IV presents an experimental and numerical investigation on low velocity perforation of AA5083-H116 aluminium plates. In the tests, square plates were mounted

in a circular frame and penetrated by a cylindrical blunt-nosed projectile. The perforation process was then computer analysed using the nonlinear finite element code LS-DYNA, in order to investigate the effects of anisotropy, dynamic strain aging and thermal softening in low velocity impacts on the present aluminium alloy. Dynamic strain aging has been shown to influence both the predicted force level and fracture, while thermal softening only influences the fracture prediction. No effect of plastic anisotropy was observed.

Acknowledgements

This work has been carried out at the Structural Impact Laboratory (SIMLab) / Department of Structural Engineering, Norwegian University of Science and Technology (NTNU). My supervisors during this project have been Adjunct Professor Tore Børvik, Professor Magnus Langseth and Professor Odd Sture Hopperstad. Their encouragements and guidance throughout this work is highly appreciated.

The assistance of the laboratory staff, in particular Mr Trond Auestad and Mr Trygve Meltzer, is gratefully acknowledged. In connection with the optical measurement technique, I acknowledge the instructive collaboration with Mr Bernt Førre, Department of Physics and Mr Egil Fagerholt who implemented the MatLab routines. I also acknowledge the fruitful collaboration with Dr Bjørn Holmedal, Department of Materials Science and Technology, who carried out the crystal plasticity calculations in part III. Further, I would like to thank my fellow PhD students and colleagues at SIMLab for providing a stimulating and friendly working environment.

This research was made possible by financial support from the Research Council of Norway, the Norwegian Defence Estates Agency and CRI-SIMLab.

Finally, I would like to thank my friends and my family for their support and encouragement and for having faith in me during these years.

Contents

Preface i
Abstract.. iii
Acknowledgements vii
Contents.. ix
Synopsis.. 1
1 Introduction 1
2 Project objective and research strategy 9
3 Organisation and summary of the thesis 10
4 Concluding remarks... 15
5 Suggestions for further work 17
References 18

Part I: Frode Grytten, Egil Fagerholt, Trond Auestad, Bernt Førre and Tore Børvik. **Out-of-plane deformation measurements of an aluminium plate during quasi-static perforation using structured light and close-range photogrammetry.** International Journal of Solids and Structures, Volume 44, Issue 17, Pages 5752-5773, 2007.

Part II: Frode Grytten, Tore Børvik, Odd Sture Hopperstad, Magnus Langseth. **Quasi-static perforation of thin aluminium plates.** Accepted for publication in International Journal of Impact Engineering.

Part III: Frode Grytten, Bjørn Holmedal, Odd Sture Hopperstad, Tore Børvik. **Evaluation of identification methods for YLD2004-18p.** Accepted for publication in International Journal of Plasticity.

Part IV: Frode Grytten, Tore Børvik, Odd Sture Hopperstad, Magnus Langseth. **Low velocity perforation of AA5083-H116 aluminium plates.** Submitted for possible journal publication.

Synopsis

1 Introduction

Structural impact has become increasingly important in structural design. Earlier, problems involving impact were primarily of military interest. Nowadays, accidental structural impact problems are also a concern in numerous civilian fields, such as the offshore industry, naval industry, aviation and space industry as well as the nuclear and process industry, just to mention some. The collision of two or more bodies can be anything from dropped objects, collision or grounding of vessels, collision of vehicles or aircrafts to accidental impacts like bird strikes in aviation and space debris and meteoroids in space. Due to the increasing focus on the impact problem, it is important to understand the material's behaviour when subjected to impulsive loading. The high strain rates and the elevated temperature associated with impact loading influence both the flow stress and the ductility of the material.

Several projects concerning structural impact have been carried out at the Department of Structural Engineering at NTNU during the last couple of decades. The projects that are of most relevance to the present work are those of Langseth (1988) who studied the plugging capacity of steel plates subjected to dropped objects and Hildrum (2002) who studied stiffened aluminium plates subjected to impact loading. Both investigations concerned the low velocity regime and the present work is a continuation those two projects. Other people who have studied penetration at the department are Børvik (2000), Dey (2004) and Seah (1006).

The fact that structural impact problems were initially of interest to the military, is reflected in the terminology. It is therefore useful to give the definitions of some terms frequently used in the structural impact literature. The reader is referred to Børvik (2003) for a more thorough presentation of the subject. *Impact* is defined as the collision between two or more bodies, where the interaction between the bodies can be elastic, plastic, fluid or any combination of these. The *impact velocity* is one of the fundamental quantities in impact dynamics. Table 1 lists the different velocity regimes and their corresponding applications and test methods. The definitions are based on Backman and Goldsmith (1978) and Børvik (2000). Note that these definitions are not absolute, and should be considered as guidelines.

Table 1 Velocity regimes and corresponding applications and test methods.

Velocity regime	Impact test equipment	Material test method	Typical applications
Low velocity 0-50 m/s	-drop hammer -pneumatic accelerator	Quasi-static testing machines: -hydraulic -servo-hydraulic -screw-driven	-dropped objects -vehicle impact -ship collision -crashworthiness of containers for hazardous materials
Sub-ordnance 50-500 m/s	-compressed air gun -gas gun	-pneumatic -hydraulic -Taylor impact tests -Split Hopkinson Pressure bar (SHPB) or Tension bar (SHTB)	-design of nuclear containment -free-falling bombs and missiles -fragments due to accidental explosions
Ordnance 500-1300 m/s	-compressed gas gun -powder gun	-Taylor tests -SHPB/SHTB	-military
Ultra-ordnance 1300-3000 m/s	-powder gun -two-stage light gas gun	-Taylor impact test	-military
Hypervelocity >3000 m/s	-two-stage light gas gun	-Taylor impact test	-space vessels exposed to meteoroid impact and space debris

According to Zukas et al. (1982), the term *projectile* can be used for any item capable of being launched. The *target* is defined as any moving or stationary object struck by the projectile. The branch of structural impact dynamics dealing with problems involving a projectile striking a target is often referred to as *terminal ballistics*. Projectiles are normally categorised as soft, semi-hard or hard depending on the material that is used and the degree of deformation it undergoes during impact. *Soft projectiles* undergo significant deformation during impact, *semi-hard projectiles* experience some deformation, while *hard projectiles* experience small or negligible deformations and the response is dominated by the target response. Further, it is usual to characterize the projectile by its initial geometry. Figure 1 shows some generic projectile shapes used to mimic real objects.

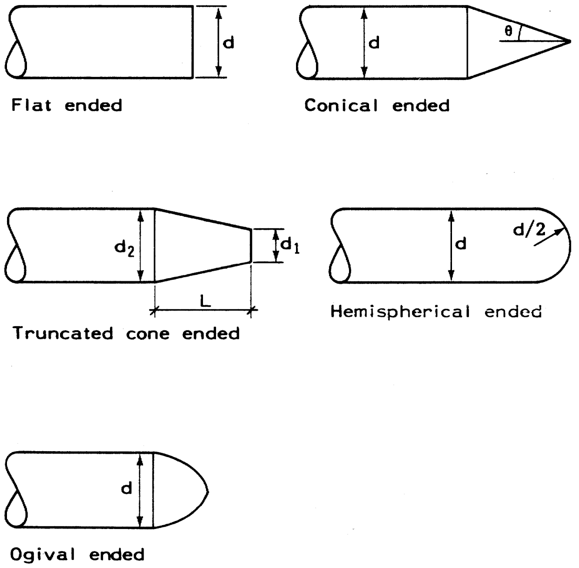
Flat ended

Conical ended

Truncated cone ended

Hemispherical ended

Ogival ended

Figure 1 Generic projectile shapes (Langseth, 1988).

It is convenient to classify targets by thickness. According to Backman and Goldsmith (1978) a target is said to be *semi-infinite* if there is no influence of the distal boundary on the penetration process. It is *thick* if there is influence of the distal boundary only after substansial travel of the projectile into the target. The target thickness is *intermediate* if the rear surface exerts considerable influence on the deformation process during nearly the entire projectile motion. Finally, the target thickness is said to be *thin* if there are no through-thickness stress gradient. Other characteristics of the target are shape (flat, curved, serrated, irregular and circular or rectangular), composition (monolithic plate, composites, spaced plates, etc.) and boundary conditions (free, simply supported and clamped).

Penetration is defined as entry of the projectile into any region of the target (Backman and Goldsmith, 1978), and includes perforation, containment and rebound. *Perforation* means that the projectile passes through the target with a final residual velocity. *Containment* or *embedment* means that the projectile is stopped during contact with the target. *Rebound* or *ricochet* means that the projectile is deflected from the target with a final rebound velocity.

A commonly used measure of a target's ability to withstand impact by a certain projectile is the *ballistic limit velocity*, defined as the greatest impact velocity the target can withstand without being perforated. The ballistic limit is often approximated by the average of the greatest velocity that do not lead to perforation and the lowest velocity leading to perforation.

It is common to divide the target response into non-perforating and perforating modes (Backman and Goldsmith, 1978). Non-perforating modes are elastic deformation, plastic deformation and cratering. Pure elastic deformation of the target can only be achieved at extremely low projectile velocities, and is an unrealistic condition during impact loading. After unloading, the deformation is totally recovered and no damage is obtained. Two types of transverse displacement due to plastic deformation normally exist in an impacted plate. A *bulge* is formed in the contact zone when the target deforms to the shape of the projectile. Dishing is induced by bending and may extend to considerable distances from the impacted area. Both bulging and dishing are illustrated in Figure 2.

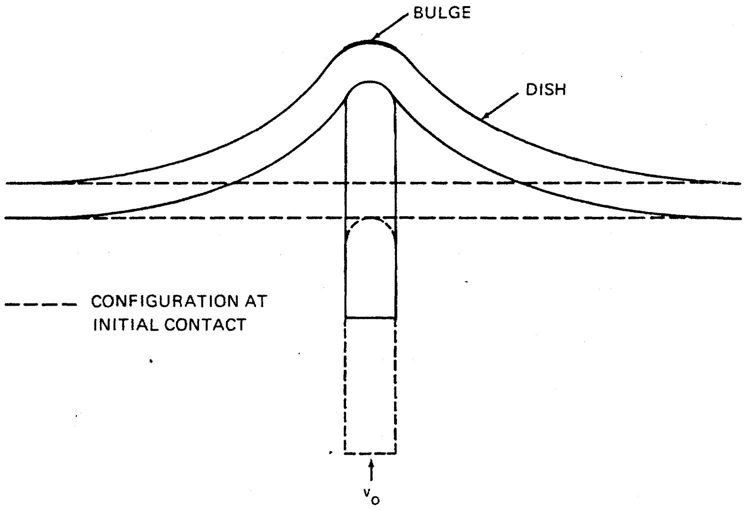

Figure 2 Deformation of a thin plate showing bulging and dishing (Backman and Goldsmith, 1978)

A variety of failure modes can lead to perforation. According to Zukas et al. (1982), the different failure modes depend on variables such as material properties, impact velocity, projectile nose shape, target geometry, support conditions, relative mass of projectile and target, etc. The most common failure modes are shown in Figure 3. Although one of these modes will dominate, the target may fail by a combination of failure modes. The most relevant failure modes in the present study are plugging and petaling. A *plugging* failure occurs when the projectile pushes a plug out of the target approximately equal in diameter to that of the projectile. This type of failure is most frequently found when blunt projectiles are used. An *isothermal shear failure* will occur for low loading rates and a conventional fracture mode with void formation and growth will occur. An *adiabatic shear failure* is related to large shearing deformations occurring at high deformation rates. During the plastic deformation most of the work is converted into heat that, because of the high deformation rate, does not have time to disperse. Strain and strain-rate hardening are overcome by thermal softening due to the local heating, causing a reduced shear capacity. The shape of the plug depends on the stress state that is triaxial (shear combined with membrane and bending stresses). If pure shear occurs at the periphery of the projectile a cylindrical plug is ejected. However, small amounts of normal stresses may change the orientation of the plane of maximum shear and a truncated cone or inverted truncated cone shaped plug can occur. *Petaling* occurs when the tensile strength is exceeded at the rear side of the target and a star-shaped crack develops around the tip of the projectile. The sectors formed are then pushed back by the motion of the projectile, forming petals.

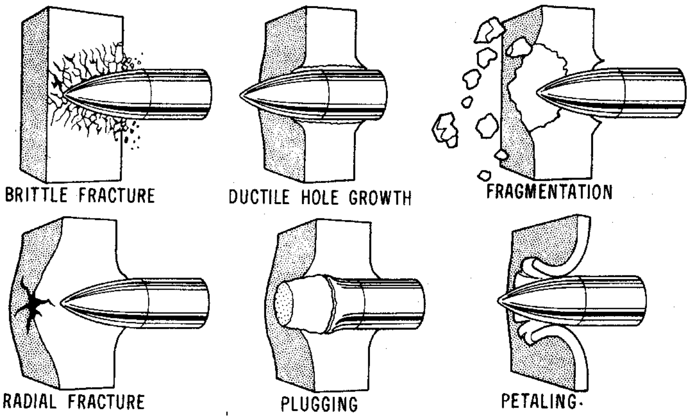

Figure 3 Common failure modes (Zukas et al., 1982).

In light of the complexity of perforation problems, it is not surprising that the bulk of the work in this area is experimental in nature. Efficient accelerators and highly sophisticated instrumentation are needed to carry out experimental investigations of penetration problems. Typical accelerators used in the various velocity ranges are listed in Table 1. The amount of data retrieved during an experiment depend on the degree of instrumentation and on the limitations of the equipment that is used (cameras, counters, gauges, or any optical, electronic or mechanical instrument used to collect data). The dynamic response of the involved materials strongly influences the impact event.

Therefore, various material testing techniques have been developed to cover a wide range of strain rates. The most common methods are listed in Table 1.

Methods to analyse the penetration process generally fall into one out of three categories. The first is the *experimental* or *empirical approach,* where large amounts of experimental data are obtained and correlated. Simple algebraic equations are then formulated based on curve fits. Such efforts are usually closely related to tests performed to discriminate between the performance characteristics of various materials or structures for a particular design objective. While this is a relatively powerful procedure for solving a specific problem, it is dangerous to extrapolate the information to other materials, geometries or velocity ranges. This approach provides little if any fundamental understanding of material behaviour or the underlying mechanisms behind the impact event. The second approach is the development and use of *engineering models* to simulate impact events. Such methods are also frequently termed *analytical models* or *phenomenological methods* in the literature. These methods are based on simplified assumptions, e.g. the projectile is rigid, no work hardening or thermal effects in the target, etc. Furthermore, almost all such analysis requires some empirical input or relies on material parameters not readily available or measurable. Another problem is that if the models become too sophisticated and too many phenomena are treated, they lose their advantage of simplicity. The final approach is the *numerical methods* which are approximate in nature, but at present, errors associated with material properties are usually far greater than errors inherent in the numerical method. Therefore, even if the solution sometimes is not quantitatively correct, it gives a reliably qualitatively answer and the method is very powerful during parametric studies. Furthermore, a lot of information (such as interface force, thermal phenomena, stress and strain distribution) that usually is very hard to get experimentally becomes available.

Each of the three procedures for solving impact problems has merits and disadvantages. Since one procedure can not always provide all the desired information concerning a complex impact phenomenon, a combination of these methods is often the best approach. A successful application of all these procedures depends upon an understanding of the related basic principles (conservation laws, the role of wave propagation, the influence of inertia, and an understanding of material behaviour under high rates of loading). Without this knowledge, any solution method will fail.

2 Project objective and research strategy

The main objective of this thesis work is to study the behaviour of monolithic aluminium plates subjected to large mass projectiles in the low velocity range and to gain a better understanding of the physical processes taking place during this type of structural problem. The work is limited to one specific aluminium alloy, namely AA5083-H116.

The objective is met through a research method based on an integrated use of experimental work (both material and component tests), material modelling and non-linear finite element analysis. To accomplish the objective, the following activities are defined:

- Experimental investigation of the material behaviour to
    - Provide experimental data on the behaviour of AA5083-H116.
    - Characterize and predict the material's response to large plastic deformations at elevated rates of strain.
    - Characterize and predict ductile fracture.
- Experimental investigation of the component behaviour to
    - Provide experimental data on the behaviour of monolithic AA5083-H116 plates subjected to large mass projectiles in the low velocity range or quasi-static perforation.
    - Validate numerical models.
- Numerical investigation of the component behaviour to
    - Investigate the influence of material properties that can not be changed in experiments.
    - Establish and validate design tools.

3 Organisation and summary of the thesis

This thesis consists of a synopsis followed by four independent journal papers. The synopsis provides the background and strategy of the work, and links the parts together. A complete list of references to the papers that form this thesis is given in Table 2. Related conference papers which are not included in the present thesis are listed in Table 3. The research strategy and the connection between the various parts of this thesis are illustrated in Figure 4.

Table 2 Contributions included in the thesis.

Part no.	Journal papers
1.	Frode Grytten, Egil Fagerholt, Trond Auestad, Bernt Forre and Tore Børvik. *Out-of-plane deformation measurements of an aluminium plate during quasi-static perforation using structured light and close-range photogrammetry*. International Journal of Solids and Structures, Volume 44, Issue 17, Pages 5752-5773, 2007.
2.	Frode Grytten, Tore Børvik, Odd Sture Hopperstad, Magnus Langseth. *Quasi-static perforation of thin aluminium plates*. Accepted for publication in International Journal of Impact Engineering.
3.	Frode Grytten, Bjørn Holmedal, Odd Sture Hopperstad, Tore Børvik. *Evaluation of identification methods for YLD2004-18p*. Accepted for publication in International Journal of Plasticity.
4.	Frode Grytten, Tore Børvik, Odd Sture Hopperstad, Magnus Langseth. *Low velocity perforation of AA5083-H116 aluminium plates*. Submitted for possible journal publication.

Table 3 Contributions not included in the thesis

Part no.	Conference papers
5.	Frode Grytten, Tore Børvik, Odd Sture Hopperstad, Magnus Langseth. *Numerical simulations of perforation of AA5083-H116 plates*. In: MekIT'05 Third national conference on Computational Mechanics. Trondheim: Tapir Akademisk Forlag 2005. ISBN 82-519-2052-3. Pages 117-134.
6.	Frode Grytten, Tore Børvik, Odd Sture Hopperstad, Magnus Langseth. *On the Quasi-Static Perforation Resistance of Circular AA5083-H116 Aluminium Plates*. In: 9th International LSDYNA Users Conference 2006. Livermore, USA: Livermore Software Technology Corporation 2006. ISBN 0-9778540-1-9.

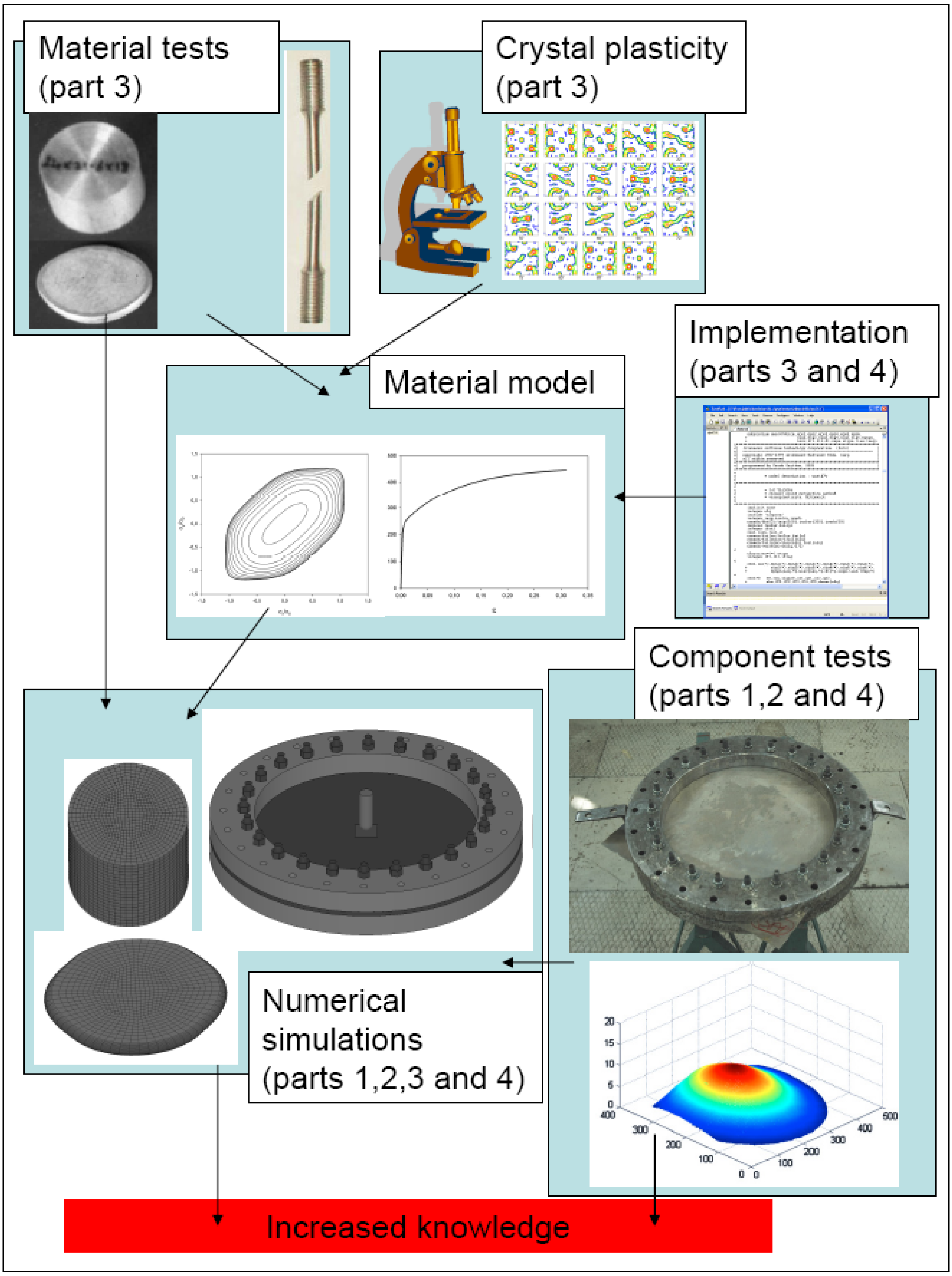

Figure 4 Research strategy

Part I presents an experimental technique for measuring the deformations the plate undergoes during impact and perforation. This information can be used both to validate numerical models and to increase the understanding of how energy is absorbed by the plate during punching or impact. The measurement principle described in this paper is based on structured light and close-range photogrammetry. During testing the rear surface of the target is illuminated with a fringe pattern. The projected pattern consists of black and white stripes, i.e. a discrete binary pattern, which is observed and recorded through a greyscale camera, providing intensity maps of the fringe pattern projected to the target surface. The fringe pattern is analysed as it appears in the intensity maps recorded by the cameras and the topography of the target is calculated using a calibrated camera model and a look-up-table which holds information on how the fringe pattern appears with varying deformation values. To obtain satisfactory absolute accuracy of the three-dimensional measurements, a camera model which corrects for radial and decentring distortion must be used and a proper calibration of the system is required (Atkinson, 1996; Heikkilä, 1997). It was also shown in this part that the boundary conditions are very important for the displacement field of the plate under quasi-static loading conditions.

Part II presents an experimental and numerical investigation on the quasi-static perforation of AA5083-H116 aluminium plates. In the tests, square plates were mounted in a circular frame and penetrated by a cylindrical punch. A full factorial design was used to investigate the effects of varying plate thickness, boundary conditions, punch diameter and nose shape. Based on the obtained results, both the main and interaction effects on the maximum force, displacement at fracture and energy absorption until perforation were determined. The perforation process was then computer analysed using the nonlinear finite element code LS-DYNA. Simulations with axisymmetric elements, brick elements and shell elements were conducted. Slightly modified versions of the Johnson-Cook constitutive relation and fracture criterion were used to model the material behaviour. It was shown that the numerical models were able to predict the trends observed in experiments.

Methods for determination of the anisotropic properties of polycrystalline metallic materials are evaluated in Part III. Four calibration methods were evaluated for the linear transformation-based anisotropic yield function YLD2004-18p (Barlat et al., 2005) and the aluminium alloy AA5083-H116. The different parameter identifications are based on least squares fits to combinations of uniaxial tensile tests in seven directions with respect to the rolling direction, compression (upsetting) tests in the normal direction and stress states found using the full-constraint (FC) Taylor model for 690 evenly distributed strain paths. An elastic-plastic constitutive model based on YLD2004-18p was implemented in a non-linear finite element code and used in finite element simulations of plane-strain tension tests, shear tests and upsetting tests. Further, it was shown that crystal plasticity calculations can not fully replace experiments at the present state of the art.

Part IV presents an experimental and numerical investigation on low velocity perforation of AA5083-H116 aluminium plates. In the tests, square plates were mounted in a circular frame and penetrated by a cylindrical blunt-nosed projectile. The perforation process was then computer analysed using the nonlinear finite element code

LS-DYNA in order to investigate the effects of anisotropy, dynamic strain aging and thermal softening in low velocity impacts on the present aluminium alloy. It was shown that dynamic strain ageing could influence both the predicted force level and fracture. In the simulations, the temperature increase only affected the fracture predictions while plastic anisotropy did not seem to have any effect on the predictions. It must be noted that a much denser element mesh than what is feasible today may give other results.

4 Concluding remarks

Conclusions for each individual part of the present work may be found at the end of each paper. However, some of the main conclusions are given in this section.

- A full-field deformation measurement technique, including an appropriate calibration routine, has been established. The methodology can in principle be applied to both quasi-static and dynamic penetration tests. However, it has only been successfully applied to the former so far.
- Based on experimental results, the effects of varying plate thickness, boundary conditions, punch diameter and nose shape on the maximum force, displacement at fracture and energy absorption until perforation in quasi-static penetration have been determined. It was found that the thickness of the plate is the single factor that influences the maximum force the most in the investigated range of parameters. The punch shape and diameter have smaller but significant effects, while the boundary condition has an almost negligible effect on the maximum force. No significant interactions were observed. It was also found that the work required to perforate the

plate is most dependent on the plate thickness in the investigated range of parameters. However, the shape of the load curve is depending on all the investigated parameters.

- It has been shown that the slightly modified Johnson-Cook constitutive model and failure criterion can predict the response of the present plates both in quasi-static and low-velocity penetration. However, great care must be taken when the two models are calibrated. Further, the results presented in Part IV of this thesis indicate that the good agreement between computer simulations and experiments may be a coincidence since important effects of dynamic strain aging and temperature dispersion are neglected. This is important to notice since the Johnson-Cook models are widely used in simulations of this type of problem.
- The possibility of determining the anisotropy constants in the YLD2004-18p yield function by texture measurements and crystal plasticity calculations has been investigated. The full-constraint Taylor model has been found inadequate for the present aluminium alloy and mechanical tests are in general recommended.
- The effects of anisotropy, dynamic strain aging and thermal softening in low velocity impacts on the present aluminium alloy have been investigated. Dynamic strain aging seems to influence both the predicted force level and fracture, while thermal softening only influences fracture prediction. No effect of plastic anisotropy has been observed.

5 Suggestions for further work

During the present investigation of low velocity perforation of aluminium plates, various related topics have been investigated while some have barely been touched. Several possible extensions of the project can be considered. Some suggestions for further research are briefly presented below.

- The established full-field measurement technique should be extensively tested, especially for dynamic impacts. This is an ongoing activity at CRI-SIMLab.
- The material model established in the present study should be further tested. Other researchers should see if the results obtained in the present study can be reproduced.
- A study similar to that presented in Part IV could be carried out with other nose-shapes and higher impact velocities.
- Non-circular and stiffened plates should be tested.
- Non-centric impact on plates should be tested.
- The effect of boundary conditions on dynamic impact response should be investigated. Several studies have reported that boundary conditions do not influence the energy absorptions. However, they may cause a part of the discrepancies between the force versus time curves obtained through experiments and simulations seen in Part IV of the present study.

References

Atkinson, KB. *Close range photogrammetry and machine vision*. Whittles Publishing; 1996.

Backman, ME., Goldsmith, W. *The mechanics of penetration of projectiles into targets*. Int. J. Eng. Sci. 1978;16:1-99.

Barlat, F., Aretz, H., Yoon, J.W., Karabin, M.E., Brem, J.C. and Dick, R.E. *Linear transformation-based anisotropic yield functions*. Int. J. Plasticity. 2005;21:1009–1039.

Børvik, T. *Ballistic penetration and perforation of steel plates*. Dr. ing. thesis, Department of Structural Engineering, Norwegian University of Science and Technology, Trondheim, Norway; 2000. ISBN 82-7984-154-7.

Børvik, T. *An introduction to impact and penetration dynamics*. Compendium, SIMLab / Department of Structural Engineering, Norwegian University of Science and Technology, December 2003.

Dey, S. *High-strength steel plates subjected to projectile impact. An experimental and numerical study*. Dr. ing. thesis, Department of Structural Engineering, Norwegian University of Science and Technology, Trondheim, Norway; 2004. ISBN 82-471-6282-2.

Heikkilä, J. *Accurate camera calibration and feature based 3D reconstruction from monocular image sequences*. Ph.D.-thesis, University of Oulo, Finland; 1997.

Hildrum, H.G. *Stiffened aluminium plates subjected to impact loading*. Dr. ing. thesis, Department of Structural Engineering, Norwegian University of Science and Technology, Trondheim, Norway; 2002. ISBN 82-471-5467-6.

Langseth, M. *Dropped Objects: Plugging Capacity of Steel Plates*. Dr.ing. thesis, Department of Structural Engineering, Norwegian Institute of Technology, Trondheim, Norway; 1988. ISBN 82-7119-042-3.

Seah, C.C. *Penetration and perforation of granite targets by hard projectiles*. Doctoral thesis, Department of Structural Engineering, Norwegian University of Science and Technology, Trondheim, Norway; 2006. ISBN 82-471-8150-9.

Zukas, JA. et al. *Impact dynamics*, John Wiley & Sons, New York; 1982.

Part I

F. Grytten, E. Fagerholt, T. Auestad, B. Førre, T. Børvik

Out-of-plane deformation measurements of an aluminium plate during quasi-static perforation using structured light and close-range photogrammetry

International Journal of Solids and Structures 44 (2007) 5752–5773

Available online at www.sciencedirect.com

ScienceDirect

International Journal of Solids and Structures 44 (2007) 5752–5773

INTERNATIONAL JOURNAL OF SOLIDS AND STRUCTURES

www.elsevier.com/locate/ijsolstr

Out-of-plane deformation measurements of an aluminium plate during quasi-static perforation using structured light and close-range photogrammetry

Frode Grytten [a], Egil Fagerholt [b], Trond Auestad [a], Bernt Førre [b], Tore Børvik [a,c,*]

[a] *Structural Impact Laboratory (SIMLab), Centre for Research-based Innovation (CRI), Department of Structural Engineering, Norwegian University of Science and Technology, NO-7491 Trondheim, Norway*

[b] *Department of Physics, Norwegian University of Science and Technology, NO-7491 Trondheim, Norway*

[c] *Norwegian Defence Estates Agency, Research and Development Department, NO-0015 Oslo, Norway*

Received 14 July 2006; received in revised form 5 January 2007
Available online 30 January 2007

Abstract

An optical system using structured light and close-range photogrammetry for full-field continuous measurements of the out-of-plane deformation of a metal plate loaded at its centre by a moving punch is presented. The system is applicable both for quasi-static and dynamic loading conditions, but in this paper focus will be on the former. In the tests, a square AA5083-H116 aluminium plate is mounted in a circular frame and penetrated from above by a cylindrical punch, while the out-of-plane deformation is observed from below. A fringe pattern is projected on the target plate surface and recorded by a camera (or more than one if required). The changing fringe positions on the plate surface during perforation are then computer processed to give topography information of the out-of-plane deformation. This paper is divided into three major parts. First, the optical technique is presented with a description of the applied method, image analysis procedures, calibration of the system and estimation of accuracy of the acquired data points. The experimental set-up is then presented, and some results from a typical test where a 5 mm thick plate with free-span diameter of 500 mm is perforated by a 20 mm diameter blunt-nose punch are given. Finally, numerical simulations of the perforation process are carried out using the non-linear finite element code LS-DYNA. The numerical predictions are compared with the experimental observations and the applicability of the experimental method is discussed based on the obtained results.

Keywords: Aluminium plates; Quasi-static perforation; Optical measurements; Profilometry; Numerical simulations

---

1. Introduction

Structural impact problems have become increasingly important for the modern society. As an example, in the design of offshore structures account must be taken of accidental loads such as dropped objects,

---

[*] Corresponding author. Tel.: +47 73 59 46 47; fax: +47 73 59 47 01.
E-mail address: tore.borvik@ntnu.no (T. Børvik).

0020-7683/$ - see front matter © 2007 Elsevier Ltd. All rights reserved.
doi:10.1016/j.ijsolstr.2007.01.026

collisions, explosions and penetration by fragments. Most of these loads are also pertinent in the design of protective structures for the process industry, fortification installations for defence purposes or in the development of protection against possible terrorist attacks. In the transport industry, energy absorption and crashworthiness are today critical issues in the design process of vehicles, vessels and aircrafts. While much of the work carried out by military and industrial research organisations has been classified, many generic studies are available in the open literature. As pointed out by Goldsmith (1999), the enormous literature on the subject encompasses a variety of different target materials and thicknesses, as well as a host of projectile geometries and a velocity range from 5 m/s to the hypervelocity domain of up to 15 km/s. Comprehensive reviews on the research into the penetration and perforation of structures by free-flying projectiles can be found in the journal papers by Backman and Goldsmith (1978) and Corbett et al. (1996), and in the books by Zukas et al. (1982, 1990).

Even so, the ballistic penetration and perforation processes of metal plates are still considered as complex problems both from an experimental, analytical and numerical point of view. Therefore, in order to validate assumptions, theoretical calculations and numerical models it is useful to perform quasi-static perforation tests, where material uncertainties associated with impact generated high strain-rate loading conditions as well as inertia effects are omitted. Such experiments are also easier to carry out with accurate measurements than impact tests using free-flying projectiles at high impact velocities. Still with these simplifications, it is difficult to establish reliable closed-form analytical solutions for this type of problem. Numerical techniques, like the finite element method (FEM), have on the other hand become increasingly powerful during the last two decades and FEM is today accepted as a general computational tool within most branches of industry. To validate that the numerical model is able to represent the real behaviour of a structure exposed to a continuously moving quasi-static punch load, accurate measurements of the deformation process are required.

Several studies on the behaviour of metal plates loaded quasi-statically by a circular punch at its centre have previously been conducted (see, e.g., Onat and Haythornthwaite, 1956; Lance and Onat, 1962; Johnson and Ghosh, 1980; Johnson et al., 1980; Langseth, 1988; Corbett et al., 1990; Langseth and Larsen, 1992; Corbett and Reid, 1993). In most studies, the experimental results have been used to validate accompanying analytical models of the penetration and perforation process. To do so, measured force-punch displacement curves have been compared to similar analytical calculations. On the other side, several optical studies have been published on different techniques to measure the out-of-plane deformation of a deforming body (see, e.g., Sainov et al., 1989; Chen et al., 1999; Martínez-Celorio et al., 2002; Salas et al., 2003; Chen et al., 2004; Su et al., 2004; Kumar et al., 2004; Barrientos et al., 2004; Tay et al., 2005). However, none of these have tried to measure the out-of-plane deformation profiles of a punched target plate at large deflections to fracture, and compared the results to detailed finite element calculations. This is somewhat strange, since this information is of major importance both in order to study the load carrying and energy absorbing capacity of the target plate (involving the coupling between local punch indentation and global target bending) and as a precision tool to validate finite element simulations of the penetration and perforation process.

In this paper, an optical system using structured light and close-range photogrammetry for full-field continuous measurements of the out-of-plane deformation of a metal plate loaded at its centre by a moving punch is presented. The system is applicable both for quasi-static and dynamic loading conditions, but in this paper focus will be on the former. In the tests, a square AA5083-H116 aluminium plate is mounted in a circular frame and penetrated from above by a cylindrical punch, while the out-of-plane deformation is observed from below. A fringe pattern is projected on the target plate surface and recorded by a camera (or more than one if required). The changing fringe positions on the plate surface during perforation are then computer processed to give topography information of the out-of-plane deformation. The paper is divided into three major parts. First, the optical technique is presented in detail. This involves a description of the applied method, image analysis procedures, calibration of the system and accuracy of the recordings. The experimental set-up is then presented, and some results from a typical test where a 5 mm thick plate with free-span diameter of 500 mm is perforated by a 20 mm diameter blunt-nose punch are given. Finally, numerical simulations of the penetration and perforation process are carried out using the non-linear finite element code LS-DYNA (LSTC, 2003). The numerical predictions are compared with the experimental data and the applicability of the experimental method is discussed based on the obtained results.

2. Out-of-plane deformation measurements

2.1. Measurement principle

The measurement principle described in this paper is based on structured light and close-range photogrammetry. During testing the rear surface of the target, i.e. the surface of which the topography is measured, is illuminated with a fringe pattern using a Kodak Carousel S-AV 1030 250W slide projector. The projector is equipped with a Kodak Retinar lens with focal length of 85 mm and 2″ high precision Ronchi rulings by Edmund Optics with 50 lines per inch. The projected pattern consists of black and white stripes, i.e. a discrete binary pattern, which is observed and recorded through a greyscale camera, providing intensity maps of the fringe pattern projected to the target surface. Two cameras are used in this study to obtain redundant measurements. The cameras are a Kodak MotionCorder SR-500 (with a maximum of 1000 fps) and a Phantom v5.0 high-speed camera (capable of maximum 62500 fps). The fringe pattern is analysed as it appears in the intensity maps recorded by the cameras and the topography of the target is calculated using a calibrated camera model and a look-up-table which holds information on how the fringe pattern appears with varying deformation values. Typical images of the changes in the projected fringe pattern during deformation will be shown in Section 4.2. To obtain satisfactory absolute accuracy of the three-dimensional measurements, a camera model which corrects for radial and decentring distortion must be used and a proper calibration of the system is required (Atkinson, 1996; Heikkilä, 1997). The measurement principle and the theoretical background for the chosen method are presented in more detail in Fagerholt (2004), and is based on the work by Heikkilä (1997).

2.2. Camera model

Fig. 1 illustrates the different coordinate systems and their relation. First, two coordinate systems are defined, namely the object coordinate system that contains the target which is going to be measured and the camera coordinate system which contains the image sensor plane of the camera. The basic transformation from object coordinates to camera coordinates is given by

$$\begin{bmatrix} x_i \\ y_i \\ z_i \end{bmatrix} = \mathbf{M} \cdot \begin{bmatrix} X_i \\ Y_i \\ Z_i \end{bmatrix} + \begin{bmatrix} x_0 \\ y_0 \\ z_0 \end{bmatrix} \tag{1}$$

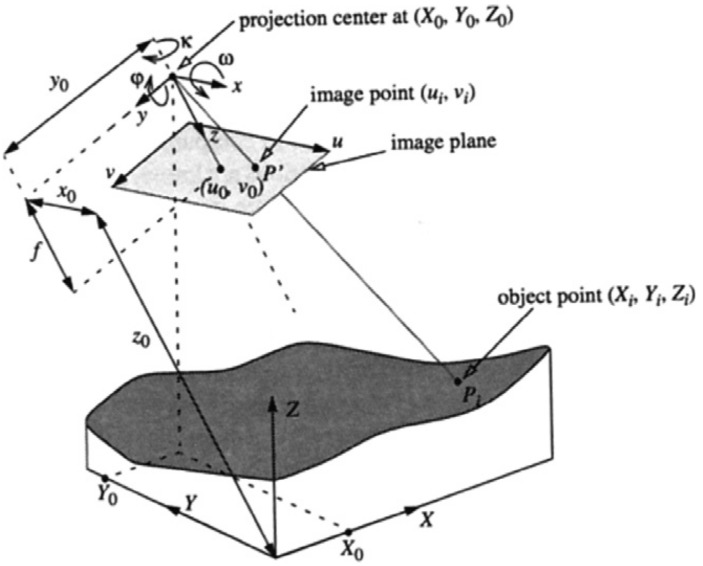

Fig. 1. Pinhole projection model (Heikkilä, 1997) that illustrates the object coordinate system (X, Y, Z), the camera coordinate system (x, y, z), the image coordinate system (u, v) and their relation.

where **M** is a 3 × 3 rotational matrix, $[x_i, y_i, z_i]^{\mathrm{T}}$ are the coordinates in the camera coordinate system, $[X_i, Y_i, Z_i]^{\mathrm{T}}$ are the coordinates in the object coordinate system and $[x_0, y_0, z_0]^{\mathrm{T}}$ are the origin of the object coordinate system denoted in camera coordinates. After the object coordinates are transformed to camera coordinates, the camera coordinates are projected on to the image sensor plane of the camera. The projection is described as

$$\begin{bmatrix} \tilde{u}_i \\ \tilde{v}_i \end{bmatrix} = \frac{f}{z_i} \begin{bmatrix} x_i \\ y_i \end{bmatrix} \tag{2}$$

where $[\tilde{u}_i, \tilde{v}_i]^{\mathrm{T}}$ are the image coordinates and f is the focal length of the camera lens. The image coordinates are then transformed from millimetres to pixels by the following equation

$$\begin{bmatrix} u'_i \\ v'_i \end{bmatrix} = \begin{bmatrix} D_U \tilde{u}_i \\ D_V s_V \tilde{v}_i \end{bmatrix} + \begin{bmatrix} u_0 \\ v_0 \end{bmatrix} \tag{3}$$

where s_V is the scale factor between the horizontal and vertical direction. D_U and D_V are the proportional constants between millimetres and pixels. So far the camera model describes a linear camera model without any distortion factors. However, in order to obtain a required accuracy, the camera model must correct for radial and decentring distortion. These distortion factors are common for most lens systems. Radial distortion is described as

$$\begin{bmatrix} \delta u_i^{(r)} \\ \delta v_i^{(r)} \end{bmatrix} = \begin{bmatrix} \tilde{u}_i(k_1 r_i^2 + k_2 r_i^4 + \ldots) \\ \tilde{v}_i(k_1 r_i^2 + k_2 r_i^4 + \ldots) \end{bmatrix} \tag{4}$$

where $k_1, k_2, \ldots, k_n$ are coefficients of the radial distortion and $r_i = \sqrt{\tilde{u}_i^2 + \tilde{v}_i^2}$. Decentring distortion is described by the following equation

$$\begin{bmatrix} \delta u_i^{(t)} \\ \delta v_i^{(t)} \end{bmatrix} = \begin{bmatrix} 2p_1 \tilde{u}_i \tilde{v}_i + p_2(r_i^2 + 2\tilde{u}_i^2) \\ p_1(r_i^2 + 2\tilde{v}_i^2) + 2p_2 \tilde{u}_i \tilde{v}_i \end{bmatrix} \tag{5}$$

where p_1 and p_2 are decentring distortion coefficients. The transformation from undistorted image coordinates in mm to distorted image coordinates in pixel values are then given by

$$\begin{bmatrix} u_i \\ v_i \end{bmatrix} = \begin{bmatrix} D_U(\tilde{u}_i + \delta u_i^{(r)} + \delta u_i^{(t)}) \\ D_V s_V(\tilde{v}_i + \delta v_i^{(r)} + \delta v_i^{(t)}) \end{bmatrix} + \begin{bmatrix} u_0 \\ v_0 \end{bmatrix} \tag{6}$$

The complete transformation from object coordinates to image pixel coordinates are thus determined by Eqs. (1), (2) and (6). All parameters used in the camera model are listed in Table 1, together with their values obtained from the camera calibration described in the next section and Section 4.1. The various parameters in Table 1 are further defined in Fig. 1.

2.3. Camera calibration

Calibration points are obtained by recording images of an accurately defined square chess pattern. The chess pattern is moved normal to its plane to obtain calibration points in three dimensions. The corners of the chess pattern are extracted from the recorded images giving a set of corresponding object and image coordinates. The calibration is performed with a least square fitting algorithm, where the sum of squared residuals is minimized. The object function to be minimized is expressed as

$$F = \sum_{i=1}^{N} (U_i - u_i)^2 + \sum_{i=1}^{N} (V_i - v_i)^2 \tag{7}$$

where N is the number of calibration points. U_i and V_i are observations of the image coordinates, whereas u_i and v_i are image coordinates calculated from the corresponding object coordinates (X_i, Y_i, Z_i) using the camera model described in Section 2.2.

Table 1
Camera parameters that determine the object to image coordinates transformation and their values from the camera calibration

Parameter	Description	Kodak	Phantom	Units
D_U	Proportional constant between millimetres and pixels	102,50	204,98	pixels/mm
D_V	Proportional constant between millimetres and pixels	96,00	212,59	pixels/mm
s_V	Scale factor between horizontal and vertical direction	1.1337	0.9993	–
f	Effective focal length	22.8519	19.6022	mm
u_0	Principal point in image pixel coordinates	462.80	1202.20	pixels
v_0	Principal point in image pixel coordinates	−115.93	280.39	pixels
k_1	Radial distortion coefficient	0.0022457	0.0022437	–
k_2	Radial distortion coefficient	−2.8207e-005	−3.9023e-005	–
p_1	Decentring distortion coefficient	−0.0039274	−0.00020071	–
p_2	Decentring distortion coefficient	0.0029374	0.0046827	–
x_0	Origin of object coordinate system in camera coordinates	−285.00	−421.51	mm
y_0	Origin of object coordinate system in camera coordinates	206.96	108.02	mm
z_0	Origin of object coordinate system in camera coordinates	1965.3	2086.3	mm
ω	Rotation of the coordinate system about x-axis	153.21	153.70	°
ϕ	Rotation of the coordinate system about y-axis	−9.2471	−9.3528	°
κ	Rotation of the coordinate system about z-axis	−3.0433	6.2308	°

The proportional constants D_U and D_V in Table 1 are proportional to the focal length f and the scale factor s_V. D_U and D_V are given in the camera specifications, and act as initial conditions for the camera calibration procedure. The remaining 14 camera parameters (i.e. the 14 last-mentioned parameters in Table 1) are optimized by the least square algorithm. However, for the least square algorithm to converge to the correct solution, proper initial values for the 14 parameters must be applied. Initial values for 9 of the 14 camera parameters, i.e. the focal length, the principal point in image pixel coordinates, the origin of object coordinates in camera coordinates and the rotation parameters of the camera coordinate system, are provided by using the Direct Linear Transform (DLT) algorithm (Abdel-Aziz and Karara, 1971; Heikkilä, 1997). As initial parameters for the optimization algorithm, the four distortion parameters are set to zero and the scale factor is set to one.

The calibration data set is obtained using a plane glass plate with a black and white square chess pattern as reference (see Fig. 2a). This pattern defines a two-dimensional coordinate system, i.e. object coordinates X and Y. The glass plate is moved through the target area perpendicular to the X–Y plane, i.e. parallel to the object coordinates Z, and at the same time observed and recorded through the camera. The Z-value is synchronically recorded both using a linear voltage transducer and a non-contacting laser gauge, and a pulse generator is used to trigger the camera images and the distance recordings (this is described in more detail in Section 3.3). The images of the square pattern is analysed and locations of the pattern corners are calculated with sub-pixel accuracy. This procedure provide corresponding object coordinates (X, Y, Z) and camera pixel coordinates (u, v) which are used as input in the camera calibration algorithms described above.

Determining the 14 camera parameters only gives the transformation of object coordinates (X, Y, Z) to image coordinates (u, v). However, the camera model does not give a solution to the inverse model where we want to recover the three-dimensional object coordinates from distorted image coordinates. Problems arise when trying to invert Eqs. (6) to obtain undistorted image coordinates from distorted image coordinates. This results in fifth order polynomials which are not trivial to solve. The solution applied is an approximation presented by Heikkilä (1997). He showed that the proposed model gives maximum residuals of 0.01 mm even with severe radial and decentring distortion. The eight parameter model which computes undistorted image coordinates from distorted image coordinates is given by the following relations

$$\tilde{u}_i = \frac{\tilde{u}'_i + \tilde{u}'_i(a_1 r_i^2 + a_2 r_i^4) + 2a_3\tilde{u}'_i\tilde{v}'_i + a_4(r_i^2 + 2\tilde{u}'^2_i)}{(a_5 r_i^2 + a_6\tilde{u}'_i + a_7\tilde{v}'_i + a_8)r_i^2 + 1} \tag{8}$$

$$\tilde{v}_i = \frac{\tilde{v}'_i + \tilde{v}'_i(a_1 r_i^2 + a_2 r_i^4) + a_3(r_i^2 + 2\tilde{v}'^2_i) + 2a_4\tilde{u}'_i\tilde{v}'_i}{(a_5 r_i^2 + a_6\tilde{u}'_i + a_7\tilde{v}_i + a_8)r_i^2 + 1} \tag{9}$$

where $\tilde{u}'_i = \frac{u_i - u_0}{D_U}$, $\tilde{v}'_i = \frac{v_i - v_0}{D_V s_V}$ and $r_i = \sqrt{\tilde{u}'^2_i + \tilde{v}'^2_i}$.

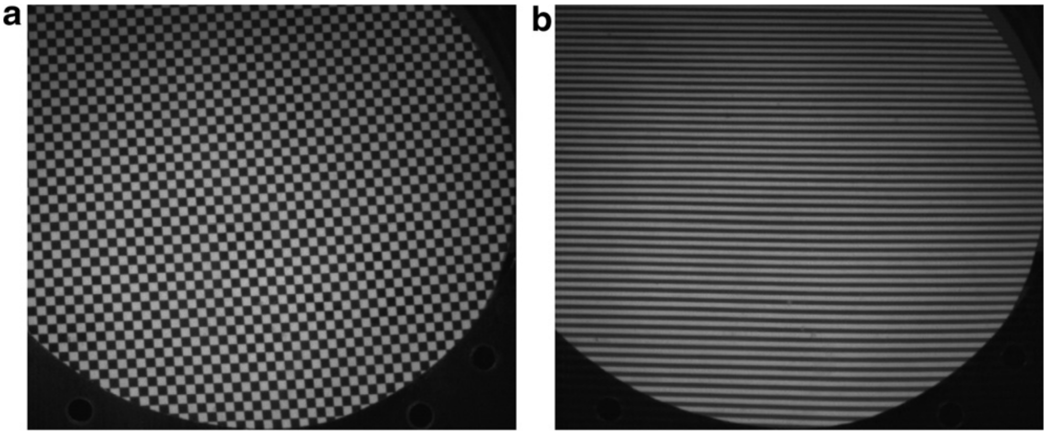

Fig. 2. Recordings of the plate with projected (a) square chess pattern and (b) line pattern used in the calibration of the camera and projector, respectively.

In order to solve the eight unknown parameters $(a_1, a_2, \ldots, a_8)$, calibration points covering the whole image area must be generated. A set of 2000 such calibration points is generated using the camera model in Section 2.2. The eight parameters are then solved using a least square fitting algorithm (Heikkilä, 1997).

2.4. Projector calibration

It is possible to use a similar geometric calibration as the one presented above for correcting radial and decentring distortion of the projector. However, a more direct and mathematically trivial approach is used. Here, a line pattern is projected on to a glass plate with a white matt surface (see Fig. 2b). The glass plate is mounted to the hydraulic actuator used in the penetration tests in order to move the glass plate parallel to the object coordinate Z-axis. The surface of the glass plate is prearranged to lie in the X–Y plane in the object coordinate system, and the fringe pattern is projected on to the glass plate surface. The camera records the variations of the pattern during this process, and a linear voltage transducer and a non-contacting laser gauge are used to record the object coordinate Z-value. The Z-values and the recorded images are synchronized using a pulse generator. This process provides information on the properties of the pattern in the relevant object space. The result is a 3D matrix with information on how each edge of the pattern varies as a function of Z. This matrix is used as a look-up table during topography measurements and the Z-values are interpolated from the values in this matrix.

2.5. Image processing

The recorded images are processed digitally. The intensities of the pixels in the recorded images are given by discrete 8 bit integer values, ranging from 0 (black) to 255 (white). Two different image analysing algorithms are used; one for analysing the fringe pattern projected by the projector, and one for analysing the square chess pattern of the camera calibration procedure. The square chess pattern is analysed using algorithms based on the corner-finder algorithm presented by Harris and Stevens (1998). An example of the square pattern and its extracted corners is presented in Fig. 3.

The fringe pattern projected by the projector is computer processed by locating the edges between the black and white stripes in the camera pixel plane. An interpolation function is developed providing sub-pixel accuracy of the location of the edges in the image pixel coordinate system (u, v). This function provides the location of all fringe edges through the whole image. Assuming the target surface to be smooth, low-pass filtering functions in the pixel plane provide an even higher sub-pixel accuracy in the location of the pattern edges, filtering out high frequency effects like interference and small-scale surface properties of the target plate. By recording images at a high rate, it is also possible to apply low-pass filtering in the time scale, provided that the surface

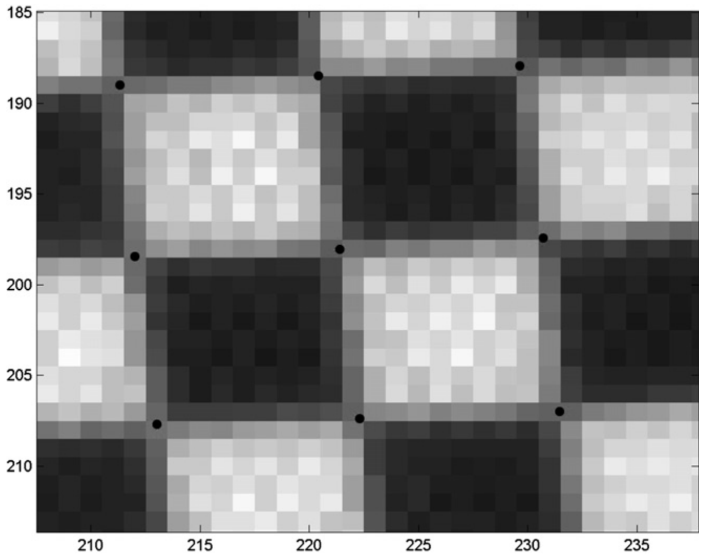

Fig. 3. A part of a calibration pattern recorded by the Kodak camera. The black dots indicate the location of the extracted calibration points.

variations of the target object are smooth. An example of the fringe pattern and its extracted edges is presented in Fig. 4.

The algorithms used to generate out-of-plane deformation data from the recorded images are implemented as scripts and functions in MATLAB (The MatWorks, 2002). The image processing is divided into five parts, which are (1) Edge Location, (2) Corner Extraction, (3) Projector Calibration, (4) Camera Calibration and (5) Topography Calculation. Fig. 5 gives the data-flow-chart used in the calculations. The Edge Location algorithm contains the algorithms for analysing series of images with fringe patterns, locating the edges of the fringes in each image. This is used for analysing the images from the Projector Calibration algorithm and the images from the perforation test. The Corner Extraction algorithm contains the algorithms for analysing series of images with square patterns, locating the corners of each square in the pattern. The data from the corner extraction is used as input to the Camera Calibration Algorithm. This algorithm calculates the camera parameters providing the transformations between object coordinates and image pixel coordinates. The

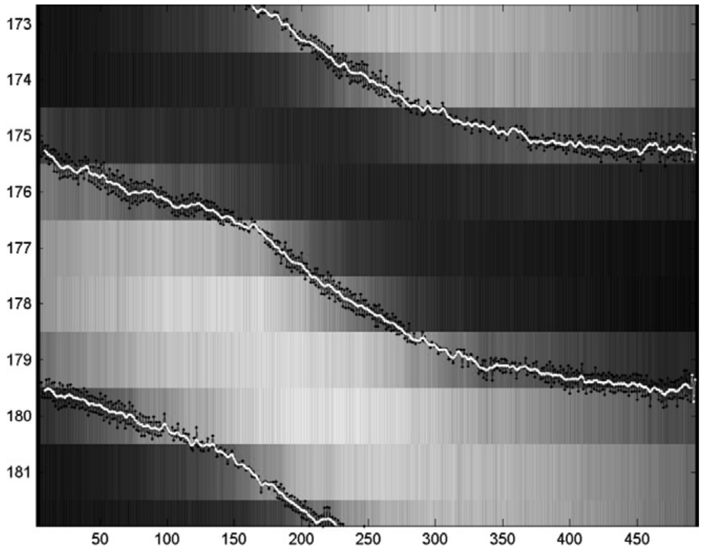

Fig. 4. A part of a fringe pattern recorded by the Kodak camera and its extracted edges. The dotted lines indicate the location of the extracted edges and the solid lines are the low-pass filtered edges.

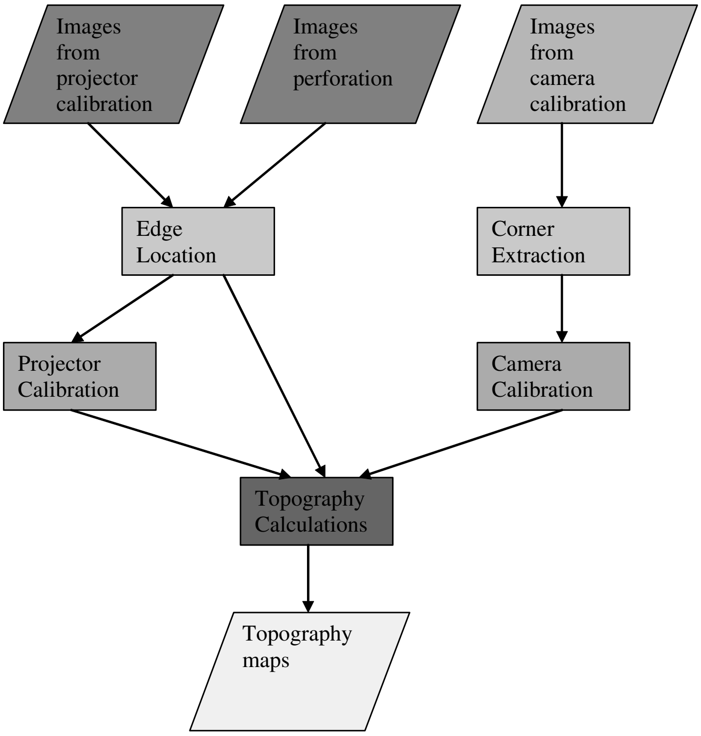

Fig. 5. Data-flow-chart for image processing of recorded images.

Projector Calibration algorithm provides information on how the edge locations vary spatially. Finally, the Topography Calculations algorithm uses input from the projector calibration, the camera calibration and the edge locations performed on the perforation test images to calculate the topography of the target surface.

2.6. Calculated accuracy of measurements

The calibration procedures presented above are performed in order to maximize the absolute accuracy of the topography measurements. Two different cameras are used in this study to obtain redundant measurements. The camera calibration procedure is performed on both cameras providing two distinct camera models. Residuals from the least square fit provide information on the accuracy of the camera calibration procedure. Calculated root-mean-square (RMS) values based on the camera calibration residuals for both the Kodak and the Phantom camera are presented in Section 4.1.

3. Experimental set-up

3.1. Target material

AA5083 is a high-strength aluminium-magnesium alloy well suited for rolling, and plates are therefore an important product. Even though the alloy has been tested for ballistic protection (see e.g. Børvik et al., 2004), the traditional use of these plates is naval structures such as ship hulls and offshore topsides due to the alloys excellent corrosion resistance. However, stress corrosion may occur in corrosive media. To avoid this problem, the special temper H116 has been developed (Hatch, 1984). The main alloying elements are magnesium with about 4.4 wt.%, manganese with 0.7 wt.% and chromium with 0.15 wt.%. Note that the amount of magnesium in the alloy is more than 3 wt.%, which is the maximum quantity to be retained in solid solution at room temperature. This implies a potential instability leading to precipitation along grain boundaries or slip planes, which again gives rise to a phenomenon denoted the Portevin-Le Chatelier (PLC) effect. The PLC effect causes serrated or jerky flow in certain ranges of temperature and strain rate, and is associated with repeated

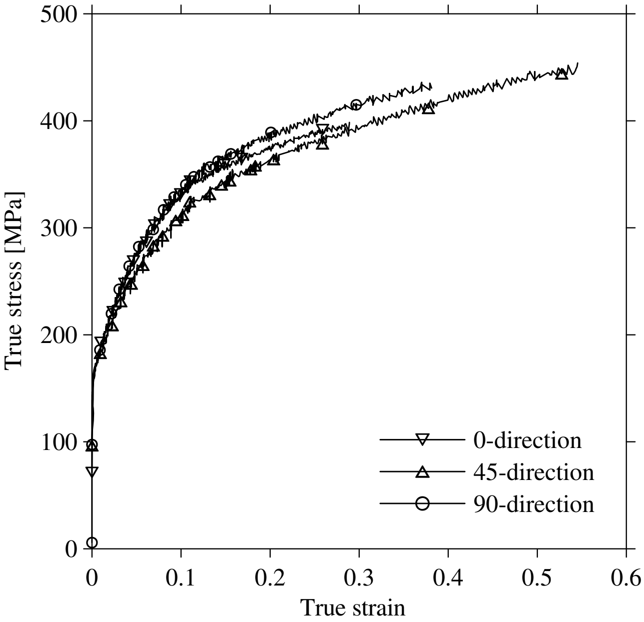

Fig. 6. Comparison between typical true stress-strain curves to fracture from different directions to the rolling direction of the target material (Clausen et al., 2004).

propagation of bands of localised plastic strain rate. The occurrence of PLC is linked to a bounded region of negative strain rate sensitivity of the flow stress, resulting from diffusion of solute atoms to dislocations temporarily arrested at obstacles in the slip path (Benallal et al., 2006).

AA5083-H116 is also found to be anisotropic both in strength and plastic flow. Both the anisotropy and the serrated flow due to PLC are illustrated in Fig. 6, which shows the true stress-strain curves from quasi-static tensile tests on smooth, axisymmetric specimens at room temperature. The specimens were taken in three different directions with respect to the rolling direction of the target plate in order to reveal the plastic anisotropy. As seen, the anisotropy in strength is moderate, while the anisotropy in plastic flow to fracture is considerable. At 45° direction with respect to the rolling direction of the material the failure strain is found to be about twice as large as the failure strain in the parallel (0°) direction. This may affect the perforation process and result in an unsymmetrical fracture mode. A material test programme on a 25 mm thick AA5083-H116 plate, determining the flow and fracture characteristics of the alloy as a function of strain rate, temperature and stress triaxiality, can be found in Clausen et al. (2004).

3.2. Test rig

The test rig used in the quasi-static punch tests is shown in Fig. 7. It consists of a 400 kN Amsler hydraulic actuator with a stroke of ±100 mm inserted in a stiff supporting frame. A replaceable punch of hardened tool steel (HRC 62) is connected to the actuator. The geometry of the cylindrical punch used in the test presented in Section 4.2 is also shown in Fig. 7. The square AA5083-H116 aluminium plate with dimensions $600 \times 600 \times 5\ \text{mm}^3$ was carefully cut from a larger plate. It was then mounted between two massive circular rings with a free-span diameter of 500 mm using 24 pre-stressed M16 bolts. Even though this was done with great care, the target can not be regarded as fully clamped in these tests, and both small rotations and contractions of the boundary were found to be present during plugging. Photographs of the target plate both before and after mounting in the clamping rings are given in Fig. 8. The rings are adjusted to make sure that the punch loaded the target directly at its centre. Thus, both the loading and boundary conditions are axisymmetric. The target and clamping rings rest on a rigid bottom frame. In order to increase the contrasts in the images, the plate was spray painted dead white on the side to be observed. During testing, the hydraulic actuator is operated in displacement control mode at a rate of 2 mm/min. At this speed, a typical experiment took

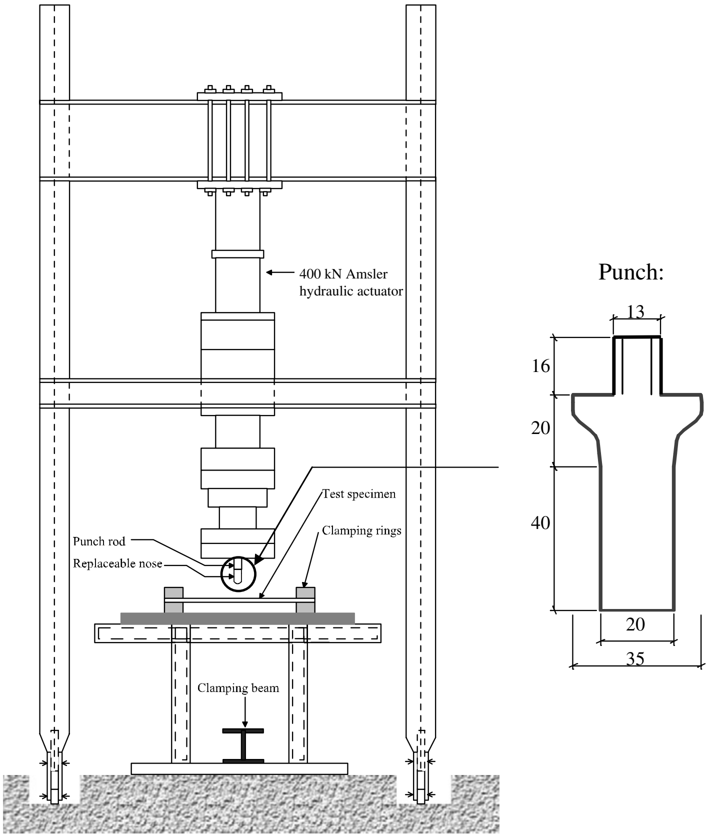

Fig. 7. Test rig and geometry of punch used during quasi-static tests.

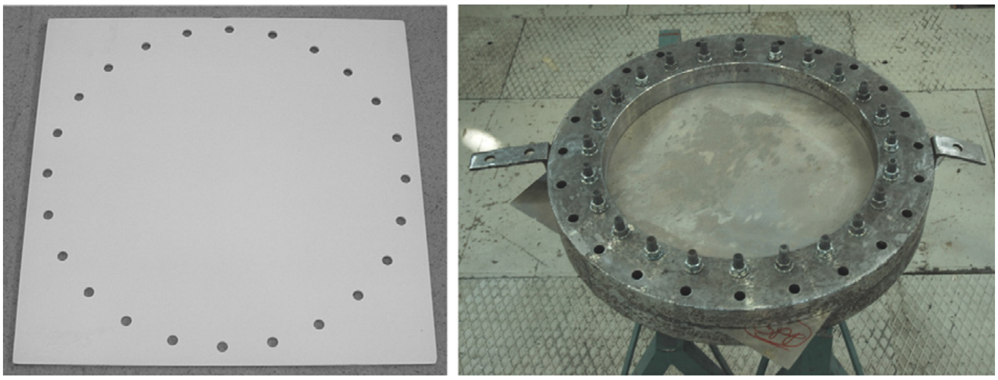

Fig. 8. Target plate before (left) and after (right) mounting in the clamping rings.

about 10–15 minutes from start until the punch perforated the plate. Thus, the penetration process can be regarded as both quasi-static and isothermal.

3.3. Instrumentation

As the punch penetrated the target plate, punch force, punch displacement and out-of-plane deformation were continuously measured. The punch force was measured by a load cell connected to the hydraulic actuator. The load cell was calibrated in an Instron servo-hydraulic testing machine, and accuracy better than ±1% at maximum force was found. The punch displacement was measured using two independently operating displacement transducers (one linear position sensor and one non-contacting laser gauge), in addition to the stroke displacement of the hydraulic actuator. However, in calculations only the linear position sensor was

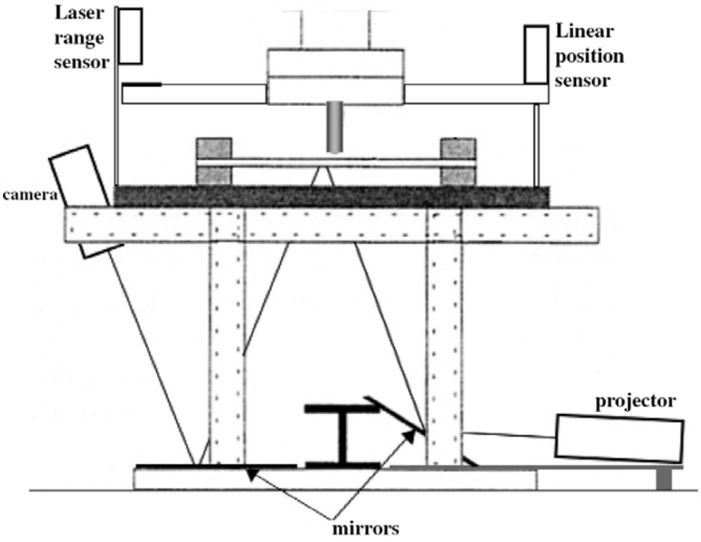

Fig. 9. Set-up of instrumentation during quasi-static punch tests.

used, since the displacement transducers were found to give identical results. The accuracy of the displacement transducers was measured to be ±0.2% of the full scale displacement of 100 mm. The set-up of the basic instrumentation is shown in Fig. 9. Also the optical out-of-plane displacement system described in Chapter 2 is sketched in Fig. 9. Here, the fringe pattern is projected from the projector via a mirror on to the plate surface. The illuminated area seen by the cameras is about $400 \times 400\ \text{mm}^2$. Two individual cameras (even though only one is shown in the sketch in Fig. 9) were used to continuously record the changes in the fringe pattern of the illuminated plate via a second mirror. The full field out-of-plane deformation of the plate was then calculated by analysing the recorded images.

Since several measuring devices were used during the experiments, the data acquisition had to be synchronised, so that each image captured by the camera could be related to the measured force or displacement. This was done by programming an Atmel AT90S8515 microcontroller to generate trigger pulses for the two cameras and the digital multimeter used to record the voltage value of the displacement transducers. The microcontroller is clocked from a crystal oscillator that gives accurate timing and allows easy programming of trigger pulses to the requirements of the different devices. The frequency of the trigger signal was set to 0.5 Hz, giving duration between each recordings of 2 s. The number of recordings was limited by the maximum number of images stored in the Kodak camera memory, which is 546 images at maximum resolution.

4. Experimental results

4.1. Calibration results

Both the Kodak and the Phantom camera are calibrated based on a set of 5-6000 calibration points. Each calibration point contains the X, Y and Z object coordinate values and its corresponding u and v image coordinates. The calibration points are distributed all over the X–Y plane and at three different values of Z ($Z = -4.0$, 81.5 and 136.3 mm). The calculated camera parameters for the Kodak and the Phantom camera based on the calibration method described in Section 2.3 are presented in Table 1. Residuals for each calibration point are calculated based on the camera model and the camera parameters indicating how well the camera model corresponds to the set of calibration points. Table 2 presents calculated root-mean-square values for the camera calibration residuals for both cameras. The RMS-values in object coordinates (X and Y) were found to be 0.61 and 0.48 mm, respectively, for the Kodak camera. For the Phantom camera the corresponding residual RMS-values were 0.93 and 0.42 mm. In the case of the full-field deformation of a circular surface with 500 mm diameter measured in a Cartesian X–Y–Z-coordinate system, where Z represents the out-of-plane deformation, the uncertainty of a single deformation measurement in Z-direction has been calculated

Table 2
RMS values of camera calibration residuals in object coordinates *X* and *Y*

	Kodak camera (mm)	Phantom camera (mm)
RMS value of residuals in *X*-direction	0.61256	0.93074
RMS value of residuals in *Y*-direction	0.48056	0.42704

to values below 0.04 mm. This is based on the uncertainty of the projector calibration and the sub-pixel accuracy of the edge-location algorithms. Due to the relatively large residuals calculated from the camera calibration procedure, the absolute accuracy of a single three-dimensional measurement has been calculated to 0.7 mm for the Kodak camera and 1.1 mm for the Phantom camera. These values are very conservative estimates and it must be noted that the absolute accuracy for this particular experiment seems to be significantly better, as will be discussed in the following sections.

The projector is calibrated by recording 500 images for both cameras with the calibration plane moving in Z-direction from $Z = -4.0$ mm to $Z = 146.0$ mm. The calibration plane is moved smoothly at 0.15 mm/s using the hydraulic actuator. Assuming the movement of the actuator to be smooth, the movement of the extracted fringes in the recorded images are low-pass filtered along the time-axis (Z-axis) to obtain a better signal-to-noise ratio. The result is a three-dimensional matrix which holds information on how each fringe in the pattern behaves as a function of the displacement (Z).

4.2. Perforation of target plate

As already stated, the target in the present test was a 5 mm thick AA5083-H116 aluminium plate with a free-span diameter of 500 mm loaded in the centre until failure by a 20 mm diameter blunt punch at a rate of 2 mm/min. The measured punch force from the load cell and the punch displacement measured with the linear position sensor gave the relation shown in Fig. 10. The figure also indicates that the scatter in measured force-displacement curves from four identical tests (test # 1–4) is negligible. In the following, only results and images from test # 1 will be used to generate out-of-plane displacement profiles. It can further be seen from Fig. 10 that the force increases monotonically until a certain point when plugging suddenly occurs at maximum load. Pictures of a typical plug and the cross-section of a sliced target plate after perforation are shown in Fig. 11.

A selection of typical images of the projected fringe pattern from the Phantom camera during the punching process is shown in Fig. 12. The punch nose after perforation can clearly be seen in the last image. In this particular test, a total of about 350 images were taken. Based on the recorded images and the calibration results for the cameras and the projector, coordinates to points on the plate surface were calculated. The out-of-plane displacement of the plate as function of radial distance from the centre could then be plotted at given times and in-plane directions. Some 3D topographic plots of the plate geometry generated in MATLAB based on

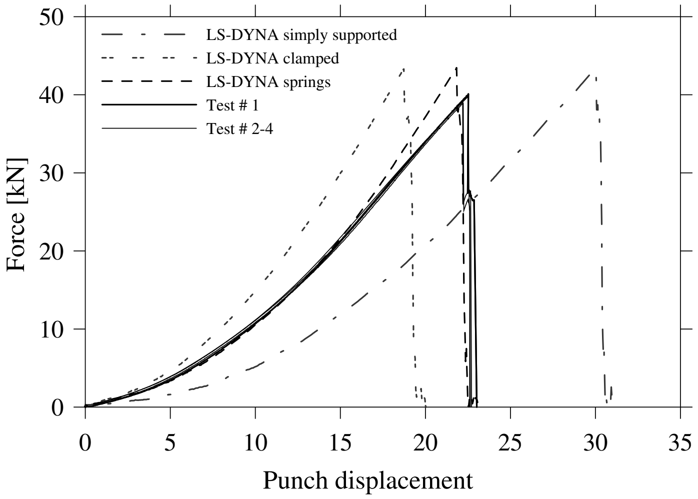

Fig. 10. Measured force-displacement curves (test # 1–4) compared to similar curves from LS-DYNA (LSTC, 2003) simulations using different boundary conditions.

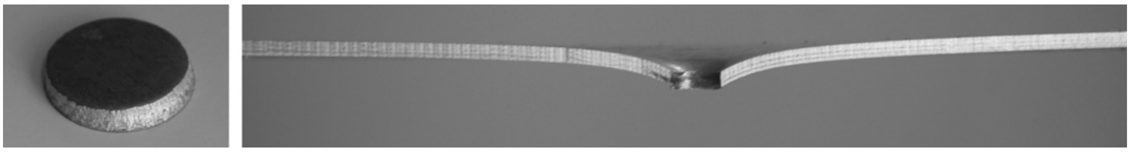

Fig. 11. Pictures of a typical plug and the cross-section of a sliced target after perforation.

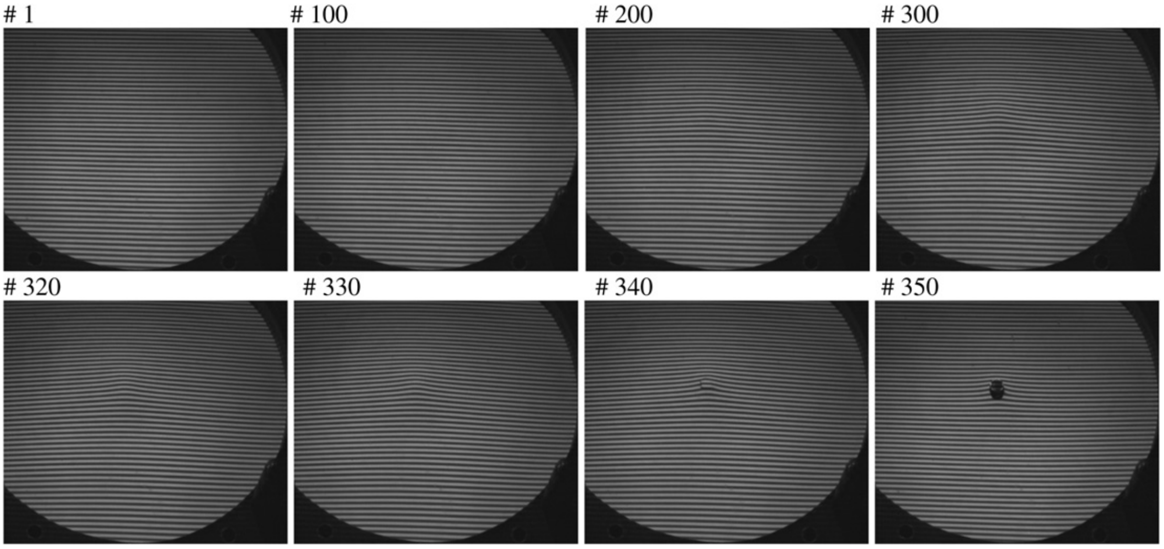

Fig. 12. A selection of typical images of the projected fringe pattern from the Phantom camera during deformation. The punch nose after perforation is seen in the last image.

raw-data from the camera images are given in Fig. 13. Based on plots like these, 2D displacement profiles from various in-plane directions may be obtained. Fig. 14 gives 64 measured displacement profiles in the rolling direction of the plate at various load levels. The thicker line in the figure indicates the permanent displacement profile after perforation and some elastic rebound of the plate. Note that in these tests a full elastic rebound of the plate is prevented by the punch. Fig. 15 shows a selection of out-of-plane displacement profiles at three different angles to the rolling direction of the target plate, comparing the results from the two cameras. As seen, very good correlation between the two independently operating cameras was observed. The results from the two cameras have been compared with each other and found to correlate with a residual RMS-value of 0.0945 mm. This gives confidence in the applied calibration technique. Another interesting effect seen in Fig. 15 is that the deformation profiles in the 45 degree direction differs slightly from the profiles in the rolling direction and orthogonal to the rolling direction at increasing load. These differences may be due to the anisotropic nature of the target material seen in Fig. 6, as will be discussed further in Chapter 6.

Finally, in order to verify the accuracy of the measurements, the measured central (maximum) displacement from the optical system was compared with data from the displacement transducers located at the front side of the target plate. The results are shown in Fig. 16 and the agreement between the different measurements is excellent. Since there is hardly any punch indentation in the target or thinning of the plug material in front of the moving punch during perforation, these measurements should coincide. Thus, this plot serves as a validation of the high accuracy of the applied optical technique, so the calculated residuals presented in Table 2 seem to be conservative.

5. Numerical simulations

5.1. Material model

Several constitutive relations have been proposed over the years for metallic materials under impact generated loading conditions for use in computational mechanics. The multiaxial stress state of the material is

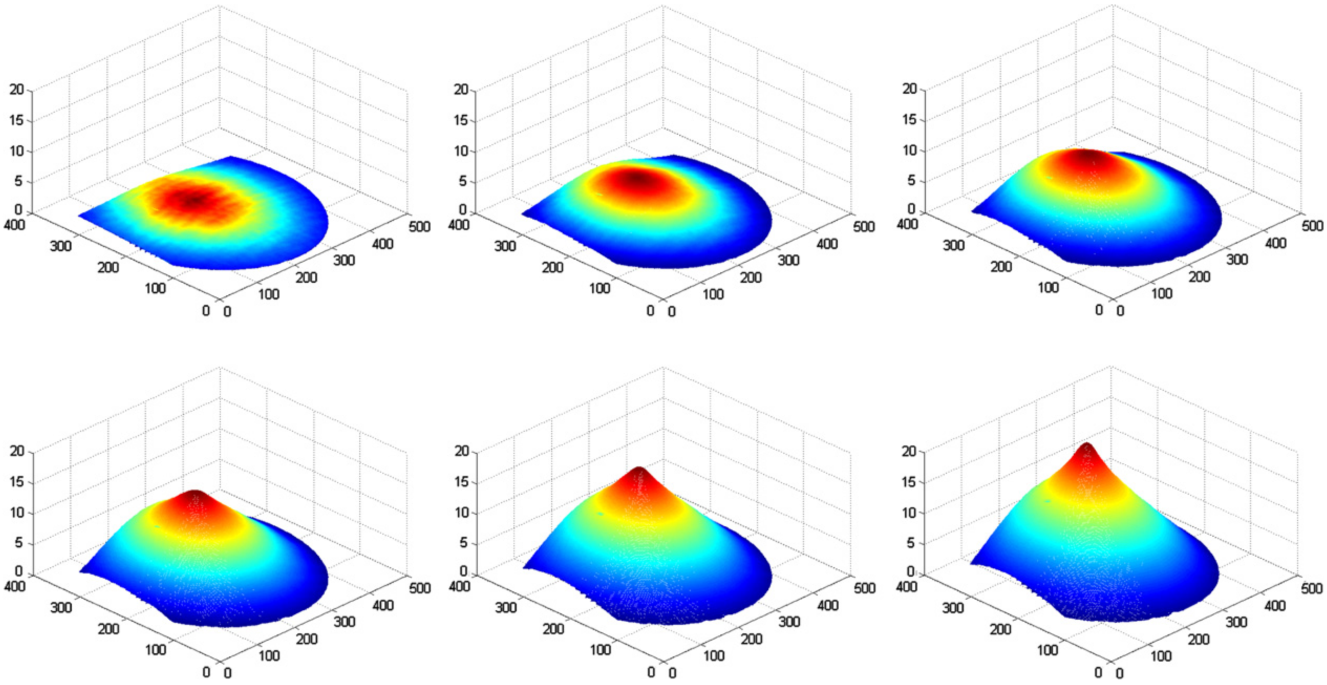

Fig. 13. Some 3D topographic plots at increasing load levels calculated based on raw-data from the Phantom camera images (where the axes are lengths in mm).

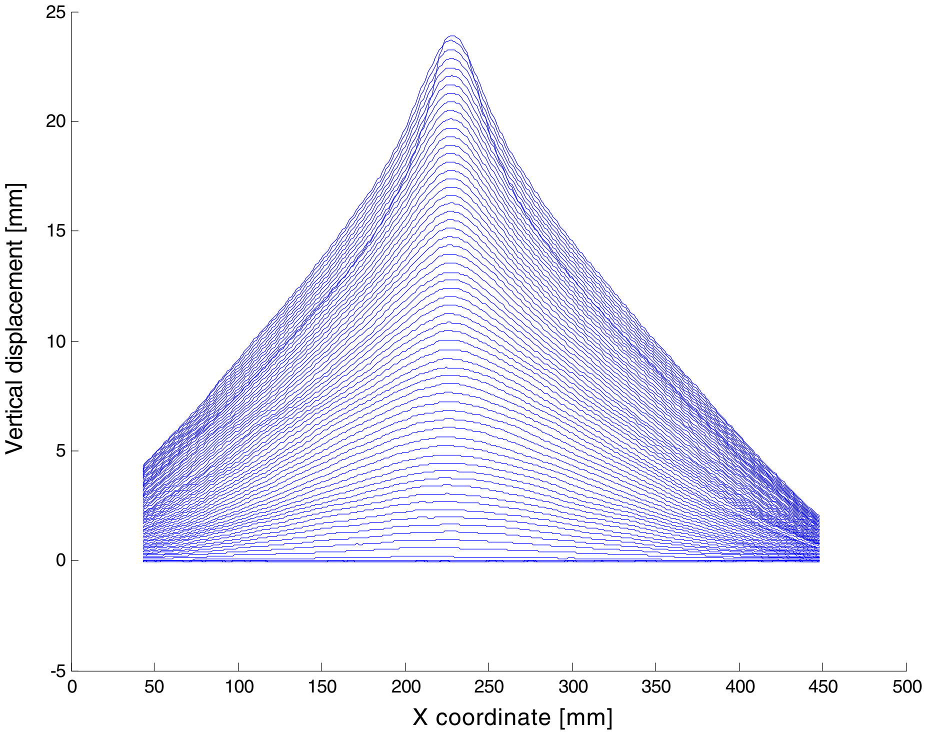

Fig. 14. Measured out-of-plane displacement profiles in the rolling direction at increasing load levels for a 5 mm thick AA5083-H116 aluminium plate loaded in the centre by a 20 mm diameter blunt punch. The 64 profiles are calculated based on images from the Phantom camera.

usually expressed in terms of the equivalent stress σ_{eq}, and many constitutive relations define this stress in terms of the accumulated plastic strain ε_{eq}, plastic strain rate $\dot{\varepsilon}_{eq}$ and temperature T as

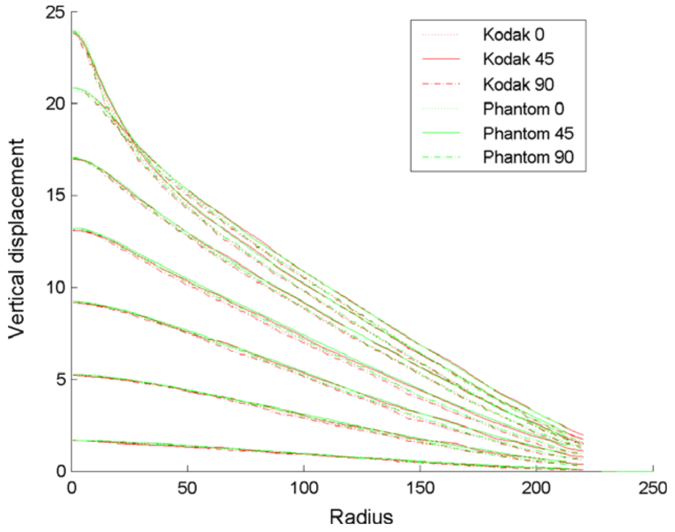

Fig. 15. A selection of out-of-plane displacement profiles for three different angles to the rolling direction, comparing the results from the two cameras.

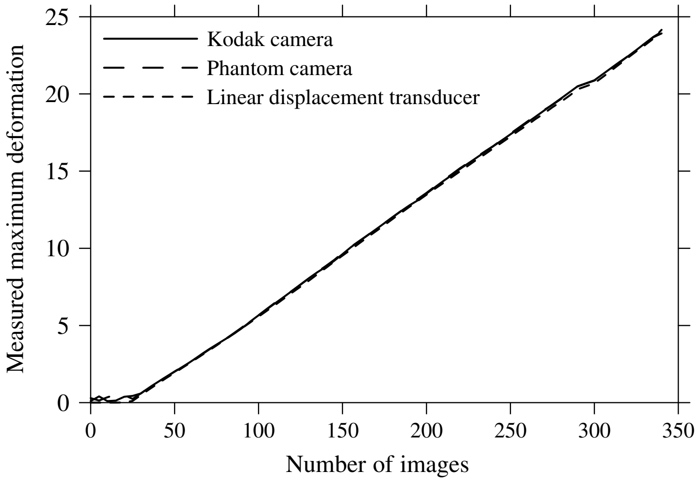

Fig. 16. Comparison of measured central (maximum) displacement of the plate from the two displacement transducers located at the top side and from the optical system located at the bottom side of the target.

$$\sigma_{\mathrm{eq}} = f(\varepsilon_{\mathrm{eq}}, \dot{\varepsilon}_{\mathrm{eq}}, T) \tag{10}$$

The form given in Eq. (10) can easily be adapted to most computer codes since it uses variables already available. Johnson and Cook (1983) proposed a phenomenological based constitutive relation, which has been frequently used in impact analysis due to its simplicity. Here, a slightly modified version of this constitutive relation proposed by Børvik et al. (2001) is used, where the equivalent von Mises stress is expressed as

$$\sigma_{\mathrm{eq}} = (A + B\varepsilon_{\mathrm{eq}}^{n})(1 + \dot{\varepsilon}_{\mathrm{eq}}^{*})^{C}(1 - T^{*m}) \tag{11}$$

The model has five material constants; A, B, C, n and m. The dimensionless strain rate is given by $\dot{\varepsilon}_{\mathrm{eq}}^{*} = \dot{\varepsilon}_{\mathrm{eq}}/\dot{\varepsilon}_0$, where $\dot{\varepsilon}_{\mathrm{eq}}$ is the equivalent plastic strain rate and $\dot{\varepsilon}_0$ is an user-defined reference strain rate. The homologous temperature is given as $T^* = (T - T_{\mathrm{r}})/(T_{\mathrm{m}} - T_{\mathrm{r}})$, where suffixes r and m indicate room and melting temperatures, respectively. The various phenomena such as strain hardening, strain rate hardening and temperature softening are uncoupled from each other. In the model, the incremental temperature increase caused by dissipation of plastic work due to adiabatic heating is calculated as

$$\Delta T = \int_0^{\varepsilon_{\mathrm{eq}}} \chi \frac{\sigma_{\mathrm{eq}} \mathrm{d}\varepsilon_{\mathrm{eq}}}{\rho C_{\mathrm{p}}} \tag{12}$$

where ρ is the material density, C_{p} is the specific heat, and χ is the Taylor–Quinney coefficient that represents the proportion of plastic work converted into heat.

Johnson and Cook (1985) also proposed a fracture criterion that accounts for strain path, strain rate, temperature and stress triaxiality. The fracture criterion is based on damage evolution, where the damage variable D of a material element is expressed as

$$D = \sum (\Delta\varepsilon_{\mathrm{eq}}/\varepsilon_{\mathrm{f}}) \tag{13}$$

Here, $\Delta\varepsilon_{\mathrm{eq}}$ is the increment of accumulated plastic strain that occurs during an integration cycle and ε_{f} is the fracture strain. Failure occurs by element erosion when D equals unity. The fracture strain is constructed in a similar way as the Johnson–Cook constitutive relation. A slightly modified version (Børvik et al., 2001) of the original model reads

$$\varepsilon_f = (D_1 + D_2 \exp(D_3\sigma*))(1 + \dot{\varepsilon}^*_{\mathrm{eq}})^{D_4}(1 + D_5 T^*) \tag{14}$$

where $D_1, \ldots, D_5$ are material constants. $\sigma*$ is the stress triaxiality ratio defined as $\sigma_{\mathrm{H}}/\sigma_{\mathrm{eq}}$, where σ_{H} is the mean stress. Again, the various phenomena accounted for in the fracture criterion are uncoupled from each other. This model has been implemented as material model # 107 in the commercial non-linear finite element code LS-DYNA (LSTC, 2003) using a backward-Euler integration algorithm.

5.2. Identification of material constants

In order to reveal the mechanical behaviour of AA5083-H116 under impact generated loading conditions, the flow and fracture characteristics of the alloy as function of strain rate, temperature and stress triaxiality have been investigated in detail by Clausen et al. (2004). The experimental programme involved more than 100 tensile tests with axisymmetric specimens taken in three different directions of the plate material. Four types of tensile tests were carried out: (1) quasi-static, smooth specimen tests; (2) quasi-static, notched specimen tests; (3) tests at different strain-rates; (4) tests at elevated temperatures using smooth specimens. Typical true stress-strain curves from quasi-static tensile tests on smooth, axisymmetric specimens at room temperature are given in Fig. 6. The experimental results were then used to calibrate the modified material model of Johnson and Cook given above. Note that the modified version of the Johnson–Cook model applied in this study does not account for the anisotropic effects observed in the material. Also note that the material coupons tested by Clausen et al. (2004) were taken from a 25 mm thick plate, while in this study a 5 mm thick plate is considered. The reduction in plate thickness is caused by mechanical rolling. This affects the work hardening as the thickness is decreased, and the material constants may therefore vary with plate thickness. To take this into account, some new tensile tests were conducted in the 0-direction (i.e. coupons taken parallel to the rolling direction), and the material constants given by Clausen et al. (2004) were adjusted accordingly. This is described in more detail in Grytten et al. (2005). Furthermore, in the present problem the effect of strain rate and temperature can be omitted in the material model due to quasi-static and isothermal conditions (see Section 3.2). Consequently, the material constants C, χ, D_4 and D_5 may all be set equal to zero in the model. The remaining material constants used in the simulations are as listed in Table 3.

5.3. Numerical models and results

2D axisymmetric volume weighted Galerkin elements with one integration point were used to model the perforation process in LS-DYNA using explicit time integration. Flanagan–Belytschko stiffness based hourglass control with exact volume integration was used to avoid spurious singular deformation modes. The section of the plate within 1.2 times the radius of the punch was defined as the local part, while the rest of the plate was defined as the global part. In the local part, 32 elements were used over the thickness, giving a characteristic element size of 0.16 mm and a total of 3072 elements in this part. The number of elements over the plate thickness was gradually reduced in the global part, from 32 at the local part to 8 elements over the

Table 3
Material constants for AA5083-H116 (Clausen et al. (2004), Grytten et al. (2005))

Elastic constants and density			Yield stress and strain hardening			Strain rate hardening	
E (GPa)	ν	ρ (kg/m^3)	A (MPa)	B (MPa)	n	$\dot{\varepsilon}_0(s^{-1})$	C
70	0.30	2700	206	423	0.36	1.0	0

Adiabatic heating and temperature softening					Fracture strain constants				
C_p (J/kgK)	χ	T_m (K)	T_0 (K)	m	D_1	D_2	D_3	D_4	D_5
910	0	893	293	0.86	0.178	0.389	−2.246	0	0

Fig. 17. Finite element model showing the blunt punch, the local part and the global part of the target plate.

thickness at the boundary, giving a total of 4056 elements in this part. The punch was modelled as a rigid body. Contact between the punch and the plate was modelled with the “contact_2d_automatic_surface_to_surface” algorithm available in LS-DYNA, while self contact in the plate was modelled using “contact_2d_automatic_single_surface”. Both algorithms are based on the penalty method. A plot showing the finite element model is given in Fig. 17.

The boundary was modelled as fully clamped, simply supported or constrained by linear and torsion springs. The elastic springs were modelled using beam elements. Their stiffness was chosen high ($k_r = 200$ (N/mm)/mm, $k_\phi = 64000$ (Nmm/rad)/mm) to allow for the small rotations and translations of the plate boundary caused by elastic deformations in the bolts during testing. In these tests, no effort was made to measure the displacements of the boundary, but both these and previous tests have shown these to be very small due to the clamping in the massive steel rings (see Fig. 8). It is therefore believed that the chosen spring stiffnesses are realistic. The load was applied as a velocity to the punch. A higher velocity was used in the numerical simulations than in the experiments in order to reduce the CPU time that may be considerable in quasi-static simulations using an explicit time integration algorithm. The ratio between internal energy and kinetic energy was later checked to assure that the target response was quasi-static, i.e. that no inertia effects were generated.

Force-displacement curves from finite element simulations of the perforation process using a clamped boundary, a simply supported boundary and a boundary constrained by stiff elastic springs are compared with the curves obtained experimentally in Fig. 10. As seen, the response of the target is very sensitive to the chosen boundary condition. The coordinates of the nodes on the bottom surface of the plate was further stored during the simulation and used to generate out-of-plane deformation profiles. Fig. 18 shows a comparison between the out-of-plane deformation profiles from simulations with clamped and simply supported boundary and the profiles from the camera measurements, while Fig. 19 shows a comparison between the results from the simulation where springs were used and the camera measurements. The data from the experiments are in the rolling direction. As also will be discussed in the next section, good agreement between simulations and camera measurements is only obtained when springs are used to model the boundary. Finally, Fig. 20 shows two typical plots of the deformation and fracturing process of the target plate during perforation, while Fig. 21 shows a close-up of the local part of the target at incipient plugging. As can be seen from these figures, the correct fracture mode is predicted and the shape of the resulting plug is close to the shape of the plugs seen in the experiments (Fig. 11). Note also that in these quasi-static experiments fracture initiated at the rear side of the plate due to tensile stretching and propagated towards the front side. This failure mode is contrary to most observations from high-velocity impact tests (see e.g. Børvik et al., 2003; Dey et al., 2004).

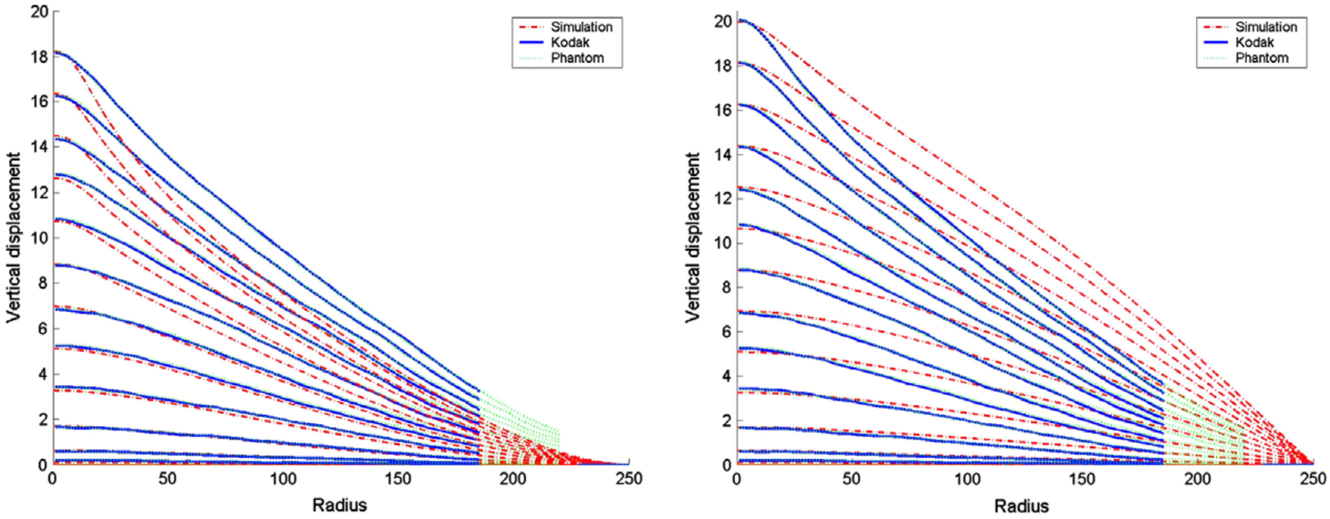

Fig. 18. Comparison between the measured out-of-plane displacement profiles and results from numerical simulations with a fixed boundary (left) and a free boundary (right).

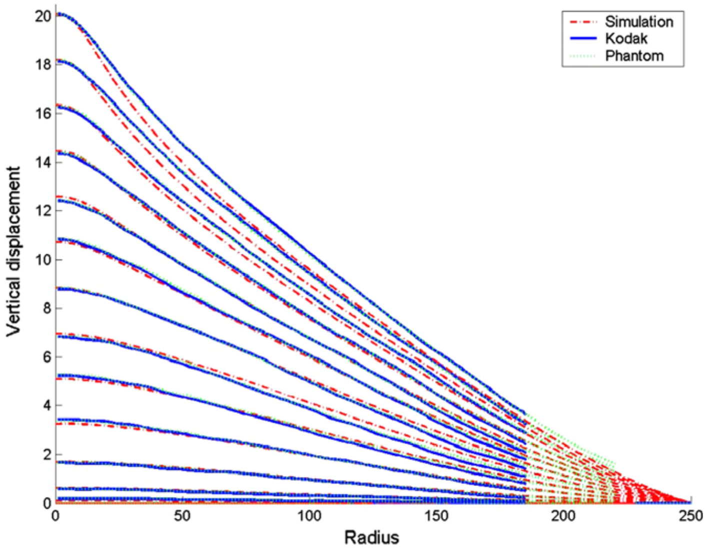

Fig. 19. Comparison between the measured out-of-plane displacement profiles and results from numerical simulations with a boundary partly fixed with springs.

5.4. Comparison between numerical simulations and experimental data

As seen from Fig. 10, the maximum force level in the simulations is almost unaffected by the boundary condition, while this is definitely not the case for the maximum punch displacement. This has also been observed in experiments (Grytten et al., 2005). If the boundary is modelled with stiff elastic springs, which is a realistic assumption in these tests, good correlation between experimental and numerical force-displacement curves is obtained. Note that the finite element simulations give good results for elastic and small plastic deformations, but may give more inaccurate results for large plastic deformations. Both Fig. 10 and Fig. 19 show excellent agreement between simulation and experiments until the deformations get large when springs are used to model the boundary. Thus, it is believed that both the camera measurements and the finite element model are accurate under these conditions. It is also seen from Fig. 10 that the finite element model with a clamped boundary exhibit too stiff a response, while the response using a simply supported boundary is too soft. As further indicated in Fig. 18, the calculated out-of-plane displacement profiles become highly inaccurate when

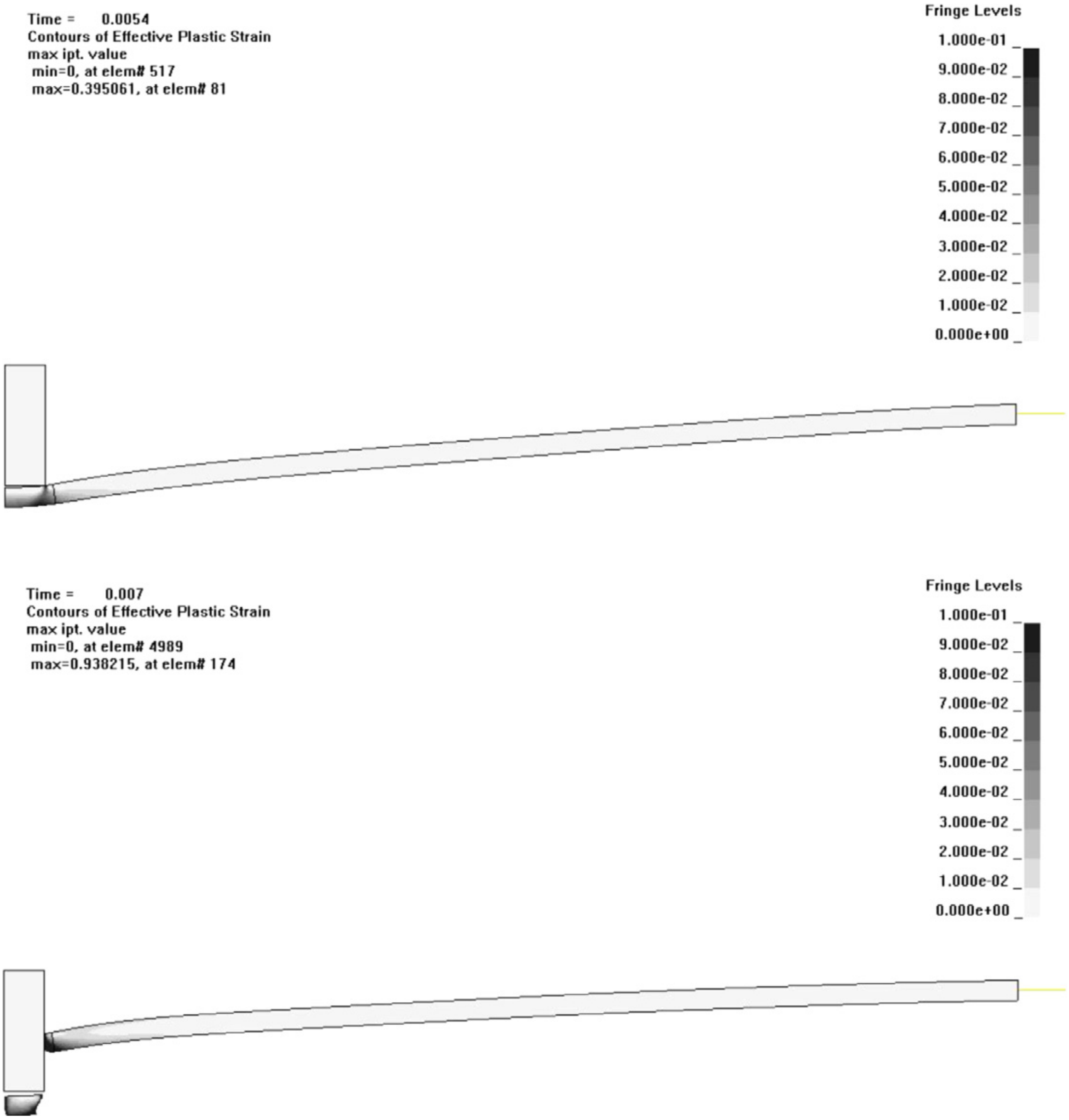

Fig. 20. Two typical fringe plots of the deformation and plugging process of the target plate during perforation.

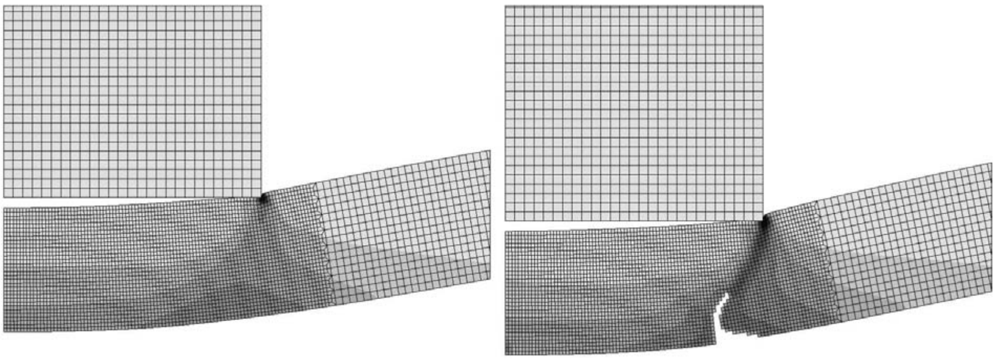

Fig. 21. Close-up of the local part in the target just before (left) and at (right) incipient plugging plotted with fringes of effective plastic strain.

the boundary is modelled as clamped or simply supported, while very well described using stiff elastic springs (see Fig. 19). This shows that the boundary conditions are of great importance when quasi-static or low velocity penetration is investigated, especially when it comes to energy absorbing capacity before failure. Thus, it is important to model the boundary correctly. The allowed displacement and rotation of the boundary constrained by springs were very small compared to those of the simply supported boundary. This proves that the boundary of the plate in the experiment was almost fixed as intended, but small rotations and displacements took place. Even so, the effect on the force-displacement curve and the out-of-plane displacement profiles was severe.

6. Discussion

The current camera calibration (see Chapter 2) has been used to show that the absolute accuracy of a single 3D measurement is at least as good as 0.7 mm for the Kodak camera and 1.1 mm for the Phantom camera under the described conditions. Since the two cameras give almost identical results (see Fig. 15, Fig. 16 and Fig. 18), with a residual RMS-value below 0.1 mm, it is assumed that the calibration target is the primary cause for the obtained inaccuracy. However, the measured deformation profiles (by both cameras in three different directions) for small displacements in Fig. 15 are much closer to each other than suggested by the estimated error. This indicates that the absolute accuracy is better than the conservative values given by the calculated residuals. Note that images of the square chess pattern used in the camera calibration procedure are analysed using algorithms based on the corner-finder algorithm presented by Harris and Stevens (1998), and that no filtering has been implemented to improve the accuracy of the locations of the corners in the images. Thus, it must be assumed that the extracted locations of the corners are degraded by a certain degree of noise. The effect of normally distributed noise in the locations of the calibration procedure input has been simulated and evaluated (Fagerholt, 2004). It was found that normally distributed noise only had a small effect on the camera calibration results. It should also in this context be mentioned that work in progress by the authors involving similar tests under dynamic loading conditions has indicated much lower residual RMS-values than those presented in Table 2. In the dynamic tests, the cameras used in this study were replaced by a Photron Ultima APX-RS camera (capable of 250000 fps) with a Nikon lens with focal length of 50 mm. Another interesting observation from Fig. 15 is that while the displacement profiles in all three directions to the rolling direction of the target seem to coincide at small displacements, the deviation between the two orthogonal directions and the 45-direction increases with increasing load. At the highest loads, there is a distinct increase in the measured displacement profile in the 45-direction compared to the 0- and 90-direction. This effect was obtained by both cameras operating independently of each other. The variation in deformation profiles may be due to the anisotropy of the aluminium alloy, and it seems like the proposed optical measuring technique is precise enough to capture direction-dependent out-of-plane displacements of the plate during perforation (especially since the calculated RMS-values to some extent reflect limited transversal resolution and accuracy).

7. Concluding remarks

A newly developed optical system using structured light and close-range photogrammetry for full-field continuous measurements of the out-of-plane deformation has been presented. Here, the system has been used to study the behaviour of an aluminium plate loaded at its centre by a moving punch. During testing, the rear side of the target plate is illuminated with a fringe pattern using a slide projector, and two independently operating cameras are used to photograph the changes in the pattern as the plate deflects. The several hundred images are computer analysed using MATLAB, which again provides 3D topographic plots of the target surface during deformation. These plots are finally used to generate 2D out-of-plane displacement profiles at different angles to the rolling direction of the target plate, which can be used to validate numerical simulations of the process. However, in order to have a satisfactory absolute accuracy of the 3D measurements, a camera model that corrects for distortions must be used in addition to a proper calibration of the system. Possible procedures for this have been proposed and demonstrated. The system is applicable both for quasi-static and dynamic loading conditions, but in this paper focus has been on the former.

2D numerical simulations of the perforation process have been carried out using the non-linear finite element code LS-DYNA. The material response during perforation was modelled using a modified Johnson–Cook model, and material data was taken from earlier studies on the same aluminium alloy. The boundary of the plate was modelled as fully clamped, simply supported or constrained by a linear and a torsion spring. When compared to measured force-displacement curves, a clamped boundary was found to exhibit a too stiff response, while the response using a simply supported boundary is too soft. If stiff elastic springs were used to model the boundary, which is a realistic assumption in these tests, very good correlation between experimental and numerical force-displacement curves was obtained. Also the calculated out-of-plane displacement profiles became highly inaccurate when the boundary was modelled as clamped or simply supported, while well described using stiff springs. This shows that the boundary conditions are of great importance when quasi-static or low velocity penetration of thin plates is investigated, especially when it comes to energy absorbing capability before failure. The great similarity between the measured and simulated force-displacement curves, and in particular between the measured and simulated out-of-plane displacement profiles, further indicates that the proposed optical measuring system has a higher absolute accuracy than the calculated RMS-values of between 0.7 and 1.1 mm.

Acknowledgements

This paper is dedicated to Professor Hans Pedersen at the Department of Physics, NTNU, who suddenly and unexpectedly passed away during the study. The financial support of this work from the Research Council of Norway, CRI-SIMLab, and the Norwegian Defence Estates Agency is gratefully acknowledged.

References

Abdel-Aziz, YI., Karara, HM., 1971. Direct linear transform into object space coordinates in close-range photogrammetry. In: Proceedings of the Symposium on Close Range Photogrammetry, Urbana, Illinois, pp. 1–18.

Atkinson, KB., 1996. Close range photogrammetry and machine vision. Whittles Publishing.

Backman, M.E., Goldsmith, W., 1978. The mechanics of penetration of projectiles into targets. Int. J. Eng. Sci. 16, 1–99.

Barrientos, B., Martínez-Celorio, R.A., López, L.M., Dirckx, J.J.J., Cywiak, M., 2004. Measurement of out-of-plane deformation by combination of speckle photography and speckle shearing interferometry. Optik - Int. J. Light Electr. Optics 115, 248–252.

Benallal, A., Berstad, T., Børvik, T., Clausen, AH., Hopperstad, OS., 2006. Dynamic strain aging and related instabilities: experimental, theoretical and numerical aspects. Eur. J. Mech.—A/Solids 25 (3), 397–424.

Børvik, T., Hopperstad, OS., Berstad, T., Langseth, M., 2001. A computational model of viscoplasticity and ductile damage for impact and penetration. Eur. J. Mech.—A/Solids 20 (5), 685–712.

Børvik, T., Hopperstad, OS., Langseth, M., Malo, KA., 2003. Effect of target thickness in blunt projectile penetration of Weldox 460E steel plates. Int. J. Impact Eng. 28, 413–464.

Børvik, T., Clausen, AH., Hopperstad, OS., Langseth, M., 2004. Perforation of AA5083-H116 aluminium plates with conical-nose steel projectiles – experimental study. Int. J. Impact Eng. 30 (4), 367–384.

Chen, W., Yang, H., Su, X., Tan, S., 1999. Error caused by sampling in Fourier transform profilometry. Opt. Eng. 38 (6), 1029–1034.

Chen, W., Su, X., Cao, Y., Xiang, L., 2004. Improving Fourier transform profilometry based on bicolour fringe pattern. Opt. Eng. 43 (1), 192–198.

Clausen, AH., Børvik, T., Hopperstad, OS., Benallal, A., 2004. Flow and fracture characteristics of aluminium alloy AA5083-H116 as function of strain rate, temperature and triaxiality. Mat. Sci. Eng. A 365, 260–272.

Corbett, GG., Reid, SR., Al-Hassani, STS., 1990. Static and dynamic penetration of steel tubes by hemispherically nosed punches. Int. J. Impact Eng. 9, 165–190.

Corbett, GG., Reid, SR., 1993. Quasi-static and dynamic local loading of monolithic simply-supported steel plate. Int. J. Impact Eng. 13 (3), 423–441.

Corbett, GG., Reid, SR., Johnson, W., 1996. Impact loading of plates and shells by free-flying projectiles. Int. J. Impact Eng. 18 (2), 141–230.

Dey, S., Børvik, T., Hopperstad, OS., Leinum, JR., Langseth, M., 2004. The effect of target strength on the perforation of steel plates using three different projectile nose shapes. Int. J. Impact Eng. 30, 1005–1038.

Fagerholt, E., 2004. Accurate measurements of out-of-plane deformations using structured light and close-range photogrammetry. MSc-Thesis, Department of Physics, Norwegian University of Science and Technology, Trondheim, Norway.

Goldsmith, W., 1999. Non-ideal projectile impact on targets. Int. J. Impact Eng. 22, 95–395.

Grytten F., Børvik T., Hopperstad OS., Langseth M., 2005. Numerical simulations of perforation of AA5083-H116 plates. In: Proceedings of MekIT'05 (National Conference in Computational Mechanics), Trondheim, Norway.

Harris C, Stevens M., 1998. A combined corner and edge detector. In: Proceedings of the 4th Alvey Vision Conference, pp. 189–192.

Hatch, JE., 1984. Aluminium: properties and physical metallurgy. Am. Soc. Metals, 353–357.

Heikkilä, J., 1997. Accurate camera calibration and feature based 3D reconstruction from monocular image sequences, Ph.D.-thesis, University of Oulo, Finland.

Johnson, W., Ghosh, SK., 1980. The quasi-static and dynamic perforation of thin aluminium plates. Aluminium 56, 142–146.

Johnson, W., Ghosh, SK., Reid, SR., 1980. Piercing and hole-flanging of sheet metals: a survey. Memoires Scientifiques Revue Metallurgie, 585–606.

Johnson, GR., Cook, WH., 1983. A constitutive model and data for metals subjected to large strains, high strain rates and high temperatures. In: Proceedings of the 7th International Symposium Ballistics, The Hague.

Johnson, GR., Cook, WH., 1985. Fracture characteristics of three metals subjected to various strains, strain rates, temperatures and pressures. Eng. Frac. Mech. 21, 31–48.

Kumar, R., Singh, IP., Shakher, C., 2004. Measurement of out-of-plane static and dynamic deformations by processing digital speckle pattern interferometry fringes using wavelet transform. Opt. Lasers Eng. 41, 81–93.

Lance, RH., Onat, ET., 1962. A comparison of experiments and theory in the plastic bending of circular plates. J. Mech. Phys. Solids 10, 301–311.

Langseth, M., 1988. Dropped objects; plugging capacity of steel plates. Dr.ing-thesis 1988:25. The Norwegian Institute of Technology, Trondheim, Norway.

Langseth, M., Larsen, PK., 1992. The behaviour of square steel plates subjected to a circular blunt ended load. Int. J. Impact Eng. 12 (4), 617–638.

LSTC., 2003. LS-DYNA Keyword User's Manual, Version 970. Livermore Software Technology Corporation, Livermore, USA.

Martínez-Celorio, RA., Barrientos, B., Sanchez-Marín, FJ., López, LM., Rayas, JA., 2002. Out-of-plane displacement measurement by electronic speckle pattern interferometry in presence of large in-plane displacement. Opt. Commun. 208, 17–24.

Onat, ET., Haythornthwaite, RH., 1956. The load-carrying capacity of circular plates at large deflections. J. Appl. Mech. 23, 49–55.

Sainov, V., Simova, E., Manoah, E., 1989. Plate bending investigations by comparative holographic moiré interferometry evaluation by the finite element method. Opt. Lasers Eng. 11, 15–25.

Salas, L., Luna, E., Salinas, J., García, V., Servín, M., 2003. Profilometry by fringe projection. Opt. Eng. 42, 3307–3314.

Su, X., Song, W., Cao, Y., Xiang, L., 2004. Phase-height mapping and coordinate calibration simultaneously in phase-measuring profilometry. Opt. Eng. 43, 708–712.

Tay, CJ., Quan, C., Huang, YH., Fu, Y., 2005. Digital image correlation for whole field out-of-plane displacement measurement using a single camera. Opt. Commun. 251, 23–36.

The MatWorks, 2002. MATLAB Version 6.5, MathWorks Inc., USA.

Zukas, JA. et al., 1982. Impact dynamics. John Wiley & Sons, New York.

Zukas, J.A. et al., 1990. High velocity impact dynamics. John Wiley & Sons, New York.

Part II

F. Grytten, T. Børvik, O.S. Hopperstad, M. Langseth

Quasi-Static Perforation of Thin Aluminium Plates

Accepted for publication in International Journal of Impact Engineering

Quasi-static perforation of thin aluminium plates

F. Grytten[a,*], T. Børvik[a,b], O.S. Hopperstad[a] and M. Langseth[a]

[a] *Structural Impact Laboratory (SIMLab), Centre for Research-based Innovation (CRI), Department of Structural Engineering, Norwegian University of Science and Technology, NO-7491, Trondheim, Norway.*

[b] *Norwegian Defence Estates Agency, Research & Development Department, PB 405, Sentrum, NO-0103, Oslo, Norway.*

Abstract

This paper presents an experimental and numerical investigation on the quasi-static perforation of aluminium plates. In the tests, square plates were mounted in a circular frame and penetrated by a cylindrical punch. A full factorial design was used to investigate the effects of varying plate thickness, boundary conditions, punch diameter and nose shape. Based on the results obtained, both the main and interaction effects on the maximum force, displacement at fracture and energy absorption until perforation were determined. The perforation process was then computer analysed using the nonlinear finite element code LS-DYNA. Simulations with axisymmetric elements, brick elements and shell elements were conducted. Quasi-static, isothermal versions of the Johnson-Cook constitutive relation and fracture criterion were used to model the material behaviour. Good qualitative agreement was in general found between the experimental results and the numerical simulations. However, some quantitative differences were observed, and the reasons for these are discussed.

Key words: Aluminium plates; Experimental tests; Numerical simulations; Johnson-Cook models; Fracture

---

[*] Corresponding author. Tel.: +47 73594700; fax: +47 73594701.

E-mail address: frode.grytten@sintef.no (F. Grytten).

1. Introduction

Low velocity impact and perforation of plated structures have become increasingly important for a number of civil and military engineering applications. Typical examples of civil applications are the design of offshore structures where account must be taken for accidental loads such as dropped objects and the design of vehicles and vessels where collisions must be considered.

Several comprehensive papers on the topic of plate structures impacted by free-flying projectiles have been published over the years. Important reviews can be found in the journal papers by Backman and Goldsmith [1], Corbett et al. [2] and Goldsmith [3], and in the books by Zukas et al. [3][5]. These reviews reveal that relatively few publications exist on the perforation of metal plates under quasi-static and low velocity impact conditions. Onat and Haythornwaite [6] studied the load carrying capacity of circular plates at large deflections. Langseth and Larsen [7][8][9][10] investigated the plugging capacity of steel and aluminium plates subjected to dropped objects. Corbett and Reid [11] examined both quasi-static and dynamic loading of steel plates, while Gupta et al. [12] carried out a similar study on thin aluminium plates. Wen and Jones [13] and Jones and Birch [14] studied low velocity perforation of various metal plates, while Atkins et al. [15] studied petaling and radial cracking during perforation of thin sheets.

Despite the extensive literature available on penetration in general, low velocity perforation of metal plates is still considered as a complex problem both from an experimental, analytical and numerical point of view. Many of the physical phenomena seen in high velocity impacts, such as strain rate and inertia effects, are prevailing also in this type of problem. In addition, the global response of the structure must be taken into account. Impacts involving a large mass travelling at low velocities have first a transient phase followed by a phase that is very similar to quasi-static loading [9]. It is therefore useful to perform quasi-static perforation tests, where material uncertainties associated with impact-generated high strain-rate loading conditions as well as inertia effects are omitted in order to validate physical assumptions, theoretical calculations and numerical models. However, also quasi-static perforation problems involve factors like large strains, contact, damage and fracture. Research in this field has therefore generally been of an empirical nature. Often, generic problems with simple geometry and boundary conditions have been studied. Some analytical models have been suggested for the generic penetration problem. These models utilize simplified material models. The effects of work hardening and strain rate are often ignored, and a simplified yield locus is used so that calculations can be carried out by hand. Then again, the increase in computer performance over the last decades has made finite element analysis more available to this type of problems. Now, complex structures and advanced material behaviour can be more accurately analysed. Engineers have started to optimize designs using finite element models and it seems to be a general opinion that the understanding of the physical processes during perforation can increase through validated numerical simulations. It is therefore of crucial importance that the numerical models are validated through comparison with experiments, especially when new materials are introduced.

In this paper an experimental and numerical investigation on the quasi-static perforation of AA5083-H116 aluminium plates is carried out to evaluate the applicability of one of the most frequently used material models for penetration (Johnson-Cook) and various finite element formulations. AA5083-H116 is a relatively strong aluminium-magnesium alloy, and is well suited for rolling. Since the alloy also has good corrosion resistance, it is often used in plates in offshore structures where accidental loads may be a concern. In the present study, square plates were mounted in a circular frame and the load was applied through a cylindrical punch. The test rig consisted of a 400 kN hydraulic actuator with a replaceable nose inserted in a stiff supporting frame. A full factorial design was used to investigate the effect of varying plate thickness, boundary conditions, punch diameter and nose shape. Based on the obtained results, both the main and interaction effects on the maximum force, displacement at fracture and energy absorption until perforation were studied. The perforation process was then computer analysed using the explicit solver of the nonlinear finite element (FE) code LS-DYNA [16], and the problem was simulated using axisymmetric elements, brick elements and shell elements. In the simulations, quasi-static, isothermal versions of the Johnson-Cook constitutive relation [17] and fracture criterion [18] were used to model the material behaviour. Good qualitative agreement was in general found between the experimental results and the numerical simulations over a wide range of test parameters. However, some quantitative differences were observed, and the reasons for these are discussed in some detail.

2. Experimental study

2.1 Material

The AA5083 is an aluminium-magnesium alloy with relatively high magnesium content. The most important alloying elements are 4.75 wt.% magnesium, 0.84 wt.% manganese and 0.18 wt.% iron, while Zn, Cr, Si, Cu, Ti, Ni, Zr and Pb are present in small amounts. The high content of magnesium in the alloy leads to a phenomenon denoted the Portevin-Le Chatelier (PLC) effect [19]. The PLC effect causes serrated or jerky flow in certain ranges of temperature and strain rate, and is associated with repeated propagation of bands of localised plastic strain rate. The occurrence of PLC is linked to a bounded region of negative strain rate sensitivity of the flow stress, resulting from diffusion of solute atoms to dislocations temporarily arrested at obstacles in the slip path [20].

Condition H116 implies a certain strength level plus special corrosion resistance. This must not be confused with the conventional states H1*, where the last digit stands for the degree of work hardening. Condition H116 can be achieved by various means, e.g. a low degree of cold rolling, specific back-annealing or hot rolling at low temperatures. Normally the thinnest plates are first hot rolled, then cold rolled and finally annealed, while thicker qualities are mostly hot rolled. In all cases, the microstructure will differ and a distinct variation in mechanical properties between different plate thicknesses can be seen.

The aluminium alloy is also found to be anisotropic in strength and plastic flow. Both the anisotropy and the serrated flow due to PLC are illustrated in Figure 1, which shows the true stress-strain curves from quasi-static tensile tests on smooth, axisymmetric specimens at room temperature. The specimens were taken in three different orientations with respect to the rolling direction of a 10 mm thick plate in order to reveal the plastic anisotropy. As seen, the anisotropy in strength is moderate, while the anisotropy in plastic strain to fracture is considerable. In the 45° direction, the failure strain is found to be about twice as large as the failure strain in the rolling (0°) direction.

As mentioned, AA5083-H116 is a strong aluminium-magnesium alloy. It is well suited for rolling and has good corrosion resistance and is therefore often used in plates in offshore structures where accidental loads must be taken into account. In order to reveal the mechanical behaviour of AA5083-H116 under impact generated loading conditions, the flow and fracture characteristics of the alloy as function of strain rate, temperature and stress triaxiality were investigated in detail by Clausen et al. [19]. The experimental programme involved more than 100 tensile tests with axisymmetric specimens taken in three different directions of the plate material. Four types of tensile tests were carried out: quasi-static smooth specimen tests, quasi-static notched specimen tests, tests at different strain-rates and tests at elevated temperatures. However, the material coupons tested by Clausen et al. [19] were taken from a 25 mm thick plate, while in the present study plates with thicknesses of 3, 5 and 10 mm are considered. Since plates of different thicknesses have different mechanical properties, new tensile tests were conducted in the rolling direction at a strain rate of 10^{-4}s^{-1} (see Figure 2). These new tests will be used to calibrate the constitutive relation, while the data of Clausen et al. [19] will be used with a correction to fit the fracture criterion. Since the rolling takes place at low stress triaxialities, it is believed that the damage accumulation must be small and that the fracture data of Clausen et al. [19] is valid also for the plates investigated in the present study.

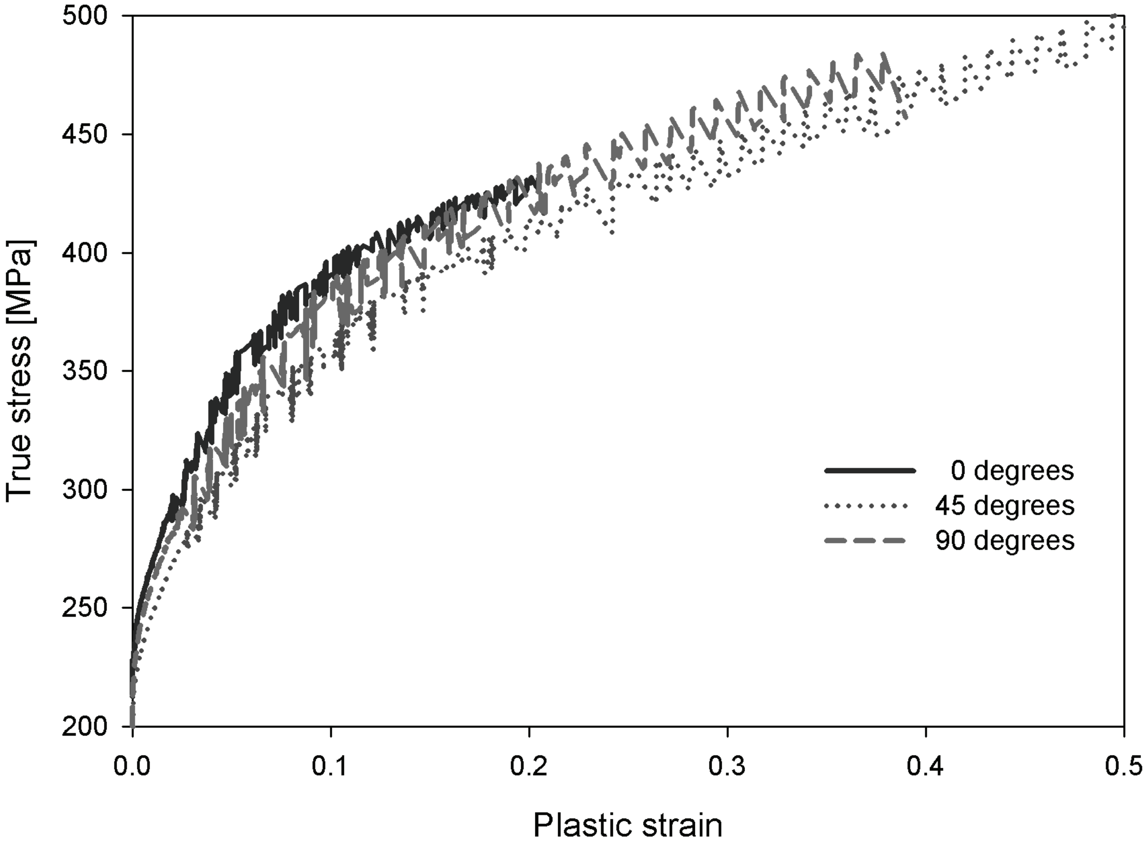

Figure 1. Anisotropic hardening with PLC and difference in ductility (from quasi-static tensile tests on smooth, axisymmetric specimens taken from a 10 mm thick plate).

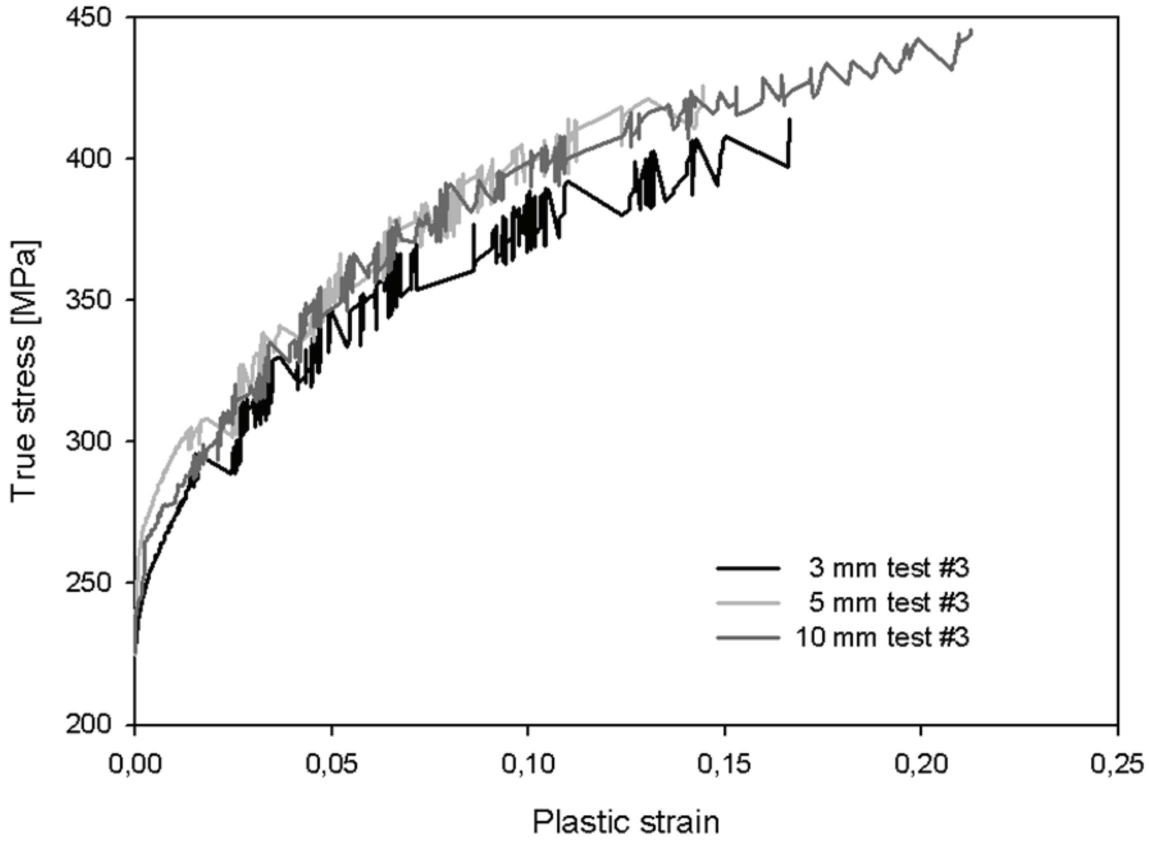

Figure 2. Hardening curves for the different thicknesses.

2.2 Experimental set-up

The test rig used in the quasi-static punch tests is shown in Figure 3. It consists of a 400 kN Amsler hydraulic actuator with a stroke length of ± 100 mm inserted in a stiff supporting frame. A replaceable punch of hardened tool steel (HRC 62) is connected to the actuator. The geometry of the circular punches used during testing is shown in Figure 4. Square 5083-H116 aluminium plates with dimensions 600x600 mm^2 were carefully cut from a larger plate and mounted between two massive circular steel rings with a free-span diameter of 500 mm using 24 pre-stressed M16 bolts. Even though this was done with great care, the target can not be regarded as fully clamped in these tests, and both small rotations and contractions of the boundary took place during loading [21]. Photographs of the target plate before and after mounting in the clamping rings are given in Figure 5. The clamping rings and the target were carefully aligned on a rigid bottom frame to ensure that the punch was applied in the centre of the plate. Thus, the loading was in principle axisymmetric. A simple support was obtained by just placing the plates on the bottom ring and omitting the upper ring and the bolts.

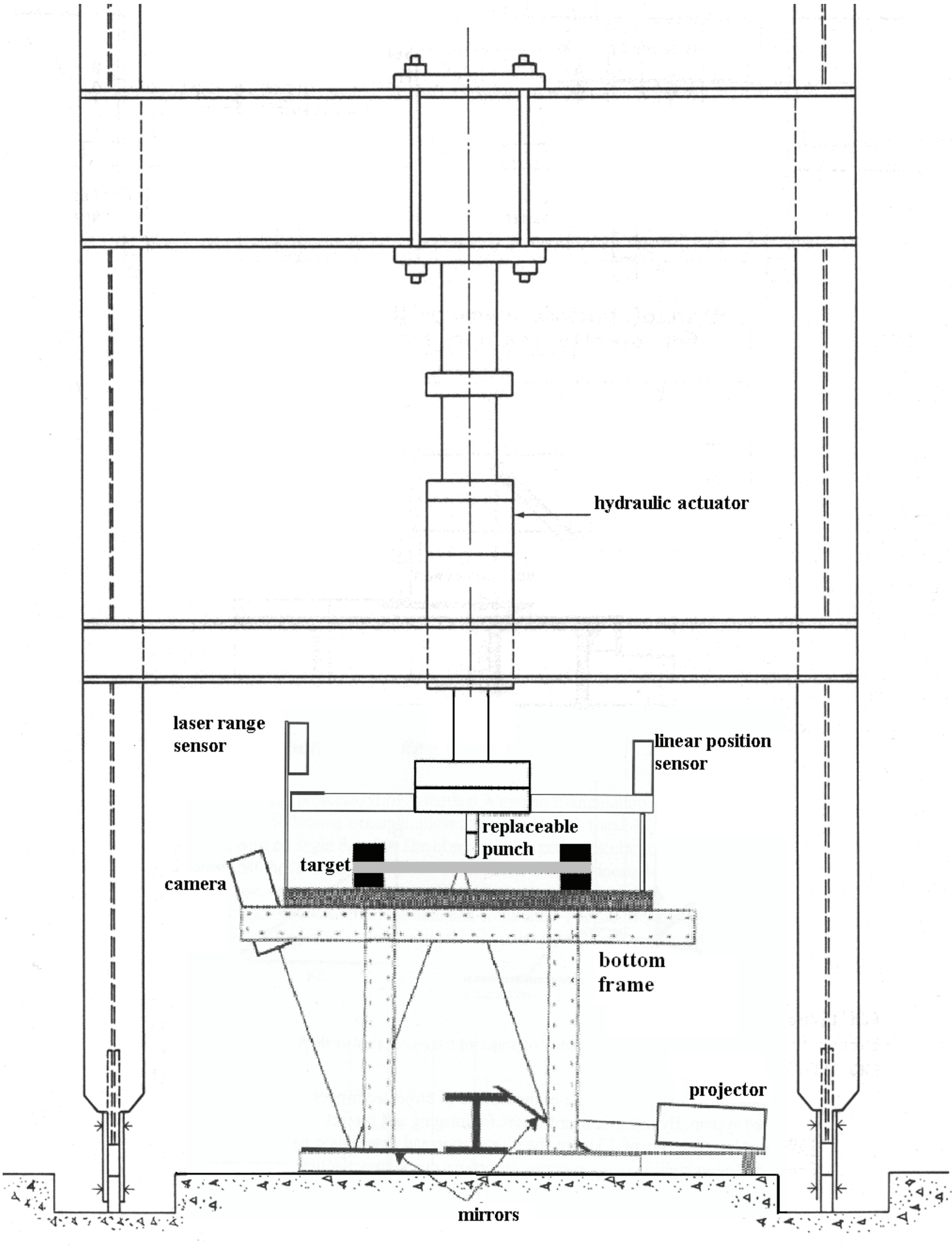

Figure 3. Test rig used during quasi-static loading.

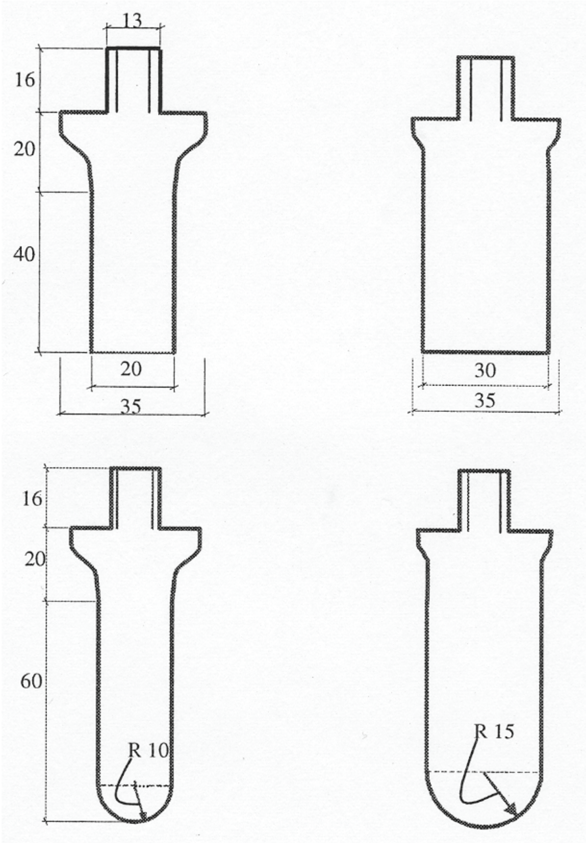

Figure 4. Geometry of punches used during quasi-static tests.

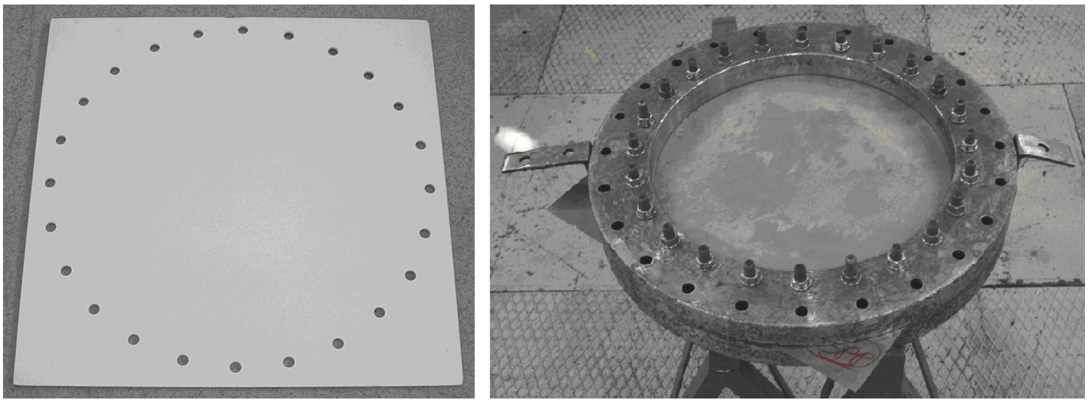

Figure 5. Target plate before (left) and after (right) mounting in the clamping rings.

During testing, the hydraulic actuator was operated in displacement control-mode at a rate of 2 mm per minute. At this speed, a typical experiment took about 10-15 minutes from start until the punch perforated the plate. The penetration process can thus be regarded as both quasi-static and isothermal. As the punch penetrated the target plate, the punch force and punch displacement were continuously measured. The punch displacement was measured using two independently operating displacement transducers (one mechanical and one non-contacting laser gauge), in addition to recording the displacement of the hydraulic actuator. The load cell of the hydraulic actuator was calibrated in an Instron servo-hydraulic testing machine and an accuracy of ± 1% at maximum force was found. The accuracy of the displacement transducers was measured to be ± 0.2% of the full scale displacement of 100 mm.

In addition to the basic instrumentation, out-of-plane displacement of the entire plate was measured optically in some of the tests. The optical out-of-plane displacement system is described in detail in Grytten et al. [21]. The measurement principle is based on structured light and close-range photogrammetry. Contour maps of the plate deformation at different load levels were made, and these could be used to generate out-of-plane displacement profiles of the plate as a function of the load level. These displacement profiles can be compared to FE simulations in order to validate the numerical models. Examples of such profiles and validation of FE models can be found in Grytten et al. [21]. The set-up of the instrumentation used in the tests is sketched in Figure 6.

2.3 Factorial design

The target thickness, punch nose-shape, punch diameter and the boundary conditions of the target plate were changed according to a factorial design (see e.g. [22]). The effects of these parameters on the maximum force the plates could resist before fracture, the displacement at fracture and the energy required to perforate the plates were studied. Plates with thicknesses 3, 5 and 10 mm were perforated with blunt and hemispherical punches having diameters of 20 and 30 mm. The boundary conditions of the plates were either clamped or simply supported.

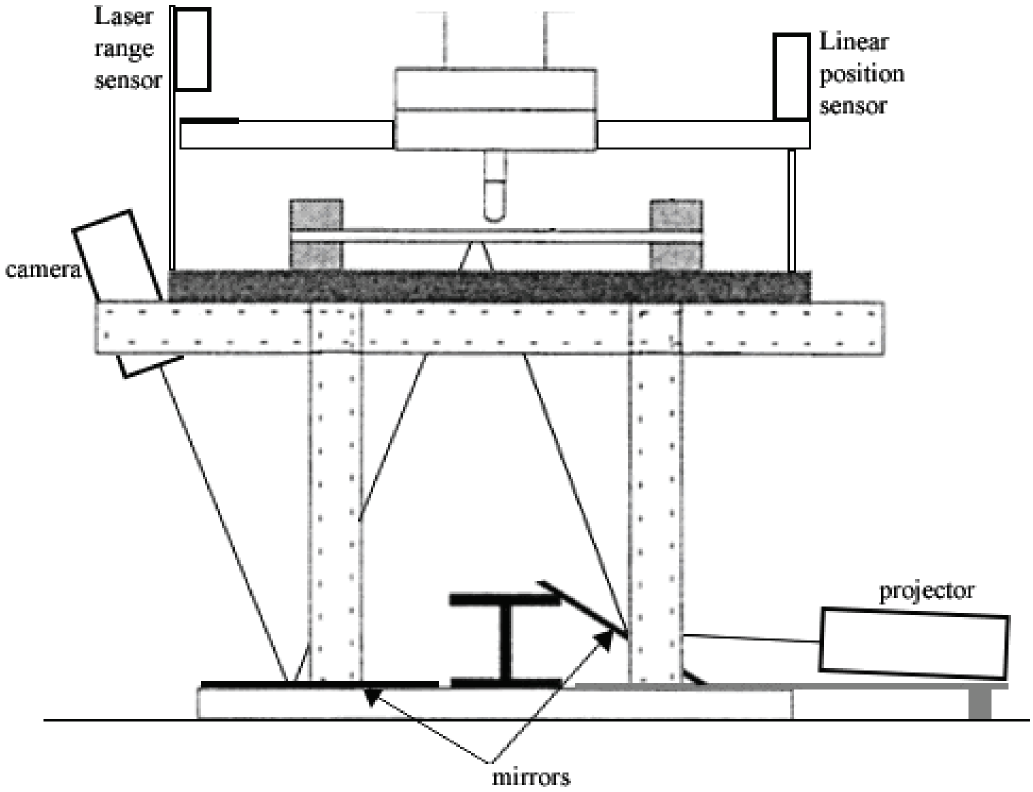

Figure 6. Set-up of instrumentation during quasi-static punch tests [21].

Since the number of factors is relatively small a full factorial design was chosen in order to have a satisfactory resolution. All possible combinations of levels of input factors must then be run, i.e. 3×2×2×2=24 different set-ups (treatments) must be tested. The 24 various set-ups used during testing are listed in Table 1 (together with some main experimental results). Based on the results obtained, the main and interaction effects on the maximum force, displacement at fracture and energy required for perforation were found. A *main effect* is the simple effect of a factor on a dependent variable. Thus, it is the effect of the factor alone averaged across the levels of other factors. For 2^k factorial designs, main effects are calculated by subtracting the average response at the low level of a factor from the average response at the high level of the same factor. For example, the main effect of the punch shape on the maximum force can be calculated by subtracting the average maximum force of all experiments with a punch diameter of 20 mm from the average maximum force of all experiments with a punch diameter of 30 mm

$$\text{Effect}_d = \bar{F}_{\max}\left(d=30\right) - \bar{F}_{\max}\left(d=20\right) \tag{1}$$

An *interaction* is the variation among the differences between means for different levels of one factor over different levels of the other factors. If a factor changes the effect of another factor, then an interaction exists. For 2^k factorial designs, second order interactions are calculated by summing the average response at the high level of both factors and at the low level of both factors and then subtracting the average response at different levels of the two factors. For example, the interaction effect of punch diameter and punch shape on the maximum force can be calculated as

$$\begin{aligned}\text{Effect}_{d*s} = {} & \bar{F}_{\max}\left(d=30, shape = hemispherical\right) + \bar{F}_{\max}\left(d=20, shape = blunt\right) \\ & -\bar{F}_{\max}\left(d=30, shape = blunt\right) - \bar{F}_{\max}\left(d=20, shape = hemispherical\right)\end{aligned} \tag{2}$$

Higher order interactions may also be calculated as explained by Box et al. [22], but these are often small and are therefore not considered here. Effects and interactions are not calculated for general factorial designs (where factors can have more than two levels). Instead, it is customary to visualize the main and interaction effects in main effect plots and interaction plots, respectively.

2.4 Experimental results

The main response values (i.e. the maximum force, the displacement at fracture and the energy absorption until fracture) for each test carried out are given in Table 1, while Figure 7 shows typical results from some of the tests. In these tests, a sudden drop in force when plugging occurred was found for plates subjected to a blunt punch, while a more gradual drop in force was observed during petaling in the plates subjected to a hemispherical punch. The maximum force is greater for a blunt punch than for a hemispherical. It is also seen that the boundary conditions do not affect the maximum force in the test results presented in Figure 7, but the shape of the force-displacement curve and the displacement at maximum force are influenced by the boundary conditions.

Table 1. Test programme based on factorial design.

Test #	Variable				Measured response		
	Plate thickness (mm)	Boundary condition	Nose shape	Punch diameter (mm)	Maximum force (kN)	Displacement at fracture (mm)	Energy absorption (Nm)
1	3	Simply supported	Blunt	20	32.2	26.3	283.0
2	3	Simply supported	Blunt	30	32.2	27.7	309.2
3	3	Simply supported	Hemispherical	20	15.1	22.5	139.4
4	3	Simply supported	Hemispherical	30	27.7	25.9	260.5
5	3	Clamped	Blunt	20	31.5	20.6	247.3
6	3	Clamped	Blunt	30	32.1	23.4	275.4
7	3	Clamped	Hemispherical	20	15.1	19.6	114.6
8	3	Clamped	Hemispherical	30	27.9	23.2	266.8
9	5	Simply supported	Blunt	20	39.6	25.7	374.7
10	5	Simply supported	Blunt	30	53.8	30.6	562.7
11	5	Simply supported	Hemispherical	20	25.3	26.8	290.6
12	5	Simply supported	Hemispherical	30	39.6	25.5	413.5
13	5	Clamped	Blunt	20	40.1	23.8	472.2
14	5	Clamped	Blunt	30	56.5	24.8	684.1
15	5	Clamped	Hemispherical	20	33.2	22.6	359.0
16	5	Clamped	Hemispherical	30	28.5	21.9	268.8
17	10	Simply supported	Blunt	20	92.9	27.4	1084.3
18	10	Simply supported	Blunt	30	99.7	23.5	944.8
19	10	Simply supported	Hemispherical	20	89.9	30.2	1453.9
20	10	Simply supported	Hemispherical	30	79.8	35.3	1491.2
21	10	Clamped	Blunt	20	92.2	23.6	1089.5
22	10	Clamped	Blunt	30	99.7	17.8	853.1
23	10	Clamped	Hemispherical	20	88.3	22.7	1109.4
24	10	Clamped	Hemispherical	30	77.0	28.3	1268.3

The results from all these tests were used to calculate the main and interaction effects on the maximum force, displacement at fracture and energy required for perforation. The main and interaction effects on the maximum force are visualized in Figure 8 and Figure 9, respectively. Figure 8 shows that the thickness of the plate is the single factor that influences the maximum force the most (the steeper the curve, the greater is the difference between the average response at the high level of the factor and the low level of the factor). It also indicates that the maximum force is almost proportional to the plate thickness. The shape and diameter of the punch have smaller but significant effects, while the boundary condition has a negligible effect. The plates can withstand a greater force when subjected to a blunt punch than subjected to a hemispherical one, and the maximum force increases slightly with increasing punch diameter. A linear relation between the maximum force and the diameter of the punch for plugging problems is usually assumed [10], but this does not seem to be a valid assumption in this case. It can be seen from Figure 8 that the maximum force just increases slightly when the punch diameter is increased from 20 to 30 mm. Note that the figure shows the average increase for all combinations of the other factors. Only small interaction between the punch diameter and the other factors can be seen in Figure 9. Note that parallel lines in Figure 9 indicate that there is no interaction between the factors [22]. It is therefore evident that the maximum force just increases slightly with increasing punch diameter for all levels of the other factors in the investigated range of parameters. The reason for the discrepancy between the established theories and the experimental results in this study is probably that the analytical models assume a pure shear stress state (with constant stress through the thickness) which does not occur in the present experiments. Fracture was observed to start at the rear surface of the plate in the present experiments, where the stress state is biaxial tension.

It can further be seen from Figure 9 that the interaction effects are smaller than the main effects on the maximum force. The same was found to be the case for the two other response parameters, so only the main effects will be considered in the rest of this paper. The main effects on the displacement at maximum force and the work required to perforate the plate are shown in Figure 10 and Figure 11, respectively. The displacement at maximum force is most dependent on the boundary conditions, while the work required to perforate the plate depends on the same variables as the maximum force. The fact that the work does not depend on the displacement at maximum force or the boundary can be explained by the change in shape of the force-displacement curve. As can be seen from Figure 7, the area under the curves is approximately the same regardless of the boundary conditions. This is also in accordance with the findings of Langseth and Larsen [8] in an investigation of steel plates.

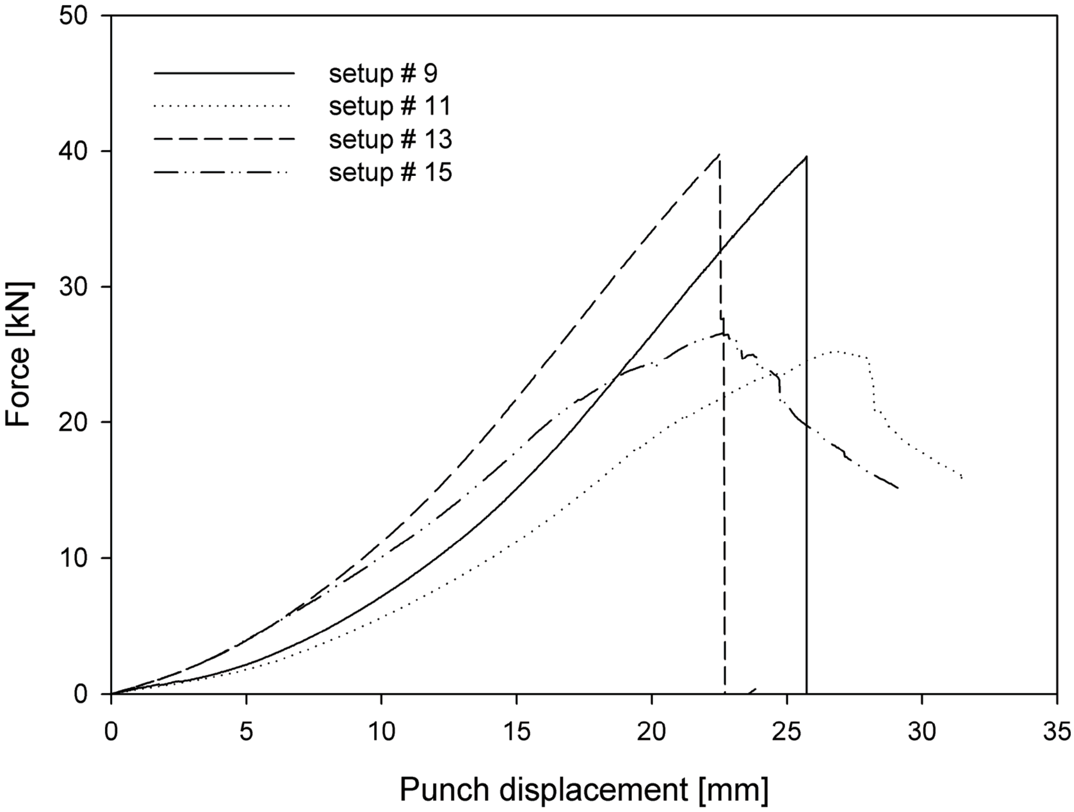

Figure 7. Some typical results from the experimental tests.

The experiments further revealed that the failure mode is strongly dependent on the nose shape of the punch and on the thickness of the plate. All plates subjected to a blunt punch failed by plugging, whereas most of the plates subjected to a hemispherical punch failed by petaling. However, some of the thickest plates failed by plugging when a hemispherical punch was used (setups 19 and 23). In those cases the force decreased slowly for a while after the maximum force was reached before a sudden drop in force was observed when plugging occurred. Investigations of the plugs revealed that a radial fracture had occurred in most of them. Some of the plates that failed by petaling also showed signs of plug formation (see

Figure 12). This indicates that the chosen range of punch diameters and target thicknesses is in a transition zone of failure modes. The number of petals seen in the plates that failed by petaling varied from 3 to 5. The boundary conditions of the plate seem to have no influence on the failure mode.

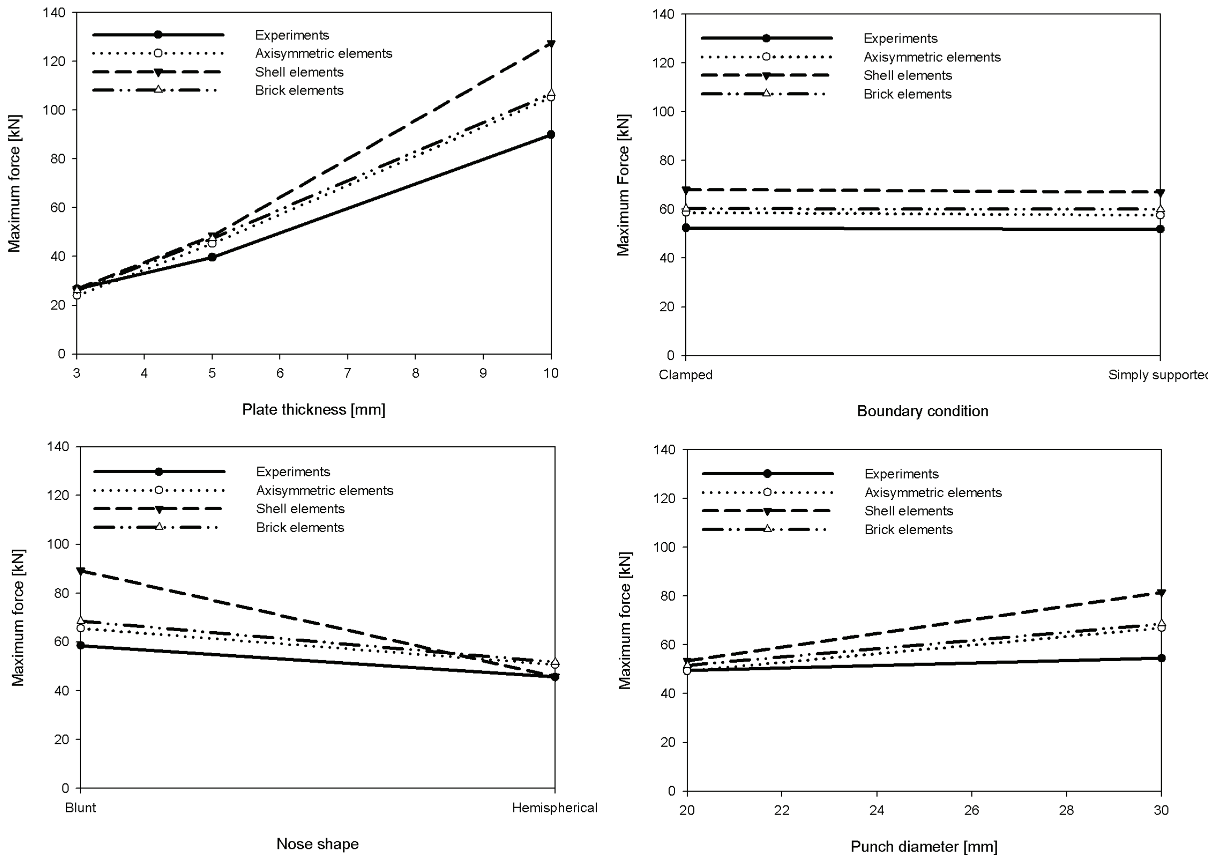

Figure 8. Comparison of main effects on the maximum force from both experiments and simulations.

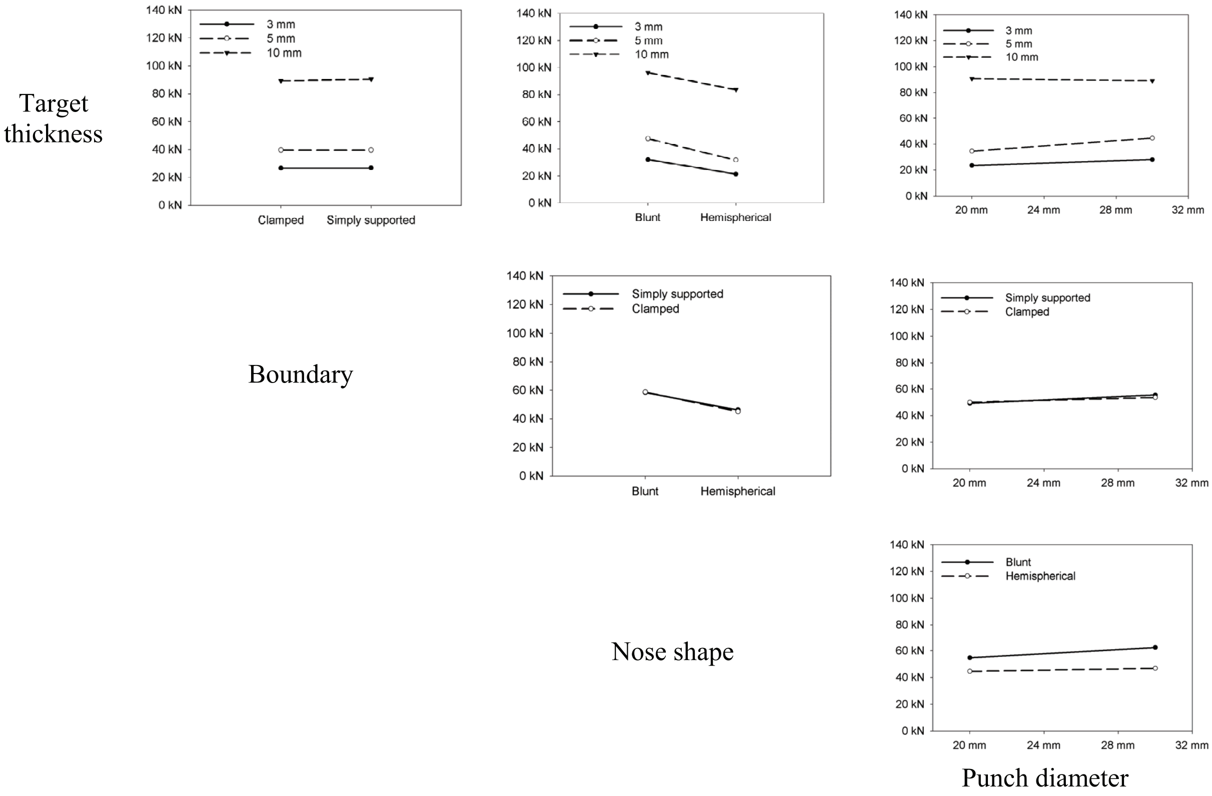

Figure 9. Interaction effects on maximum force from experiments.

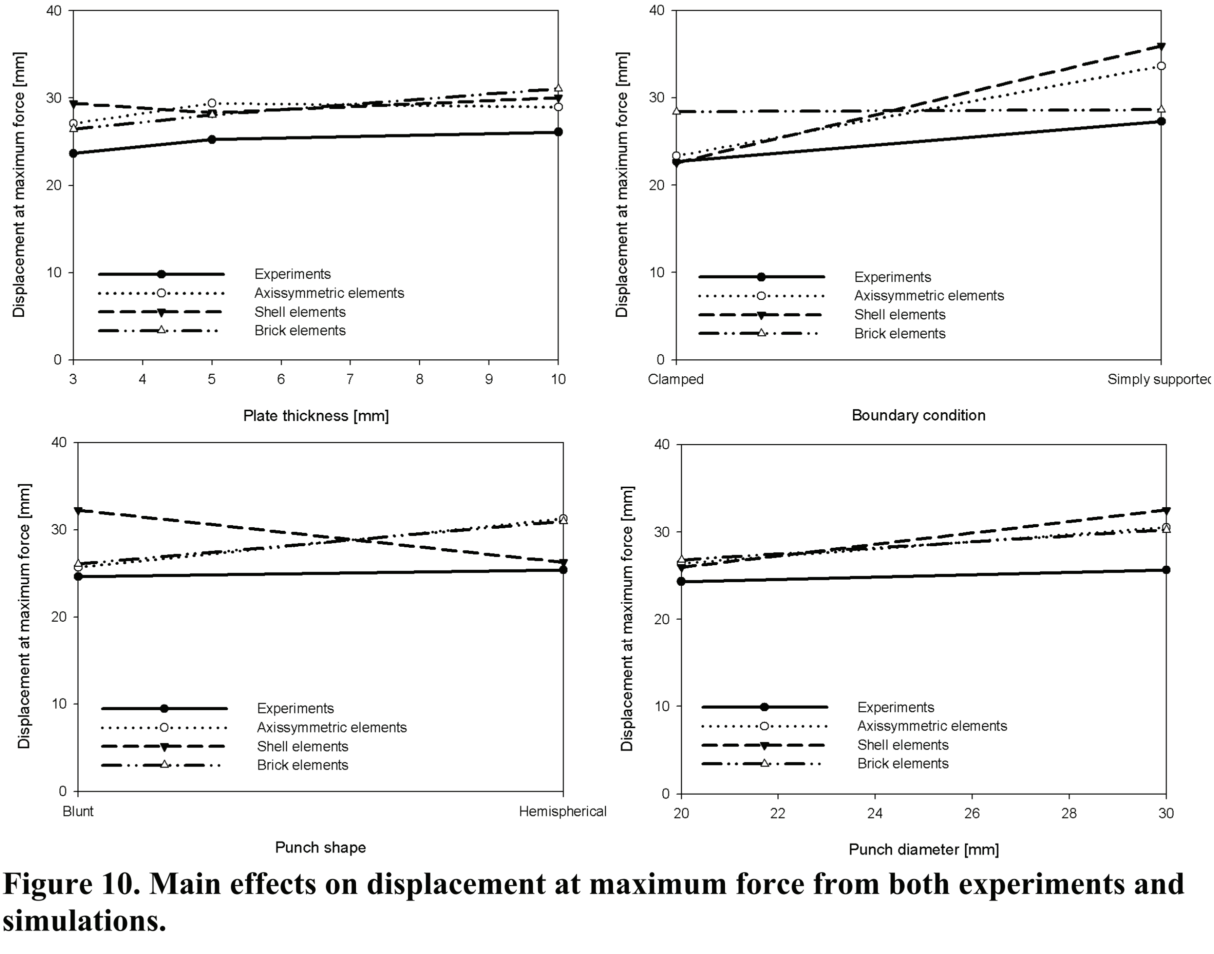

Figure 10. Main effects on displacement at maximum force from both experiments and simulations.

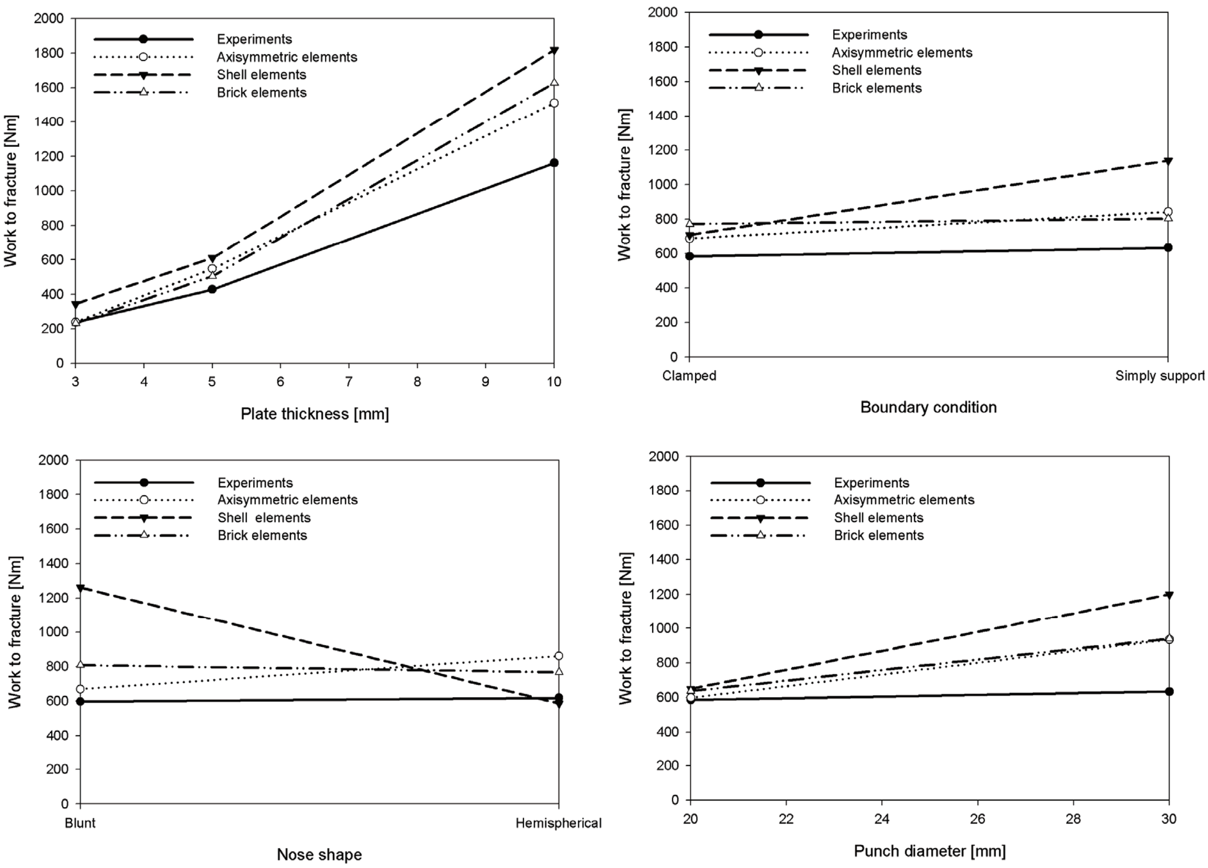

Figure 11. Comparison of main effects on energy dissipation from both experiments and simulations.

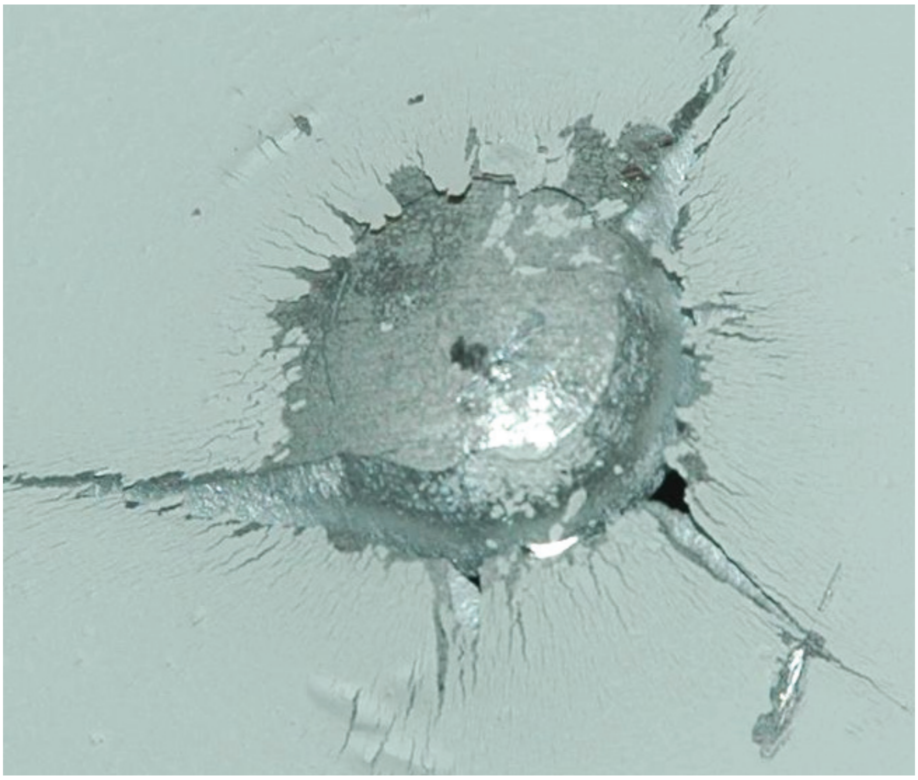

Figure 12. Petaling with plug formation.

3. Numerical simulations

3.1 Constitutive relation and fracture criterion

Several constitutive relations have been proposed over the years for use in numerical simulations of perforation of metallic materials. The multi-axial stress state of the material is usually expressed in terms of the equivalent stress $\bar{\sigma}$, and many constitutive relations define this stress in terms of the equivalent plastic strain $\bar{\varepsilon}$, equivalent plastic strain rate $\dot{\bar{\varepsilon}}$ and temperature *T* as

$$\bar{\sigma} = f\left(\bar{\varepsilon}, \dot{\bar{\varepsilon}}, T\right) \tag{3}$$

Johnson and Cook [17] proposed such a phenomenological constitutive relation, which is frequently used in impact analysis due to its simplicity. Since quasi-static perforation is investigated in the present study, strain rate effects are assumed to be negligible. Further, the long duration of the perforation process is believed to allow the generated heat to disperse in the plate and therefore gives a negligible temperature increase. Thus, only the work hardening part of the Johnson and Cook model will be used here and the factors governing strain rate and temperature will be set equal to unity. The constitutive relation then reduces to Ludwik's equation

$$\bar{\sigma} = \mathrm{A} + \mathrm{B}\bar{\varepsilon}^{\mathrm{n}} \tag{4}$$

where A, B and n are material constants.

Johnson and Cook [18] also proposed a fracture criterion that accounts for strain path, strain rate, temperature and stress triaxiality. The fracture criterion is based on damage evolution where the damage variable *D* of a material element is expressed as

$$D = \int_0^{\bar{\varepsilon}} \frac{d\bar{\varepsilon}}{\varepsilon_f} \leq 1 \qquad (5)$$

where ε_f is the fracture strain for a given stress, strain rate and temperature state. Failure occurs when *D* equals unity. Then all stress components in the integration point are set equal to zero and the element is eroded when failure has occurred in a certain number of integration points inside the element. When the factors governing strain rate and temperature are set equal to unity, the equivalent strain at fracture is given by

$$\varepsilon_\mathrm{f} = \mathrm{D}_1 + \mathrm{D}_2 \exp\left(\mathrm{D}_3 \sigma^*\right) \qquad (6)$$

where D_1, D_2 and D_3 are material constants, and σ^* is the stress triaxiality ratio defined as $\sigma_m / \bar{\sigma}$, where σ_m is the mean stress.

The parameters A, B and n were all determined based on the material tests described in Section 2.1. Some differences in yield stress and hardening properties were found between the 3 mm thick plates and the two thicker plates due to different degrees of work hardening in the rolling process. This was accounted for by using two different sets of hardening parameters; one for the 3 mm thick plates and one for both the 5 and 10 mm thick plates. The hardening parameters for the various thicknesses are given in Table 2.

Table 2. Parameters of the Johnson-Cook constitutive relation.

Plate thickness	A [MPa]	B [MPa]	n
5 and 10 mm	206.2	424.0	0.362
3 mm	223.8	423.3	0.441

The fracture parameters D_1, D_2 and D_3 were found by a fit to the data obtained by Clausen et al. [19] on smooth and notched specimens. Since rolling takes place at low stress triaxialities, the damage accumulation during rolling is assumed to be negligible. Thus, the fracture data of Clausen et al. [19] is believed to be valid also for the plates in the present study. The same set of damage parameters were used for all thicknesses since the initial damage is assumed to be the same. Only fracture strains calculated from cross sectional areas measured in the microscope were used in the fitting, since those were regarded as the most accurate. The fracture parameters obtained are listed in Table 3.

Table 3. Parameters of the Johnson-Cook fracture criterion.

D_1	D_2	D_3
0.178	0.389	-2.25

All material tests of Clausen et al. [19] were for positive stress triaxialities. Thus, an extrapolation into the region of negative stress triaxialities is required. This procedure may lead to substantial errors, since no experimental data is available to guide the extrapolation when $\sigma^* < 1/3$ in this study. In introductory simulations with a hemispherical punch (the numerical models will be presented in detail in Section 3.2) and fracture parameters from a best fit to the data by Clausen et al. [19], the plate just crumbled away under the punch, showing a very brittle behaviour. This is illustrated in Figure 13. The failure strain at $\sigma^* = -1/3$ was therefore set equal to 1. This additional constraint to the curve fitting prevents premature fracture in the compressive parts of the structure without influencing the failure strain at positive triaxialities too much. Measured and fitted failure strains as function of stress triaxiality ratio are shown in Figure 14. This is in some accordance with the findings of Bao and Wierzbicki [24], who claimed based on upsetting tests that fracture could never occur for stress triaxialities below $-1/3$. They also found that the ductility dropped for stress triaxialities near zero when they investigated the aluminium alloy Al2024-T351. Based on this they proposed an alternative fracture criterion with a cut-off at $-1/3$ and a drop in failure strain around zero.

3.2 Numerical models

The perforation process has been simulated with axisymmetric elements, brick elements and shell elements, and a comparison of the results obtained with the different models has been made. When modelling the plate with axisymmetric elements, a characteristic element size of approximately 0.15 mm was chosen in the local region of the plate (defined as 1.2 times the diameter of the punch). The actual number of elements over the plate thickness was 20, 32 and 64 for plates with thickness 3, 5 and 10 mm, respectively. The element size was doubled in the global part of the plate. Figure 15 shows an axisymmetric model of a plate that is about to be perforated by a hemispherical punch. Under-integrated axisymmetric elements with one integration point and Flanagan-Belytschko stiffness-based hourglass control with exact volume integration were used. The axisymmetric simulations took from 7 to 20 CPU hours to complete with a 3 GHz Intel Pentium 4 processor. Simulations with half the element size were run for some test configurations in order to study the mesh size dependency. This was also done for brick and shell element models and no significant mesh size dependency was observed. This is in contrast to what is normally seen in impacts at greater velocities. At greater velocities, the deformation tends to localize, e.g. in adiabatic shear bands [25]. However, the deformation did not seem to localize before fracture in the present experiments and simulations.

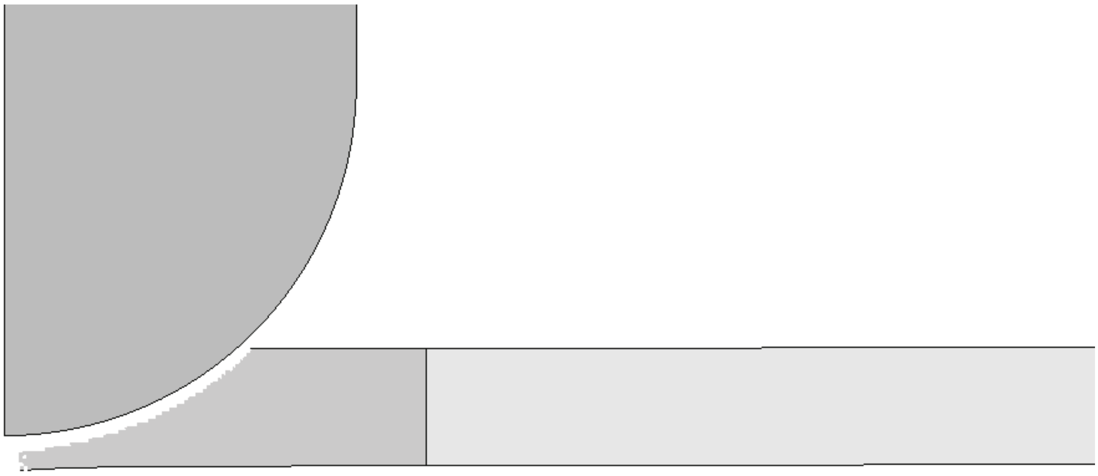

Figure 13. The plate crumbles away under the hemispherical punch without a constraint on the fracture criterion.

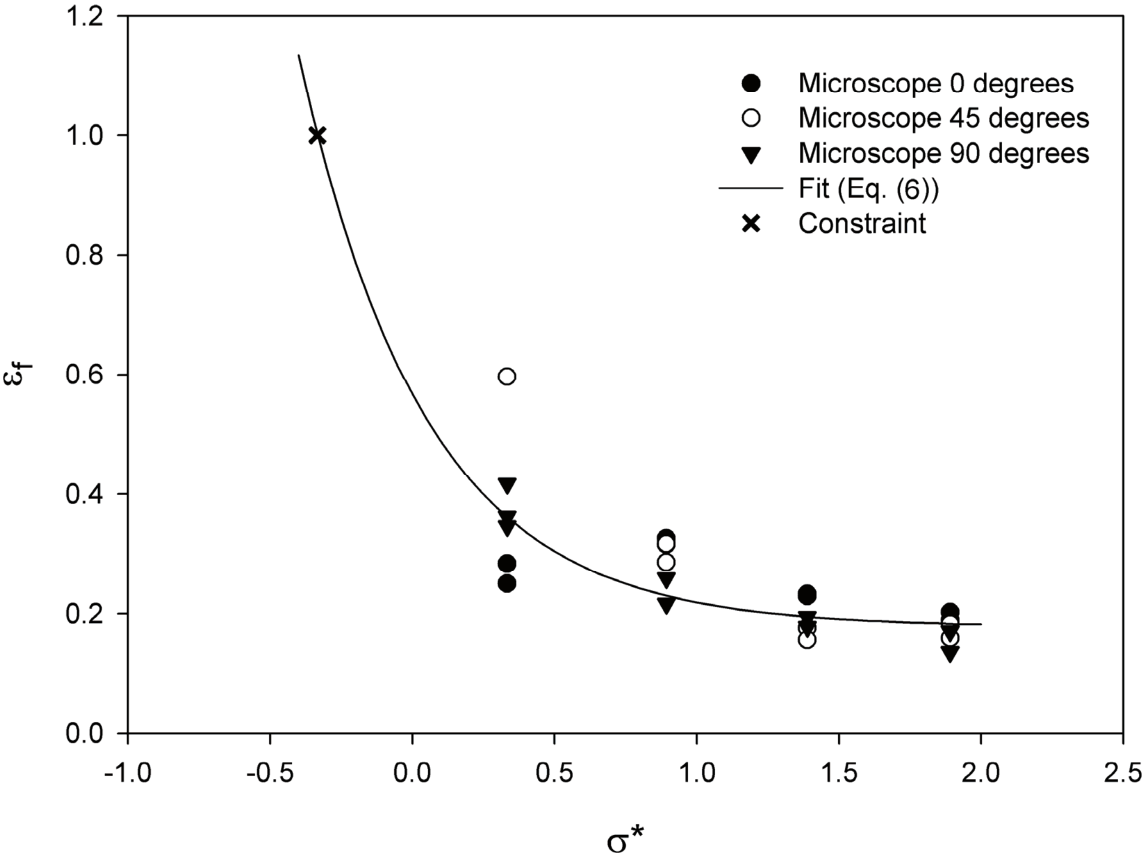

Figure 14. Failure strain as function of stress triaxiality ratio.

When using 8 node constant-stress brick elements, the characteristic element size was increased to the range 0.4 – 1 mm. This was required in order to keep the computational time reasonable. The actual number of elements over the plate thickness was 5, 8 and 16 for plates with thickness 3, 5 and 10 mm, respectively. The local part was defined as a rectangle with sides equal to the diameter of the local part in the axisymmetric and shell element models. The entire plate was modelled in order to be able predict petaling in a realistic way (since symmetry planes are not known a priori). The full model is shown in Figure 16 (left). Here the boundary conditions of the plate were introduced by also modelling the clamping rings. The experiments with a blunt punch could in fact have been modelled with only $1/48$ of the plate, as indicated in Figure 16 (right), since plugging is axisymmetric in nature and there are 24 symmetry planes intersecting the plate, the punch, the bolts and the clamping rings. With such a model one would still be able to describe the boundary conditions well and at the same time reduce the computational time significantly. However, all simulations were run with a full model in this study. Note that the plate was modelled as circular, i.e. the corners were not modelled. Each simulation took from 70 to 200 CPU hours to run.

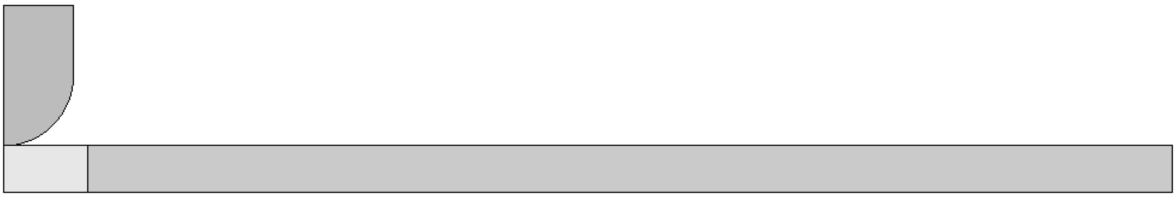

Figure 15. Axisymmetric model of a plate and a hemispherical punch.

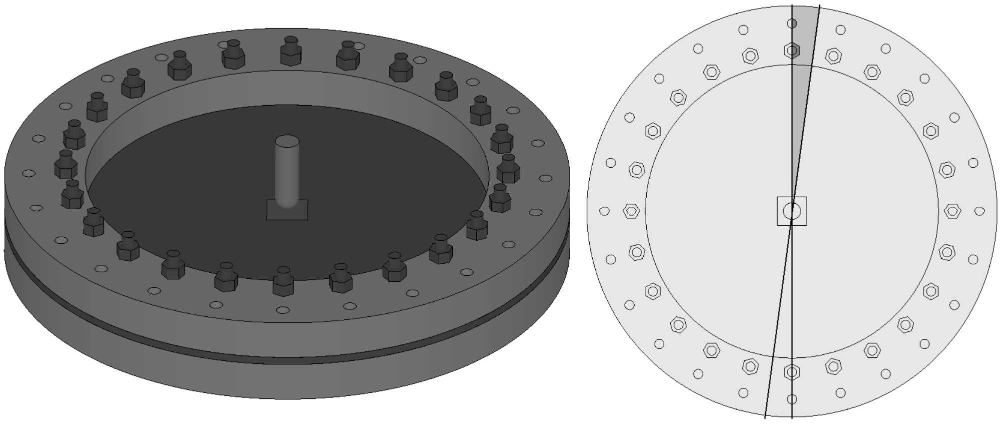

Figure 16. Full brick element model (left) and a 7.5° slice exploiting symmetry planes (right).

In addition to modelling the penetration process with brick and axisymmetric elements, it was also modelled with Belytschko-Tsay shell elements. A typical model is shown in Figure 17. Ten integration points were used through the plate thickness in the local part, while only 4 integration points were used in the rest of the plate. As for the brick element model, the entire plate was modelled even if symmetry could have been used to reduce computational time. Note that only the part of the plate that is inside the clamping rings was modelled. A typical simulation using shell elements required approximately 3 CPU hours. Approximately 10 % of the CPU time was spent in the contact algorithms for the brick and shell element models, while more than 99 % of the time was spent on element processing in the axisymmetric models.

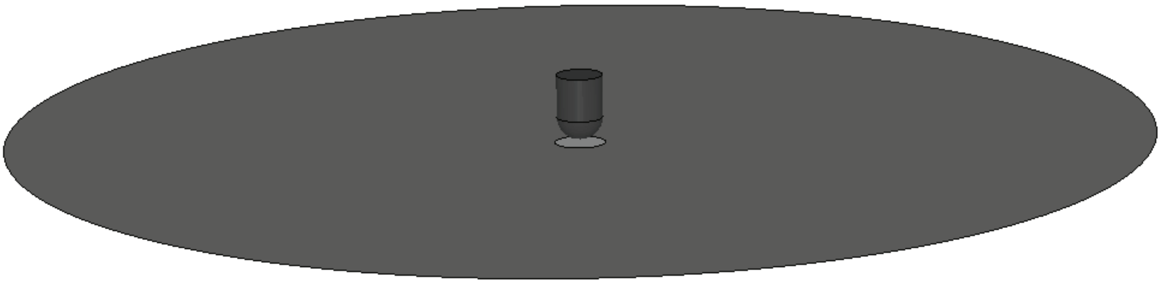

Figure 17. Shell element model.

3.3 Numerical results compared to experimental results

All axisymmetric models failed by plugging since radial cracking and petaling are not possible when axisymmetry is assumed. Axisymmetry therefore led to extensive element erosion in most simulations where a hemispherical punch was used, as shown in Figure 18 (left). Even so, the behaviour until fracture initiation was well described and thus the maximum forces obtained with axisymmetric models agree well with the ones obtained in experiments, especially for the thinnest plates (see Figure 8).

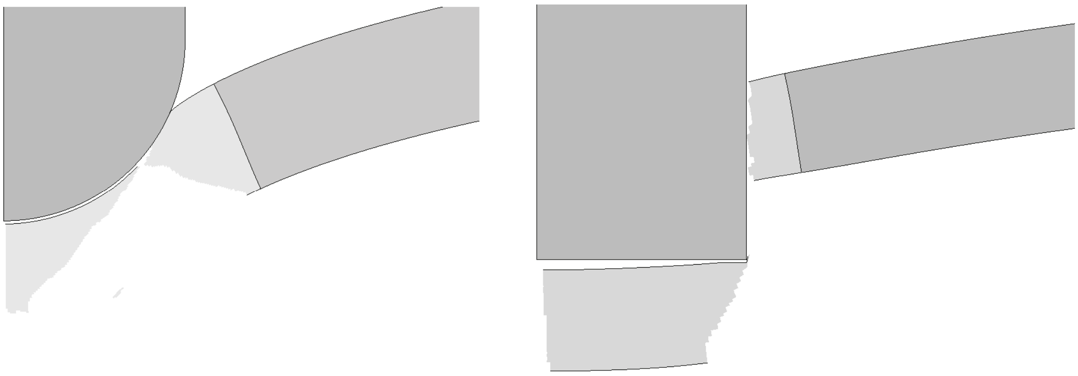

Figure 18. Failure modes in axisymmetric models.

The fracture modes observed using brick element models correspond well to the fracture modes observed in the experiments (see Figure 19). All plates loaded by a blunt punch failed by plugging as in the experiments. Furthermore, some of the plates loaded by a hemispherical punch failed by petaling and some by plugging. A relatively good correlation was observed between the maximum force found with brick elements and the maximum force observed in the experiments. Excellent agreement with the results from axisymmetric element models was also observed (Figure 8).

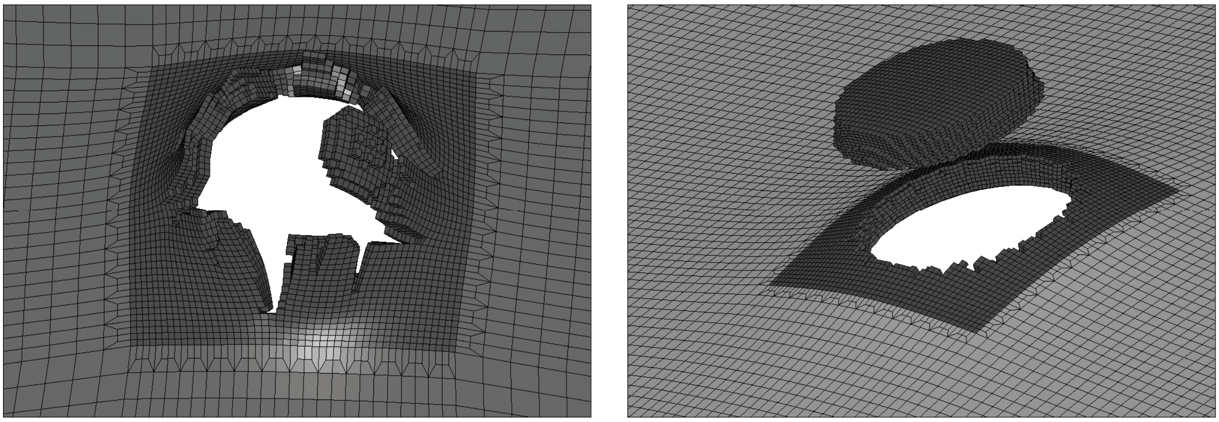

Figure 19. Failure modes in brick element models, petaling (left) and plugging (right).

The shell element models were able to describe both plugging and petaling. Plugging is normally caused by transverse shear, and it was therefore not evident that the shell model should be capable of describing this. However, it seems like plugging is partly caused by tension on the rear side of these relatively thin plates, and this is probably the reason why it worked after all. Figure 20 shows respectively petaling and plugging failure in shell element models. Note that when element erosion is used to describe crack propagation, the crack tends to grow along rows of elements. It is therefore important to have a good mesh in order to predict the fracture accurately. The circular mesh seen at the outer part of the local part of the plate made it possible to predict both an arbitrary number of petals and a plug. With a rectangular mesh one would only get four petals and the resulting plug would have been serrated.

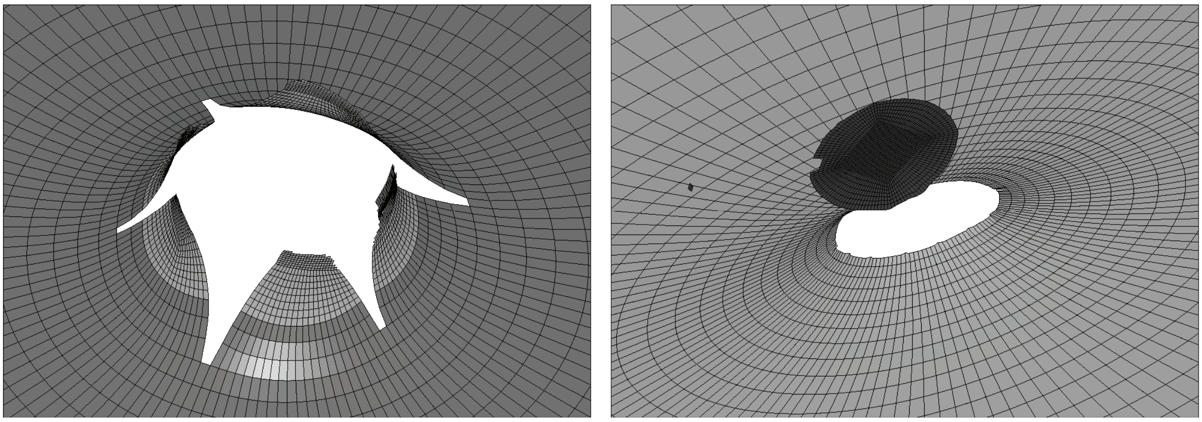

Figure 20. Failure modes in shell element models.

Figure 8 shows a comparison of the main effects on the maximum force from experiments and the various finite element models. Excellent agreement is observed between the results from experiments and all the finite element models for the 3 mm and 5 mm thick plates, while the maximum force for the 10 mm thick plates is somewhat overpredicted by all finite element models (and especially by the shell models). However, the axisymmetric and the brick element models give almost identical results also for the 10 mm thick plates. Since all models, including the shell element model, are capable of predicting fracture accurately for the thinnest plates, it is believed that the in-plane stresses dominate also near the punch. It was seen from both experiments and simulations that the fracture started from the rear side of the plates, i.e. the stress triaxiality was positive in the region where fracture initiated. This is in contrast to what is usually seen in impacts at greater velocities, where fracture occurs in localized shear bands (see e.g. [25]).

The axisymmetric and the brick element models gave identical results for the 10 mm thick plates (see Figure 8). These models are capable of describing a general 3D stress state as long as the mesh is dense enough, and they should therefore be capable of predicting the correct stress state even for bulky plates. It is seen from the numerical simulations that the through-thickness shear stress component is of the same magnitude as the in-plane stress components. It is believed that this causes the difference between the predictions from the shell element models and the two other types of models. Since the axisymmetric and brick element models predict identical maximum loads, it is believed that the discrepancies between the experimental results and the finite element predictions are caused by the defectiveness of the fracture criterion for this particular aluminium alloy. As also discussed by Bao and Wierzbicki [24], the Johnson-Cook fracture criterion seems to overpredict the ductility for stress triaxialities near zero, i.e. near pure shear, for some materials.

Main effects on the work required to perforate the plate have also been calculated. A comparison of the effects from experiments and simulations is shown in Figure 11. The trends are the same as for the maximum force, but the divergences are larger. This is because the displacement at fracture also becomes overpredicted when the maximum force is overpredicted. Thus, the area under the force-displacement curve becomes even more overpredicted. Figure 10 reveals that the displacement at maximum force is overpredicted in general by all finite element models. The strongest effect comes from the boundary conditions, and is overpredicted by both the shell and axisymmetric models. The brick element models on the other hand, overpredicted the displacement for clamped plates and therefore underpredicted the significance of the boundary. The reason could be that no pre-stress was prescribed in the bolts in the numerical models (see also [21]).

4. Concluding remarks

This paper has presented an experimental and numerical investigation on the quasi-static perforation of thin AA5083-H116 aluminium plates. In the tests, square plates were mounted in a circular frame and perforated by a cylindrical punch. A full factorial design was used to investigate the effect of varying plate thickness, boundary conditions, punch diameter and nose shape. From the experimental tests it was found that the thickness of the plate is the single factor that influences the maximum force the most in the investigated range of parameters. The punch shape and diameter have smaller but significant effects, while the boundary condition has a negligible effect. Only small interaction effects were observed. It was also found that the work required to perforate the plate only depends on the plate thickness in the investigated range of parameters. However, the shape of the load curve is depending on all the investigated parameters.

The perforation process was then analysed using the nonlinear finite element code LS-DYNA [16], and the problem was simulated using axisymmetric elements, brick elements and shell elements. All finite element models were capable of predicting the onset of fracture accurately for 3 and 5 mm thick plates. The shell and brick element models also predicted the correct fracture mode, while the axisymmetric models could only predict plugging. None of the models were capable of predicting the onset of fracture accurately for the 10 mm thick plates. Since the shell element models are not capable of predicting the correct stress state when it becomes three-dimensional, the predicted maximum force from shell element simulations deviates from the predictions of the axisymmetric and brick element models. Even with a more sophisticated fracture criterion for this alloy, the shell models would overpredict the maximum force for thick plates. However, these models are the fastest and give as accurate predictions as the axisymmetric and brick element models for the 3 mm and 5 mm thick plates. They are also able to predict the correct fracture mode.

The axisymmetric models predict the correct stress state even for a three-dimensional stress state and are therefore capable of predicting the onset of fracture if the applied fracture criterion is capable of doing so. However, axisymmetric models can not predict arbitrary fracture modes, only axisymmetric fracture like plugging. Due to computational efficiency axisymmetric models are preferred over brick models for bulky plates if the fracture mode is axisymmetric.

Brick element models are the most general, but they are expensive in the sense of computational time. The computational cost is larger for brick element models than for axisymmetric element models even if symmetry is exploited to some extent. Brick element models should therefore only be used if the target is bulky and it is important to predict the evolution of an arbitrary fracture mode.

Acknowledgements

The financial support of this work from the Research Council of Norway, SIMLab – Centre for Research-based Innovation, NTNU and the Norwegian Defence Estates Agency is gratefully acknowledged.

References

[1] Backman ME, Goldsmith W. The mechanics of penetration of projectiles into targets. Int. J. Eng. Sci. 1978;16:1-99.

[2] Corbett GG, Reid SR, Johnson W. Impact loading of plates and shells by free-flying projectiles. Int. J. Impact Eng. 1996;18(2):141-230.

[3] Goldsmith W. Review: Non-ideal projectile impact on targets. Int J Impact Eng 1999;22:95-395.

[4] Zukas JA et al. Impact dynamics, John Wiley & Sons, New York; 1982.

[5] Zukas JA et al. High velocity impact dynamics, John Wiley & Sons, New York; 1990.

[6] Onat ET, Haythornwaite RM. The load-carrying capacity of circular plates at large deflection, J. Appl. Mech.1956;23:49-55.

[7] Langseth M, Larsen PK. Dropped Objects. Plugging Capacity of Steel Plates. BOSS'88. Proceedings of the International Conference on Bahviour of Offshore Structures. (eds Moan, T., Janbu, N. & Faltinsen, O.),Trondheim, Norway, 1988.

[8] Langseth M, Larsen PK. The Behaviour of Square Steel Plates Subjected to a Circular Blunt Ended Load. Int J Impact Eng. 1992;12(4):617-638.

[9] Langseth M, Larsen PK. Dropped objects' plugging capacity of steel plates: An experimental investigation. Int J Impact Eng. 1990;9(3):289-316.

[10] Langseth M, Larsen PK. Dropped objects' plugging capacity of aluminium alloy plates. Int J Impact Eng. 1994;15(3):225-241.

[11] Corbett GG, Reid SR. Quasi-static and dynamic local loading of monolithic simply supported steel plate. Int. J. Impact Eng. 1993;13(3), 423-441.

[12] Gupta NK, Ansari R, Gupta SK. Normal impact of ogive nosed projectiles on thin plates. Int J Impact Eng. 2001;25:641-660.

[13] Wen HM, Jones N. Low-velocity perforation of punch-impact-loaded metal plates. Journal of Pressure Vessel Technology. 1996;118:181-187.

[14] Jones N, Birch RS. Low velocity perforation design of metal plates. Proc 9th Int. Conf. on Structures under Shock and Impact, SUSI IX. Eds. N. Jones and C.A. Brebbia, WIT Transactions ob the built environment, Vol. 87, pp. 179-186, 2006.

[15] Atkins AG, Afzal Khan M, Liu JH. Necking and radial cracking around perforations in thin sheets at normal incidence. Int. J. of Impact Eng. 1998;21(7):521-539.

[16] Hallquist JO. LS-DYNA keyword user’s manual, version 970. Livermore Software Technology Corporation, 2003.

[17] Johnson GR, Cook WH. A constitutive model and data for metals subjected to large strains, high strain rates and high temperatures. In: Proceedings of 7th Int. Sym. Ballistics, The Hague; 1983.

[18] Johnson GR, Cook WH. Fracture characteristics of three metals subjected to various strains, strain rates, temperatures and pressures. Eng. Frac. Mech. 1985;21:31-48.

[19] Clausen AH, Børvik T, Hopperstad OS, Benallal A. Flow and fracture characteristics of aluminium alloy AA5083-H116 as function of strain rate, temperature and triaxiality. Mat. Sci. Eng. A 2004;365:260-272.

[20] Benallal A, Berstad T, Børvik T, Clausen AH, Hopperstad OS. Dynamic strain aging and related instabilities: experimental, theoretical and numerical aspects, European Journal of Mechanics - A/Solids. 2006;25(3):397-424.

[21] Grytten F, Fagerholt E, Auestad T, Førre B, Børvik T. Out-of-plane deformation measurements of an aluminium plate during quasi-static perforation using structured light and close-range photogrammetry. Int J Solids and Structures. 2007 doi: 10.1016/j.ijsolstr.2007.01.026.

[22] Box GEP, Hunter WG, Hunter JS. Statistics for Experimenters, John Wiley & Sons. 1978.

[23] Kapoor R and Nemat-Nasser S. Determination of temperature rise during high strain rate deformation. Mechanics of Materials. 1998;27:1-12.

[24] Bao Y, Wierzbicki T. On the cut-off value of negative triaxiality for fracture. Eng. Frac. Mech. 2005;72(7):1049-1069.

[25] T. Børvik, O. S. Hopperstad, T. Berstad and M. Langseth, Numerical simulation of plugging failure in ballistic penetration, Int J Solids and Structures, 2001;38:6241-6264.

Part III

F. Grytten, B. Holmedal, O.S. Hopperstad, T. Børvik

Evaluation of identification methods for YLD2004-18p

Accepted for publication in International Journal of Plasticity

ARTICLE IN PRESS

Available online at www.sciencedirect.com

ScienceDirect

International Journal of Plasticity xxx (2008) xxx–xxx

INTERNATIONAL JOURNAL OF Plasticity

www.elsevier.com/locate/ijplas

Evaluation of identification methods for YLD2004-18p

F. Grytten [a,*], B. Holmedal [a,b], O.S. Hopperstad [a], T. Børvik [a,c]

[a] *Structural Impact Laboratory (SIMLab), Centre for Research-based Innovation,*
Department of Structural Engineering, Norwegian University of Science and Technology,
NO-7491 Trondheim, Norway
[b] *Department of Materials Science and Engineering, Norwegian University of Science and Technology,*
NO-7491 Trondheim, Norway
[c] *Research and Development Department, Norwegian Defence Estates Agency, NO-0103 Oslo, Norway*

Received 31 August 2007; received in final revised form 13 November 2007

Abstract

Four calibration methods have been evaluated for the linear transformation-based anisotropic yield function YLD2004-18p (Barlat, F., Aretz, H., Yoon, J.W., Karabin, M.E., Brem, J.C., Dick, R.E., 2005. Linear transformation-based anisotropic yield functions. Int. J. Plasticity 21, 1009–1039) and the aluminium alloy AA5083-H116. The different parameter identifications are based on least squares fits to combinations of uniaxial tensile tests in seven directions with respect to the rolling direction, compression (upsetting) tests in the normal direction and stress states found using the full-constraint (FC) Taylor model for 690 evenly distributed strain paths. An elastic–plastic constitutive model based on YLD2004-18p has been implemented in a non-linear finite element code and used in finite element simulations of plane-strain tension tests, shear tests and upsetting tests. The experimental results as well as the Taylor model predictions can be satisfactorily reproduced by the considered yield function. However, the lacking ability of the Taylor model to quantitatively reproduce the experiments calls for more advanced crystal plasticity models.

Keywords: B. Anisotropic materials; C. Mechanical testing; A. Yield condition; C. Finite elements; Aluminium alloy

---

[*] Corresponding author. Tel.: +47 93012077; fax: +47 22067350.
E-mail address: frode.grytten@sintef.no (F. Grytten).

0749-6419/$ - see front matter © 2007 Elsevier Ltd. All rights reserved.
doi:10.1016/j.ijplas.2007.11.005

Please cite this article in press as: Grytten, F. et al., Evaluation of identification methods ..., Int. J. Plasticity (2008), doi:10.1016/j.ijplas.2007.11.005

1. Introduction

Rolled aluminium plates typically have crystallographic texture. This means that the grains are not randomly oriented, but tend towards particular orientations. The texture leads to anisotropy in strength, plastic flow and ductility. An increasing demand for optimized components made out of plate and sheet materials, forces engineers to take the anisotropy of the material into account. At the same time, there is a wish to use finite element simulations to reduce the development time and the number of expensive experiments. This leads to a growing demand for anisotropic material models to be implemented into existing finite element codes.

There are two principal approaches to describe the plasticity of polycrystalline metallic materials. The first is to use a polycrystalline plasticity model, like the full-constraint Taylor model (Taylor, 1938; Bishop and Hill, 1951a,b). This approach is based on the physical aspects of plastic deformation (slip in crystals) and on averaging the response over a large number of grains. The crystallographic texture is the main input to these models (Hosford, 1993; Wenk and van Houtte, 2004). The second approach is to use a phenomenological yield function. While the former approach requires extensive computational power and may lack sufficient detail of physical mechanisms that are playing a role in deformation, the latter requires a significant number of material tests when a flexible yield function is used (Barlat et al., 2005). A more serious problem with both approaches, however, is that neither are currently reliable for arbitrary loading conditions. Today, the latter approach is most common in large scale finite element simulations.

Several phenomenological yield functions have been proposed for metals over the years, both for plane stress states and full three-dimensional stress states. The Tresca (1864) and the Von Mises (1913) criteria have been widely used for isotropic materials. Hill (1948) put forward the first anisotropic yield criterion for materials with orthotropic symmetry, a quadratic function that reduces to the von Mises criterion for isotropic materials. Hosford (1972) introduced a non-quadratic yield function with a variable exponent for isotropic materials. He also showed, based on crystal plasticity calculations for isotropic, polycrystalline metals, that using an exponent equal to 6 and 8 produced better results for BCC and FCC metals, respectively. This criterion was later generalized to anisotropic materials (Hosford, 1979). Barlat and Lian (1989) further extended Hosford's criterion. Later on, Barlat et al. (1991, 1997b, 2005) and Karafillis and Boyce (1993) proposed yield functions where anisotropy is introduced by means of linear transformations of the stress tensor. A detailed overview of linear transformation-based yield functions can be found in Barlat et al. (2007).

Yoon et al. (2006) implemented the anisotropic yield function YLD2004-18p, which was proposed by Barlat et al. (2005) for full three-dimensional stress states, in a finite element code and showed that the yield function was able to predict 6 and 8 ears in cup drawing simulations. The YLD2004-18p criterion is a linear transformation-based yield criterion with 18 anisotropy parameters and an exponent that can be varied. To determine the coefficients of the criterion, Yoon et al. (2006) used results from seven uniaxial tensile tests and an equibiaxial tensile test for the in-plane properties, while crystal plasticity calculations were used to determine four parameters governing the out-of-plane properties.

Based on a measured crystallographic texture, virtual experiments can provide as many data points as desired covering the entire stress space by means of crystal plasticity calculations. The question arises: are the predictions by such models sufficiently precise to replace real experiments? If so, this approach is inexpensive and strain paths not accessible in idealised experiments can be included in the calibration. However, the uncertainty associated with material variation seen in experiments is persistent also in this approach. Several modified versions of the original full-constraint Taylor model exist, most of them designed to correctly predict rolling textures and account for local grain interactions by relaxation of some of the stress components on selected symmetry planes. Most of them are valid only for rolling due to their assumptions about the rolling symmetry planes (relaxed constraints, lath, pancake, lamel, GIA; see Van Houtte et al., 2005). Some coordinate system invariant approaches are: the full-constraint Taylor model, the self-consistent model, the ALamel model and the crystal plasticity finite element method (CPFEM). The full-constraint Taylor model is simple and without additional fitting parameters. However, global and local stress equilibriums are not accounted for. The self consistent model relaxes the local grain to the global stresses and in this way accounts for a global stress balance. It is particularly suited for handling heterogeneous inclusions. Additional parameters concerning stiffness and strain-rate sensitivity must be fitted for each material. The recently published ALamel model (Van Houtte et al., 2005) generalises the validity of one of the relaxed Taylor type of models from the special case of rolling to other deformation modes. This is achieved by the introduction of a statistical distribution function for the orientations of the relaxation planes instead of a relaxation of only the rolling plane. This approach is mentioned here because it is coordinate invariant and because of the reported promising results on texture evolution. However, how well it predicts mechanical anisotropy, e.g. the shape of the yield locus, is not yet investigated. The crystal plasticity finite element method (CPFEM) ideally requires a mesh including shape and size of the grains which is generally difficult to measure, instead simplified structured meshes are commonly used. Still both global and local grain interactions are accounted for. The CPFEM is closest to including all the physical mechanisms but the approach is demanding with respect to mesh and requires two orders of magnitude more calculation time than the Taylor type of approaches. Therefore the options for most applications will be the FC-Taylor model and the self-consistent model. Here the FC-Taylor model is a natural starting point due to its simplicity and no need for fitting additional parameters.

In the present work, an elastic–plastic constitutive model based on the anisotropic yield function YLD2004-18p has been implemented in the commercial non-linear finite element code LS-DYNA (LSTC, 2007). In Section 2, the elastic–plastic constitutive model and the associated stress-update scheme are formulated. The theory behind the crystal plasticity calculations with the FC-Taylor model is briefly recalled in Section 3, and the virtual experiments performed to obtain stress points on the yield surface are described. Section 4 deals with the material testing and the identification of parameters. The various experiments and corresponding instrumentations are described. Four different approaches to fit the parameters of the anisotropic yield function YLD2004-18p are described in Section 5. Section 6 deals with the finite element simulations of the various experiments and compares the results for the aluminium alloy AA5083-H116. The applicability of the proposed parameter identification procedures are discussed in Section 7, while conclusions are presented in Section 8.

2. Constitutive model and stress integration

A hypoelastic–plastic constitutive model based on the YLD2004-18p has been formulated. The model includes isotropic elasticity, anisotropic yielding, associated plastic flow and isotropic strain hardening. It is assumed that the elastic strains are small, while the plastic strains may be finite. A corotational formulation was adopted in order to simplify the formulation of plastic anisotropy. The local coordinate system constructed at each integration point coincides with the material anisotropy axes. It is assumed that the anisotropic axes of the material remain orthogonal during deformations.

The corotational Cauchy stress and corotational rate-of-deformation tensors are defined by (Belytschko et al., 2000)

$$\hat{\boldsymbol{\sigma}} = \mathbf{R}^{\mathrm{T}} \cdot \boldsymbol{\sigma} \cdot \mathbf{R}; \quad \widehat{\mathbf{D}} = \mathbf{R}^{\mathrm{T}} \cdot \mathbf{D} \cdot \mathbf{R} \tag{1}$$

where $\boldsymbol{\sigma}$ is the Cauchy stress tensor and $\mathbf{D}$ is the rate-of-deformation tensor. The rotation tensor $\mathbf{R}$ is defined from the polar decomposition of the deformation gradient, $\mathbf{F} = \mathbf{R} \cdot \mathbf{U}$, where $\mathbf{U}$ is the right stretch tensor. The corotational rate-of-deformation can be decomposed into elastic and plastic parts

$$\widehat{\mathbf{D}} = \widehat{\mathbf{D}}^{\mathrm{e}} + \widehat{\mathbf{D}}^{\mathrm{p}} \tag{2}$$

For a hypoelastic material, the rate of the corotational Cauchy stress can be expressed as a linear function of the elastic corotational rate-of-deformation (Belytschko et al., 2000)

$$\frac{\mathrm{D}\hat{\boldsymbol{\sigma}}}{\mathrm{D}t} = \widehat{\mathbf{C}}^{\sigma}_{\mathrm{el}} : \widehat{\mathbf{D}}^{\mathrm{e}} = \widehat{\mathbf{C}}^{\sigma}_{\mathrm{el}} : (\widehat{\mathbf{D}} - \widehat{\mathbf{D}}^{\mathrm{p}}) \tag{3}$$

where $\widehat{\mathbf{C}}^{\sigma}_{\mathrm{el}}$ is the elastic tangent modulus tensor. Since elastic isotropy is assumed, $\widehat{\mathbf{C}}^{\sigma}_{\mathrm{el}}$ is uniquely defined by the bulk modulus K and shear modulus G as

$$\widehat{\mathbf{C}}^{\sigma}_{\mathrm{el}} = K\mathbf{I} \otimes \mathbf{I} + 2G\left(\boldsymbol{I} - \frac{1}{3}\mathbf{I} \otimes \mathbf{I}\right) \tag{4}$$

where $\mathbf{I}$ is the second-order unit tensor and $\boldsymbol{I}$ is the fourth-order, symmetric unit tensor.

The yield function is written in the form

$$f(\hat{\boldsymbol{\sigma}}, \bar{\varepsilon}) = \bar{\sigma}(\hat{\boldsymbol{\sigma}}) - \kappa(\bar{\varepsilon}) \tag{5}$$

where $\bar{\sigma}$ is the effective stress, κ is the flow stress in uniaxial tension and $\bar{\varepsilon}$ is the equivalent plastic strain. It is assumed that f is a convex function of $\hat{\boldsymbol{\sigma}}$, and a positive homogeneous function of order one. The generalized associated flow rule is adopted, and the plastic rate-of-deformation and the effective plastic strain-rate are defined as (Lemaitre and Chaboche, 1990)

$$\widehat{\mathbf{D}}^{\mathrm{p}} = \dot{\lambda}\frac{\partial f}{\partial \hat{\boldsymbol{\sigma}}} = \dot{\bar{\varepsilon}}\frac{\partial f}{\partial \hat{\boldsymbol{\sigma}}}, \quad \dot{\bar{\varepsilon}} = -\dot{\lambda}\frac{\partial f}{\partial \kappa} = \dot{\lambda} \tag{6}$$

where $\dot{\lambda}$ is the plastic parameter. The loading–unloading conditions are stated in Kuhn–Tucker form

$$\dot{\lambda} \geqslant 0, \quad f \leqslant 0, \quad \dot{\lambda} f = 0 \tag{7}$$

The first of these conditions implies that the plastic parameter is non-negative, while the second implies that the stress must lie on or within the yield surface. The last condition requires the stress to lie on the yield surface during plastic loading.

The yield function Yld2004-18p of Barlat et al. (2005) is adopted. The effective stress is defined by

$$\bar{\sigma} = \left(\frac{1}{4}\phi\right)^{\frac{1}{m}} \tag{8}$$

where

$$\begin{aligned}\phi = \phi(\widetilde{\mathbf{S}}', \widetilde{\mathbf{S}}'') &= |\widetilde{S}'_1 - \widetilde{S}''_1|^m + |\widetilde{S}'_1 - \widetilde{S}''_2|^m + |\widetilde{S}'_1 - \widetilde{S}''_3|^m + |\widetilde{S}'_2 - \widetilde{S}''_1|^m + |\widetilde{S}'_2 - \widetilde{S}''_2|^m \\ &+ |\widetilde{S}'_2 - \widetilde{S}''_3|^m + |\widetilde{S}'_3 - \widetilde{S}''_1|^m + |\widetilde{S}'_3 - \widetilde{S}''_2|^m + |\widetilde{S}'_3 - \widetilde{S}''_3|^m\end{aligned} \tag{9}$$

In Eq. (9), $\widetilde{\mathbf{S}}'$ and $\widetilde{\mathbf{S}}''$ are collections of the principal values $\widetilde{S}'_i$ and $\widetilde{S}''_j$ of the tensors $\tilde{\mathbf{s}}'$ and $\tilde{\mathbf{s}}''$, defined by two linear transformations of the deviator of the corotational Cauchy stress

$$\tilde{\mathbf{s}}' = \mathbf{C}' : \hat{\mathbf{s}} = \mathbf{C}' : \mathbf{T} : \hat{\boldsymbol{\sigma}}, \quad \tilde{\mathbf{s}}'' = \mathbf{C}'' : \hat{\mathbf{s}} = \mathbf{C}'' : \mathbf{T} : \hat{\boldsymbol{\sigma}} \tag{10}$$

where $\hat{\mathbf{s}} = \mathbf{T} : \hat{\boldsymbol{\sigma}}$ is the deviator of the corotational Cauchy stress. The fourth-order tensors $\mathbf{C}'$ and $\mathbf{C}''$ contain the anisotropy constants, and in Voigt notation (see, e.g. Belytschko et al., 2000) they read

$$\begin{aligned}\mathbf{C}' &= \begin{bmatrix} 0 & -c'_{12} & -c'_{13} & 0 & 0 & 0 \\ -c'_{21} & 0 & -c'_{23} & 0 & 0 & 0 \\ -c'_{31} & -c'_{32} & 0 & 0 & 0 & 0 \\ 0 & 0 & 0 & c'_{44} & 0 & 0 \\ 0 & 0 & 0 & 0 & c'_{55} & 0 \\ 0 & 0 & 0 & 0 & 0 & c'_{66} \end{bmatrix}, \\ \mathbf{C}'' &= \begin{bmatrix} 0 & -c''_{12} & -c''_{13} & 0 & 0 & 0 \\ -c''_{21} & 0 & -c''_{23} & 0 & 0 & 0 \\ -c''_{31} & -c''_{32} & 0 & 0 & 0 & 0 \\ 0 & 0 & 0 & c''_{44} & 0 & 0 \\ 0 & 0 & 0 & 0 & c''_{55} & 0 \\ 0 & 0 & 0 & 0 & 0 & c''_{66} \end{bmatrix}\end{aligned} \tag{11}$$

The fourth-order tensor $\mathbf{T}$ transforms the stress tensor to its deviator, and in Voigt notation it reads

$$\mathbf{T} = \frac{1}{3}\begin{bmatrix} 2 & -1 & -1 & 0 & 0 & 0 \\ -1 & 2 & -1 & 0 & 0 & 0 \\ -1 & -1 & 2 & 0 & 0 & 0 \\ 0 & 0 & 0 & 3 & 0 & 0 \\ 0 & 0 & 0 & 0 & 3 & 0 \\ 0 & 0 & 0 & 0 & 0 & 3 \end{bmatrix} \tag{12}$$

Assuming isotropic hardening, the two-term Voce hardening rule was adopted to define the evolution of the flow stress

$$\kappa(\bar{\varepsilon}) = \sigma_0 + \sum_{i=1}^{2} Q_i(1 - \exp(-C_i\bar{\varepsilon})) \tag{13}$$

where σ_0, Q_i and C_i are material parameters.

The described material model was implemented in the commercial non-linear finite element code LS-DYNA (LSTC, 2007) by means of a user-defined material subroutine. The current state variables and the total strain increment to the next state are input variables to the subroutine. The problem is to find the elastic and plastic parts of the strain increment, the final stress state and the updated history variables. For the actual constitutive model, the current state is represented by the corotational stress $\hat{\boldsymbol{\sigma}}_n$ and the equivalent plastic strain $\bar{\varepsilon}_n$ at point of time t_n. The strain increment $\Delta\hat{\boldsymbol{\varepsilon}}_{n+1}$ during the time step $\Delta t_{n+1} = t_{n+1} - t_n$ is given by $\Delta\hat{\boldsymbol{\varepsilon}}_{n+1} = \widehat{\mathbf{D}}_{n+1/2}\Delta t_{n+1}$, where $\widehat{\mathbf{D}}_{n+1/2}$ is the corotational rate-of-deformation at point of time $t_{n+1/2} = t_n + \Delta t_{n+1}/2$. It is recalled that the central difference method is used for temporal integration in the explicit solver of LS-DYNA.

A fully implicit elastic predictor–plastic corrector method is used to obtain the next stress state. The predictor is represented by

$$\hat{\boldsymbol{\sigma}}_{n+1}^{\mathrm{trial}} = \hat{\boldsymbol{\sigma}}_n + \widehat{\mathbf{C}}_{\mathrm{el}}^{\sigma} : \Delta\hat{\boldsymbol{\varepsilon}}_{n+1}, \quad \bar{\varepsilon}_{n+1}^{\mathrm{trial}} = \bar{\varepsilon}_n \tag{14}$$

which is referred to as the elastic trial state. If the yield condition is fulfilled in the elastic trial state, the strain increment $\Delta\hat{\boldsymbol{\varepsilon}}_{n+1}$ is purely elastic and the trial state coincides with the real state at t_{n+1}, i.e.

$$\hat{\boldsymbol{\sigma}}_{n+1} = \hat{\boldsymbol{\sigma}}_{n+1}^{\mathrm{trial}}, \quad \bar{\varepsilon}_{n+1} = \bar{\varepsilon}_{n+1}^{\mathrm{trial}} \tag{15}$$

However, if the yield condition is violated, plastic loading has taken place and consistency has to be re-established. This is achieved through a fully implicit iteration scheme including a primitive form of line search, viz.

$$\begin{aligned}
\hat{\boldsymbol{\sigma}}_{n+1}^{(k+1)} &= \hat{\boldsymbol{\sigma}}_{n+1}^{\mathrm{trial}} - \widehat{\mathbf{C}}_{\mathrm{el}}^{\sigma} : \Delta\hat{\boldsymbol{\varepsilon}}_{n+1}^{p(k+1)} = \hat{\boldsymbol{\sigma}}_{n+1}^{\mathrm{trial}} - \Delta\bar{\varepsilon}_{n+1}^{(k+1)}\widehat{\mathbf{C}}_{\mathrm{el}}^{\sigma} : \left.\frac{\partial f}{\partial\hat{\boldsymbol{\sigma}}}\right|_{n+1}^{(k)} \\
\Delta\hat{\boldsymbol{\varepsilon}}_{n+1}^{p(k+1)} &= \Delta\bar{\varepsilon}_{n+1}^{(k+1)}\frac{\partial f}{\partial\hat{\boldsymbol{\sigma}}}\Big|_{n+1}^{(k)} \\
\bar{\varepsilon}_{n+1}^{(k+1)} &= \bar{\varepsilon}_n + \Delta\bar{\varepsilon}_{n+1}^{(k+1)} \\
f_{n+1}^{(k+1)} &= \bar{\sigma}_{n+1}^{(k+1)} - \kappa_{n+1}^{(k+1)} = \bar{\sigma}_{n+1}^{(k+1)} - \sigma_0 - \sum_{i=1}^{2} Q_i\left(1 - \exp\left(-C_i\bar{\varepsilon}_{n+1}^{(k+1)}\right)\right) = 0
\end{aligned} \tag{16}$$

In Eq. (16), the superscript (k) refers to iteration number k, and $k = 0$ refers to the elastic trial stress. Since the gradient to the yield surface from the previous iteration $\partial f/\partial\hat{\boldsymbol{\sigma}}|_{n+1}^{(k)}$ (which is a known quantity) is used in the flow rule, there is only one independent variable in Eq. (16), namely the equivalent plastic strain increment, $\Delta\bar{\varepsilon}_{n+1}^{(k+1)}$. The best value of $\Delta\bar{\varepsilon}_{n+1}^{(k+1)}$ is sought along the $\partial f/\partial\hat{\boldsymbol{\sigma}}|_{n+1}^{(k)}$ direction before the direction is updated. This is called line search. The initial lower limit of $\Delta\bar{\varepsilon}_{n+1}^{(k+1)}$ is set equal to zero. Newton's method is applied on $f_{n+1}^{(k+1)}$ until a minimum or a root is bracketed. If a minimum has been bracketed, the Golden Section method is used to find the point along the plastic strain path that is closest to the yield surface $f_{n+1}^{(k+1)} = 0$. This method guarantees linear convergence for continuous functions in one-dimension. If a negative value of $f_{n+1}^{(k+1)}$ is achieved during the Newton or Golden Section iterations, a root has been bracketed and the Bisection method is applied to find the root. Also this method guarantees linear convergence. After a minimum or a root has been found, the normal to the yield surface, $\partial f/\partial\hat{\boldsymbol{\sigma}}|_{n+1}^{(k+1)}$, is updated and the procedure is repeated. Iterations are carried out until the following criteria are met

Please cite this article in press as: Grytten, F. et al., Evaluation of identification methods ..., Int. J. Plasticity (2008), doi:10.1016/j.ijplas.2007.11.005

$$\frac{\left|f_{n+1}^{(k+1)}\right|}{\kappa_{n+1}^{(k+1)}} \leqslant 10^{-5} \quad \text{and} \quad \frac{\frac{\partial f}{\partial \hat{\boldsymbol{\sigma}}}\Big|_{n+1}^{(k)} : \frac{\partial f}{\partial \hat{\boldsymbol{\sigma}}}\Big|_{n+1}^{(k+1)}}{\left|\frac{\partial f}{\partial \hat{\boldsymbol{\sigma}}}\Big|_{n+1}^{(k)}\right| \left|\frac{\partial f}{\partial \hat{\boldsymbol{\sigma}}}\Big|_{n+1}^{(k+1)}\right|} = \cos\varphi \geqslant 0.995 \tag{17}$$

The first criterion ensures that the obtained stress state is very close to the yield surface, while the second criterion requires that the plastic straining direction is orthogonal to the yield surface. The angle φ between the gradient at the end of the plastic increment and the direction used in the increment must be less than 0.6 degrees. In this way normality is enforced at the end of the plastic increment and the method is therefore fully implicit. Line search makes it necessary to check for normality at the end of the plastic increment since one will normally hit the yield surface in the first direction that is tried. The stress state and history variables are updated when consistency is established.

Avoiding updating the gradient for every iteration makes up for the relatively slow convergence in the line search described in this iteration scheme. In addition, the radius of convergence seems to be good. Hence, the stress-update algorithm is robust. The described material model has been extended to include a model for the Portevin–Le Chatelier (PLC) effect and dynamic strain ageing (DSA), and will be used in future studies by the present authors to investigate the combined effect of yield locus and negative strain-rate sensitivity. The severe non-linearity of these problems gave rise to the need for a robust return mapping scheme that has been utilized in the present study, even if a simpler approach would suffice. Note that Yoon et al. (2006) applied a multi-stage predictor–corrector scheme based on the Newton–Raphson method and the control of the potential residual, and thus avoided using a line searching algorithm.

3. Virtual experiments by the full-constraint Taylor model

A strain-rate insensitive, full-constraint Taylor model is applied. The model is outlined below for the sake of completeness. Further details may be found in Delannay et al. (2002) and Van Houtte et al. (2005, 2006). Elastic strain rates are neglected, and thus it is assumed that $\mathbf{D} \approx \mathbf{D}^{\mathrm{p}}$. The plastic rate-of-deformation tensor $\mathbf{D}^{\mathrm{p}}$ is related to the slip activity of each considered grain by

$$\mathbf{D}^{\mathrm{p}} = \sum_{\alpha} \frac{1}{2} \dot{\gamma}^{\alpha} (\mathbf{b}^{\alpha} \otimes \mathbf{n}^{\alpha} + \mathbf{n}^{\alpha} \otimes \mathbf{b}^{\alpha}) \tag{18}$$

where $\dot{\gamma}^{\alpha}$ is the slip rate of slip system α of the considered grain defined by its slip direction $\mathbf{b}^{\alpha}$ and slip plane normal $\mathbf{n}^{\alpha}$. Since Eq. (18) has multiple solutions, a solution that minimizes the rate of internally dissipated frictional work is chosen

$$P = \sum_{\alpha} \tau_{\alpha}^{\mathrm{c}} |\dot{\gamma}^{\alpha}| = \min \tag{19}$$

where $\tau_{\alpha}^{\mathrm{c}}$ is the critical resolved shear stress of slip system α. Because of the Taylor ambiguity, this constrained minimization of the plastic work may not have a unique solution. Hence, an additional criterion is defined to select a valid solution. The simplest approach is to pick one of the solutions randomly. However, in this work the approach proposed by Delannay et al. (2002) is adopted, and the selected solution is the one that minimizes

Please cite this article in press as: Grytten, F. et al., Evaluation of identification methods ..., Int. J. Plasticity (2008), doi:10.1016/j.ijplas.2007.11.005

$$T = \frac{\sum_\alpha (\dot{\gamma}^\alpha)^2}{\left(\sum_\alpha \dot{\gamma}^\alpha\right)^2} \tag{20}$$

This criterion ensures that the slip activity is distributed as much as possible on all critically stressed slip systems.

The resulting non-zero $\dot{\gamma}^\alpha$ values identify the active slip systems, for which the generalized Schmid law equates the resolved shear stress τ^{r}_α of slip system α to its critical resolved shear stress τ^{c}_α, i.e.

$$\tau^{\mathrm{r}}_\alpha = \frac{1}{2}(\mathbf{b}^\alpha \otimes \mathbf{n}^\alpha + \mathbf{n}^\alpha \otimes \mathbf{b}^\alpha) : \mathbf{s}^{\mathrm{g}} = \tau^{\mathrm{c}}_\alpha \mathrm{sign}(\dot{\gamma}^\alpha) \tag{21}$$

where $\mathbf{s}^{\mathrm{g}}$ denotes the deviatoric Cauchy stress tensor in the considered grain. For the inactive slip systems, for which $\dot{\gamma}^\alpha = 0$, the following equation holds

$$|\tau^{\mathrm{r}}_\alpha| = \left|\frac{1}{2}(\mathbf{b}^\alpha \otimes \mathbf{n}^\alpha + \mathbf{n}^\alpha \otimes \mathbf{b}^\alpha) : \mathbf{s}^{\mathrm{g}}\right| \leqslant \tau^{\mathrm{c}}_\alpha \tag{22}$$

The five independent components of the deviatoric Cauchy stress tensor $\mathbf{s}^{\mathrm{g}}$ are solved from Eq. (21). Finally, the deviatoric Cauchy stress $\mathbf{s}$ of the considered aggregate is calculated as the simple average of the stress response of each grain (Asaro and Needleman, 1985; Kalidindi et al., 1992), viz.

$$\mathbf{s} = \frac{1}{N}\sum_{g=1}^{N} \mathbf{s}^{\mathrm{g}} \tag{23}$$

The measured crystallographic texture, i.e. the aggregate of $N = 1000$ grains, was used as input to the FC-Taylor model to calculate 690 stress states at yielding. A uniform distribution of strain-rate directions is convenient, since the rate-of-deformation tensor is the prescribed input of the FC-Taylor model. However, the points will not become evenly distributed in stress space, but will be condensed where the gradient of the yield surface changes most rapidly. This provides a natural adaptive distribution of the stress directions.

The problem of obtaining a uniform distribution of the strain-rate directions reduces to finding a uniform distribution of points on a five-dimensional hyper-sphere. It is recalled that the plastic rate-of-deformation has only five independent components due to plastic incompressibility. Analytical integer solutions can easily be determined for the two-dimensional circle by dividing it into an integer number of sectors. Such solutions are hard to find in higher dimensions, even by numerical iteration schemes. However, it is straightforward to distribute points evenly on a hyper-cube. The projection of these points onto a hyper-sphere yields an increased density of points towards the corners, where the deviation between the cube and the sphere is largest and this difference obviously increases in higher dimensions.

As already mentioned, the plastic rate-of-deformation space is five-dimensional for plastically incompressible materials. A contraction of the plastic rate-of-deformation tensor D^{p}_{ij} into a five-dimensional vector D^{p}_k is performed (Leqeue et al., 1987; Van Houtte, 1988)

Please cite this article in press as: Grytten, F. et al., Evaluation of identification methods ..., Int. J. Plasticity (2008), doi:10.1016/j.ijplas.2007.11.005

$$\begin{aligned}
D_1^{\mathrm{p}} &= \frac{1}{2}\left(\sqrt{3}+1\right)D_{11}^{\mathrm{p}} + \frac{1}{2}\left(\sqrt{3}-1\right)D_{22}^{\mathrm{p}}\\
D_2^{\mathrm{p}} &= \frac{1}{2}\left(\sqrt{3}-1\right)D_{11}^{\mathrm{p}} + \frac{1}{2}\left(\sqrt{3}+1\right)D_{22}^{\mathrm{p}}\\
D_3^{\mathrm{p}} &= \sqrt{2}D_{23}^{\mathrm{p}}\\
D_4^{\mathrm{p}} &= \sqrt{2}D_{31}^{\mathrm{p}}\\
D_5^{\mathrm{p}} &= \sqrt{2}D_{12}^{\mathrm{p}}
\end{aligned} \tag{24}$$

A distribution of the strain-rate directions on the hyper-cube in this five-dimensional, contracted strain-rate space is chosen, using a resolution of three points in each axis direction. This gives 690 points on the hyper-cube surface, each corresponding to a given direction. (A similar resolution in two dimensions counts two positive and two negative axis intersections and four corners, in all eight directions.) The corresponding components of the plastic rate-of-deformation tensor follow from the inverse transformation by

$$\begin{aligned}
D_{11}^{\mathrm{p}} &= \frac{1}{6}\left(\sqrt{3}+3\right)D_1^{\mathrm{p}} + \frac{1}{6}\left(\sqrt{3}-3\right)D_2^{\mathrm{p}}\\
D_{22}^{\mathrm{p}} &= \frac{1}{6}\left(\sqrt{3}-3\right)D_1^{\mathrm{p}} + \frac{1}{6}\left(\sqrt{3}+3\right)D_2^{\mathrm{p}}\\
D_{33}^{\mathrm{p}} &= -\frac{1}{3}\sqrt{3}D_1^{\mathrm{p}} - \frac{1}{3}\sqrt{3}D_2^{\mathrm{p}}\\
D_{23}^{\mathrm{p}} &= \frac{1}{2}\sqrt{2}D_3^{\mathrm{p}}\\
D_{31}^{\mathrm{p}} &= \frac{1}{2}\sqrt{2}D_4^{\mathrm{p}}\\
D_{12}^{\mathrm{p}} &= \frac{1}{2}\sqrt{2}D_5^{\mathrm{p}}
\end{aligned} \tag{25}$$

Using the described space-filling algorithm in combination with the FC-Taylor theory, 690 deviatoric stress states $\mathbf{s}$ at incipient yielding were determined. These results will be used to calibrate the phenomenological yield surface.

4. Material characterization

4.1. AA5083-H116

AA5083 is a high-strength aluminium–magnesium alloy well suited for rolling, and plates are therefore an important product. Even though the alloy has been tested for ballistic protection (see, e.g. Børvik et al., 2004), the traditional use of these plates is naval structures such as ship hulls and offshore topsides due to the alloy's excellent corrosion resistance. However, stress corrosion may occur in corrosive media. To avoid this problem, the special temper H116 has been developed (Hatch, 1984). The main alloying elements are magnesium with about 4.4 wt%, manganese with 0.7 wt% and chromium with 0.15 wt%. Note that the high amount of magnesium in the alloy implies a potential instability denoted the Portevin–Le Chatelier (PLC) effect. The PLC effect causes serrated or jerky flow in certain ranges of temperature and strain-rate, and is associated with repeated propagation of bands of localized plastic strain-rate. The occurrence of PLC is linked to a

Please cite this article in press as: Grytten, F. et al., Evaluation of identification methods ..., Int. J. Plasticity (2008), doi:10.1016/j.ijplas.2007.11.005

bounded region of negative steady-state strain-rate sensitivity of the flow stress. The negative strain-rate sensitivity is believed to result from diffusion of solute atoms to dislocations temporarily arrested at obstacles in the slip path (Cottrell, 1953; Van den Beukel, 1975; McCormick, 1988; Mesarovic, 1995; Rizzi and Hähner, 2004; Benallal et al., 2006).

Clausen et al. (2004) found the flow stress at 5% plastic strain as a function of the steady-state strain-rate for AA5083-H116. Their results from tensile tests carried out on specimens taken in the rolling direction are shown in Fig. 1. It can be seen that AA5083-H116 exhibits negative steady-state strain-rate sensitivity for intermediate strain rates, which is the cause of the serrated yielding seen for this alloy. Note that their study was on plates of another thickness than the one considered here, so that a direct comparison of stress levels cannot be made due to different levels of work hardening in the cold rolling process.

The considered AA5083-H116 alloy is a 10 mm thick plate in a rolled condition with pancake shaped grains elongated in the rolling direction (RD) and transverse directions (TD), as can be seen in Fig. 2. The grain size as measured by line intercept in the normal direction (ND) is in the range 10–30 μm with less elongation of the grains near the surface. A substantial fraction of rather large constituent particles is present in the material (see Fig. 3).

Grain orientation data were measured at the thickness centre position of the rolled plate, assuming a uniform texture through the thickness. A Hitachi S-3500N-LV SEM equipped with a Nordif digital EBSD detector and TSL OIM4 EBSD software was used, with a step size of 10 μm and covering approximately 20 mm^2. An aggregate of 1000 points were chosen for the FC-Taylor calculations. The alloy exhibits a classical rolling texture (see, e.g. Kocks et al., 1998). A visualization of the orientation distribution function (ODF) is given in Fig. 4. The β-fibre is dominating, with some Cube present.

4.2. Experiments

Several uniaxial tensile test specimens were taken from the plate at every 15° from the rolling direction (0°). The geometry of the specimens used in these tests is shown in Fig. 5,

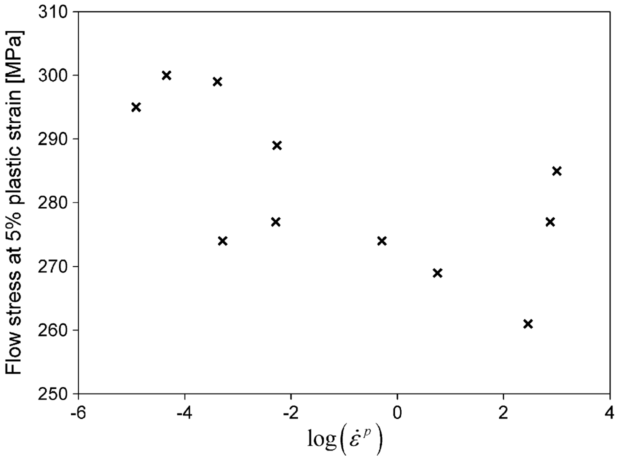

Fig. 1. Negative steady-state strain rate sensitivity of AA5083-H116 (Clausen et al., 2004).

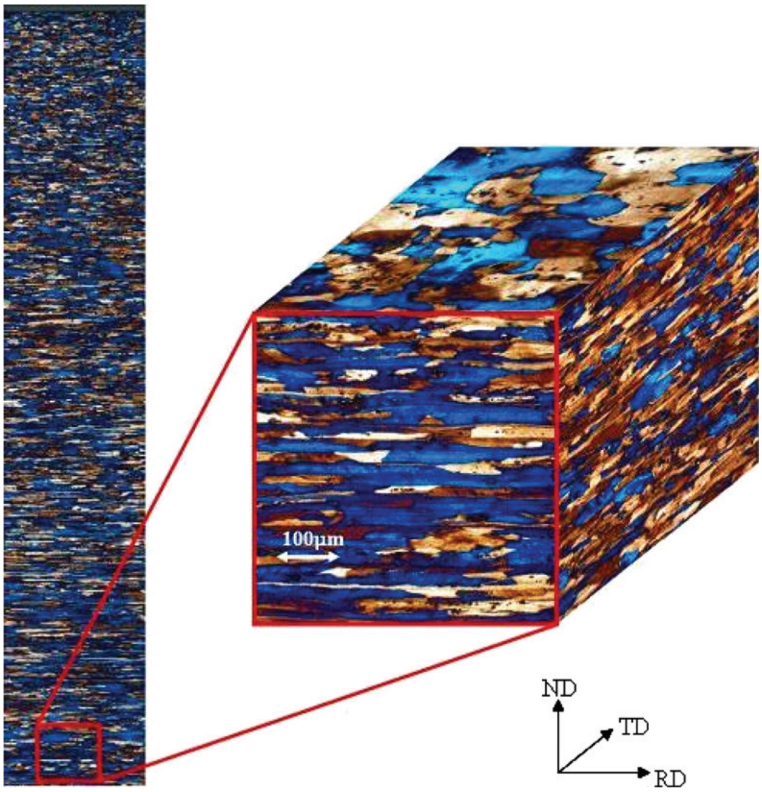

Fig. 2. Optical microscopy images of AA5083-H116 (RD = rolling direction, TD = transverse direction, ND = normal direction).

while Fig. 6 shows the true stress–strain curves in three selected directions. The experiments were carried out with a nominal strain rate of $5 \times 10^{-4}\ \mathrm{s}^{-1}$. During testing, the minimum diameter of the specimen was continuously measured in both the in-plane and through thickness direction (Søvik, 1996; Børvik et al., 2001). The apparatus that was used consists of four inductive displacement gauges mounted in a frame surrounding the specimen. Two of the gauges measured the diameter reduction in the thickness direction of the plate and two of the gauges measured the diameter reduction in the in-plane direction of the plate. This made it easy to calculate the R-ratios defined as

$$R = \frac{\dot{\varepsilon}^{\mathrm{p}}_{\mathrm{w}}}{\dot{\varepsilon}^{\mathrm{p}}_{\mathrm{t}}} \approx \frac{\dot{\varepsilon}_{\mathrm{w}}}{\dot{\varepsilon}_{\mathrm{t}}} \tag{26}$$

where $(\dot{\varepsilon}_{\mathrm{w}}, \dot{\varepsilon}_{\mathrm{t}})$ and $(\dot{\varepsilon}^{\mathrm{p}}_{\mathrm{w}}, \dot{\varepsilon}^{\mathrm{p}}_{\mathrm{t}})$ are the true total and plastic strain rates in the width and thickness directions of the tensile specimen, respectively. Fig. 7 shows the plastic width strain as a function of the plastic thickness strain for typical tensile tests in three orientations with respect to the rolling direction. The nearly linear relations between $\varepsilon^{\mathrm{p}}_{\mathrm{t}}$ and $\varepsilon^{\mathrm{p}}_{\mathrm{w}}$ indicate that the R-ratios are approximately constant during loading. Assuming plastic incompressibility, this measurement method also made it possible to determine true strains even after necking. By using the Bridgman (1964) correction, work hardening curves $\kappa = \kappa(\bar{\varepsilon})$ were

Please cite this article in press as: Grytten, F. et al., Evaluation of identification methods ..., Int. J. Plasticity (2008), doi:10.1016/j.ijplas.2007.11.005

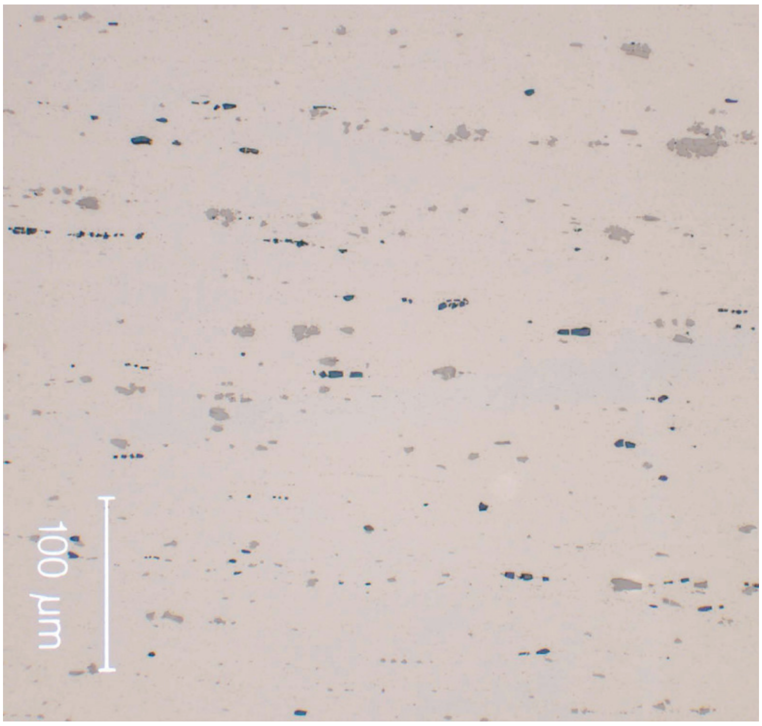

Fig. 3. Optical microscopy image showing constituent particles in the AA5083-H116.

estimated all the way to fracture. The curves obtained for the rolling direction were then used to determine the parameters of the isotropic hardening rule defined by Eq. (11).

Figs. 6 and 7 show that AA5083-H116 is anisotropic in strength, ductility and plastic flow. Serrated flow is illustrated in Fig. 6, which is an evidence of the Portevin–Le Chatelier effect. The anisotropy in strength is weak, while the anisotropy in plastic strain to fracture is considerable. At the 45° direction with respect to the rolling direction of the material, the failure strain is found to be about twice as large as the failure strain in the rolling (0°) direction. The directional yield stresses can be determined at equal plastic strains or at equal amounts of plastic work (Barlat et al., 1997a,b, 2003a,b). Both methods were tested, and found to produce almost identical results for the present material, as is shown in Fig. 8. This figure also presents model results that will be discussed in Section 5. The normalized yield stress is defined as the ratio of the directional yield stress to the yield stress in the rolling direction at the same level of plastic strain or specific plastic work. It follows that the normalized yield stress in the rolling direction is unity per definition. The data given in Fig. 8 are average values of the normalized yield stress up to a plastic strain of 20% and specific plastic work of 70 MPa. The true stress–plastic strain curves from the experiments had to be filtered since the present aluminium alloy exhibits PLC. It is clearly seen from Fig. 8 that the strength anisotropy of the alloy is moderate and well within 10%, but the variation of the directional yield stress with tensile direction is quite complex. The highest strength is found at 60°, while the material is weakest in the 45° orientation. The variation of the R-ratio with tensile direction with respect to the rolling direction of the plate is plotted in Fig. 9. The experiments show a marked and complex

Please cite this article in press as: Grytten, F. et al., Evaluation of identification methods ..., Int. J. Plasticity (2008), doi:10.1016/j.ijplas.2007.11.005

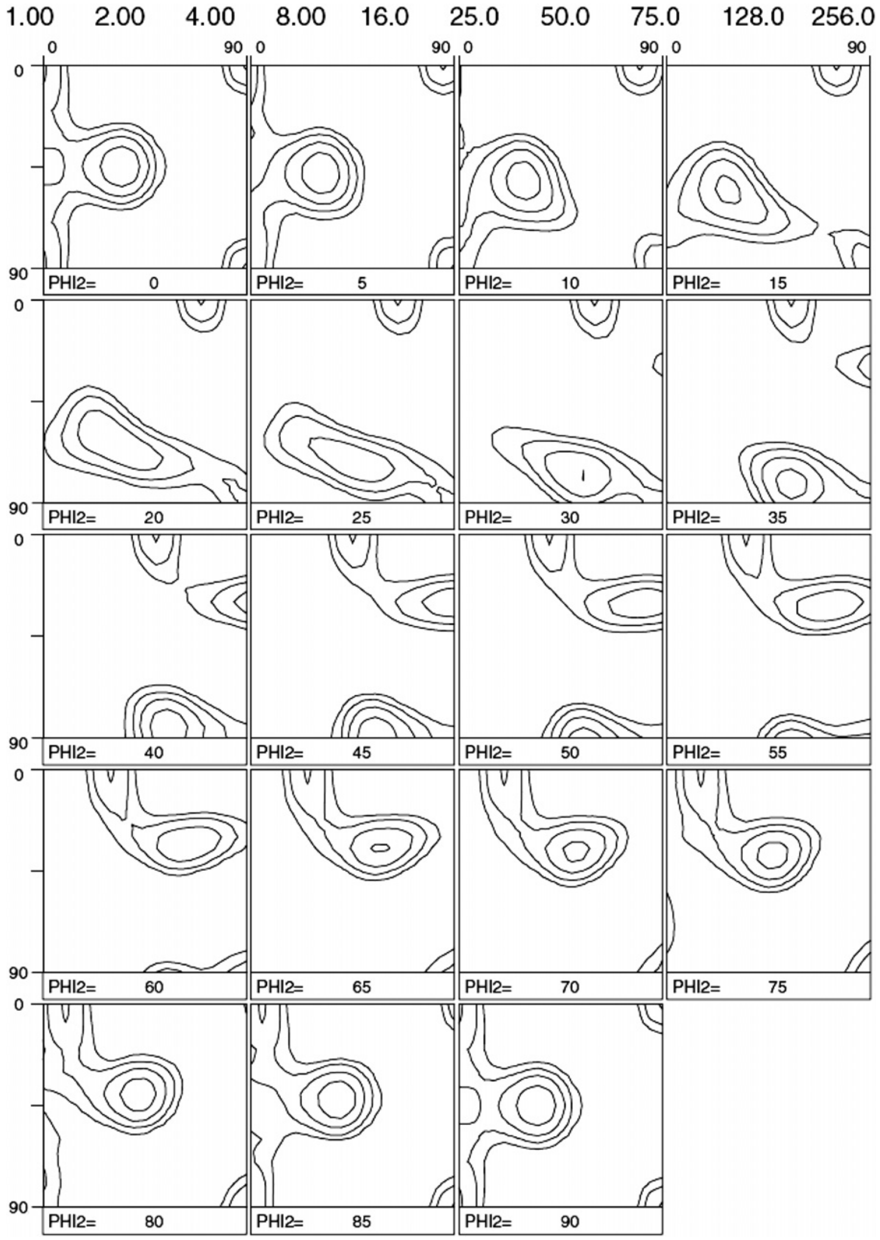

Fig. 4. Orientation distribution function (ODF) for aluminium alloy AA5083-H116.

variation of the *R*-ratio, which is evidence of anisotropy in the plastic flow. The *R*-ratio is lowest in the rolling direction and highest in the 45° and transverse directions of the plate, while for intermediate orientations the *R*-ratio fluctuates between 0.43 and 1.18.

Plane-strain tension test specimens were cut from the plate at 0°, 45° and 90° to the rolling direction. The geometry of these specimens is shown in Fig. 10. The specimens were 2 mm thick and machined from the thickness centre of the 10 mm thick plate. The strain

Please cite this article in press as: Grytten, F. et al., Evaluation of identification methods ..., Int. J. Plasticity (2008), doi:10.1016/j.ijplas.2007.11.005

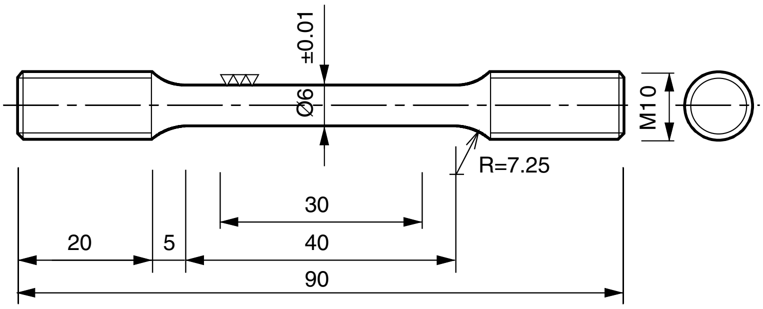

Fig. 5. Uniaxial tensile test specimen (all measures are in mm).

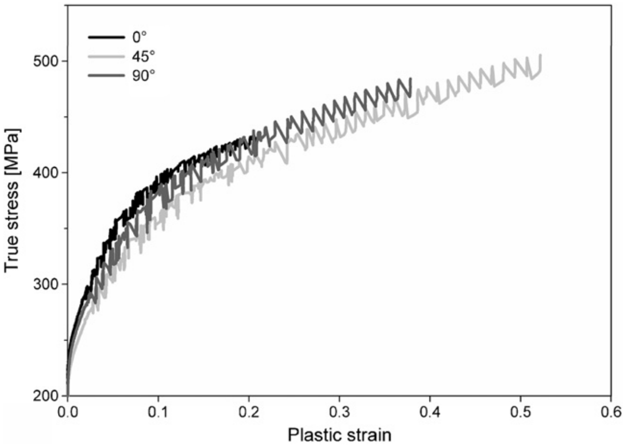

Fig. 6. True stress–strain curves of AA5083-H116 exhibiting plastic anisotropy and serrated flow.

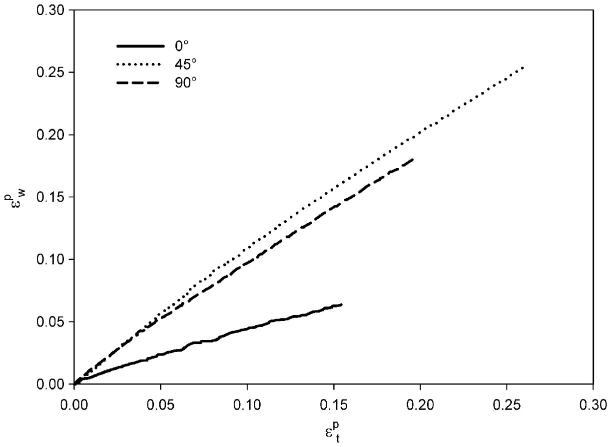

Fig. 7. Orthogonal plastic strains at three in-plane tension directions.

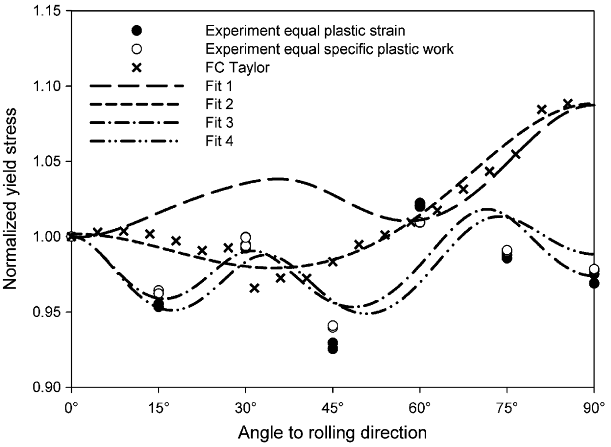

Fig. 8. Normalized yield stress versus angle to the rolling direction obtained from experiments, FC-Taylor theory and fitted yield surfaces.

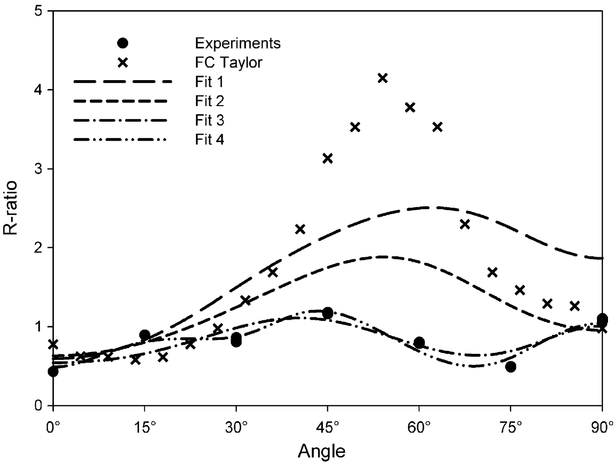

Fig. 9. *R*-ratios obtained from experiments, FC-Taylor theory and fitted yield surfaces as function of angle to the rolling direction.

rate in the deformation zone increased from approximately 1×10^{-4} s^{-1} in the beginning of the test to approximately 5×10^{-4} s^{-1} at the end of the test. The force was measured continuously during testing by use of the internal load cell of the testing machine, along with elongation measured with an extensometer having a gauge length of 40 mm.

Fig. 11 shows the force–displacement curves from the plane-strain tests along with the results from numerical simulations described later. It is seen that duplicate tests in the 45° and 90° directions produce similar results. Moreover, the behaviour in the three orientations is similar both with respect to strength level and displacement at fracture. Digital image correlation (Besnard et al., 2006) was used to measure the displacement field and calculate the strains of the test specimens. These calculations revealed that the transverse

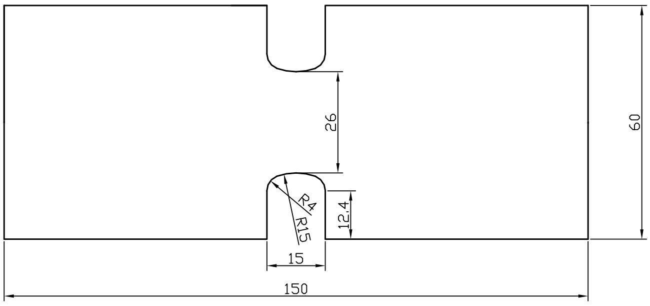

Fig. 10. Plane-strain tension test specimen (all measures are in mm).

strain was approximately 10% of the strain in the longitudinal direction. Ideally, there should not have been any strain in the transverse direction. However, the test is useful for model evaluation.

Shear tests were performed on specimens taken parallel and at 45° to the rolling direction. The geometry of these specimens is given in Fig. 12 and was proposed by Eriksson et al. (2006). Also these specimens were 2 mm thick and spark eroded from the thickness centre of the plate. During testing the strain-rate varied in the range $1 \times 10^{-3} - 5 \times 10^{-3}\ \mathrm{s}^{-1}$. Force and elongation were continuously registered during the test. The force was measured by the load cell of the testing machine, while the elongation was measured by an extensometer with gauge length equal to 70 mm.

Fig. 13 shows the resulting force–displacement curves compared to numerical predictions by the finite element models described in Section 6. Some scatter between duplicate tests is found in the rolling direction, while in the 45° direction the results from duplicate tests are consistent. There is a marked difference in both strength and displacement to fracture between the two orientations. It is recalled that this was not the case for the plane-strain tension tests.

Upsetting tests were carried out to find the flow stress in the thickness direction along with the ratio between the plastic flow in the rolling and transverse directions. Both the initial height and diameter of the cylindrical specimens were 10 mm. Graphite paste was used as lubricant to reduce friction and barrelling. The cylindrical specimen was compressed between two rigid platens of hardened tool steel. An extensometer was connected to the rigid platens to measure the displacement, while the force was measured by the load cell of the testing machine. The nominal strain rate used in the experiments was $1 \times 10^{-4}\ \mathrm{s}^{-1}$.

The upsetting test gives the same deviatoric stress state as an equibiaxial tensile test. Hence, the equibiaxial strain ratio $R_\mathrm{b} = \varepsilon^\mathrm{p}_{yy}/\varepsilon^\mathrm{p}_{xx}$, where $\varepsilon^\mathrm{p}_{xx}$ and $\varepsilon^\mathrm{p}_{yy}$ are the true plastic strains in the rolling and transverse directions, and the equibiaxial yield stress can be found from these tests, provided the friction is sufficiently small, isotropic and homogenous not to influence the stress and strain states significantly. However, the friction is often found to influence the stress state and thus the load level at which yielding occurs. Accordingly, the measured equibiaxial yield stress is inaccurate and cannot uncritically be used for calibration purposes. As will be discussed in Section 6, finite element simulations of the upsetting tests indicate that for the actual specimen geometry, the effect of friction is negligible for small deformations. The force–displacement curves will therefore only be used for model evaluation.

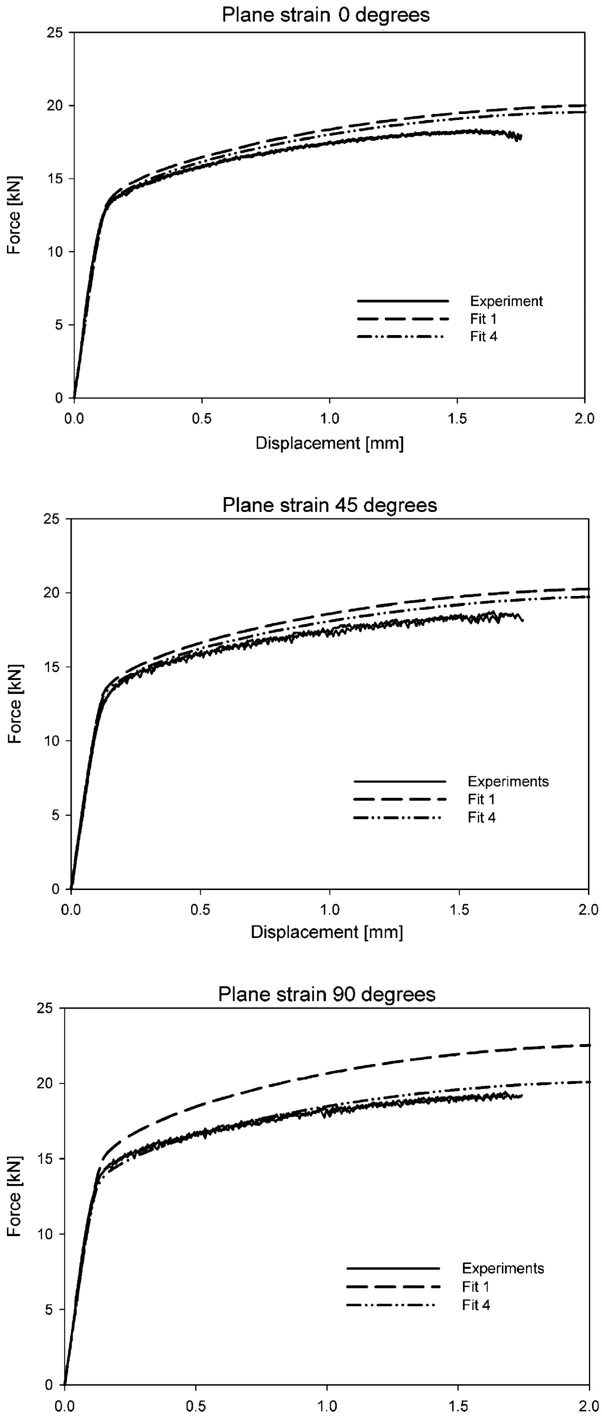

Fig. 11. Results from plane-strain tension tests and simulations in three directions.

Please cite this article in press as: Grytten, F. et al., Evaluation of identification methods ..., Int. J. Plasticity (2008), doi:10.1016/j.ijplas.2007.11.005

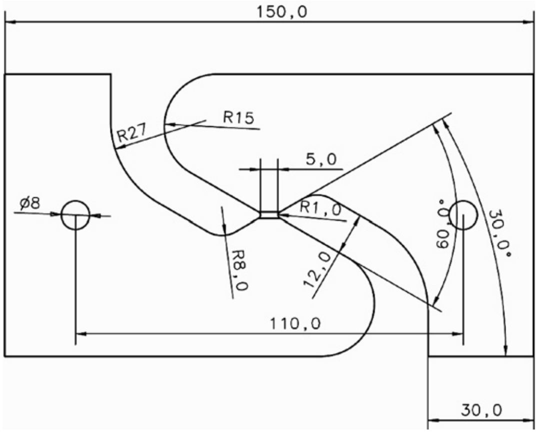

Fig. 12. Specimen for shear testing (all measures are in mm).

The force–displacement curves from the upsetting experiments are shown in Fig. 14 along with the curves predicted by the numerical models. Five duplicate tests were performed. However, successful measurements of force and displacement were only achieved in three of them. Two of these gave consistent results, while the third showed significantly lower forces. The reason for this is unknown. The equibiaxial yield stress is estimated to 225 MPa based on these results. This gives a ratio between the equibiaxial yield stress and the reference yield stress (from the tension test in the rolling direction) equal to 1.02. The equibiaxial strain ratio $R_\mathrm{b} = \varepsilon^\mathrm{p}_{yy}/\varepsilon^\mathrm{p}_{xx}$ was calculated from plastic strains measured optically during experiments and with a slide calliper afterwards. Note that the stress state is close to a sharp corner on the yield surface and just a small perturbation of the stress state could alter the normal significantly. This is also reflected in the relatively large standard deviation of the strain ratios seen in the experiments. The mean value and standard deviation from the five tests were calculated to 0.78 and 0.07, respectively. All results were in the range from 0.66 to 0.85.

5. Parameter identification

The yield function YLD2004-18p contains 18 anisotropy parameters, where 14 are related to the in-plane properties of the sheet (Yoon et al., 2006). These can typically be determined by conducting uniaxial tension tests at every 15° from the rolling direction, giving seven yield stresses and R-ratios. Alternatively, they can be determined from crystal plasticity calculations if the crystallographic texture of the material is measured. The four remaining parameters associated with out-of-plane properties can not easily be measured on plate material. However these can easily be determined by the use of crystal plasticity calculations. If texture data are not available, an alternative is to approximate the remaining parameters by setting them to their isotropic values.

The main role of the exponent m of the yield criterion is to determine the radius of curvature of the corners of the yield locus, which cannot be properly resolved without at least three experimental points in each direction closely centred at each corner. In order to perform the required experiments virtually by the FC-Taylor model the exact location of cor-

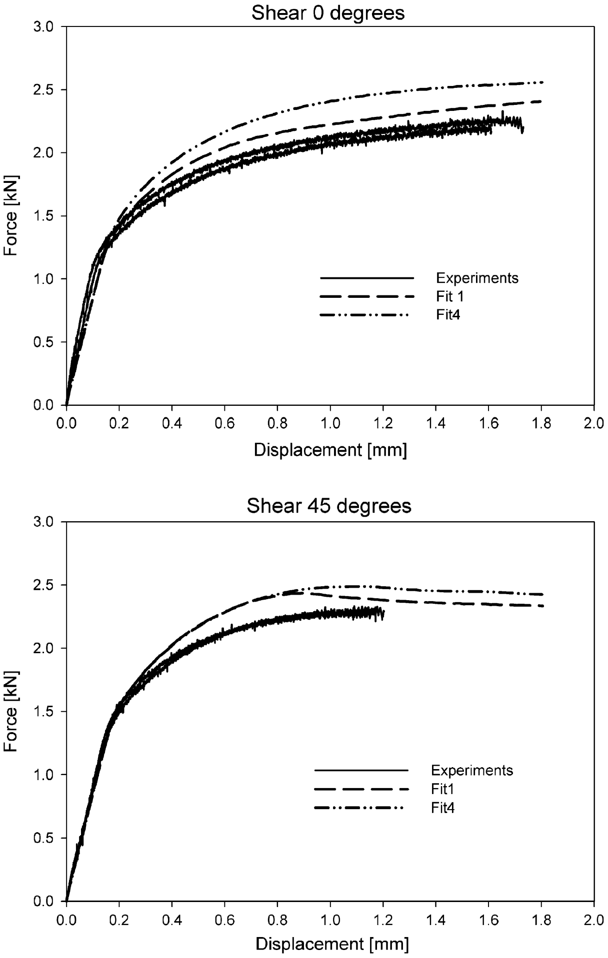

Fig. 13. Results from shear tests and simulations at 0 and 45 degrees to the rolling direction.

ners would first have to be identified. Such an algorithm would be computationally demanding and has not been implemented. The 690 stress states at yielding determined in this work are not sufficient to accurately fit the exponent of the yield function. Thus, an exponent m equal to 8 is applied instead, corresponding to the case of a random FCC texture (Hosford, 1972).

In the following, four procedures for fitting the anisotropy parameters will be tested and evaluated. The first approach is to use only the 690 stress states at yielding predicted by the FC-Taylor model to determine the constants of YLD2004-18p. All the stress points were given equal weight. This method will be denoted “Fit 1”. The function to be minimized is

$$\sum_{i=1}^{N} w_i \left(\frac{\bar{\sigma}_i}{\sigma_0} - 1 \right)^2 = \min \tag{27}$$

Please cite this article in press as: Grytten, F. et al., Evaluation of identification methods ..., Int. J. Plasticity (2008), doi:10.1016/j.ijplas.2007.11.005

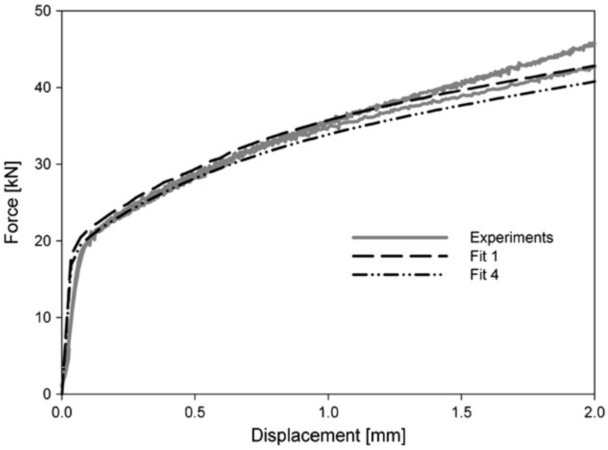

Fig. 14. Results from upsetting tests and simulations.

where w_i is a weight factor and $\bar{\sigma}_i = \bar{\sigma}(\boldsymbol{\sigma}_i)$ is the value of the effective stress for a stress $\boldsymbol{\sigma}_i$ predicted by the FC-Taylor model to be on the yield surface. The calculated effective stress is supposed to be equal to the yield stress σ_0 in uniaxial tension in the rolling direction for all these points. The rolling direction is used as reference direction. A constraint was added to ensure that the effective stress at yielding in the rolling direction was equal to the yield stress in the same direction.

The second approach, "Fit 2", is to use the FC-Taylor model to generate 63 extra points near the xy-plane (where the x and y axes are parallel to the rolling and transverse directions) and give them extra weight (ten times the weight of the 690 original points) in the least squares fitting. The motivation for weighting the xy-plane higher than the rest of the stress space is that the in-plane stresses often dominate in a load-carrying plate.

In the third approach, "Fit 3", measured directional yield stresses and R-ratios from the seven in-plane uniaxial tensile tests will be included in the fitting along with the 690 original stress points predicted by the FC-Taylor model. Since the number of experiments is much lower than the number of stress points calculated with the FC-Taylor model, the experimental data had to be given higher weight than the stress points from the crystal plasticity calculations (200 times the weight of the FC-Taylor points was chosen).

The final approach, "Fit 4", is to only use experimental data from the seven tensile tests and the upsetting test to determine the constants. From the upsetting test, only the equibiaxial strain ratio was used. The force–displacement curves from the upsetting test are used to assess the calibration procedure. The constants $c'_{44} = c'_{55} = c''_{44} = c''_{55} = 1$ in Fit 4, while they were fitted to the data in the other approaches. The same weight was given to the normalized yield stresses, the R-ratios and the equibiaxial strain ratio in this fitting procedure.

Table 1 shows the anisotropy constants found for the AA5083-H116 aluminium alloy using the four different approaches. To compare the obtained phenomenological yield loci to the predictions of the FC-Taylor model, a root-mean-square value will be calculated for all loci using the 690 stress points. This value is also given in Table 1. The five parameters of the two-term Voce hardening rule given by Eq. (11), namely σ_0, Q_1, C_1, Q_2 and C_2, were determined through a least squares fit to the true stress–plastic strain curve obtained with Bridgman corrections from a tensile test performed in the rolling direction. The resulting parameters are listed in Table 2.

The phenomenological yield criterion was used to determine the directional yield stresses in uniaxial tension for Fit 1–4. The calculated normalized yield stresses are shown in Fig. 8 along with the experimental data and the FC-Taylor theory. As already mentioned, the aluminium alloy AA5083-H116 exhibits a weak but complex variation in the yield stress in uniaxial tension with varying tensile directions. Fit 3 and Fit 4 of YLD2004-18p, which were calibrated to these points, give a relatively good representation of this variation. This shows that YLD2004-18p is sufficiently flexible to describe the observed strength anisotropy. The FC-Taylor model predicts the flow stress in the transverse direction to be greater than the flow stress in the rolling direction, while the tests show that the flow stress is greater in the rolling direction. Hence, the calibrations Fit 1 and Fit 2, which are based solely on the FC-Taylor crystal plasticity calculations, are less accurate and over-estimate the yield stress in the transverse direction by about 15%.

Also the R-ratios were calculated directly from the four fits of the phenomenological yield surface and FC-Taylor theory, and a comparison of the calculated and measured R-ratios is shown in Fig. 9. Fit 3 and Fit 4 of YLD2004-18p, which are calibrated to these data, describe the complex variation of the R-ratio with good accuracy. This demonstrates the ability of the YLD2004-18p criterion to describe the complex anisotropy in plastic flow exhibited by the alloy. On the contrary, Fit 1 and Fit 2 are quite inaccurate. The reason for this inaccuracy is the large discrepancies seen between the experimental data and the crystal plasticity calculations for tensile angles in the range 30–70°.

The equibiaxial strain ratio R_b resulting from the considered fits are given in Table 3 together with the measured value. It is seen that Fit 4 is reasonably accurate, while the

Table 1
Fitted parameters of the phenomenological yield surface

	Fit 1	Fit 2	Fit 3	Fit 4
c'_{12}	0.813	0.879	0.272	−0.440
c'_{13}	0.705	0.457	1.970	1.688
c'_{21}	0.181	0.658	0.404	1.645
c'_{23}	0.578	0.632	−0.499	2.526
c'_{31}	0.808	1.108	−0.624	0.480
c'_{32}	0.195	1.352	0.363	−2.000
c'_{44}	0.922	0.588	−0.768	1.000
c'_{55}	0.637	1.145	−1.196	1.000
c'_{66}	0.901	0.919	−1.186	0.974
c''_{12}	0.824	1.372	0.900	−1.126
c''_{13}	1.239	1.101	0.959	1.631
c''_{21}	1.166	0.586	1.014	0.611
c''_{23}	1.012	0.175	1.133	1.130
c''_{31}	0.873	0.908	−0.571	0.123
c''_{32}	1.375	1.325	0.468	−0.491
c''_{44}	0.914	1.282	0.974	1.000
c''_{55}	1.376	0.861	0.636	1.000
c''_{66}	1.246	1.189	0.776	1.069
m	8.000	8.000	8.000	8.000
RMS	0.0202	0.0218	0.0417	0.1216

Please cite this article in press as: Grytten, F. et al., Evaluation of identification methods ..., Int. J. Plasticity (2008), doi:10.1016/j.ijplas.2007.11.005

Table 2
Hardening parameters

σ_0	Q_1	C_1	Q_2	C_2
218.6 MPa	20.05 MPa	718.5	179.9 MPa	17.97

Table 3
Equibiaxial strain and stress ratios

	Experiments	Fit 1	Fit 2	Fit 3	Fit 4
R_b	0.78	1.26	0.36	2.94	0.88
σ_b/σ_0	1.02	1.04	1.04	0.97	0.97

other approaches give large discrepancies. Consequently only Fit 4, based entirely on experiments, is a viable model definition for this alloy. In what follows, we will restrict our attention to Fit 4 and also include the purely crystal plasticity based Fit 1, which is interesting for the discussion of the experiments that are not part of Fit 4.

Fig. 15 shows a comparison between the Fit 1 and Fit 4 surfaces and the stress points generated by the FC-Taylor theory near the *xy*-plane. It is seen that there are marked differences between the yield loci with Fit 1 calibrated to crystal plasticity and Fit 4 calibrated entirely to experiments, both with respect to shape and strength level. It is mentioned that the YLD2004-18p criterion (with Fit 2) is capable of fitting perfectly all points generated from FC-Taylor theory in the *xy*-plane. Note further that stress points can be generated in the two other normal-stress planes shown in Fig. 15 by just adding a hydrostatic pressure to the points generated in the *xy*-plane. The plots of the *yz*-plane and the *zx*-plane do therefore not give any new information about the flexibility of the yield function, but they are included here to illustrate the shape of the yield surface.

6. Finite element simulations

Finite element simulations of all the material tests were carried out using LS-DYNA (LSTC, 2007). Eight node brick elements with one integration point and Flanagan–Belytschko stiffness-based hourglass control with exact volume integration were used in all simulations. Invariant node numbering was applied.

Simulations of the tensile tests were performed to verify the implementation of the user-defined material model in LS-DYNA. All directional yield stresses and *R*-ratios calculated from the finite element simulations were very close to the values calculated directly from the yield function. Furthermore, the true stress–plastic strain curve obtained from the simulation of tension in the rolling direction coincided with the reference hardening curve indicating that the implemented material model was working as intended. Some discrepancies were seen for the nominal stress–strain curves at large strains, i.e. in the post-necking region. However, it was the initial shape of the yield locus that was of main interest in the present study and uncertainties associated with large deformations were not considered.

Finite element simulations of the plane-strain tests were run next. Fig. 16 shows the finite element model with contours of equivalent plastic strain. Three elements were used across the thickness. The load was applied through rigid bodies at the end of the specimen,

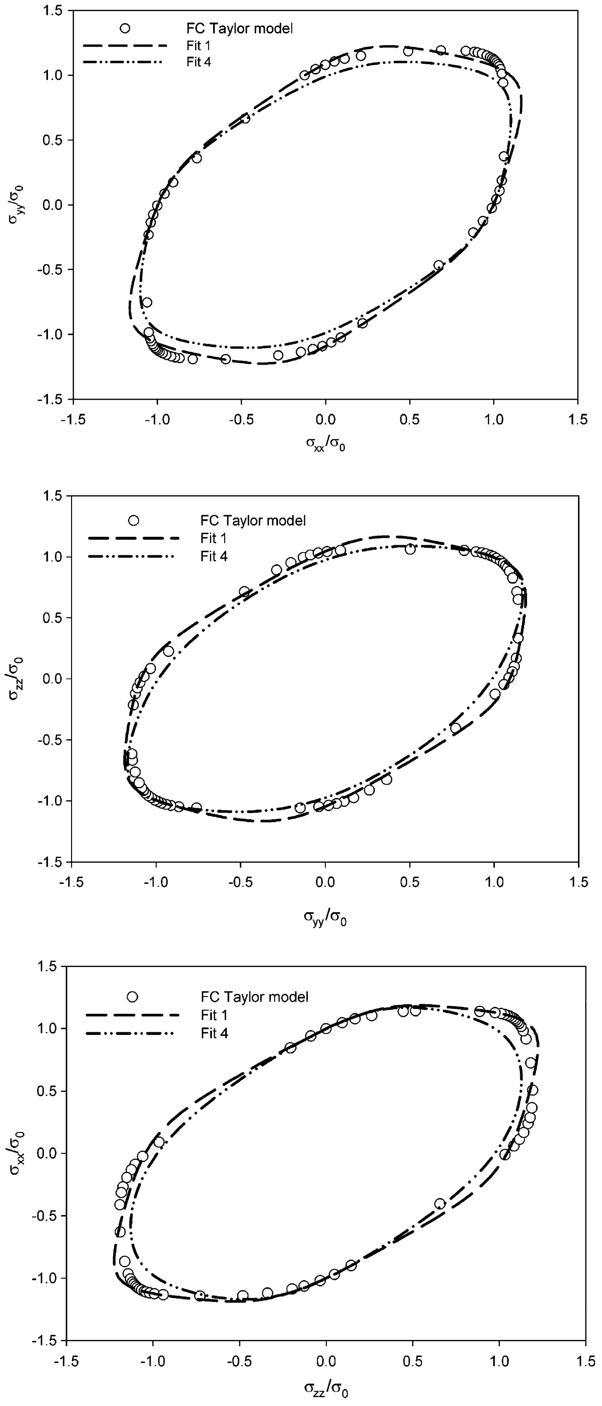

Fig. 15. Comparison of the fitted yield loci and some stress points obtained by the full-constraints Taylor model. (The *x*-axis is parallel to the rolling direction, the *y*-axis is parallel to the transverse direction, and the *z*-axis is parallel to the normal direction.)

Please cite this article in press as: Grytten, F. et al., Evaluation of identification methods ..., Int. J. Plasticity (2008), doi:10.1016/j.ijplas.2007.11.005

while the relative displacement of nodes located where the extensometer was in contact with the specimen was used to calculate the elongation. Finite element simulations were run using all parameter fits, however, only results from Fit 1 and Fit 4 will be presented in the following for reasons discussed in Section 5. The resulting force–displacement curves from Fit 1 and Fit 4 are compared to the curves obtained from the experiments in Fig. 11. Even if the hardening is over-estimated, both parameter fits give reasonably good results in simulations of the plane-strain tension tests in the rolling direction. However, Fit 1 gives slightly inferior results compared with the other fitting procedure. Regarding the 45° direction the force level is well predicted for small plastic strains, while the force is over-predicted in the transverse direction by Fit 1 based on FC-Taylor theory. This is in some accordance with the findings for uniaxial tension, as can be seen from Figs. 9 and 10 concerning the capability of the FC-Taylor model to predict the observed planar anisotropy, which will be further discussed in Section 7. The reason for this similarity is that due to unwanted transverse strains in the plane-strain tension tests, the resulting stress state was not as far from uniaxial tension as desired. However, the stress state was sufficiently different from uniaxial tension to still be useful for model evaluation.

The spatial discretization of the shear test specimens is illustrated in Fig. 17. A mesh with five elements through the thickness was used. Fig. 13 shows a comparison of the force–displacement curves from tests and finite element predictions. The force level was in general over-predicted in all simulations of the shear tests both in the 0° and 45° directions (see Fig. 13). However, the initial yielding is quite well predicted. Note also that the fit based solely on the FC-Taylor model gives the results that are closest to the experimental results in the 0° direction.

Finally, finite element simulations of the upsetting tests were run. Fig. 18 shows the initial finite element mesh (a) and the resulting unsymmetrical geometry after some plastic deformation (b,c). A characteristic element size of 0.3 mm was used. The loading was applied through planar rigid walls with a Coulomb friction coefficient of 0.2. The influence of the friction coefficient was studied by running simulations without friction and with no sliding after contact. These simulations indicated that the effect of the friction coefficient was insignificant for small deformations. Fig. 14 compares the force–displacement curves from experiments and simulations using Fit 1 and Fit 4. Both simulations of the upsetting test gave reasonable force predictions as compared to the experimental results for moder-

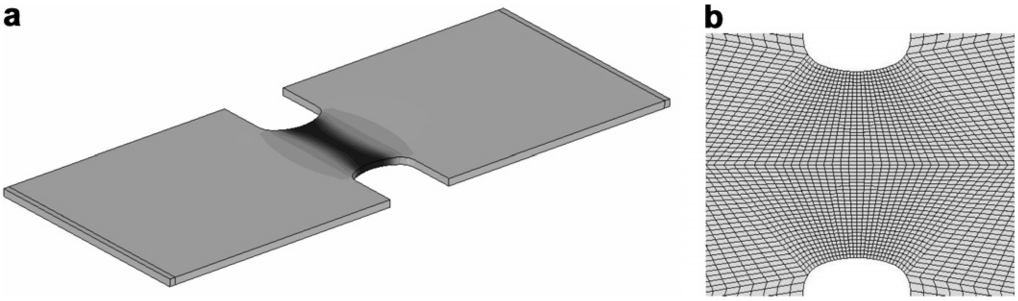

Fig. 16. Contours of plastic strain in simulation of a plane-strain tension test (a) and the element mesh in the notched section (b).

Please cite this article in press as: Grytten, F. et al., Evaluation of identification methods ..., Int. J. Plasticity (2008), doi:10.1016/j.ijplas.2007.11.005

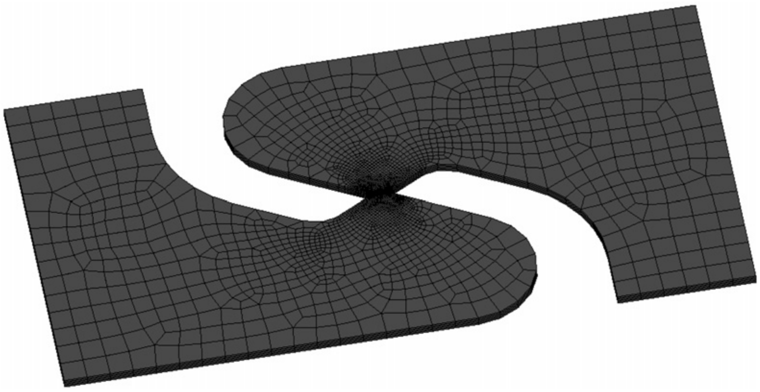

Fig. 17. Finite element model of shear test specimen.

ate displacements. It can be seen from Fig. 14 that these two fits gave almost the same yield stress in equibiaxial tension (as mentioned above, the deviatoric stress state is the same for an upsetting test as for an equibiaxial tensile test), where the fit based on the FC-Taylor model gave a slightly better prediction of the force at which first yielding occurs.

The four fitting procedures produced significantly different normals to the yield surface for equibiaxial tension, and thus the equibiaxial strain ratio varied significantly between the fits. This is seen in Table 3 and illustrated by Fig. 18, where the resulting shapes for Fit 2 and Fit 3 are compared (the rolling direction is aligned horizontally in the figure). Only Fit 4, which included the balanced biaxial gradient in the fitting procedure, gave a reasonable prediction of the strain ratios. It is worth noting that an isotropic yield function would have predicted an equibiaxial gradient closer to the experimental values than the ones involving crystal plasticity.

7. Discussion

Fit 3 and Fit 4 are based on the seven uniaxial tensile tests and the equibiaxial strain ratio derived from upsetting tests, which together provide less information than required to fit all the 18 parameters. These two calibration methods provide good fits to the observed planar anisotropy. However, only the plane strain tension tests, the shear tests and the equibiaxial stress of the upsetting test can be used for assessment of the resulting yield loci.

Regarding Fit 1 and Fit 2, the fits to the tensile tests and the upsetting test rest on the capability of the FC-Taylor model to predict the planar anisotropy of the alloy. This part may be improved by switching to more advanced texture models. Assuming a qualitatively correct prediction by the FC-Taylor model one can assess the ability of the yield function YLD2004-18p to fit the entire stress space. It is found that the built-in shape of this locus with an exponent equal to eight fits the entire virtual stress space as predicted by the FC-Taylor model surprisingly well.

The simulation of the two shear tests and the force required to cause plastic yielding in the equibiaxial upsetting test represent results that are not directly determined by the experiments involved in the fitting procedures. It is interesting to note, firstly that none

Please cite this article in press as: Grytten, F. et al., Evaluation of identification methods ..., Int. J. Plasticity (2008), doi:10.1016/j.ijplas.2007.11.005

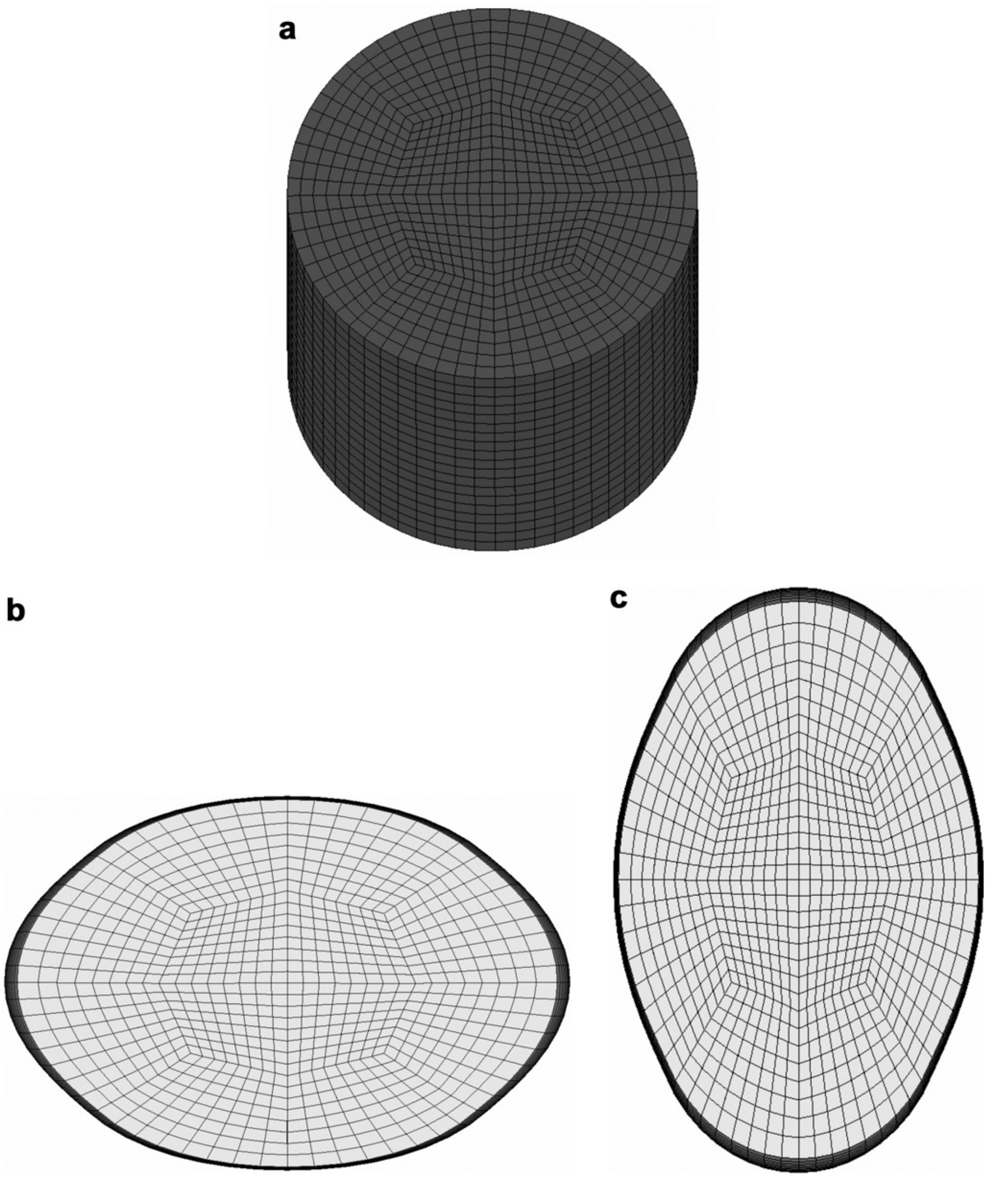

Fig. 18. Finite element model of upsetting test (a) and the resulting shapes for Fit 2 (b) and Fit 3 (c).

of these fits matched, secondly that for all these cases Fit 1 and Fit 2 being based on texture calculations were slightly closer to the experiments.

Uniaxial tensile tests were used to evaluate the applicability of the FC-Taylor model to predict the shape of the yield locus. Considerable discrepancies between experimental results and crystal plasticity calculations were observed. It is evident from Figs. 8 and 9 that the FC-Taylor model (and thus the yield loci fitted to it) is not capable of reproducing the planar anisotropy of the AA5083-H116 plate material. The *R*-ratios for tensile directions between 30° and 70° to the rolling directions are particularly over-estimated by the FC-Taylor model. This is consistent with a study by Choi and Barlat (1999) on an Al–Li sheet with a strong Brass texture component, for which the FC-Taylor model over-estimated the *R*-ratios for directions between 45° and 60° to the rolling direction. They showed that the over-estimation of the mentioned R-values vanished when using the self consistent viscoplastic texture model. Li et al. (2005) found that also a relaxed-constraint Taylor model is capable of reproducing the planar anisotropy correctly. The main reasons for the discrepancies are believed to derive partly from the pancake shaped grain structure (as can be seen in Fig. 2) and partly from the weakness of the FC-Taylor model to handle the texture components typical for rolled materials due to a lack of global stress equilibrium. A more advanced texture model than the FC-Taylor model is required (see Choi et al. (2000) for a relevant discussion). One can conclude from this that the FC-Taylor model has weaknesses. One can, however, not conclude which texture model is best for general purposes. It is mentioned that Li et al. (2005) showed that for a recrystallized material the FC-Taylor model was the best choice for planar anisotropy.

The variation of *R*-ratios is essential in simulation of sheet forming processes, e.g. to predict earing in cup drawing (see, e.g. Yoon et al., 1998, 2000, 2004, 2006), and the need for accurate predictions of the *R*-ratios is an important part of the motivation for developing sophisticated yield criteria. However, in more general three-dimensional applications other parts of the yield surface may be of greater importance. The crystal plasticity model that gives the most accurate predictions for sheet metal forming does not necessarily give the best predictions in other parts of the stress space. It is therefore difficult to determine a priori which theory will give the best results for a given texture and application.

The AA5083-H116 alloy exhibits dynamic strain ageing and the Portevin–Le Chatelier effect. Based on the experimental data of Clausen et al. (2004), it seems reasonable to assume the strengthening effect of dynamic strain ageing to be isotropic for this alloy. Since the tests are carried out at the same strain-rate in all directions, Fig. 8 should reflect the real shape of the yield locus. It is noteworthy that even if all the experiments were designed to have approximately the same nominal strain-rate, the true strain-rate varied slightly during testing. As already mentioned, the variation in normalized directional yield stress is relatively small for the present alloy, ranging from 0.93 to 1.02. However, it can be seen from Fig. 8 that there are, though small, distinct variations in the yield stress for different directions. This variation is obviously captured well by the yield functions for which the directional stresses are included in the fitting (Fit 3 and Fit 4). The FC-Taylor model, on the other hand, does not predict the oscillating nature (with a frequency equal to or higher than the measured 15 degrees variation) of the stress. Its largest error is the over-estimation of the yield stress in the transverse direction by approximately 10%.

While the AA5083-H116 alloy exhibits complex variations of the directional yield strength and *R*-ratio with tensile direction, the deviations from unity are not dramatic. The normalized directional yield stress is between 0.93 and 1.02, while the *R*-ratio varies between 0.43 and 1.18. Similarly, the equibiaxial yield stresses and strain ratios are reasonably close to the values implied by isotropy. Based on these observations it is evident that the FC-Taylor model does not provide any improvement to the calibration of even a limited set of the YLD2004-18p model parameters for the particular anisotropy of the material considered in this paper.

Please cite this article in press as: Grytten, F. et al., Evaluation of identification methods ..., Int. J. Plasticity (2008), doi:10.1016/j.ijplas.2007.11.005

8. Conclusions

In the present study, the anisotropic mechanical properties of aluminium alloy AA5083-H116 have been investigated. The alloy has pancake shaped grains elongated in the rolling plane and a moderate rolling texture. Only a small variation in yield stress was observed for tensile test in various directions to the rolling direction, while the variation of the *R*-ratio was distinct.

The linear transformation-based anisotropic yield function YLD2004-18p proposed by Barlat et al. (2005) for a full 3D stress state contains 18 parameters and the choice of procedure to determine these is of major importance. This yield function is flexible enough to give a reasonable description of the plastic anisotropy of the present sheet material by matching not only the experiments to which it was fitted, but also by matching well the nearby plane-strain tests and by reproducing qualitatively shear tests in the 0° and 45° directions and predicting the stress of an upsetting test satisfactorily.

The two fitting procedures based solely on FC-Taylor model calculations failed to predict the experiments used as a basis for Fit 3 and Fit 4 correctly. They over-predicted the force in the plane-strain test in the 90° direction by a similar amount as the tensile test in the same direction, which is not a surprise since these two strain paths are quite close. The *R*-value variation is of great importance in applications and the FC-Taylor model predictions were in that respect not good enough. Indeed, for the particular material studied here, these predictions turned out to be worse than simply assuming planar isotropy. However, Fit 1 and Fit 2, which were based entirely on FC-Taylor theory, gave the most accurate predictions for the tests that were not included in any fitting procedure, i.e. the two shear tests and the force in the upsetting test.

Crystal plasticity theories and the FC-Taylor model in particular have weaknesses and it is difficult a priori to decide which model gives the best results for a given combination of texture and grain morphology. It is therefore the authors' recommendation to use material tests to calibrate the yield surface. If it is not feasible to determine all parameters by such tests, some kind of assumption of isotropy in these portions of the stress space might be a better alternative than using the FC-Taylor model, in particular when considering weakly anisotropic materials with moderate textures like the one considered here. Crystal plasticity models should be used with care until improved texture models are developed and knowledge about their performances is documented.

Acknowledgements

The present work was carried out with financial support from CRI-SIMLab, the Research Council of Norway and the Norwegian Defence Estates Agency. The authors are grateful to Magnus Eriksson who provided the finite element mesh for the shear test specimens and to Snorre Kjørstad Fjeldbo who carried out the measurements of the crystallographic texture.

References

Asaro, R.J., Needleman, A., 1985. Texture development and strain hardening in rate dependent polycrystals. Acta Metall. 33, 923–953.

Barlat, F., Lian, J., 1989. Plastic behaviour and stretchability of sheet metals. Part I: a yield function for orthotropic sheets under plane stress conditions. Int. J. Plasticity 5, 51–66.

Barlat, F., Lege, D.J., Brem, J.C., 1991. A six-component yield function for anisotropic materials. Int. J. Plasticity 7, 693–712.

Barlat, F., Becker, R.C., Hayashida, Y., Maeda, Y., Yanagawa, M., Chung, K., Brem, J.C., Lege, D.J., Matsui, K., Murtha, S.J., Hattori, S., 1997a. Yielding description for solution strengthened aluminum alloys. Int. J. Plasticity 13, 385–401.

Barlat, F., Maeda, Y., Chung, K., Yanagava, M., Berm, J.C., Hayashida, Y., Lege, D.J., Matsui, K., Murtha, S.J., Hattori, S., Becker, R.C., Makosey, S., 1997b. Yield function development for aluminium alloy sheets. J. Mech. Phys. Solids 45, 1727–1763.

Barlat, F., Brem, J.C., Yoon, J.W., Chung, K., Dick, R.E., Lege, D.J., Pourboghrat, F., Choi, S.H., Chu, E., 2003a. Plane stress yield function for aluminium alloy sheets–part I: theory. Int. J. Plasticity 19, 1297–1319.

Barlat, F., Ferreira Duarte, J.M., Gracio, J.J., Lopes, A.B., Rauch, E.F., 2003b. Plastic flow for non-monotonic loading conditions of an aluminium alloy sheet sample. Int. J. Plasticity 19, 1215–1244.

Barlat, F., Aretz, H., Yoon, J.W., Karabin, M.E., Brem, J.C., Dick, R.E., 2005. Linear transformation-based anisotropic yield functions. Int. J. Plasticity 21, 1009–1039.

Barlat, F., Yoon, J.W., Cazacu, O., 2007. On linear transformations of stress tensors for the description of plastic anisotropy. Int. J. Plasticity 23, 876–896.

Belytschko, T., Liu, W.K., Moran, B., 2000. Nonlinear Finite Elements for Continua and Structures. Wiley, ISBN 0-471-98774-3.

Benallal, A., Berstad, T., Børvik, T., Clausen, AH., Hopperstad, OS., 2006. Dynamic strain aging and related instabilities: experimental, theoretical and numerical aspects. Eur. J. Mech. A/Solids 25 (3), 397–424.

Besnard, G., Hild, F., Roux, S., 2006. "Finite-Element" displacement fields analysis from digital images: application to Portevin–Le Câtelier bands. Exp. Mech. 46, 789–803.

Bishop, J.F.W., Hill, R., 1951a. A theory of the plastic distortion of a polycrystalline aggregate under combined stresses. Philos. Mag. 42, 414–427.

Bishop, J.F.W., Hill, R., 1951b. A theoretical derivation of the plastic properties of a face-centred metal. Philos. Mag. 42, 1298–1307.

Bridgman, PW., 1964. Studies in Large Plastic Flow and Fracture. Harvard University Press, Cambridge.

Børvik, T., Hopperstad, O.S., Berstad, T., Langseth, M., 2001. A computational model of viscoplasticity and ductile damage for impact and penetration. Eur. J. Mech. A/Solids 20, 685–712.

Børvik, T., Clausen, A.H., Hopperstad, O., Langseth, M., 2004. Perforation of AA5083-H116 aluminium plates with conical-nose steel projectiles—experimental study. Int. J. Impact Eng. 30 (4), 367–384.

Choi, S.-H., Barlat, F., 1999. Prediction of macroscopic anisotropy in rolled aluminum–lithium sheet. Scripta Mater. 41 (9), 981–987.

Choi, S.-H., Brem, J.C., Barlat, F., Oh, K.H., 2000. Macroscopic anisotropy in AA5019A sheets. Acta Mater. 48, 1853–1863.

Clausen, AH., Børvik, T., Hopperstad, OS., Benallal, A., 2004. Flow and fracture characteristics of aluminium alloy AA5083-H116 as function of strain rate, temperature and triaxiality. Mat. Sci. Eng. A 365, 260–272.

Cottrell, A.H., 1953. A note on the Portevin–Le Chatelier effect. Philos. Mag. (seventh series) 44 (335), 829–832.

Delannay, L., Kalidindi, S.R., Van Houtte, P., 2002. Quantitative prediction of textures in aluminium cold rolled to moderate strains. Mater. Sci. Eng. A 336, 233–244.

Eriksson, M., Lademo, O.-G., Hopperstad, O.S., 2006. Development and use of in-plane shear tests to identify ductile failure parameters of aluminium alloys. In: Proceedings of the 9th International Conference on Material Forming, ESAFOM 2006, Glasgow, UK, pp. 331–334.

Hatch, JE., 1984. Aluminium: properties and physical metallurgy. Am. Soc. Metals, 353–357.

Hill, R., 1948. A theory of the yielding and plastic flow of anisotropic metals. Proc. Royal Soc. London A 193, 281.

Hosford, W.F., 1972. A generalized isotropic yield criterion. J. Appl. Mech. Trans. ASME 39, 607–609.

Hosford, W.F., 1979. On yield loci of anisotropic cubic metals. In: Proceedings of the Seventh North American Metalworking Conference, Dearborn, pp. 191–197.

Hosford, W.F., 1993. The Mechanics of Crystals and Textured Polycrystals. Oxford Science Publications.

Kalidindi, S.R., Bronkhorst, C.A., Anand, L., 1992. Crystallographic texture evolution in bulk deformation processing of FCC metals. J. Mech. Phys. Solids 40, 537–569.

Karafillis, A.P., Boyce, M.C., 1993. A general anisotropic yield criterion using bounds and a transformation weighting tensor. J. Mech. Phys. Solids 41, 1859–1886.

Kocks, U.F., Tomé, C.N., Wenk, H.-R., 1998. Texture and Anisotropy: Preferred Orientations in Polycrystals and their Effect on Materials Properties. Cambridge University Press, ISBN 0-521-79420-X.

Leqeue, P.H., Gilormini, P., Montheillet, F., Bacroix, B., Jonas, J.J., 1987. Yield surfaces for textured polycrystals –I. Crystallographic approach. Acta Mater. 35, 439–451.

Lemaitre, J., Chaboche, J.L., 1990. Mechanics of Solid Materials. Cambridge University Press.

Li, S., Engler, O., Van Houtte, P., 2005. Plastic anisotropy and texture evolution during tensile testing of extruded aluminium profiles. Modell. Simulat. Mater. Sci. Eng. 13, 783–795.

Livermore Software Technology Corporation (LSTC), 2007. LS-DYNA Keyword User's Manual, Version 971.

McCormick, P.G., 1988. Theory of flow localisation due to dynamic strain ageing. Acta Metal. 36 (12), 3061–3067.

Mesarovic, S.DJ., 1995. Dynamic strain aging and plastic instabilities. J. Mech. Phys. Solids 43 (5), 671–700.

Rizzi, E., Hähner, P., 2004. On the Portevin–Le Chatelier effect: theoretical modeling and numerical results. Int. J. Plasticity 20, 121–165.

Søvik, O.P, 1996. Numerical modelling of ductile fracture – a damage mechanics approach. Dr. ing. thesis 1996:78. Department of Machine Design and Materials Technology, Norwegian University of Science and Technology, Trondheim, Norway, ISBN 82-7119-968-4.

Taylor, G.I., 1938. Plastic strain in metals. J. Inst. Metals 62, 307–324.

Tresca, H., 1864. Sur l'écoulement des corps solides soumis à des portes pressions. Comp. Rend. Acad. Sci. Paris 59, 754.

Van den Beukel, A., 1975. Theory of effect of dynamic strain aging on mechanical-properties. Phys. Status Solidi (A) 30, 197.

Van Houtte, P., 1988. A comprehensive mathematical formulation of an extended Taylor–Bishop–Hill model featuring relaxed constraints, the Renouard–Wintenberger theory and a strain rate sensitivity model. Textures Microstruct. 8–9, 313–350.

Van Houtte, P., Li, S., Seefeldt, M., Delannay, L., 2005. Deformation texture predictions: from the Taylor model to the advance Lamel model. Int. J. Plasticity 21, 589–624.

Van Houtte, P., Kanjarla, A.K., Van Bael, A., Seefeldt, M., Delannay, L., 2006. Multiscale modeling of the plastic anisotropy and deformation texture of polycrystalline materials. Eur. J. Mech. A/Solids 25, 634–648.

Von Mises, R., 1913. Mechanik der festen Körper im plastisch-deformablen Zustand. In: Nachr, Königl. Ges. Wiss. Göttingen, Math.-Phys. Kl., pp. 582–593.

Wenk, H.-R., van Houtte, P., 2004. Texture and anisotropy. Rep. Prog. Phys. 67, 1367–1428.

Yoon, J.W., Barlat, F., Chung, K., Pourboghrat, F., Yang, D.Y., 1998. Influence of initial back stress on the earing prediction of drawn cups for planar anisotropic aluminium sheets. J. Mater. Proc. Tech. 80–81, 433–437.

Yoon, J.W., Barlat, F., Chung, K., Pourboghrat, F., Yang, D.Y., 2000. Earing predictions based on asymmetric nonquadratic yield function. Int. J. Plasticity 16, 1075–1104.

Yoon, J.W., Barlat, F., Dick, R.E., Chung, K., Kang, T.J., 2004. Plane stress yield function for aluminium alloy sheets–part II: FE formulation and its implementation. Int. J. Plasticity 20, 495–522.

Yoon, J.W., Barlat, F., Dick, R.E., Karabin, M.E., 2006. Prediction of six or eight ears in a drawn cup based on a new anisotropic yield function. Int. J. Plasticity 22, 174–193.

Please cite this article in press as: Grytten, F. et al., Evaluation of identification methods ..., Int. J. Plasticity (2008), doi:10.1016/j.ijplas.2007.11.005

Part IV

F. Grytten, T. Børvik, O.S. Hopperstad, M. Langseth

Low velocity perforation of AA5083-H116 aluminium plates

Submitted for possible journal publication

Low velocity perforation of AA5083-H116 aluminium plates

F. Grytten[a,b,*], T. Børvik[a,b,c], O.S. Hopperstad[a,b] and M. Langseth[a,b]

[a] *Structural Impact Laboratory (SIMLab), Centre for Research-based Innovation (CRI),*
Norwegian University of Science and Technology, NO-7491, Trondheim, Norway.
[b] *Department of Structural Engineering,*
Faculty of Engineering Science and Technology,
Norwegian University of Science and Technology, NO-7491, Trondheim, Norway.
[c] *Norwegian Defence Estates Agency, Research and Development Section, PB 405, Sentrum, NO-0103,*
Oslo, Norway.

Abstract

This paper presents an experimental and numerical investigation on low velocity perforation of AA5083-H116 aluminium plates. In the tests, square plates were mounted in a circular frame and penetrated by a cylindrical blunt-nosed projectile. The perforation process was then computer analysed using the nonlinear finite element code LS-DYNA in order to investigate the effects of anisotropy, dynamic strain aging and thermal softening in low velocity impacts on the present aluminium alloy. Dynamic strain aging has been shown to influence both the predicted force level and fracture, while thermal softening only influences fracture prediction. No effect of plastic anisotropy has been observed.

Key words: Aluminium, Plates, Perforation, Fracture.

---

[*] Corresponding author. Tel.: +47 73594700; fax: +47 73594701.
E-mail address: frode.grytten@sintef.no (F. Grytten).

1 Introduction

Structural impact has become increasingly important in structural design. Earlier, such problems were primarily of military interest. Nowadays, accidental structural impact problems are a concern in numerous civilian fields, such as the offshore industry, naval industry, aviation and space industry as well as the nuclear and process industry. The low velocity domain covers dropped objects, vehicle impacts, ship collisions and groundings, crashworthiness of containers for hazardous materials, etc. Even though more and more research is put into these fields, the vast majority of papers concerning the penetration problem are still on penetration at greater impact velocities. Most common, the research aims to find or predict the ballistic limit velocity. Work covering low velocity impact has been reported by for example Wen and Jones [1][2], Langseth and Larsen [3][4][5] and Langseth et al. [6]. Comprehensive reviews on penetration and perforation in general can be found in the journal papers of Goldsmith [7], Backman and Goldsmith [8] and Corbett et al. [9], and in the books by Zukas et al. [10][11].

As part of gaining a better understanding of the impact problem and to develop design tools, it is important to understand the material's behaviour when subjected to impulsive loading. The high strain rates and the elevated temperature associated with impact loading influence both the flow stress and the ductility of the material.

The present material, AA5083, is a high-strength aluminium-magnesium alloy well suited for rolling, and plates are therefore an important product. Even though the alloy has been tested for ballistic protection (see e.g. Børvik et al. [12]), the traditional use of these plates is naval structures such as ship hulls and offshore topsides due to the alloy's excellent corrosion resistance. However, stress corrosion may occur in corrosive media. To avoid this problem, the special temper H116 was developed [13]. The main alloying elements are magnesium with about 4.4 wt.%, manganese with 0.7 wt.% and chromium with 0.15 wt.%. Note that the high amount of magnesium in the alloy leads to dynamic strain aging (DSA) and a potential instability denoted the Portevin-Le Chatelier (PLC) effect. The PLC effect causes serrated or jerky flow in certain ranges of temperature and strain rate, and is associated with repeated propagation of bands of localized plastic strain rate. The occurrence of PLC is linked to a bounded region of negative steady-state strain rate sensitivity of the flow stress. The negative strain rate sensitivity is believed to result from diffusion of solute atoms to dislocations temporarily arrested at obstacles in the slip path [14]-[19].

Clausen et al. [20] carried out an extensive study on aluminium alloy AA5083-H116 in order to find the flow and fracture characteristics as function of strain rate, temperature and stress triaxiality. Some of their findings are given in the following for completeness. The flow stress at 5% plastic strain as a function of the steady state strain rate for AA5083-H116 is shown in Figure 1. It is seen that AA5083-H116 exhibits negative steady-state strain rate sensitivity for intermediate strain rates, which is the cause of the serrated yielding observed for this alloy. The anisotropy in flow stress can also be seen. Note that the study of Clausen et al. [20] was on plates of another thickness than the one considered here, so that a direct comparison of stress levels cannot be made due to different levels of work-hardening in the cold rolling process. Nominal stress-strain curves for the plate material used in the present study are shown in Figure 2. The difference in flow stress between the 3 mm thick plate and the 5 and 10 mm thick plates can clearly be seen along with the PLC effect. Note that these curves were obtained using a conventional extensometer. As a band of localised plastic strain rate passes a section of the test specimen, it leaves behind an increase in plastic strain. After the band has passed, the plastic strain remains constant in that section until the band returns or other bands pass by. However, the nominal strain will continue to increase as long as the band is inside the gauge section of the extensometer. This results in the plateaus seen in Figure 2 and renders this method inadequate when it comes to determine the true stress-strain curve. Therefore, an alternative strain measurement technique has been utilised. This will be described in section 2.1.

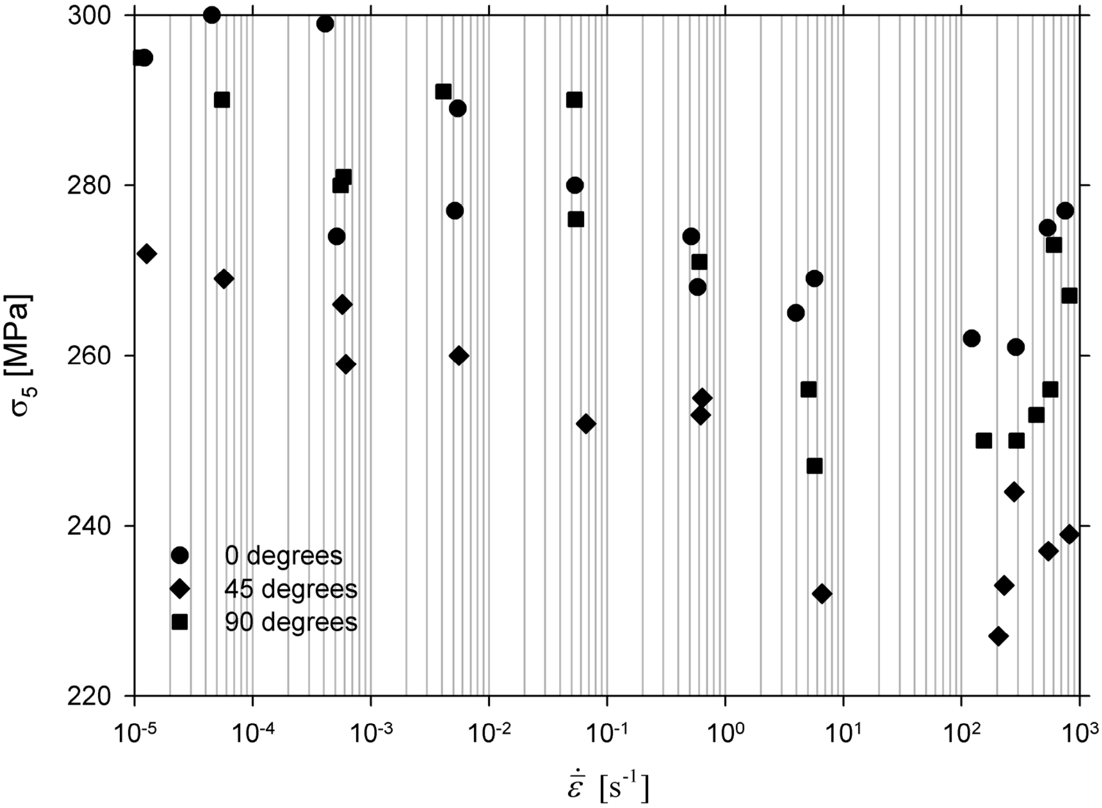

Figure 1 True flow stress at 5% plastic strain at room temperature as function of the steady state plastic strain rate [20].

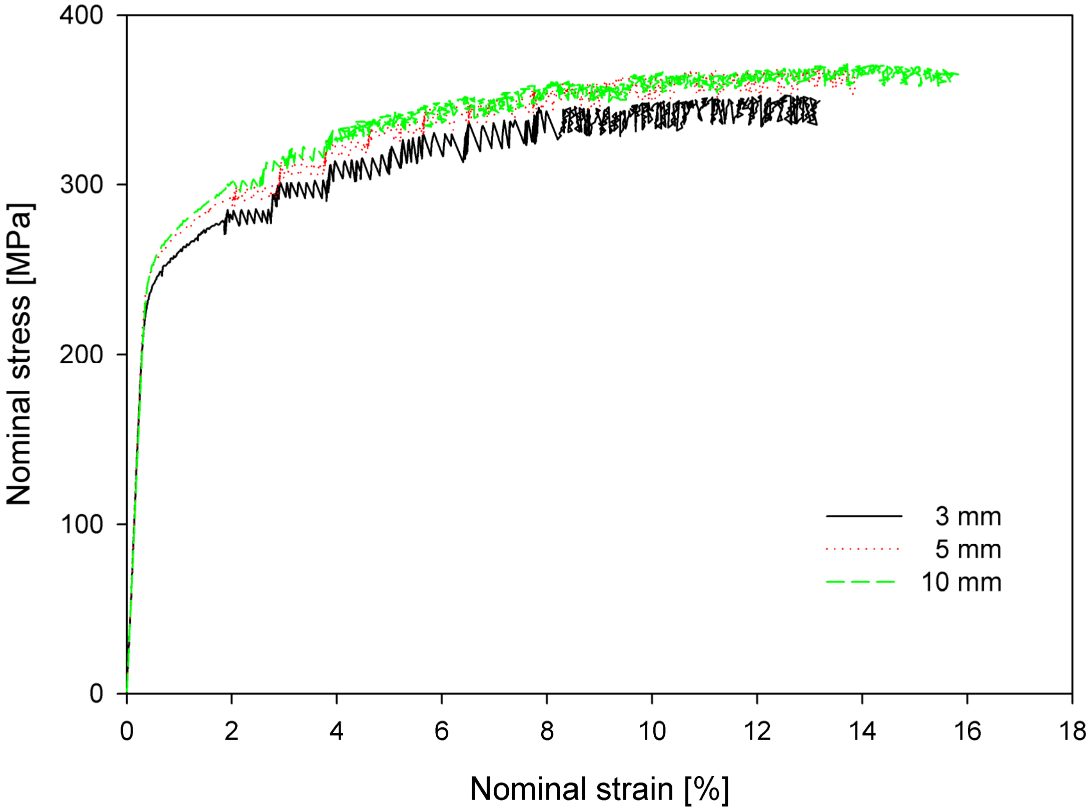

Figure 2 Nominal stress-strain curves for plates of different thickness at room temperature.

Thermal softening takes place at relatively low temperatures in aluminium. Some of the nominal curves obtained at different temperatures by Clausen at al. [20] are shown in Figure 3. It can be seen that a significant softening starts to take place between 100 and 200 °C, and that the ductility is in general increasing with increasing temperature. It was pointed out by Clausen et al. [20] that the seeming decrease in ductility between 20 and 100 °C is an artefact. Another feature worth noting is that the PLC effect ceases to exist when the temperature exceeds approximately 100 °C. Rolled aluminium plates typically have crystallographic texture, i.e. the grains are not randomly oriented but tend towards particular orientations. The texture leads to anisotropy in strength, plastic flow and ductility. This was also investigated by Clausen et al. [20] to some extent.

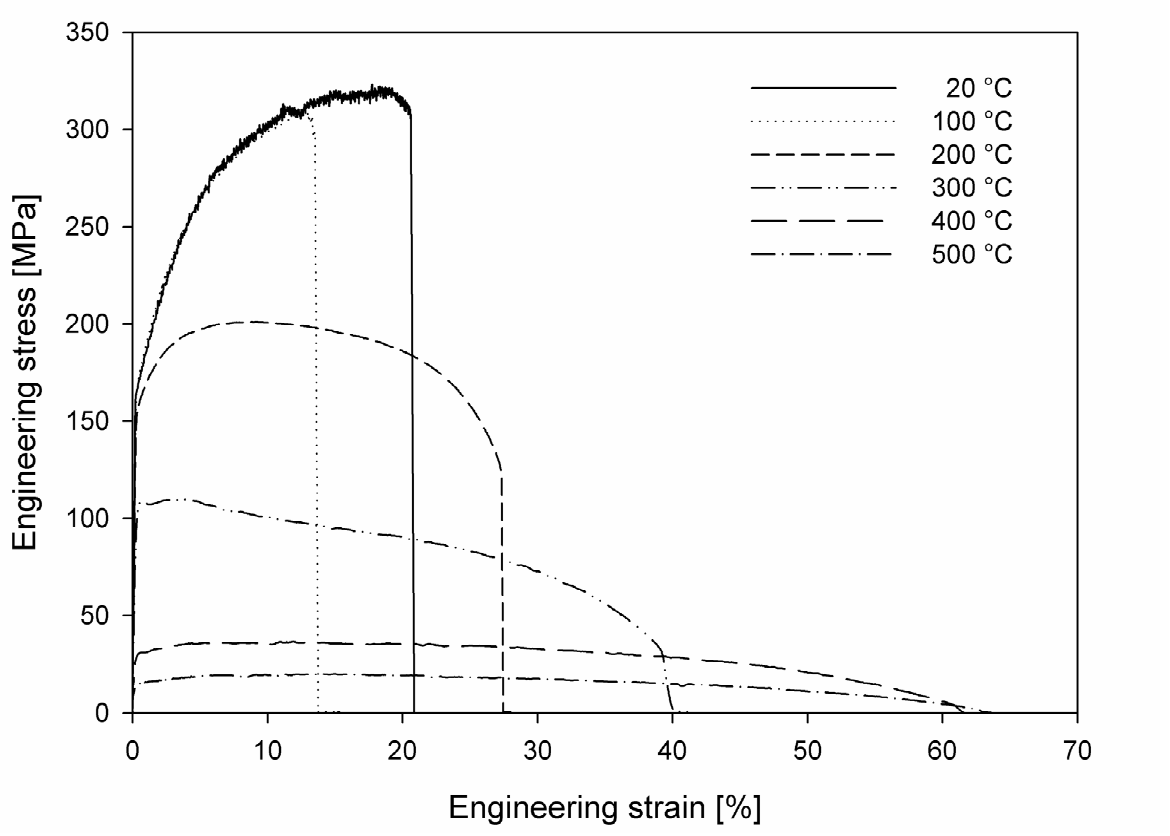

Figure 3 Representative engineering stress-strain curves at different temperatures [20].

The present work aims at investigating the influence of strain rate, thermal softening and anisotropy on low velocity impact on aluminium plates of the alloy AA5083-H116. Section 2.1 deals with material tests carried out on the present material to complement the data of Clausen et al. [20] in the characterisation of the material. These tests were necessary because new plate thicknesses were investigated, and also to investigate the plastic anisotropy in more detail. The low velocity penetration tests are described in Section 2.2. Finite element models of the experiments are presented in Section 3 along with a discussion about their applicability to the low velocity penetration problem. Finally, some concluding remarks are given in Section 4.

2 Experiments

2.1 Material tests

A representative engineering stress-strain curve for each thickness is shown in Figure 2, and some of the nominal values are given in Table 1. As already mentioned, the PLC effect causes the plastic strain in a uniaxial tensile test to be non-homogenous. This renders conventional instrumentation with an extensometer inadequate when it comes to determine the work-hardening curve. Instead, diameter reduction measurements were carried out on round tensile specimens. During testing, the minimum diameter of the specimen was continuously measured in both the in-plane and through thickness direction [21][22]. The apparatus used consists of four inductive displacement gauges mounted in a frame surrounding the specimen. Two of the gauges measured the diameter reduction in the thickness direction of the plate and two of the gauges measured the diameter reduction in the in-plane direction of the plate. This made it easy to calculate the R-ratios defined as

$$R = \frac{\dot{\varepsilon}_w^p}{\dot{\varepsilon}_t^p} \tag{1}$$

where $\left(\dot{\varepsilon}_w^p, \dot{\varepsilon}_t^p\right)$ are the plastic strain rates in the width and thickness directions of the tensile specimen, respectively. Assuming plastic incompressibility, this measurement method also made it possible to determine true strains even after necking. By using

Bridgman's correction [23], work-hardening curves $\kappa = \kappa(\bar{\varepsilon})$ were obtained all the way to fracture. The rolling direction was used as a reference and the curves found from tensile tests in that direction were used to fit all the parameters of the work-hardening model. Representative true stress-equivalent plastic strain curves for the three plate thicknesses used in the present study are shown in Figure 4.

Table 1 Nominal values for the different plate thicknesses

Thickness [mm]	$\sigma_{0.2}$ [MPa]	σ_u [MPa]	ε_u [%]	$\frac{\sigma_u}{\sigma_{0.2}}$
3	249	344	13.1	1.38
5	261	360	14.0	1.38
10	262	360	15.9	1.37

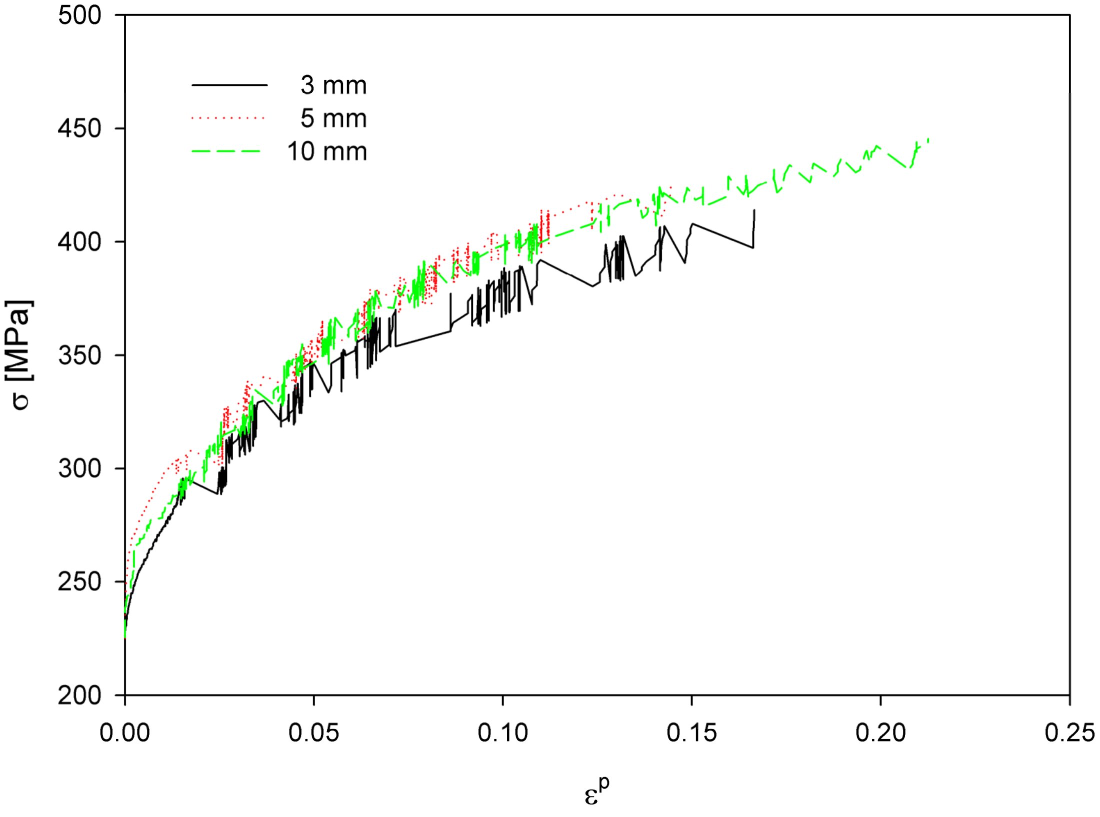

Figure 4 Difference in work-hardening for the three plate thicknesses.

In order to investigate the plastic anisotropy of the present material, quasi-static tensile tests at room temperature were carried out in 7 in-plane directions on specimens from the 10 mm thick plates. The resulting R-ratios and normalised yield stresses are plotted in Figure 5 and Figure 6, respectively. In addition, upsetting tests were carried out to find the flow stress in the thickness direction along with the ratio between the plastic flow in the rolling and transverse directions. Both the initial height and diameter of the cylindrical specimens were 10 mm. Graphite paste was used as lubricant to reduce friction and barrelling. The cylindrical specimen was compressed between two rigid platens of hardened tool steel. An extensometer was connected to the rigid platens to measure the displacement, while the force was measured by the load cell of the testing machine. The nominal strain rate used in the experiments was $1 \cdot 10^{-4}$ s^{-1}.

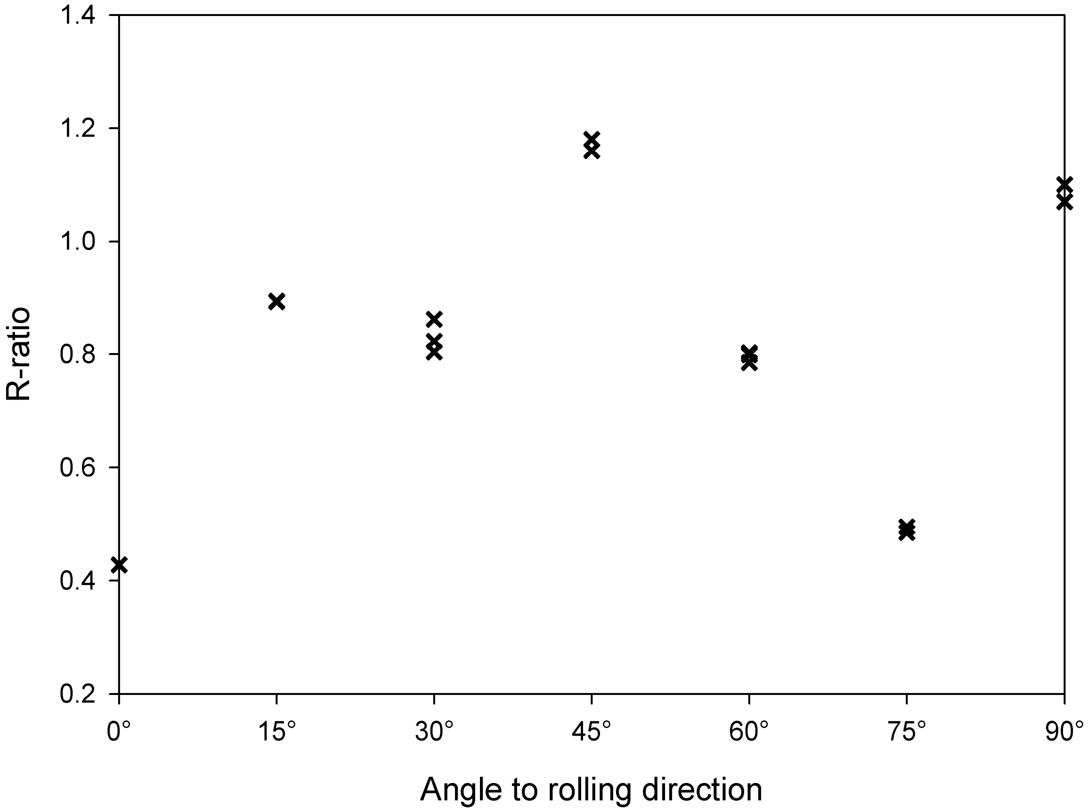

Figure 5 R-ratios for the 10 mm thick plate.

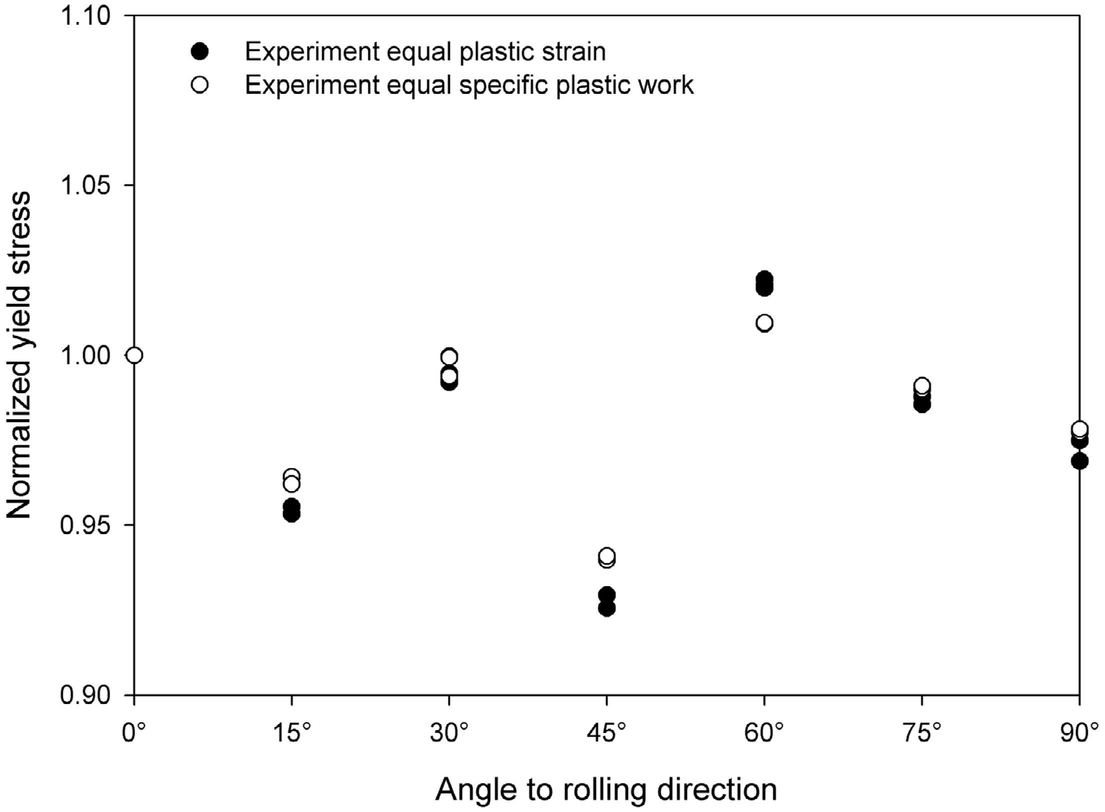

Figure 6 Normalized yield stress as function of the angle to the rolling direction for the 10 mm thick plates.

2.2 Penetration tests

The penetration tests were carried out using a pneumatic accelerator [3], consisting of a pressure chamber which is connected to a vertical accelerator tube (see Figure 7). The projectile, which is designed to act as a piston in the accelerator tube, accelerates down the tube when it is released from the top pressure chamber. By varying the pressure in the pressure chamber, the impact velocity can be varied. Two lasers placed at the muzzle of the tube are used to trigger the timing device. This is illustrated in Figure 8. Knowing the distance between the lasers and the time it takes for the projectile to travel that distance, the velocity can be calculated by assuming that gravity is the only force acting on the projectile during free fall after it has left the acceleration tube. Conservation of energy gives

$$\frac{1}{2}mv_0^2 = \frac{1}{2}m\left(\frac{L_1}{t}+\frac{gt}{2}\right)^2 + mgL_2 \Leftrightarrow v_0 = \sqrt{\left(\frac{L_1}{t}+\frac{gt}{2}\right)^2 + 2gL_2} \tag{2}$$

where v_0 is the impact velocity, m is the mass of the projectile, g is the acceleration due to gravity, t is the elapsed time between the two lasers, L_1 is the distance between the two lasers and L_2 is the distance between the lower laser and the upper surface of the target plate.

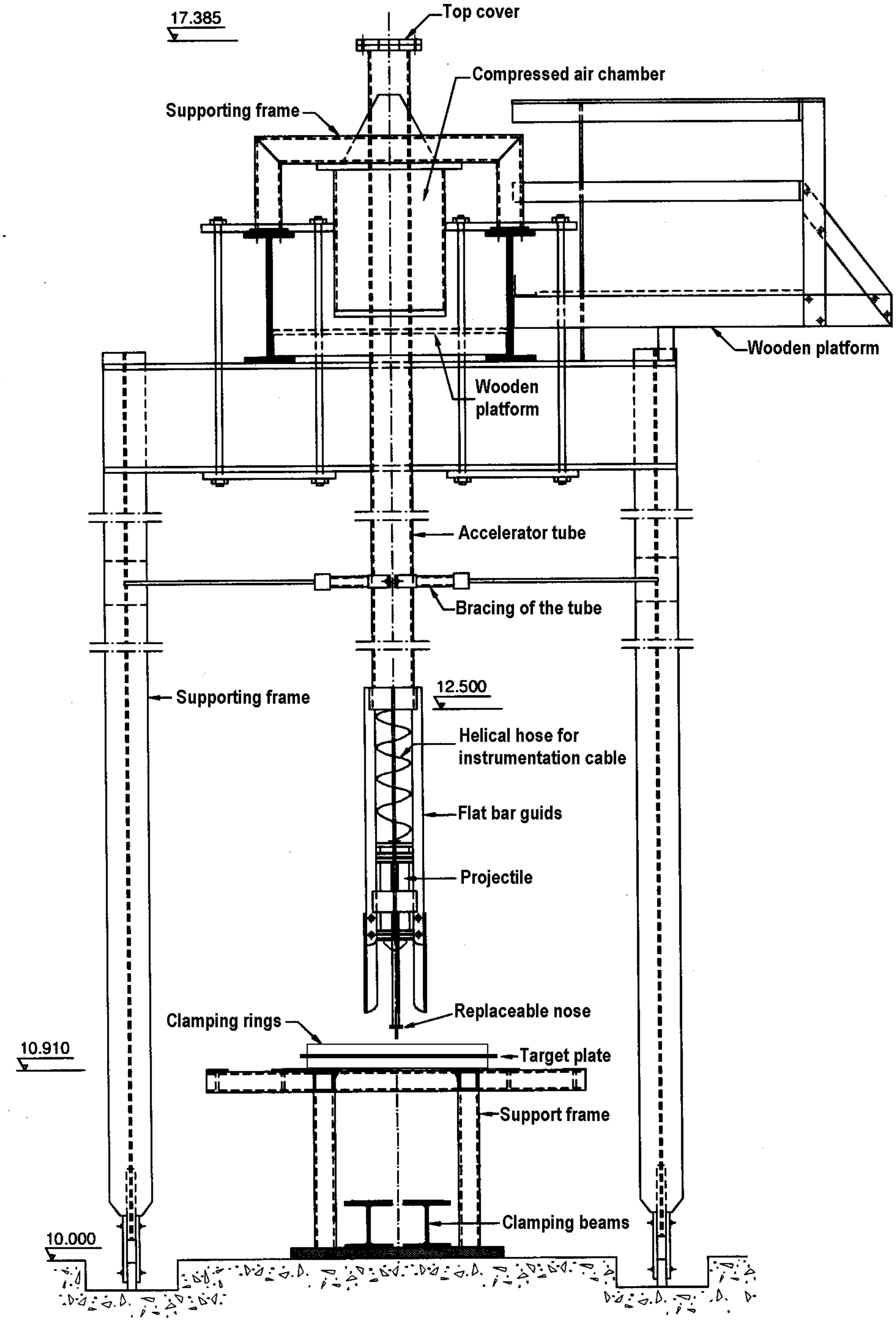

Figure 7 Dynamic test rig [3].

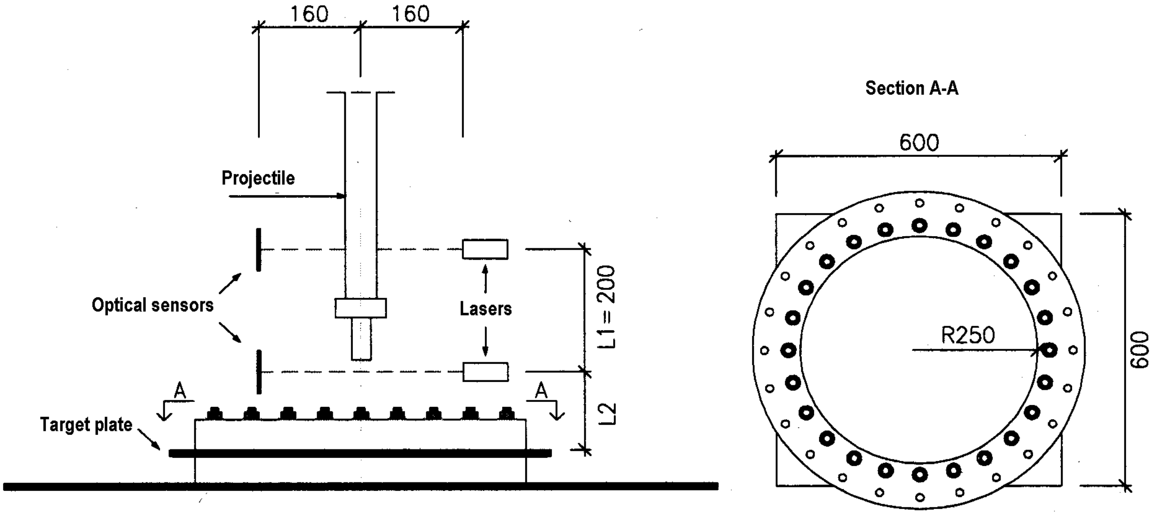

Figure 8 Velocity measurements in the dynamic tests and geometry of the target.

The projectile consists of a central rod, a replaceable nose, an interchangeable mass and guides of aluminium equipped with nylon rings and a gasket rubber ring. Blunt hardened steel noses with diameter 20 mm and 30 mm were used in this study. The mass was kept constant except for the difference in mass of the replaceable noses. The total mass was therefore 18.7 kg and 19.0 kg for all projectiles with nose diameter 20 mm and 30 mm, respectively. Strain gauges were attached to the central rod in order to measure the interface force acting between the projectile and the target plate [3]. The wire was led from these through a helical hose to the top of the pressure chamber.

Square 5083-H116 aluminium plates with dimensions 600x600 mm^2 were carefully cut from larger plates and mounted between two massive circular steel rings with a free-span diameter of 500 mm using 24 pre-stressed M16 bolts. The thickness of the target plate was either 3, 5 or 10 mm. The clamping rings and the target were carefully aligned on a rigid bottom frame to make sure that the projectile would hit in the centre of the plate. Thus, the loading was in principle axisymmetric. Experimental results are summarised in Table 2. The first digit(s) in the test number indicate the thickness of the target plate in mm. The middle digits indicate the diameter of the projectile nose in mm and the last digit(s) indicate the consecutive number of the tests within a given test configuration. Due to technical problems with the velocity measurement system, reliable velocities could not be calculated for all tests. The tests without reliable impact velocities are omitted in Table 2. Both the target thickness and the projectile diameter were varied in the present study, and their effect on the plugging capacity was studied to some extent. The scaled impact energy versus scaled target thickness from experiments is shown in Figure 9. As can be seen, the critical impact energy required to perforate the target plate is an increasing function of the scaled target thickness. When failure occurred, it was by plugging. Then a plug with increased temperature was separated from the plate causing a marked drop in force level. Some representative force-time curves are shown in Figure 10.

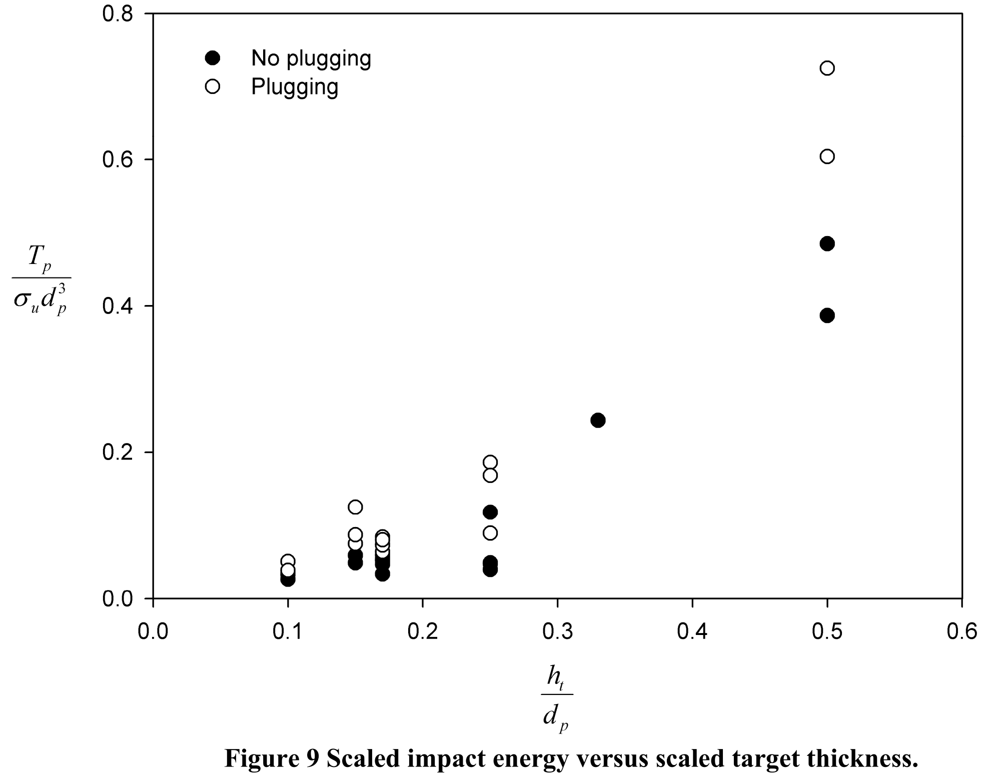

Figure 9 Scaled impact energy versus scaled target thickness.

Table 2 Test results

Test #	Response				Dimensionless scaled values	
	Impact velocity [m/s]	Plugging Yes/No	Impact Energy [J]	Maximum Force [kN]	$\frac{h_t}{d_p}$	$\frac{T_p}{\sigma_u d_p^3}$
3-20-1	4.16	N	161.81	22.58	0.15	0.059
3-20-2	4.70	Y	206.54	27.61	0.15	0.075
3-20-3	6.06	Y	343.37	25.86	0.15	0.125
3-20-4	5.06	Y	239.39	24.99	0.15	0.087
3-20-5	3.78	N	133.60	20.20	0.15	0.049
3-30-1	7.07	Y	474.86	33.79	0.10	0.051
3-30-2	5.16	N	252.94	30.00	0.10	0.027
3-30-3	5.65	N	303.26	32.46	0.10	0.033
3-30-4	6.18	Y	362.83	33.23	0.10	0.039
5-20-4	5.19	Y	255.89	40.27	0.25	0.089
5-20-5	5.99	N	340.86	39.14	0.25	0.118
5-20-6	7.50	Y	534.38	42.12	0.25	0.186
5-20-7	7.14	Y	484.31	42.76	0.25	0.168
5-20-8	3.50	N	114.54	-	0.25	0.040
5-20-9	3.89	N	141.49	29.02	0.25	0.049
5-20-10	3.86	N	139.31	38.64	0.25	0.048
5-30-1	9.28	Y	818.12	54.73	0.17	0.084
5-30-2	7.39	N	518.81	-	0.17	0.053
5-30-3	8.68	Y	715.75	55.55	0.17	0.074
5-30-4	8.09	Y	621.76	53.88	0.17	0.064
5-30-5	8.63	Y	707.53	47.95	0.17	0.073
5-30-6	9.02	Y	772.92	52.22	0.17	0.080
5-30-7	7.74	N	569.12	50.96	0.17	0.059
5-30-8	7.29	N	504.87	47.13	0.17	0.052
5-30-9	5.92	N	332.94	49.09	0.17	0.034
5-30-10	7.85	N	585.41	-	0.17	0.060
5-30-11	6.90	N	452.30	46.15	0.17	0.047
5-30-12	7.76	N	572.07	52.30	0.17	0.059
5-30-13	7.51	N	535.80	50.27	0.17	0.055
10-20-1	10.83	N	1114.24	92.34	0.50	0.387
10-20-2	12.13	N	1397.80	97.34	0.50	0.485
10-20-3	14.83	Y	2089.32	97.76	0.50	0.725
10-20-4	13.53	Y	1739.08	93.06	0.50	0.604
10-30-6	15.79	N	2368.58	135.45	0.33	0.244

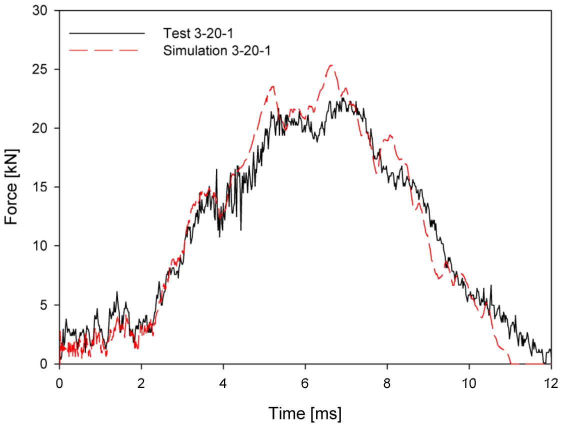
Test 3-20-1
Simulation 3-20-1
Force [kN]
Time [ms]
0
5
10
15
20
25
30
0
2
4
6
8
10
12

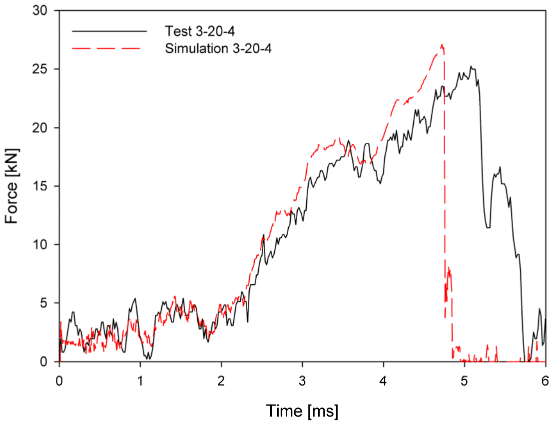
Test 3-20-4
Simulation 3-20-4
Force [kN]
Time [ms]
0
5
10
15
20
25
30
0
1
2
3
4
5
6

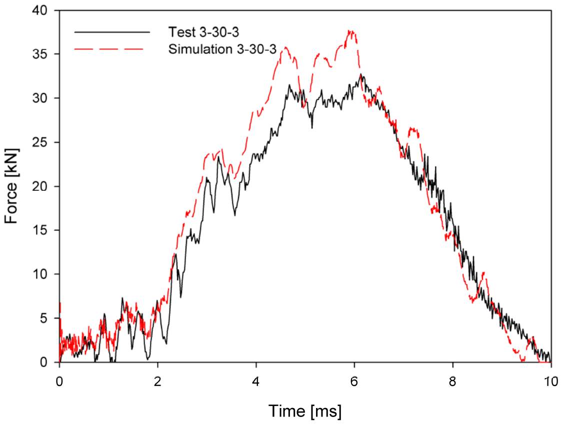
Test 3-30-3
Simulation 3-30-3
Force [kN]
Time [ms]
0
5
10
15
20
25
30
35
40
0
2
4
6
8
10

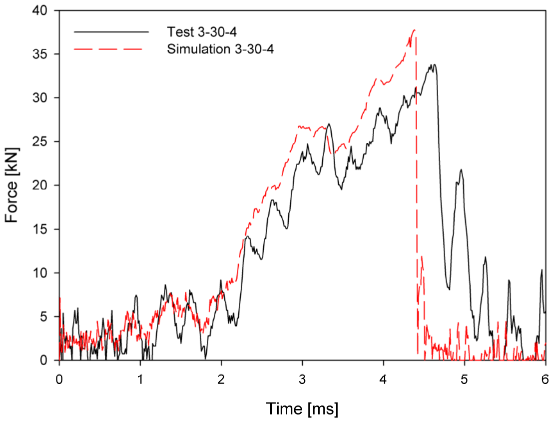
Test 3-30-4
Simulation 3-30-4
Force [kN]
Time [ms]
0
5
10
15
20
25
30
35
40
0
1
2
3
4
5
6

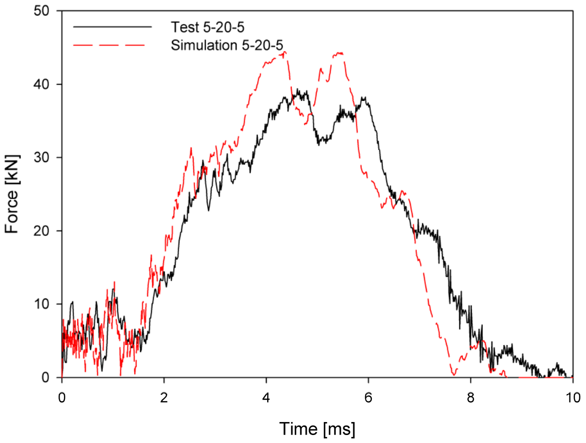
Test 5-20-5
Simulation 5-20-5
Force [kN]
Time [ms]
0
10
20
30
40
50
0
2
4
6
8
10

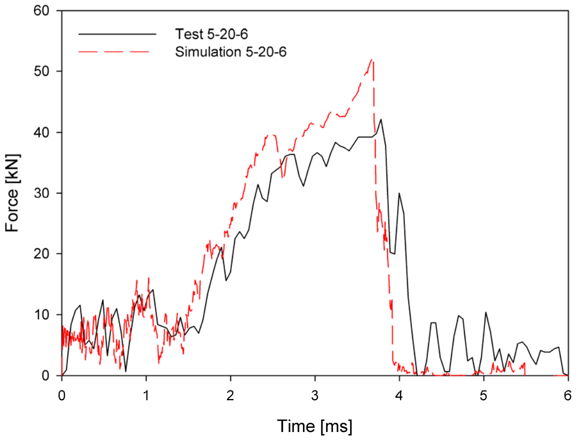
Test 5-20-6
Simulation 5-20-6
Force [kN]
Time [ms]
0
10
20
30
40
50
60
0
1
2
3
4
5
6

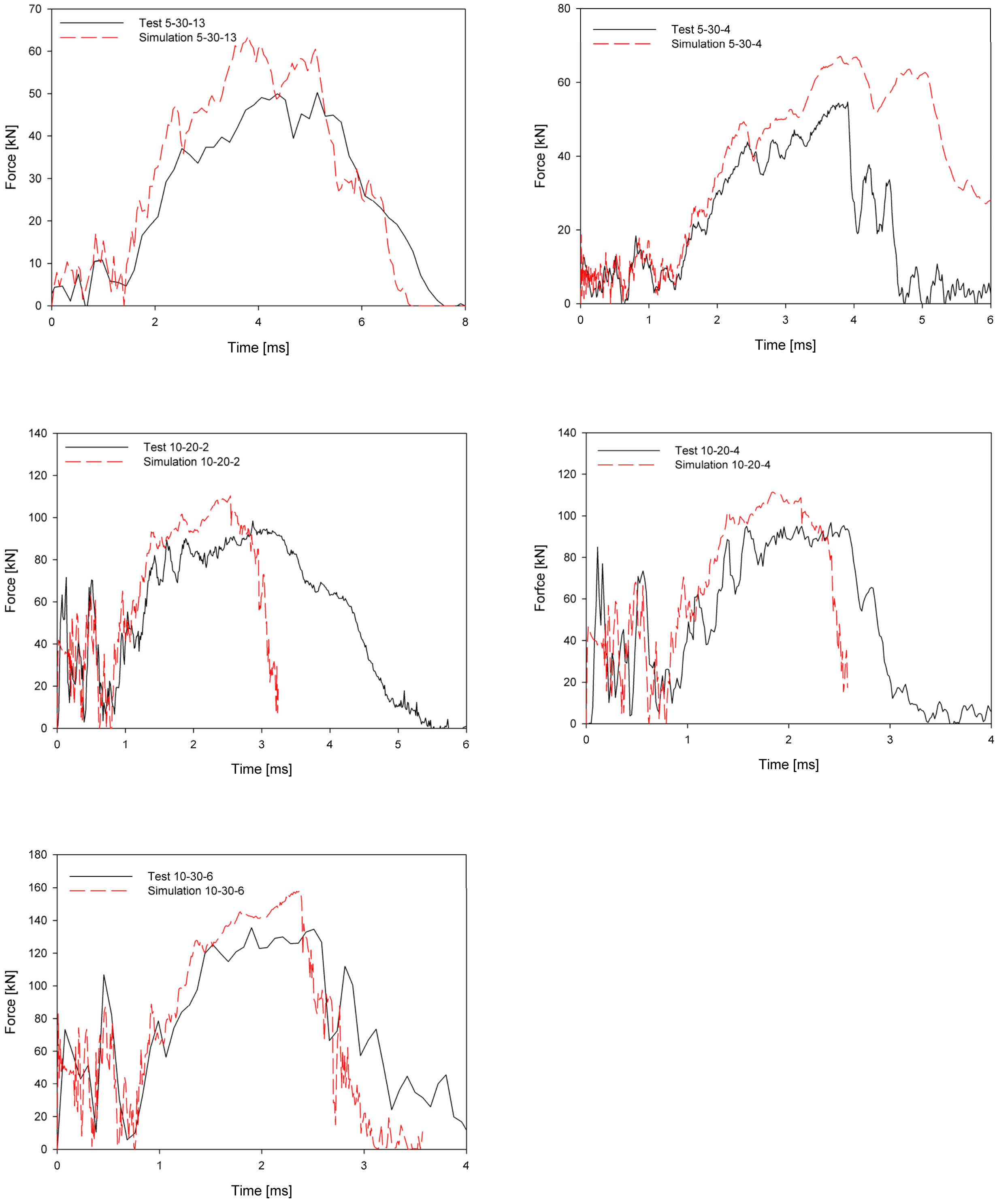

Figure 10 Force versus time curves from tests and simulations assuming axisymmetric plasticity and no temperature or strain rate effects.

3 Finite element simulations

3.1 Constitutive relation and fracture criterion

A hypoelastic-viscoplastic constitutive model based on modified versions [22] of the Johnson-Cook constitutive relation [24] and fracture criterion [25], extended to include the YLD2004-18p yield function proposed by Barlat et al. [26] and a model for dynamic strain aging based on the work of McCormick [16], has been formulated. The model includes isotropic elasticity, anisotropic yielding, associated plastic flow and isotropic strain hardening. It is assumed that the elastic strains are small, while the plastic strains may be finite. A corotational formulation was adopted in order to simplify the formulation of plastic anisotropy. The local coordinate system constructed at each integration point coincides with the material anisotropy axes. It is assumed that the anisotropic axes of the material remain orthogonal during deformations.

The corotational Cauchy stress and corotational rate-of-deformation tensors are defined by [27]

$$\hat{\boldsymbol{\sigma}} = \mathbf{R}^{\mathrm{T}} \cdot \boldsymbol{\sigma} \cdot \mathbf{R}; \quad \hat{\mathbf{D}} = \mathbf{R}^{\mathrm{T}} \cdot \mathbf{D} \cdot \mathbf{R} \tag{3}$$

where $\boldsymbol{\sigma}$ is the Cauchy stress tensor and $\mathbf{D}$ is the rate-of-deformation tensor. The rotation tensor $\mathbf{R}$ is defined from the polar decomposition of the deformation gradient, $\mathbf{F} = \mathbf{R} \cdot \mathbf{U}$, where $\mathbf{U}$ is the right stretch tensor. The corotational rate-of deformation can be decomposed into elastic, plastic and thermal parts

$$\hat{\mathbf{D}} = \hat{\mathbf{D}}^{\mathrm{e}} + \hat{\mathbf{D}}^{\mathrm{p}} + \hat{\mathbf{D}}^{\mathrm{t}} \tag{4}$$

where the corotational thermal rate-of-deformation is defined by

$$\hat{\mathbf{D}}^{\mathrm{t}} = \alpha \dot{T} \mathbf{I} \tag{5}$$

The incremental temperature increase due to adiabatic heating caused by dissipation of plastic work is calculated as

$$\dot{T} = \chi \frac{\bar{\sigma} \cdot \dot{\bar{\varepsilon}}}{\rho C_p} \tag{6}$$

where ρ is the mass density, C_p is the spesiffic heat capacity, $\bar{\sigma}$ is the effective stress, $\dot{\bar{\varepsilon}}$ is the effective plastic strain rate and χ is the Taylor-Quinney coefficient that represents the proportion of plastic work converted into heat. This fraction is usually assumed to be 90-95%. However, tests reported by Kapoor and Nemat-Nasser [28] for several metals suggest that the value is essentially equal to one for large plastic strains.

For a hypoelastic material, the rate of the corotational Cauchy stress can be expressed as a linear function of the elastic corotational rate-of-deformation [27]

$$\frac{D\hat{\boldsymbol{\sigma}}}{Dt} = \hat{\mathbf{C}}_{\mathrm{el}}^{\sigma} : \hat{\mathbf{D}}^{\mathrm{e}} = \hat{\mathbf{C}}_{\mathrm{el}}^{\sigma} : \left(\hat{\mathbf{D}} - \hat{\mathbf{D}}^{\mathrm{p}} - \hat{\mathbf{D}}^{\mathrm{t}} \right) \tag{7}$$

where $\hat{\mathbf{C}}_{\mathrm{el}}^{\sigma}$ is the elastic tangent modulus tensor. Since elastic isotropy is assumed, $\hat{\mathbf{C}}_{\mathrm{el}}^{\sigma}$ is uniquely defined by the bulk modulus K and shear modulus G as

$$\hat{\mathbf{C}}_{\mathrm{el}}^{\sigma} = K\mathbf{I} \otimes \mathbf{I} + 2G\left(\boldsymbol{I} - \frac{1}{3}\mathbf{I} \otimes \mathbf{I}\right) \tag{8}$$

where $\mathbf{I}$ is the second-order unit tensor and $\boldsymbol{I}$ is the fourth-order, symmetric unit tensor.

The yield function is written in the form

$$f\left(\hat{\boldsymbol{\sigma}}, \bar{\varepsilon}, \dot{\bar{\varepsilon}}, T\right) = \bar{\sigma}\left(\hat{\boldsymbol{\sigma}}\right) - \kappa\left(\bar{\varepsilon}, \dot{\bar{\varepsilon}}, T\right) \tag{9}$$

where $\bar{\sigma}$ is the effective stress, κ is the flow stress and $\bar{\varepsilon}$ is the equivalent plastic strain. It is assumed that f is a convex function of $\hat{\boldsymbol{\sigma}}$, and a positive homogeneous function of order one. The generalized associated flow rule is adopted, and the plastic rate-of-deformation and the effective plastic strain rate are defined as [29]

$$\hat{\mathbf{D}}^{\mathrm{p}} = \dot{\lambda}\frac{\partial f}{\partial \hat{\boldsymbol{\sigma}}} = \dot{\bar{\varepsilon}}\frac{\partial f}{\partial \hat{\boldsymbol{\sigma}}}, \quad \dot{\bar{\varepsilon}} = -\dot{\lambda}\frac{\partial f}{\partial \kappa} = \dot{\lambda} \tag{10}$$

where $\dot{\lambda}$ is the plastic parameter. The loading-unloading conditions are stated in Kuhn-Tucker form

$$\dot{\lambda} \geq 0, \;\; f \leq 0, \;\; \dot{\lambda} f = 0 \tag{11}$$

The first of these conditions implies that the plastic parameter is non-negative, while the second implies that the stress must lie on or within the yield surface. The last condition requires the stress to lie on the yield surface during plastic loading.

The yield function Yld2004-18p of Barlat et al. [26] is adopted. The effective stress is defined by

$$\bar{\sigma} = \left(\frac{1}{4} \phi \right)^{\frac{1}{m}} \tag{12}$$

where

$$\begin{aligned} \phi = \phi\left(\tilde{\mathbf{S}}', \tilde{\mathbf{S}}''\right) = & \left|\tilde{S}_1' - \tilde{S}_1''\right|^m + \left|\tilde{S}_1' - \tilde{S}_2''\right|^m + \left|\tilde{S}_1' - \tilde{S}_3''\right|^m + \left|\tilde{S}_2' - \tilde{S}_1''\right|^m \\ & + \left|\tilde{S}_2' - \tilde{S}_2''\right|^m + \left|\tilde{S}_2' - \tilde{S}_3''\right|^m + \left|\tilde{S}_3' - \tilde{S}_1''\right|^m + \left|\tilde{S}_3' - \tilde{S}_2''\right|^m + \left|\tilde{S}_3' - \tilde{S}_3''\right|^m \end{aligned} \tag{13}$$

In Equation (13), $\tilde{\mathbf{S}}'$ and $\tilde{\mathbf{S}}''$ are collections of the principal values $\tilde{S}_i'$ and $\tilde{S}_j''$ of the tensors $\tilde{\mathbf{s}}'$ and $\tilde{\mathbf{s}}''$, defined by two linear transformations of the deviator of the corotational Cauchy stress

$$\tilde{\mathbf{s}}' = \mathbf{C}' : \hat{\mathbf{s}} = \mathbf{C}' : \mathbf{T} : \hat{\boldsymbol{\sigma}}, \quad \tilde{\mathbf{s}}'' = \mathbf{C}'' : \hat{\mathbf{s}} = \mathbf{C}'' : \mathbf{T} : \hat{\boldsymbol{\sigma}} \tag{14}$$

where $\hat{\mathbf{s}} = \mathbf{T} : \hat{\boldsymbol{\sigma}}$ is the deviator of the corotational Cauchy stress. The fourth-order tensors $\mathbf{C}'$ and $\mathbf{C}''$ contain the anisotropy constants, and in Voigt notation (see e.g. Belytschko et al. [27]) they read

$$\mathbf{C}' = \begin{bmatrix} 0 & -c'_{12} & -c'_{13} & 0 & 0 & 0 \\ -c'_{21} & 0 & -c'_{23} & 0 & 0 & 0 \\ -c'_{31} & -c'_{32} & 0 & 0 & 0 & 0 \\ 0 & 0 & 0 & c'_{44} & 0 & 0 \\ 0 & 0 & 0 & 0 & c'_{55} & 0 \\ 0 & 0 & 0 & 0 & 0 & c'_{66} \end{bmatrix}, \quad \mathbf{C}'' = \begin{bmatrix} 0 & -c''_{12} & -c''_{13} & 0 & 0 & 0 \\ -c''_{21} & 0 & -c''_{23} & 0 & 0 & 0 \\ -c''_{31} & -c''_{32} & 0 & 0 & 0 & 0 \\ 0 & 0 & 0 & c''_{44} & 0 & 0 \\ 0 & 0 & 0 & 0 & c''_{55} & 0 \\ 0 & 0 & 0 & 0 & 0 & c''_{66} \end{bmatrix}$$

The fourth-order tensor $\mathbf{T}$ transforms the stress tensor to its deviator, and in Voigt notation it becomes

$$\mathbf{T} = \frac{1}{3}\begin{bmatrix} 2 & -1 & -1 & 0 & 0 & 0 \\ -1 & 2 & -1 & 0 & 0 & 0 \\ -1 & -1 & 2 & 0 & 0 & 0 \\ 0 & 0 & 0 & 3 & 0 & 0 \\ 0 & 0 & 0 & 0 & 3 & 0 \\ 0 & 0 & 0 & 0 & 0 & 3 \end{bmatrix} \tag{15}$$

Assuming isotropic hardening, the two-term Voce hardening rule was adopted to define the evolution of the flow stress. Viscoplasticity is introduced through the modified [22] J-C strain-rate factor [24], while a model based on the work of McCormick [16] is used to describe dynamic strain aging. The standard J-C thermal softening factor [24] is used. The total expression for the flow stress reads

$$\kappa\left(\bar{\varepsilon},\dot{\bar{\varepsilon}},T\right) = \left[\left[\sigma_0 + \sum_{i=1}^{2} Q_i\left(1-\exp\left(-C_i\bar{\varepsilon}\right)\right)\right]\left(1+\frac{\dot{\bar{\varepsilon}}}{\dot{\varepsilon}_0}\right)^c + \sigma_{DSA}\right]\left[1-\left(\frac{T-T_r}{T_m-T_r}\right)^m\right] \tag{16}$$

where σ_0, Q_i, C_i $\dot{\varepsilon}_0$, c and m are material parameters, T_r is the room temperature (or initial temperature) and T_m is the melting temperature. The strengthening effect of dynamic strain aging, σ_{DSA}, is given by

$$\sigma_{DSA} = SH\left(1-\exp\left(-\left(\frac{t_a}{t_d}\right)^{\alpha}\right)\right) \tag{17}$$

where the average waiting time t_a is defined by the evolution equation $\dot{t}_a = 1-\frac{t_a\dot{\bar{\varepsilon}}}{\Omega}$, $\Omega = \omega_1 + \omega_2\bar{\varepsilon}^{\beta}$ and SH, t_d, α, ω_1, ω_2 and β are material constants. Note that the strain rate and thermal effects are uncoupled in the constitutive model, while in reality there is a strong link between the two. The combined effect of strain rate and temperature will therefore not be investigated in the present study.

The Johnson-Cook fracture model [25] accounts for strain path, strain rate, temperature and stress triaxiality. The fracture criterion is based on damage evolution, where the damage variable *D* of a material element is expressed as

$$D = \int_0^{\bar{\varepsilon}} \frac{d\bar{\varepsilon}}{\varepsilon_f} \leq 1 \tag{18}$$

where ε_f is the fracture strain for the given stress, strain rate and temperature state. Failure occurs when *D* = 1 and then the element is eroded. The equivalent strain at fracture is constructed in a similar way as the constitutive relation. A slightly modified version [22] of the original Johnson-Cook failure strain model [25] reads

$$\varepsilon_f = \left(D_1 + D_2 \exp\left(D_3 \sigma^*\right)\right)\left(1+\dot{\bar{\varepsilon}}^*\right)^{D_4}\left(1+D_5 T^*\right) \tag{19}$$

where D_1, …, D_5 are material constants, and σ^* is the stress triaxiality ratio defined as $\sigma^* = \sigma_m / \bar{\sigma}$, where σ_m is the mean stress. The various phenomena accounted for in the fracture criterion are uncoupled from each other as in the constitutive relation. No coupling between the constitutive relation and the damage model was chosen in the present study.

The described material model was implemented in the commercial non-linear finite element code LS-DYNA [30] by means of a user-defined material subroutine. A fully implicit elastic predictor-plastic corrector method was used.

3.2 Parameter identification

The material model described above contains several material parameters that have to be determined. Work-hardening and anisotropy parameters have been identified based on material tests carried out in the present study. No material tests at elevated strain rates or temperatures were carried out in this study, and strain rate data from Clausen et al. [20] was used to determine the parameters of the dynamic strain aging model. It is believed that the strain rate behaviour observed by Clausen et al. [20] is representative also for the present material. The same is the case for the thermal properties and data from Clausen et al. [20] was used to determine the parameters governing temperature effects. Their data was also used to determine the parameters of the modified Johnson-Cook fracture criterion. Representative values for aluminium found in the literature have been chosen for the mass density, Young's modulus, Poisson's ratio, specific heat, thermal conductivity and the thermal expansion coefficient.

Tensile tests were performed at room temperature as described in section 2.1 with a strain rate of 10^{-4} s^{-1} in order to determine the work-hardening parameters. As seen in Figure 4, the properties of the 3 mm thick plate differed from those of the 5 and 10 mm thick plates. The strengthening effect of the dynamic strain aging had to be subtracted from the yield stress. Work-hardening parameters are listed in Table 3 and anisotropy constants in Table 4.

Table 3 Work-hardening parameters for aluminium alloy AA5083-H116

Plate thickness	σ_0	Q_1	C_1	Q_2	C_2
3 mm	192.2	386.5	1.791	78.22	58.87
5 & 10 mm	175.4	326.8	2.296	102.6	83.03

Table 4 Anisotropy constants for aluminium alloy AA5083-H116

c'_{12}	c'_{13}	c'_{21}	c'_{23}	c'_{31}	c'_{32}	c'_{44}	c'_{55}	c'_{66}
-0.440	1.688	1.645	2.526	0.480	-2.000	1.000	1.000	0.974
c''_{12}	c''_{13}	c''_{21}	c''_{23}	c''_{31}	c''_{32}	c''_{44}	c''_{55}	c''_{66}
-1.126	1.631	0.611	1.130	0.123	-0.491	1.000	1.000	1.069
m								
8.000								

Strain rate data from Clausen et al. [20] was used to determine the parameters of the dynamic strain aging model. The parameters SH, α and Ω/t_d can be determined from constant strain rate tests at different strain rates. Then Ω and t_d can be determined from the transient phase of a jump test. Based on Mesarovic [17] the parameter Ω was set equal to 0.0001 (ω_1=0.0001, ω_2=0.0 and β=1.0). The constants governing the viscous stress can be determined from the instantaneous stress change in jump tests or from constant strain rate test at greater strain rates. The latter approach was chosen in this study. All the fitted strain rate parameters are listed in Table 5 and the flow stress at 5 % plastic strain as function of the strain rate as predicted by the model is shown in Figure 11. Due to differences in deformation history, a direct comparison to the curves of Clausen et al. [20] can not be made.

Table 5 Some material parameters for aluminium alloy AA5083-H116

ρ [kg/m^3]	E [MPa]	ν	$\dot{\varepsilon}_0$ [s^{-1}]	c	
$2.66\cdot10^3$	70000	0.33	200	0.09	
SH [MPa]	ω_1	ω_2	β	t_d	α
50	10^{-4}	0.0	1.0	0.04	0.3
χ	C_p [J/(kg K)]	k [W/(m K)]	α [K^{-1}]	T_r/T_0 [K]	T_m [K]
0.95	904	117	$2.6\cdot10^{-5}$	293	862

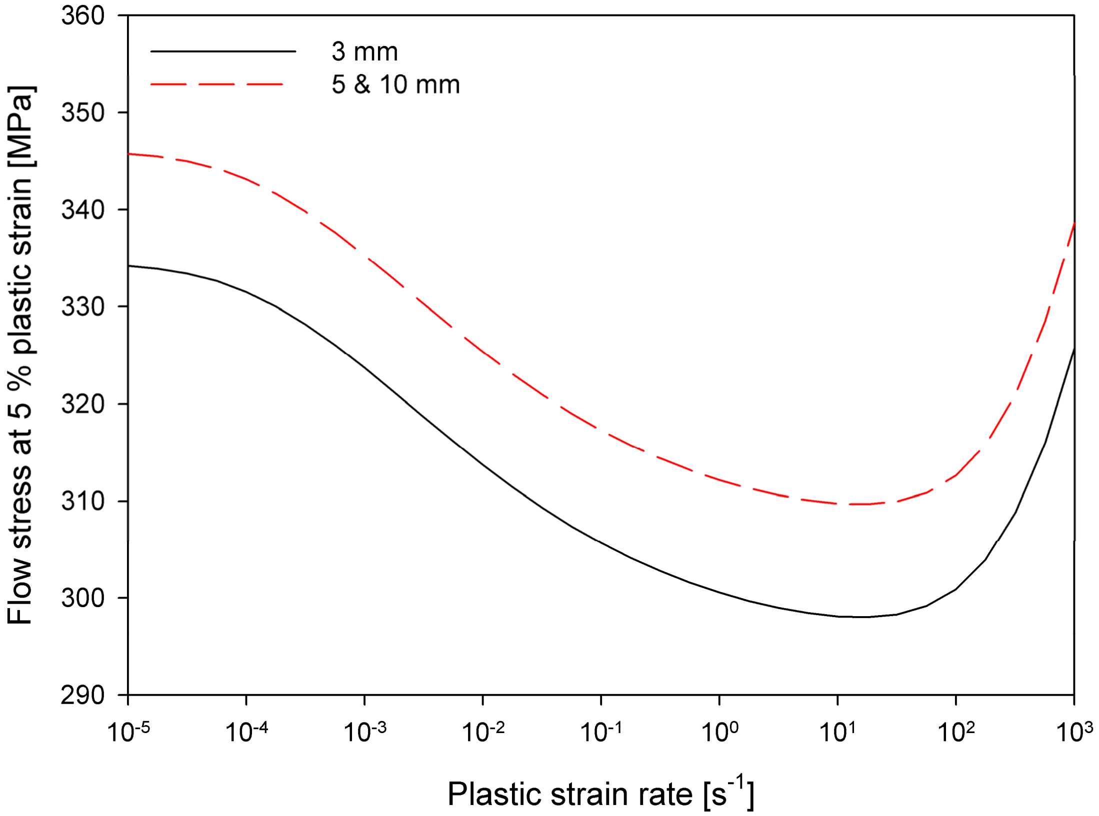

Figure 11 DSA model.

The fracture parameters D_1, D_2 and D_3 were found by a fit to the data obtained by Clausen et al. [20] from tensile tests on smooth and notched specimens. Only fracture strains calculated from cross sectional areas measured in the microscope were used in the fitting, since those were regarded as the most accurate. However, all material tests of Clausen et al. [20] were for positive stress triaxialities. Thus, an extrapolation into the region of negative stress triaxialities is required. This procedure may lead to substantial errors, since no experimental data is available to guide the extrapolation when $\sigma^* < 1/3$. Bao and Wierzbicki [31] claimed, based on upsetting tests, that fracture could never occur for stress triaxialities below $-1/3$. The failure strain at $\sigma^* = -1/3$ was therefore set equal to 1. This additional constraint to the curve fitting prevents premature fracture in the compressive parts of the structure while not influencing the failure strain at positive triaxialities too much. The fracture data and the model predictions are shown in Figure 12.

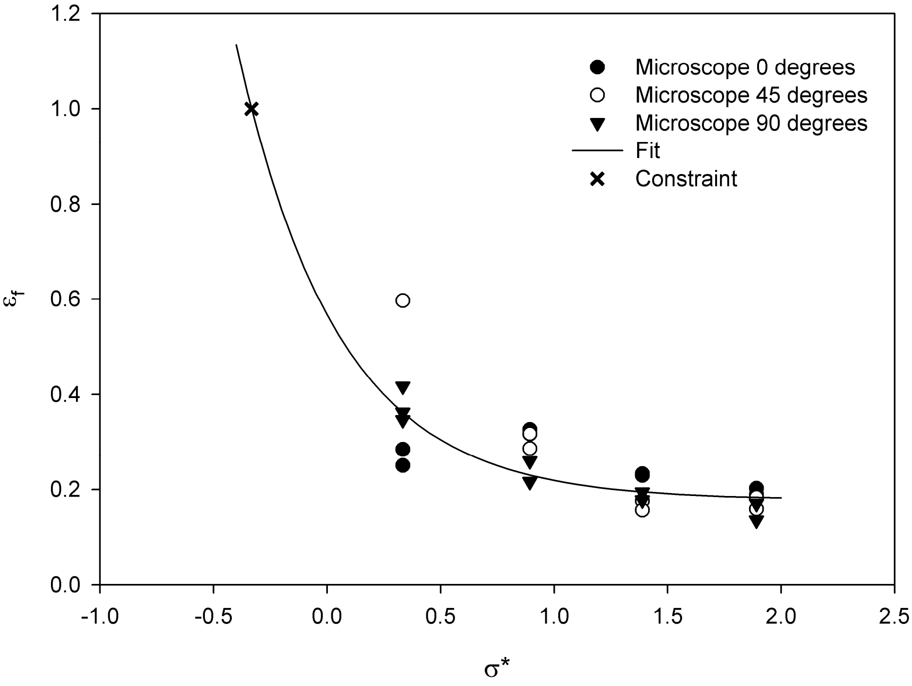

Figure 12 Fracture strain as function of stress triaxiality.

The fracture parameter D_4 was also fitted using the data of Clausen et al. [20]. Their data was normalised with respect to the fracture strain at the lowest strain rate, making it possible to determine the strain rate factor of the fracture criterion directly. A plot of the normalized data and the fitted curve is shown Figure 13. Finally, the thermal parameters m and D_5 of Clausen et al. [20] were adopted in the present study. All the fracture parameters are given in Table 6.

Table 6 Fracture parameters for aluminium alloy AA5083-H116

D_1	D_2	D_3	D_4	D_5
0.178	0.389	-2.25	0.147	16.8

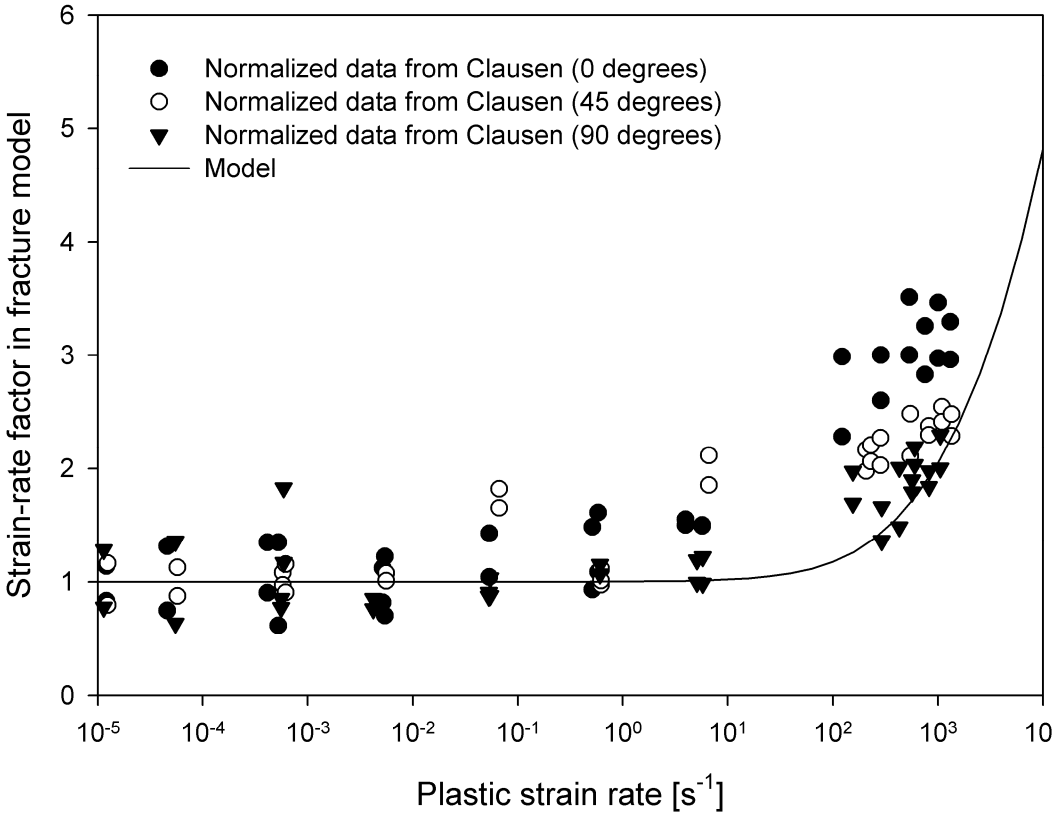

Figure 13 Normalized fracture strains from Clausen et al. [20] compared to the strain rate factor used in the model.

3.3 Finite element models and results

Axisymmetric finite element models were applied in all simulations where isotropic plasticity was assumed. One quadrant of the plate was modelled with brick elements in the simulations where orthotropic plasticity was applied. When modelling the plate with axisymmetric elements, a characteristic element size of $1/18$ mm was chosen in the local region of the plate (defined as 1.2 times the diameter of the projectile). The element size was increased to nine times that in the global part of the plate, giving an element size of 0.5mm. Under-integrated axisymmetric elements with one integration point and Flanagan-Belytschko stiffness-based hourglass control with exact volume integration were used. Note that the Jaumann rate of the Cauchy stress was used instead of a corotational formulation in the axisymmetric models. When using 8 node constant-stress brick elements, the characteristic element size in the local region was increased to 0.25 mm in order to keep the computational time reasonable. The mesh was gradually coarsened towards the boundary.

As a first approach, some of the penetration tests were simulated without any strain rate or temperature effects using the von Mises yield criterion and axisymmetric elements (i.e. assuming isotropic plasticity). The resulting force versus time curves are compared to experimental data in Figure 10. In general, good agreement between experimental results and finite element predictions was observed. However, all finite element models seem to be a bit too stiff, especially after some plastic deformation. In addition, plugging occurred in test 5-30-4, but not in the corresponding simulation, while the opposite was the case for test 10-20-2.

One possible reason for the overestimation of the stiffness is that the negative strain rate sensitivity was neglected in these simulations. The strain rates observed in large parts of the FE models were in the range where a reduced flow stress is expected. In order to test the effect of including dynamic strain aging in the model, tests 3-20-1 and 5-30-4 were simulated with strain rate effects in the constitutive equation but not in the fracture criterion. The resulting force versus time curves are shown in Figure 14. It can be seen that the discrepancy in force level is reduced when dynamic strain aging is included in the constitutive equation. It is therefore likely that dynamic strain aging is one of the main reasons for stiff response in the initial simulations. However, premature fracture was observed in both simulations. This shows that the penetration problem is sensitive to strain rate effects in the material. Since the ductility is known to increase with increasing strain rate, simulations where the strain rate effect was included also in the fracture criterion were run next. The resulting force versus time curves for these simulations are also shown in Figure 14. Now fracture was not observed in any of the two simulations. Again, this shows the problem's sensitivity to strain rate effects.

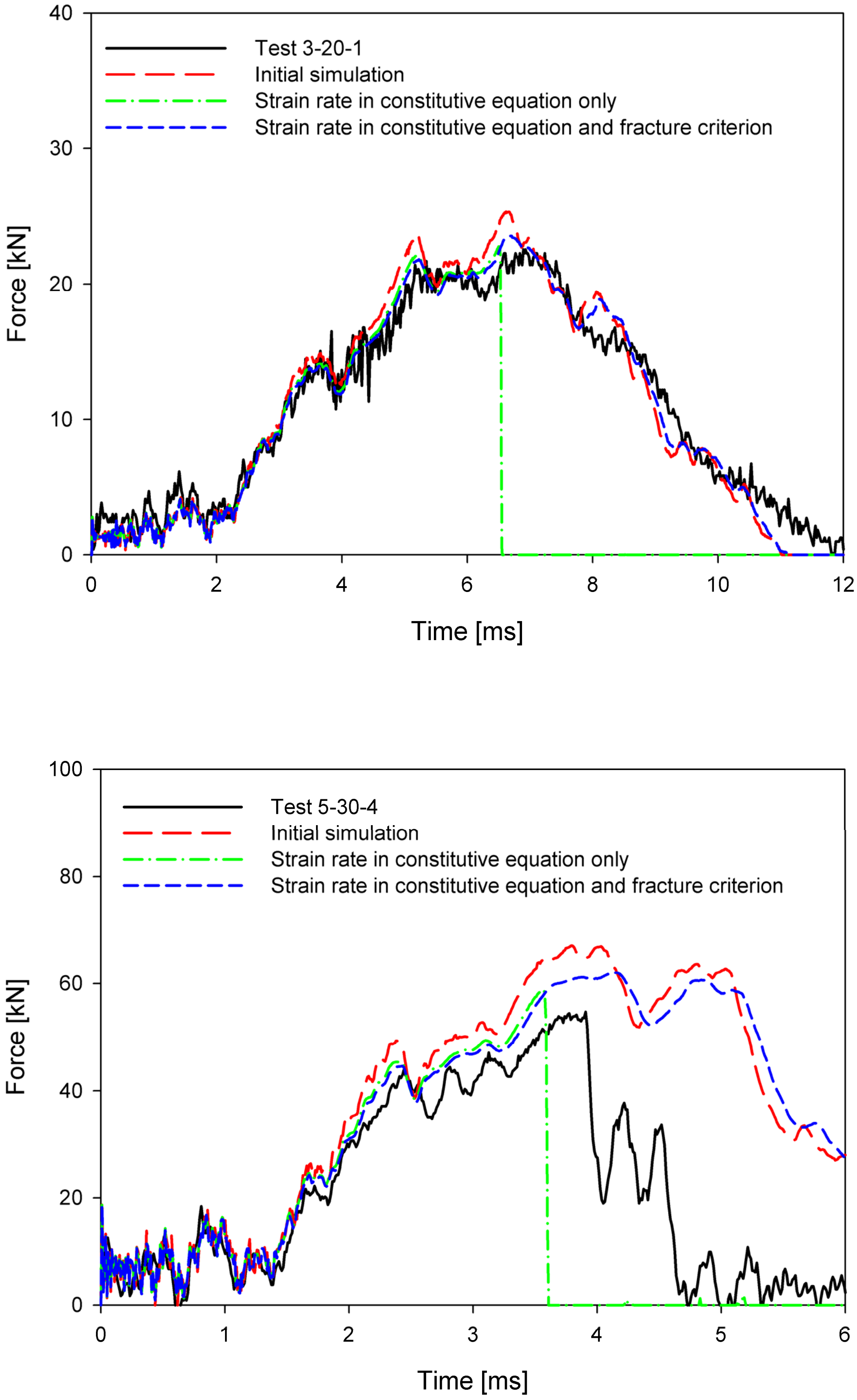

Figure 14 The effect of including strain rate in the constitutive equation and fracture criterion.

In impact problems at greater velocities, thermal effects are regarded as equally important as strain rate effects. At such impact velocities the duration of the impact is so short that the perforation process can be treated as adiabatic. However, in low velocity impacts the process is much slower and can not be treated as adiabatic. Instead, it is usually regarded as isothermal. Both approaches are approximations valid only in a certain range of impact velocities. Ideally, a fully coupled thermo-mechanical analysis should be made. In order to determine the maximum thermal effect on low velocity impacts, adiabatic finite element simulations were run in this study. The resulting force versus time curves are shown in Figure 15. As can be seen, thermal softening had virtually no influence on the force level, but a great impact on fracture predictions. Only a small part of the plate near the rim of the projectile undergoes large plastic deformations, while large parts of the plate undergo small or modest plastic deformations. The plastic work is therefore too small to cause significant heating in most of the plate. Hence, the force level is unaffected by adiabatic heating. Fracture, however, takes place after significant plastic strain and is therefore more sensitive to heating effects. From Figure 16 it can be seen that elevated temperatures only occur in the vicinity of the eroded elements in the adiabatic simulation of case 3-20-1. Here the maximum temperature is approximately 230 °C which leads to significant softening and increased strain localization. In the rest of the plate the temperature is close to the initial temperature.

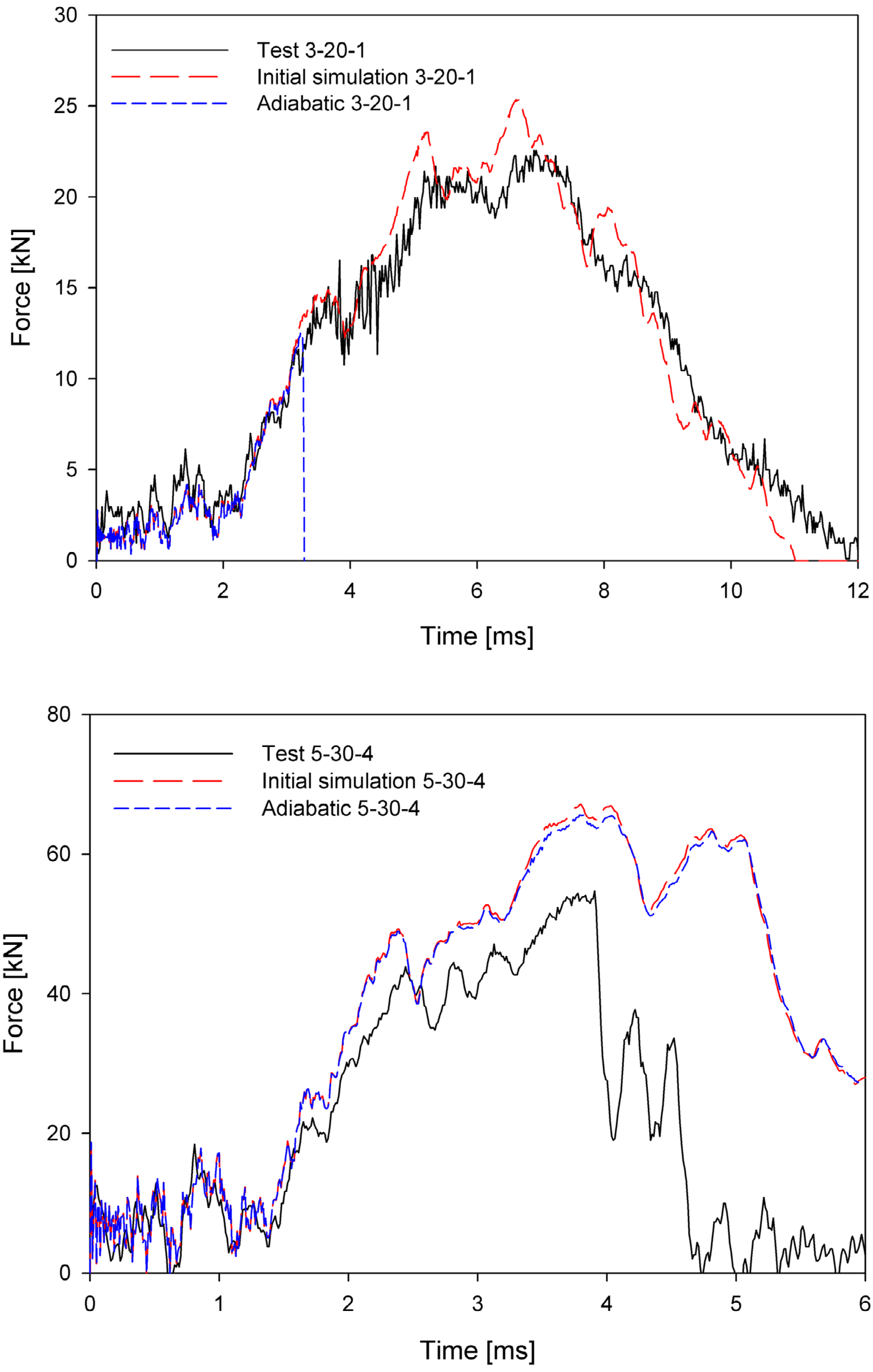

Figure 15 Adiabatic simulations.

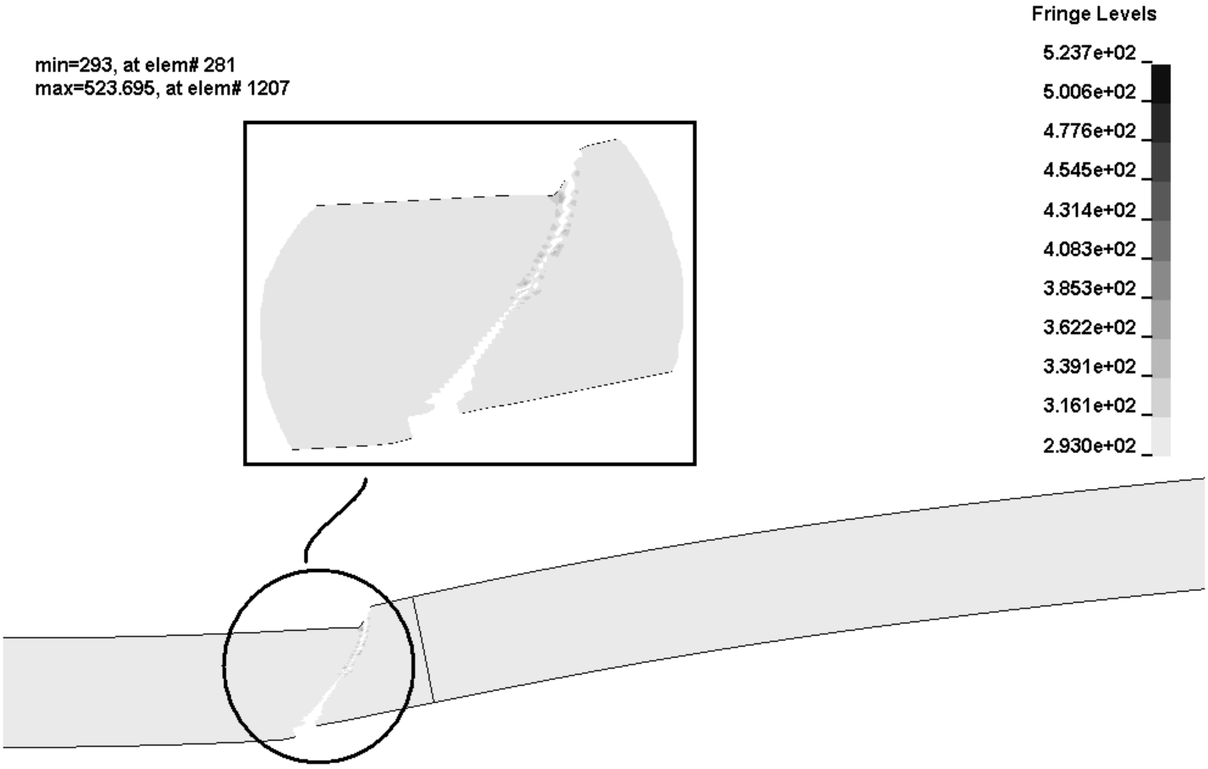

Figure 16 Temperature predicted by the adiabatic model of 3-20-1.

Since the material surrounding the localized zone undergoes much smaller plastic deformations, there may be a strong temperature gradient. The duration of low velocity impacts may also allow some temperature dispersion. Therefore, a fully coupled thermo-mechanical simulation was run for the case 3-20-1 and the resulting force versus time curve is compared to the corresponding adiabatic prediction in Figure 17. Note that fracture occurred also in this simulation, but at a much more realistic time than in the adiabatic simulation. Since no fracture was observed in the initial simulation, this shows that heating does influence fracture prediction even when heat dispersion is taken into account. Figure 18 shows the temperature field just before plugging. The maximum temperature observed just after plugging was 305 K (12 °C above initial temperature). Note that the temperature in the deleted elements may have been significantly higher.

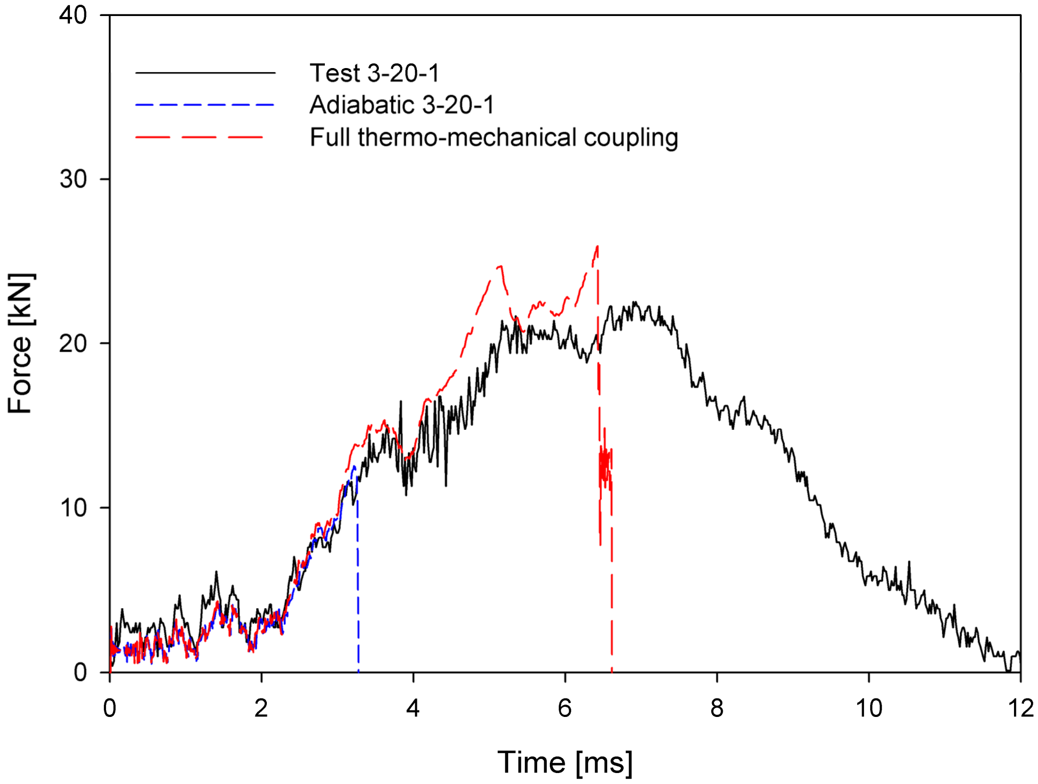

Figure 17 Results from fully coupled thermo-mechanical simulation compared to adiabatic predictions.

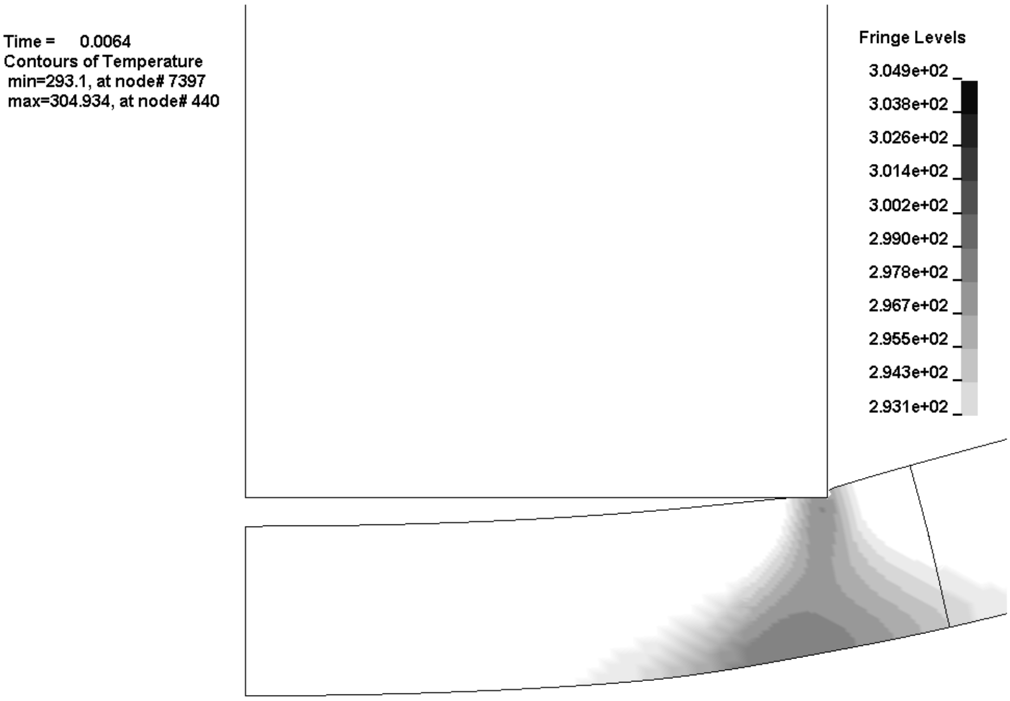

Figure 18 Temperature field predicted by coupled model.

Brick element models had to be made in order to test the effect of anisotropy on the perforation problem. Since the results of a brick element model cannot readily be compared to those of an axisymmetric model, a brick element simulation was first run with the same material input as in the initial simulations to serve as a reference for later comparison to the anisotropic models. Figure 19 shows the brick element model of one quadrant of the plate used in the simulations. The mesh becomes coarser towards the boundary of the plate, but in order to avoid tile shaped elements and shear locking, the mesh had to be refined in the outer half of the plate as shown in Figure 20. Force versus time curves from the brick element simulations are shown in Figure 21. As can be seen, the difference between the brick element models and the axisymmetric model is greater than the difference between the isotropic and the anisotropic brick models. Figure 22 shows deformation profiles in three directions at different stages of the impact. No significant differences between the directions were observed. This is in some contrast to the observations made by Grytten et al. [32] during quasi-static perforation of the same plate material. At least for the present aluminium alloy, the anisotropy does not seem to influence the response of the plates. In order to study the effect of anisotropy on plugging, only the inner quarter of one quadrant of the plate was modelled using an element size of 0.125 mm. When using half the element size in a 3D model the number of elements becomes 8 times as large while the stable time step is reduced to the half, causing the runtime to be approximately 16 times as long as the original. It is therefore not possible to apply a significantly denser mesh today. Using the described mesh, no difference in plugging prediction was observed between the isotropic and the anisotropic models.

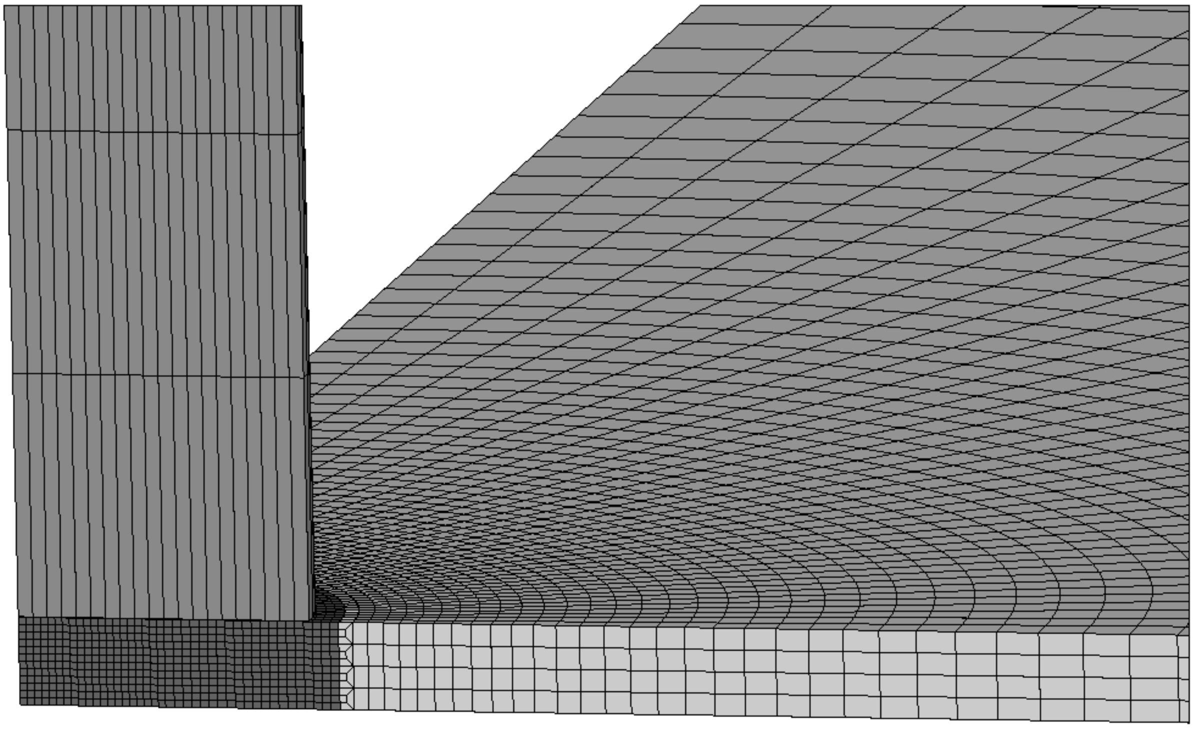

Figure 19 Brick element model of one quadrant.

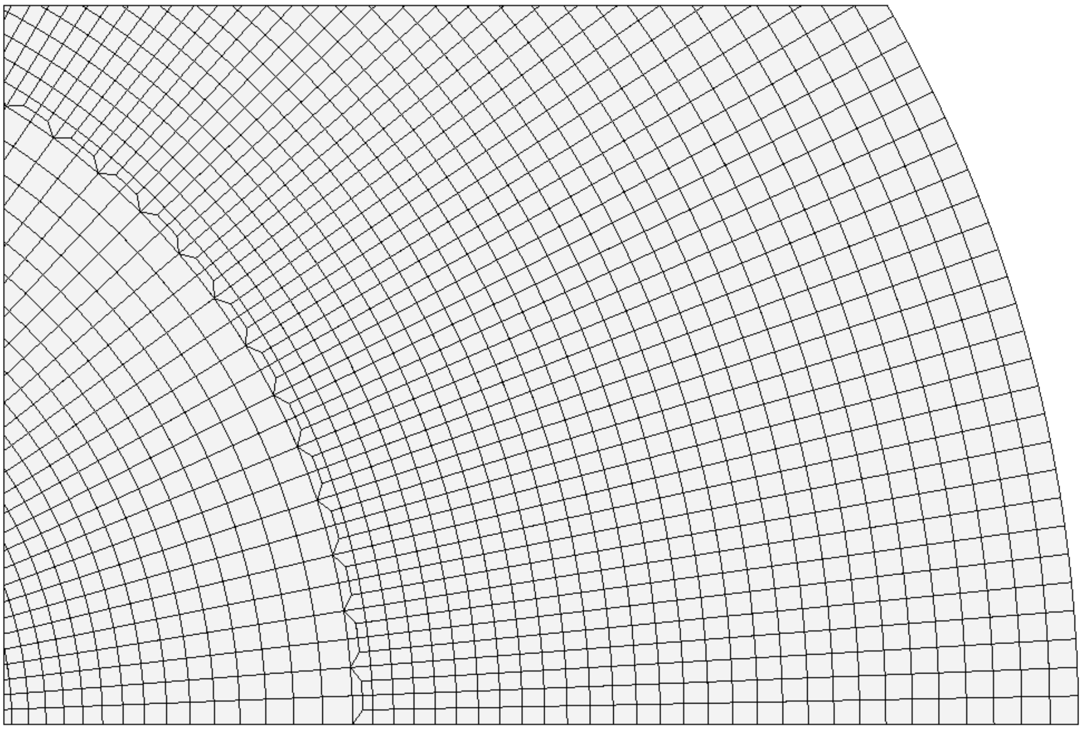

Figure 20 Refinement of brick mesh to avoid tile-shaped elements and shear locking.

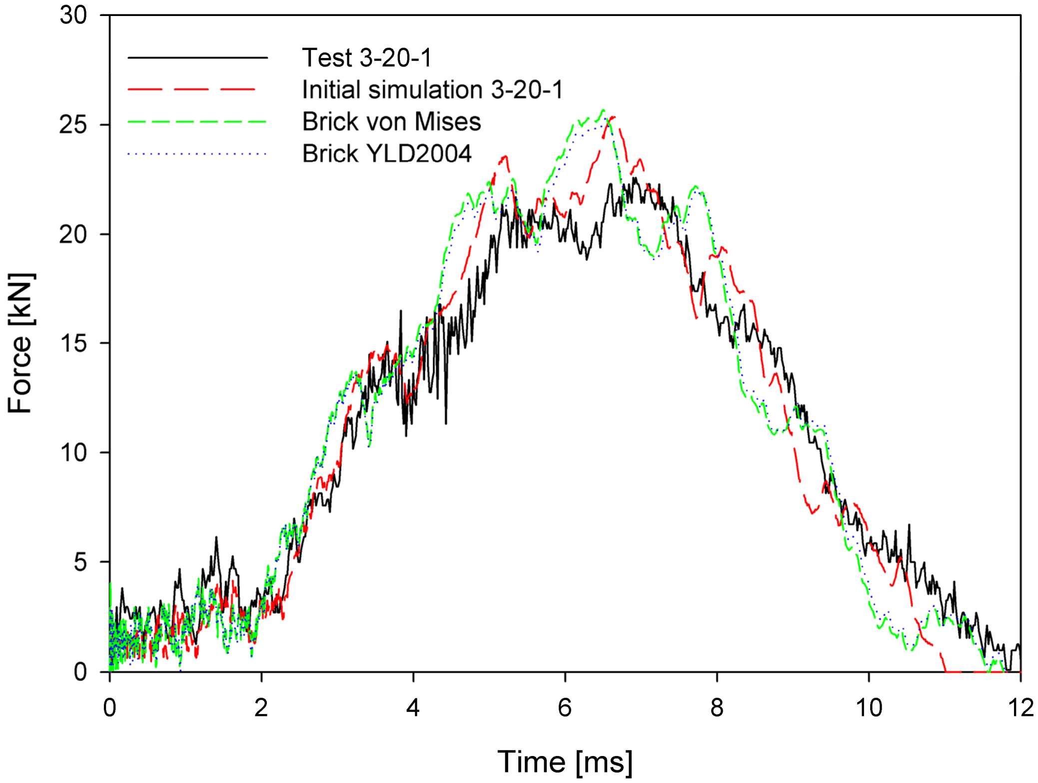

Figure 21 Force versus time curves from the two brick models compared to those obtained in experiments and axisymmetric simulations.

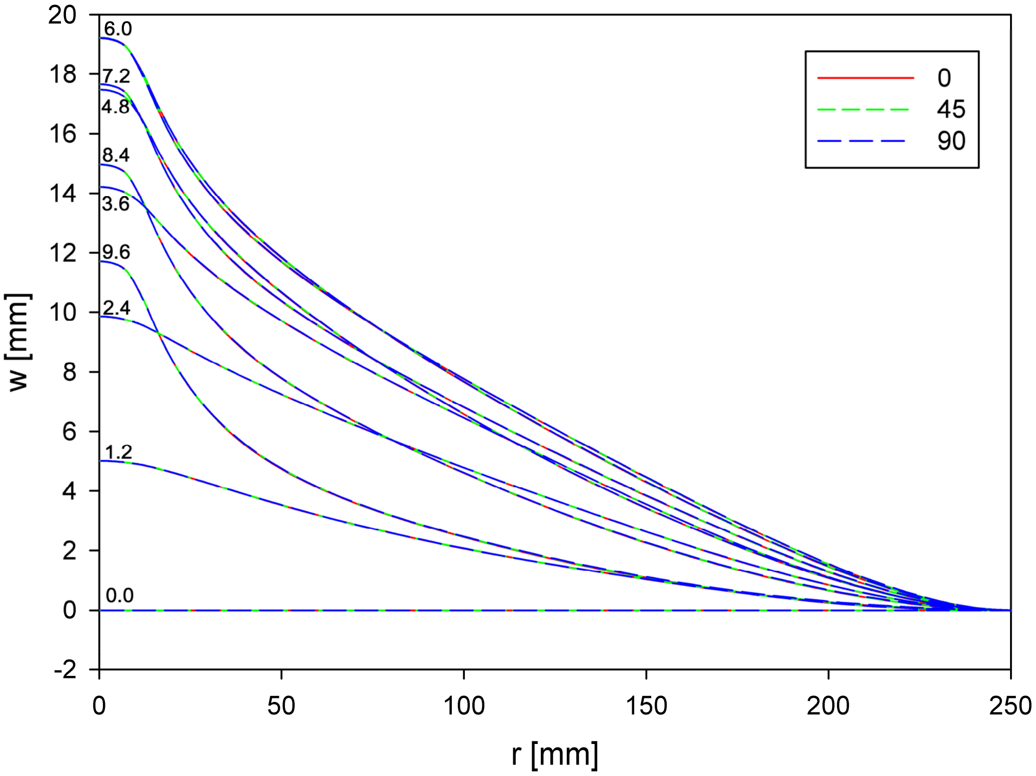

Figure 22 Deformation profiles from the brick model using YLD2004 at every 1.2 ms in three directions with respect to the rolling direction.

4 Concluding remarks

The present study has shown that low velocity impact and penetration problems can be relatively well predicted using simple models for the present material. Good agreement between experimental data and finite element simulations was observed when using the von Mises yield criterion and axisymmetric elements without including neither strain-rate nor temperature effects. However, when omitting strain rate effects in the constitutive equation, the finite element simulations predicted a somewhat stiff response. It has been shown that when including strain rate effects through the proposed constitutive equation, an even better prediction of the force level can be made. It has further been shown that including strain rate effects in the constitutive relation and fracture criterion has a strong impact on fracture predictions. The same is the case for temperature effects. The finite element simulations carried out in the present study indicate that anisotropy plays an insignificant role in low velocity penetration of the present plate material.

Based on the results from the initial simulations, one may jump to the conclusion that low velocity penetration problems are simple and easy to model using the finite element method. However, it has been shown that low velocity penetration problems are in fact very complex and that we are far from understanding the processes taking place during perforation. From an engineering point of view, the simple models may suffice. However, it is difficult to tell when one can rely on the models that are clearly based on incorrect assumptions.

Note that only plugging failure has been investigated in the present study. The effect of temperature, strain rate and anisotropy on other types of failure, like for instance petaling, remains unknown.

Acknowledgements

The financial support of this work from the Research Council of Norway, SIMLab – Centre for Research-based Innovation, NTNU and the Norwegian Defence Estates Agency is gratefully acknowledged. The authors would also like to thank Professor A. H. Clausen who provided experimental data on AA5083-H116.

References

[1] Wen, H-M., Jones, N. Experimental Investigations into the Dynamic Plastic Response and Perforation of a Clamped Circular Plate Struck by a Mass. Journal of Mechanical Engineering Science. 1994;208(C2):113-137.
[2] Wen, H-M., Jones, N. Low-Velocity Perforation of Punch-Impact-Loaded Metal Plates. Journal of Pressure Vessel Technology.1996;118:181-187.
[3] Langseth, M., Larsen, P. K. Dropped objects' plugging capacity of steel plates: An experimental investigation. Int. J. Impact Eng. 1990;9(3):289-316.
[4] Langseth, M., Larsen, P. K. The behaviour of square steel plates subjected to a circular blunt ended load. Int. J. Impact Eng. 1992;12(4):617-638.
[5] Langseth, M., Larsen, P. K. Dropped objects' plugging capacity of aluminium alloy plates. Int. J. Impact Eng. 1994;15(3):221-241.
[6] Langseth, M., Hopperstad, O.S., Berstad, T. Impact loading of plates: Validation of numerical simulations by testing. International Journal of Offshore and Polar Engineering. 1999;9(1):10-15.
[7] Goldsmith W. Review: Non-ideal projectile impact on targets. Int J Impact Eng 1999;22:95-395.
[8] Backman ME, Goldsmith W. The mechanics of penetration of projectiles into targets. Int. J. Eng. Sci. 1978;16:1-99.
[9] Corbett GG, Reid SR, Johnson W. Impact loading of plates and shells by free-flying projectiles. Int. J. Impact Eng. 1996;18(2):141-230.
[10] Zukas JA et al. Impact dynamics, John Wiley & Sons, New York; 1982.

[11] Zukas JA et al. High velocity impact dynamics, John Wiley & Sons, New York; 1990.

[12] Børvik, T., Clausen, A.H., Hopperstad, O., Langseth, M. Perforation of AA5083-H116 aluminium plates with conical-nose steel projectiles—experimental study. Int. J. Impact Eng. 2004;30(4):367-384.

[13] Hatch, JE. Aluminium: properties and physical metallurgy. Am. Soc. Metals. 1984;353–357.

[14] Cottrell, A.H. A note on the Portevin–Le Chatelier effect. Philosophical Magazine (seventh series) 1953;44(335):829–832.

[15] Van den Beukel, A. Theory of effect of dynamic strain aging on mechanical-properties. Physica status solidi (A) 1975;30:197.

[16] McCormick, P.G. Theory of flow localisation due to dynamic strain ageing. Acta metal. 1988;36(12):3061-3067.

[17] Mesarovic, S.DJ. Dynamic strain aging and plastic instabilities. J. Mech. Phys. Solids. 1995;43(5):671-700.

[18] Rizzi, E., Hähner, P. On the Portevin-Le Chatelier effect: theoretical modeling and numerical results. Int. J. Plasticity 2004;20:121-165.

[19] Benallal, A., Berstad, T., Børvik, T., Clausen, AH., Hopperstad, OS. Dynamic strain aging and related instabilities: experimental, theoretical and numerical aspects. Eur. J. Mech.—A/Solids 2006;25(3):397–424.

[20] Clausen, AH., Børvik, T., Hopperstad, OS., Benallal, A. Flow and fracture characteristics of aluminium alloy AA5083-H116 as function of strain rate, temperature and triaxiality. Mat. Sci. Eng. A 2004;365:260–272.

[21] Søvik, O.P, 1996. Numerical modelling of ductile fracture – a damage mechanics approach. Dr. ing. thesis 1996-78. Department of Machine Design and Materials Technology, Norwegian Uniaversity of Science and Technology, Trondheim, Norway, ISBN 82-7119-968-4.

[22] Børvik, T., Hopperstad, O.S., Berstad, T., Langseth, M. A computational model of viscoplasticity and ductile damage for impact and penetration. Eur. J. Mech. A/Solids 2001;20:685-712.

[23] Bridgman, PW. Studies in large plastic flow and fracture. Harvard University Press, Cambridge,1964.

[24] Johnson GR, Cook WH. A constitutive model and data for metals subjected to large strains, high strain rates and high temperatures. In: Proceedings of 7th Int. Sym. Ballistics, The Hague, 1983.

[25] Johnson GR, Cook WH. Fracture characteristics of three metals subjected to various strains, strain rates, temperatures and pressures. Eng. Frac. Mech. 1985;21:31-48.

[26] Barlat, F., Aretz, H., Yoon, J.W., Karabin, M.E., Brem, J.C. and Dick, R.E. Linear transformation-based anisotropic yield functions. Int. J. Plasticity, 2005;21:1009–1039.

[27] Belytschko, T., Liu, W.K., Moran, B.Nonlinear Finite Elements for Continua and Structures. John Wiley & Sons. 2000.

[28] Kapoor, R. and Nemat-Nasser, S. Determination of temperature rise during high strain rate deformation. Mechanics of Materials. 1998;27:1-12.

[29] Lemaitre, J., Chaboche, J.L. Mechanics of Solid Materials. Cambridge University Press, 1990.

[30] Livermore Software Technology Corporation (LSTC). LS-DYNA Keyword User's Manual, Version 971, 2007.
[31] Bao, Y., Wierzbicki, T. On the cut-off value of negative triaxiality for fracture. Eng. Frac. Mech. 2005;72(7):1049-1069.
[32] Grytten, F., Fagerholt, E., Auestad, T., Førre, B., Børvik, T. Out-of-plane deformation measurements of an aluminium plate during quasi-static perforation using structured light and close-range photogrammetry. Int. J. Solids and Structures. 2007;44:5752-5773.

DEPARTMENT OF STRUCTURAL ENGINEERING
NORWEGIAN UNIVERSITY OF SCIENCE AND TECHNOLOGY

N–7491 TRONDHEIM, NORWAY
Telephone: +47 73 59 47 00   Telefax: +47 73 59 47 01

"Reliability Analysis of Structural Systems using Nonlinear Finite Element Methods",
C. A. Holm, 1990:23, ISBN 82-7119-178-0.

"Uniform Stratified Flow Interaction with a Submerged Horizontal Cylinder",
Ø. Arntsen, 1990:32, ISBN 82-7119-188-8.

"Large Displacement Analysis of Flexible and Rigid Systems Considering Displacement-Dependent Loads and Nonlinear Constraints", K. M. Mathisen, 1990:33, ISBN 82-7119-189-6.

"Solid Mechanics and Material Models including Large Deformations",
E. Levold, 1990:56, ISBN 82-7119-214-0, ISSN 0802-3271.

"Inelastic Deformation Capacity of Flexurally-Loaded Aluminium Alloy Structures",
T. Welo, 1990:62, ISBN 82-7119-220-5, ISSN 0802-3271.

"Visualization of Results from Mechanical Engineering Analysis",
K. Aamnes, 1990:63, ISBN 82-7119-221-3, ISSN 0802-3271.

"Object-Oriented Product Modeling for Structural Design",
S. I. Dale, 1991:6, ISBN 82-7119-258-2, ISSN 0802-3271.

"Parallel Techniques for Solving Finite Element Problems on Transputer Networks",
T. H. Hansen, 1991:19, ISBN 82-7119-273-6, ISSN 0802-3271.

"Statistical Description and Estimation of Ocean Drift Ice Environments",
R. Korsnes, 1991:24, ISBN 82-7119-278-7, ISSN 0802-3271.

“Properties of concrete related to fatigue damage: with emphasis on high strength concrete”,
G. Petkovic, 1991:35, ISBN 82-7119-290-6, ISSN 0802-3271.

"Turbidity Current Modelling",
B. Brørs, 1991:38, ISBN 82-7119-293-0, ISSN 0802-3271.

"Zero-Slump Concrete: Rheology, Degree of Compaction and Strength. Effects of Fillers as Part Cement-Replacement",
C. Sørensen, 1992:8, ISBN 82-7119-357-0, ISSN 0802-3271.

"Nonlinear Analysis of Reinforced Concrete Structures Exposed to Transient Loading",
K. V. Høiseth, 1992:15, ISBN 82-7119-364-3, ISSN 0802-3271.

"Finite Element Formulations and Solution Algorithms for Buckling and Collapse Analysis of Thin Shells", R. O. Bjærum, 1992:30, ISBN 82-7119-380-5, ISSN 0802-3271.

"Response Statistics of Nonlinear Dynamic Systems",
J. M. Johnsen, 1992:42, ISBN 82-7119-393-7, ISSN 0802-3271.

"Digital Models in Engineering. A Study on why and how engineers build and operate digital models for decisison support", J. Høyte, 1992:75, ISBN 82-7119-429-1, ISSN 0802-3271.

"Sparse Solution of Finite Element Equations",
A. C. Damhaug, 1992:76, ISBN 82-7119-430-5, ISSN 0802-3271.

"Some Aspects of Floating Ice Related to Sea Surface Operations in the Barents Sea",
S. Løset, 1992:95, ISBN 82-7119-452-6, ISSN 0802-3271.

"Modelling of Cyclic Plasticity with Application to Steel and Aluminium Structures",
O. S. Hopperstad, 1993:7, ISBN 82-7119-461-5, ISSN 0802-3271.

"The Free Formulation: Linear Theory and Extensions with Applications to Tetrahedral Elements with Rotational Freedoms", G. Skeie, 1993:17, ISBN 82-7119-472-0, ISSN 0802-3271.

"Høyfast betongs motstand mot piggdekkslitasje. Analyse av resultater fra prøving i Veisliter'n",
T. Tveter, 1993:62, ISBN 82-7119-522-0, ISSN 0802-3271.

"A Nonlinear Finite Element Based on Free Formulation Theory for Analysis of Sandwich Structures", O. Aamlid, 1993:72, ISBN 82-7119-534-4, ISSN 0802-3271.

"The Effect of Curing Temperature and Silica Fume on Chloride Migration and Pore Structure of High Strength Concrete", C. J. Hauck, 1993:90, ISBN 82-7119-553-0, ISSN 0802-3271.

"Failure of Concrete under Compressive Strain Gradients",
G. Markeset, 1993:110, ISBN 82-7119-575-1, ISSN 0802-3271.

"An experimental study of internal tidal amphidromes in Vestfjorden",
J. H. Nilsen, 1994:39, ISBN 82-7119-640-5, ISSN 0802-3271.

"Structural analysis of oil wells with emphasis on conductor design",
H. Larsen, 1994:46, ISBN 82-7119-648-0, ISSN 0802-3271.

"Adaptive methods for non-linear finite element analysis of shell structures",
K. M. Okstad, 1994:66, ISBN 82-7119-670-7, ISSN 0802-3271.

"On constitutive modelling in nonlinear analysis of concrete structures",
O. Fyrileiv, 1994:115, ISBN 82-7119-725-8, ISSN 0802-3271.

"Fluctuating wind load and response of a line-like engineering structure with emphasis on motion-induced wind forces",
J. Bogunovic Jakobsen, 1995:62, ISBN 82-7119-809-2, ISSN 0802-3271.

"An experimental study of beam-columns subjected to combined torsion, bending and axial actions", A. Aalberg, 1995:66, ISBN 82-7119-813-0, ISSN 0802-3271.

"Scaling and cracking in unsealed freeze/thaw testing of Portland cement and silica fume concretes", S. Jacobsen, 1995:101, ISBN 82-7119-851-3, ISSN 0802-3271.

"Damping of water waves by submerged vegetation. A case study of laminaria hyperborea",
A. M. Dubi, 1995:108, ISBN 82-7119-859-9, ISSN 0802-3271.

"The dynamics of a slope current in the Barents Sea",
Sheng Li, 1995:109, ISBN 82-7119-860-2, ISSN 0802-3271.

"Modellering av delmaterialenes betydning for betongens konsistens",
Ernst Mørtsell, 1996:12, ISBN 82-7119-894-7, ISSN 0802-3271.

"Bending of thin-walled aluminium extrusions",
Birgit Søvik Opheim, 1996:60, ISBN 82-7119-947-1, ISSN 0802-3271.

"Material modelling of aluminium for crashworthiness analysis",
Torodd Berstad, 1996:89, ISBN 82-7119-980-3, ISSN 0802-3271.

"Estimation of structural parameters from response measurements on submerged floating tunnels",
Rolf Magne Larssen, 1996:119, ISBN 82-471-0014-2, ISSN 0802-3271.

“Numerical modelling of plain and reinforced concrete by damage mechanics”,
Mario A. Polanco-Loria, 1997:20, ISBN 82-471-0049-5, ISSN 0802-3271.

“Nonlinear random vibrations - numerical analysis by path integration methods”,
Vibeke Moe, 1997:26, ISBN 82-471-0056-8, ISSN 0802-3271.

“Numerical prediction of vortex-induced vibration by the finite element method”,
Joar Martin Dalheim, 1997:63, ISBN 82-471-0096-7, ISSN 0802-3271.

“Time domain calculations of buffeting response for wind sensitive structures”,
Ketil Aas-Jakobsen, 1997:148, ISBN 82-471-0189-0, ISSN 0802-3271.

"A numerical study of flow about fixed and flexibly mounted circular cylinders",
Trond Stokka Meling, 1998:48, ISBN 82-471-0244-7, ISSN 0802-3271.

“Estimation of chloride penetration into concrete bridges in coastal areas”,
Per Egil Steen, 1998:89, ISBN 82-471-0290-0, ISSN 0802-3271.

“Stress-resultant material models for reinforced concrete plates and shells”,
Jan Arve Øverli, 1998:95, ISBN 82-471-0297-8, ISSN 0802-3271.

“Chloride binding in concrete. Effect of surrounding environment and concrete composition”,
Claus Kenneth Larsen, 1998:101, ISBN 82-471-0337-0, ISSN 0802-3271.

“Rotational capacity of aluminium alloy beams”,
Lars A. Moen, 1999:1, ISBN 82-471-0365-6, ISSN 0802-3271.

“Stretch Bending of Aluminium Extrusions”,
Arild H. Clausen, 1999:29, ISBN 82-471-0396-6, ISSN 0802-3271.

“Aluminium and Steel Beams under Concentrated Loading”,
Tore Tryland, 1999:30, ISBN 82-471-0397-4, ISSN 0802-3271.

"Engineering Models of Elastoplasticity and Fracture for Aluminium Alloys",
Odd-Geir Lademo, 1999:39, ISBN 82-471-0406-7, ISSN 0802-3271.

"Kapasitet og duktilitet av dybelforbindelser i trekonstruksjoner",
Jan Siem, 1999:46, ISBN 82-471-0414-8, ISSN 0802-3271.

“Etablering av distribuert ingeniørarbeid; Teknologiske og organisatoriske erfaringer fra en norsk ingeniørbedrift”, Lars Line, 1999:52, ISBN 82-471-0420-2, ISSN 0802-3271.

“Estimation of Earthquake-Induced Response”, Símon Ólafsson, 1999:73, ISBN 82-471-0443-1, ISSN 0802-3271.

“Coastal Concrete Bridges: Moisture State, Chloride Permeability and Aging Effects”
Ragnhild Holen Relling, 1999:74, ISBN 82-471-0445-8, ISSN 0802-3271.

”Capacity Assessment of Titanium Pipes Subjected to Bending and External Pressure”,
Arve Bjørset, 1999:100, ISBN 82-471-0473-3, ISSN 0802-3271.

“Validation of Numerical Collapse Behaviour of Thin-Walled Corrugated Panels”,
Håvar Ilstad, 1999:101, ISBN 82-471-0474-1, ISSN 0802-3271.

“Strength and Ductility of Welded Structures in Aluminium Alloys”,
Miroslaw Matusiak, 1999:113, ISBN 82-471-0487-3, ISSN 0802-3271.

“Thermal Dilation and Autogenous Deformation as Driving Forces to Self-Induced Stresses in High Performance Concrete”,
Øyvind Bjøntegaard, 1999:121, ISBN 82-7984-002-8, ISSN 0802-3271.

“Some Aspects of Ski Base Sliding Friction and Ski Base Structure”,
Dag Anders Moldestad, 1999:137, ISBN 82-7984-019-2, ISSN 0802-3271.

"Electrode reactions and corrosion resistance for steel in mortar and concrete",
Roy Antonsen, 2000:10, ISBN 82-7984-030-3, ISSN 0802-3271.

"Hydro-Physical Conditions in Kelp Forests and the Effect on Wave Damping and Dune Erosion. A case study on Laminaria Hyperborea",
Stig Magnar Løvås, 2000:28, ISBN 82-7984-050-8, ISSN 0802-3271.

"Random Vibration and the Path Integral Method",
Christian Skaug, 2000:39, ISBN 82-7984-061-3, ISSN 0802-3271.

"Buckling and geometrical nonlinear beam-type analyses of timber structures",
Trond Even Eggen, 2000:56, ISBN 82-7984-081-8, ISSN 0802-3271.

”Structural Crashworthiness of Aluminium Foam-Based Components”,
Arve Grønsund Hanssen, 2000:76, ISBN 82-7984-102-4, ISSN 0809-103X.

“Measurements and simulations of the consolidation in first-year sea ice ridges, and some aspects of mechanical behaviour”, Knut V. Høyland, 2000:94, ISBN 82-7984-121-0, ISSN 0809-103X.

”Kinematics in Regular and Irregular Waves based on a Lagrangian Formulation”,
Svein Helge Gjøsund, 2000-86, ISBN 82-7984-112-1, ISSN 0809-103X.

”Self-Induced Cracking Problems in Hardening Concrete Structures”,
Daniela Bosnjak, 2000-121, ISBN 82-7984-151-2, ISSN 0809-103X.

"Ballistic Penetration and Perforation of Steel Plates",
Tore Børvik, 2000:124, ISBN 82-7984-154-7, ISSN 0809-103X.

"Freeze-Thaw resistance of Concrete. Effect of: Curing Conditions, Moisture Exchange and Materials", Terje Finnerup Rønning, 2001:14, ISBN 82-7984-165-2, ISSN 0809-103X

Structural behaviour of post tensioned concrete structures. Flat slab. Slabs on ground",
Steinar Trygstad, 2001:52, ISBN 82-471-5314-9, ISSN 0809-103X.

"Slipforming of Vertical Concrete Structures. Friction between concrete and slipform panel",
Kjell Tore Fosså, 2001:61, ISBN 82-471-5325-4, ISSN 0809-103X.

"Some numerical methods for the simulation of laminar and turbulent incompressible flows",
Jens Holmen, 2002:6, ISBN 82-471-5396-3, ISSN 0809-103X.

“Improved Fatigue Performance of Threaded Drillstring Connections by Cold Rolling”,
Steinar Kristoffersen, 2002:11, ISBN: 82-421-5402-1, ISSN 0809-103X.

"Deformations in Concrete Cantilever Bridges: Observations and Theoretical Modelling",
Peter F. Takâcs, 2002:23, ISBN 82-471-5415-3, ISSN 0809-103X.

"Stiffened aluminium plates subjected to impact loading",
Hilde Giæver Hildrum, 2002:69, ISBN 82-471-5467-6, ISSN 0809-103X.

"Full- and model scale study of wind effects on a medium-rise building in a built up area",
Jónas Thór Snæbjørnsson, 2002:95, ISBN82-471-5495-1, ISSN 0809-103X.

“Evaluation of Concepts for Loading of Hydrocarbons in Ice-infested water”,
Arnor Jensen, 2002:114, ISBN 82-417-5506-0, ISSN 0809-103X.

”Numerical and Physical Modelling of Oil Spreading in Broken Ice”,
Janne K. Økland Gjøsteen, 2002:130, ISBN 82-471-5523-0, ISSN 0809-103X.

”Diagnosis and protection of corroding steel in concrete”,
Franz Pruckner, 20002:140, ISBN 82-471-5555-4, ISSN 0809-103X.

“Tensile and Compressive Creep of Young Concrete: Testing and Modelling”,
Dawood Atrushi, 2003:17, ISBN 82-471-5565-6, ISSN 0809-103X.

“Rheology of Particle Suspensions. Fresh Concrete, Mortar and Cement Paste with Various Types of Lignosulfonates”,
Jon Elvar Wallevik, 2003:18, ISBN 82-471-5566-4, ISSN 0809-103X.

“Oblique Loading of Aluminium Crash Components”, Aase Reyes, 2003:15, ISBN 82-471-5562-1, ISSN 0809-103X.

“Utilization of Ethiopian Natural Pozzolans”, Surafel Ketema Desta, 2003:26,
ISSN 82-471-5574-5, ISSN:0809-103X.

“Behaviour and strength prediction of reinforced concrete structures with discontinuity regions”,
Helge Brå, 2004:11, ISBN 82-471-6222-9, ISSN 1503-8181.

“High-strength steel plates subjected to projectile impact. An experimental and numerical study”,
Sumita Dey, 2004:38, ISBN 82-471-6281-4 (elektr. Utg.), ISBN 82-471-6282-2 (trykt utg.),
ISSN 1503-8181.

“Alkali-reactive and inert fillers in concrete. Rheology of fresh mixtures and expansive reactions.”
Bård M. Pedersen, 2004:92, ISBN 82-471-6401-9 (trykt utg.), ISBN 82-471-6400-0 (elektr. utg.),
ISSN 1503-8181.

“On the Shear Capacity of Steel Girders with Large Web Openings”. Nils Christian Hagen, 2005:9
ISBN 82-471-6878-2 (trykt utg.), ISBN 82-471-6877-4 (elektr. utg.), ISSN 1503-8181.

”Behaviour of aluminium extrusions subjected to axial loading”. Østen Jensen, 2005:7, ISBN 82-471-6872-3 (elektr. utg.) , ISBN 82-471-6873-1 (trykt utg.), ISSN 1503-8181.

”Thermal Aspects of corrosion of Steel in Concrete”. Jan-Magnus Østvik, 2005:5, ISBN 82-471-6869-3 (trykt utg.) ISBN 82-471-6868 (elektr.utg), ISSN 1503-8181.

”Mechanical and adaptive behaviour of bone in relation to hip replacement.” A study of bone remodelling and bone grafting. Sébastien Muller, 2005:34, ISBN 82-471-6933-9 (trykt utg.) (ISBN 82-471-6932-0 (elektr.utg), ISSN 1503-8181.

“Analysis of geometrical nonlinearities with applications to timber structures”. Lars Wollebæk, 2005:74, ISBN 82-471-7050-5 (trykt utg.), ISBN 82-471-7019-1 (elektr. Utg.), ISSN 1503-8181.

“Pedestrian induced lateral vibrations of slender footbridges”, Anders Rönnquist, 2005:102, ISBN 82-471-7082-5 (trykt utg.), ISBN 82-471-7081-7 (elektr.utg.), ISSN 1503-8181.

“Initial Strength Development of Fly Ash and Limestone Blended Cements at Various Temperatures Predicted by Ultrasonic Pulse Velocity”, Tom Ivar Fredvik, 2005:112, ISBN 82-471-7105-8 (trykt utg.), ISBN 82-471-7103-1 (elektr.utg.), ISSN 1503-8181.

“Behaviour and modelling of thin-walled cast components”, Cato Dørum, 2005:128, ISBN 82-471-7140-6 (trykt utg.), ISBN 82-471-7139-2 (elektr. utg.), ISSN 1503-8181.

“Behaviour and modelling of selfpiercing riveted connections”, Raffaele Porcaro, 2005:165, ISBN 82-471-7219-4 (trykt utg.), ISBN 82-471-7218-6 (elektr.utg.), ISSN 1503-8181.

”Behaviour and Modelling og Aluminium Plates subjected to Compressive Load”, Lars Rønning, 2005:154, ISBN 82-471-7169-1 (trykt utg.), ISBN 82-471-7195-3 (elektr.utg.), ISSN 1503-8181

”Bumper beam-longitudinal system subjected to offset impact loading”, Satyanarayana Kokkula, 2005:193, ISBN 82-471-7280-1 (trykt utg.), ISBN 82-471-7279-8 (elektr.utg.), ISSN 1503-8181.

“Control of Chloride Penetration into Concrete Structures at Early Age”, Guofei Liu, 2006:46, ISBN 82-471-7838-9 (trykt utg.), ISBN 82-471-7837-0 (elektr. utgave), ISSN 1503-8181.

“Modelling of Welded Thin-Walled Aluminium Structures”, Ting Wang, 2006:78, ISBN 82-471-7907-5 (trykt utg.), ISBN 82-471-7906-7 (elektr.utg.), ISSN 1503-8181.

”Time-variant reliability of dynamic systems by importance sampling and probabilistic analysis of ice loads”, Anna Ivanova Olsen, 2006:139, ISBN 82-471-8041-3 (trykt utg.), ISBN 82-471-8040-5 (elektr.utg.), ISSN 1503-8181.

“Fatigue life prediction of an aluminium alloy automotive component using finite element analysis of surface topography”. Sigmund Kyrre Ås, 2006:25, ISBN 82-471-7791-9 (trykt utg.), ISBN 82-471-7791-9 (elektr.utg.), ISSN 1503-8181.

”Constitutive models of elastoplasticity and fracture for aluminium alloys under strain path change”, Dasharatha Achani, 2006:76, ISBN 82-471-7903-2 (trykt utg.), ISBN 82-471-7902-4 (elektr.utg.), ISSN 1503-8181.
“Simulations of 2D dynamic brittle fracture by the Element-free Galerkin method and linear fracture mechanics”, Tommy Karlsson, 2006:125, ISBN 82-471-8011-1 (trykt utg.), ISBN 82-471-8010-3 (elektr.utg.), ISSN 1503-8181.

“Penetration and Perforation of Granite Targets by Hard Projectiles”, Chong Chiang Seah, 2006:188, ISBN 82-471-8150-9 (printed ver.), ISBN 82-471-8149-5 (electronic ver.) ISSN 1503-8181.

“Deformations, strain capacity and cracking of concrete in plastic and early hardening phases”, Tor Arne Hammer, 2007:234, ISBN 978-82-471-5191-4 (trykt utg.), ISBN 978-82-471-5207-2 (elektr.utg.) ISSN 1503-8181.

“Crashworthiness of dual-phase high-strength steel: Material and Component behaviour”, Venkatapathi Tarigopula, 2007:230, ISB 82-471-5076-4 (trykt utg.) ISBN 82-471-5093-1 (elektr.utg.) ISSN 1503-8181.

“Fibre reinforcement in load carrying concrete structures”, Døssland, Åse Lyslo, 2008:50, ISBN 978-82-471-6910-0 (trykt utg.) 2008:50 ISBN 978-82-471-6924-7 (elektr. utg), ISSN 1503-8181.